
Theses and Dissertations

Spring 2014

Heterogeneous chemistry and photochemistry of atmospherically relevant gases on oxide surfaces

Charith Eranga Nanayakkara
University of Iowa

Copyright 2014 Charith Eranga Nanayakkara

This dissertation is available at Iowa Research Online: <http://ir.uiowa.edu/etd/4705>

Recommended Citation

Nanayakkara, Charith Eranga. "Heterogeneous chemistry and photochemistry of atmospherically relevant gases on oxide surfaces."
PhD (Doctor of Philosophy) thesis, University of Iowa, 2014.
<http://ir.uiowa.edu/etd/4705>.

Follow this and additional works at: <http://ir.uiowa.edu/etd>

 Part of the [Chemistry Commons](#)

HETEROGENEOUS CHEMISTRY AND PHOTOCHEMISTRY OF
ATMOSPHERICALLY RELEVANT GASES ON OXIDE SURFACES

by

Charith Eranga Nanayakkara

A thesis submitted in partial fulfillment
of the requirements for the Doctor of
Philosophy degree in Chemistry
in the Graduate College of
The University of Iowa

May 2014

Thesis Supervisor: Professor Vicki H. Grassian

Copyright by
CHARITH ERANGA NANAYAKKARA
2014
All Rights Reserved

Graduate College
The University of Iowa
Iowa City, Iowa

CERTIFICATE OF APPROVAL

PH.D. THESIS

This is to certify that the Ph.D. thesis of

Charith Eranga Nanayakkara

has been approved by the Examining Committee
for the thesis requirement for the Doctor of
Philosophy degree in Chemistry
at the May 2014 graduation.

Thesis Committee:

Vicki H. Grassian, Thesis Supervisor

Sarah C. Larsen

Edward G. Gillan

Christopher M. Cheatum

David M. Cwiertny

To my Wife,
and
Parents

ACKNOWLEDGMENTS

First and foremost, I would like to thank my advisor, Professor Vicki Grassian, for all the opportunities and the learning experiences that I received to become the scientist that I am today. I am truly happy about joining the Grassian group. My success has come from your direction, guidance, and challenges that pushed me to a level that I would be able to accomplish. Many thanks also to my past and present committee members, Professors Sarah Larsen, Edward Gillan, Christopher Cheatum, Gary Small, and David Cwiertny, for all of your support, encouragement, conversations, and help whenever I walked into your office.

A special thank you goes to former and present members of the Grassian research group, for the great help and friendship. A special thank you to Dr. Jonas Baltrusaitis, Dr. Pragati Galhotra, and Dr. Gayan Rubasinghege for all the experiences I gathered from you while working in the lab.

I wish to thank all my school teachers from my childhood to the high school, at the Preschool and Primary School, Deraniyagala, President's College, Rajagiriya, and D.S. Senanayake College, Colombo. Furthermore, I would like to thank all the Professors who instructed me at the University of Kelaniya and University of Iowa.

In addition, I would like to express my gratitude to several former and present staff members at the University of Iowa, Janet Kugley, Earlene Erbe, Sharon Robertson, Mike Estenson, Frank Turner, Peter Hatch, Timothy Koon, Andrew Lynch, Gene Hauge, Benjamin Revis, David Sansbury, Jackie Jensen and Bryan Ringen. I appreciate their help, patience, and support.

Most importantly, a very special thank you for my parents for endless support and love from my birthday all the way to this very special moment. You always trusted me, had faith on me, continuously inspired me to pursue the goals in my life and stayed with me in all the happy and sad moments. Then my loving wife Ayeshani, who always stayed by my side, encouraged and supported to complete my experiments, publications, and thesis to achieve best in my career. Special thank to you for the support and understanding throughout my graduate study and encouragement during my thesis writing.

ABSTRACT

Metal oxides in the atmosphere emitted from various natural and anthropogenic processes alter the chemical balance of the Earth's atmosphere due to heterogeneous and photochemical processes with atmospheric trace gases. Therefore, understanding the heterogeneous chemistry and heterogeneous photochemistry of atmospheric trace gases on these oxide surfaces has become vital to precisely predict the effect of mineral dust loading on the Earth's atmosphere. Among the various components of mineral dust, light absorbing oxides play a significantly important role during the daytime.

The work reported herein has focused mainly on TiO_2 and $\alpha\text{-Fe}_2\text{O}_3$. These are light adsorbing components found in atmospheric mineral dust. Apart from being a component of mineral dust, TiO_2 is heavily used in a number of industrial applications ranging from uses in self-cleaning, water purification to cosmetics. These applications have led to their presence in the atmosphere as anthropogenic dust particles and in contact with the atmosphere as a stationary phase. Iron-containing particles are transferred to the atmosphere mainly from wind and volcanic activities in the form of iron-containing mineral dust and volcanic ash aerosols. $\alpha\text{-Fe}_2\text{O}_3$ is the most stable iron containing compound found in the Earth's crust which constitutes in significant amounts in mineral dust. The presence of these oxide surfaces in the atmosphere can play a major role in heterogeneous chemistry and photochemistry.

In this dissertation research, transmission FTIR spectroscopy and X-ray photoelectron spectroscopy are used to probe the details of heterogeneous chemistry and photochemistry of CO_2 , SO_2 , NO_2 , HCOOH , and HNO_3 on titanium dioxide and hematite

surfaces. Adsorption sites, surface speciation and surface species stability have been determined from analysis of FTIR and XPS spectra. Isotope labeling experiments were also carried out in order to obtain mechanistic information about the details of surface hydroxyl group reactivity on these oxide particle surfaces. Furthermore, heterogeneous photochemical reactions of adsorbates from atmospheric trace gas adsorption on TiO_2 and $\alpha\text{-Fe}_2\text{O}_3$ were investigated under the conditions pertinent to troposphere. The role of adsorbed water on the stability of adsorbed species that form as a result of heterogeneous reactions and the effect of relative humidity on photochemistry on these oxide particles surfaces has also been investigated due to its important implications in the atmospheric chemistry of oxide surfaces. The research adds to our overall scientific understanding of the molecular level details of heterogeneous chemistry and photochemistry of light absorbing components in the atmosphere.

TABLE OF CONTENTS

LIST OF TABLES	xi
LIST OF FIGURES	xii
CHAPTER	
1. INTRODUCTION	1
1.1 Metal Oxides in the Atmosphere	1
1.2 Semiconductor Metal Oxides.....	5
1.3 Semiconductor Oxides Studied Under Dissertation Research	7
1.3.1 Titanium Dioxide	7
1.3.2 Titanium-Containing Mineral Dust Aerosol	9
1.3.3 Other Sources of TiO ₂ in the Atmosphere	11
1.3.4 Sources of TiO ₂ Particles in Contact with the Atmosphere	12
1.3.5 Iron Oxide	14
1.3.6 Iron-Containing Mineral Dust Aerosol	15
1.3.7 Iron from Fly Ash	16
1.3.8 Iron Deposition into Aqueous Environment	17
1.4 Atmospheric Trace Gases	19
1.4.1 Roles of Water Vapor and Molecular Oxygen	23
1.4.2 Atmospherically Processed Particles in Aqueous Environment	24
1.5 Thesis Overview and Objectives	24
2. EXPERIMENTAL METHODS	27
2.1 Fourier Transform Infrared (FTIR) Spectroscopy	27
2.1.1 Transmission FTIR Spectroscopy: Experimental Setup	28
2.1.2 Experimental Method.....	31
2.1.3 Transmission FTIR Spectroscopy: Photochemical Studies	33
2.2 Quartz Crystal Microbalance (QCM) Measurements	34
2.2.1 Flow cell for QCM Measurements	34
2.2.2 QCM Analysis and the Sauerbrey Equation	34
2.2.3 Experimental Method.....	35
2.3 X-ray Photoelectron Spectroscopy	37
2.3.1 XPS Experimental Setup.....	38
2.3.2 Data Processing of Core Photoelectron Spectra	41
2.3.3 Experimental Method.....	41
2.4 Aqueous Phase Studies of Oxide Particles Reacted with Trace Gases	42

2.4.1	Solution Phase Behavior of Metal Oxide Particles Reacted with Trace Atmospheric Gases	42
2.4.2	Iron Dissolution Experiments	42
2.5	Complementary Physical and Chemical Characterization Techniques	43
2.5.1	Transmission Electron Microscopy (TEM)	43
2.5.2	Scanning Electron Microscopy (SEM)	44
2.5.3	X-ray Diffraction (XRD)	44
2.5.4	Brunauer, Emmett and Teller (BET) Surface Area Measurements	44
2.6	Materials and Reagents	45
2.6.1	Oxide Powders	45
2.6.2	Liquid and Gas Reagents	46
3.	SULFUR DIOXIDE ADSORPTION AND PHOOTOOXIDATION ON ISOTOPICALLY-LABELLED TITANIUM DIOXIDE NANOPARTICLE SURFACES: ROLES OF SURFACE HYDROXYL GROUPS AND ADSORBED WATER IN THE FORMATION AND STABILITY OF ADSORBED SULFITE AND SULFATE	48
3.1	Abstract	48
3.2	Introduction	49
3.3	Experimental Methods	51
3.3.1	Sources and Purity of Gases	51
3.3.2	Source of TiO ₂ and Nanoparticle Characterization	52
3.3.3	Transmission FTIR Spectroscopy	52
3.3.4	X-ray Photoelectron Spectroscopy (XPS)	53
3.4	Results and Discussion	54
3.4.1	Characterization of TiO ₂ Nanoparticles	54
3.4.2	Surface Hydroxyl Groups and Adsorbed Water on TiO ₂ Nanoparticles	54
3.4.3	SO ₂ Adsorption on TiO ₂ Particles	57
3.4.4	Photooxidation of Adsorbed Sulfite/bisulfite	67
3.4.5	Effect of Water Vapor on Adsorbed Sulfite and Sulfate on TiO ₂ Particles	69
3.5	Conclusions and Environmental Implications	74
4.	TITANIUM DIOXIDE NANOPARTICLE REACTIVITY WITH CO ₂ , SO ₂ AND NO ₂ : ROLES OF SURFACE HYDROXYL GROUPS AND ADSORBED WATER IN THE FORMATION AND STABILITY OF ADSORBED PRODUCTS	76
4.1	Abstract	76
4.2	Introduction	77
4.3	Experimental Methods	80
4.3.1	Sources and Purity of Gases	80

4.3.2	Source of TiO ₂ Nanoparticles and Nanoparticle Characterization	80
4.3.3	Adsorption and Surface Chemistry Monitored by Transmission FTIR Spectroscopy.....	80
4.3.4	Quantitative Uptake Measurements Using a Quartz Crystal Microbalance Flow Cell	82
4.4	Results and Discussion	83
4.4.1	Characterization of TiO ₂ Nanoparticles.....	83
4.4.2	Reactivity of Surface Hydroxyl Groups on TiO ₂ Nanoparticles	83
4.4.3	Water Uptake on Particles Reacted with CO ₂ , SO ₂ and NO ₂	96
4.5	Conclusions.....	108
5.	SURFACE ADSORPTION AND PHOTOCHEMISTRY OF FORMIC ACID ON TiO ₂ NANOPARTICLES: THE ROLE OF ADSORBED WATER IN THE ADSORPTION KINETICS, SURFACE COORDINATION MODE AND RATE OF PHOTOPRODUCT FORMATION.....	110
5.1	Abstract	110
5.2	Introduction.....	111
5.3	Experimental Methods	113
5.3.1	Transmission FTIR Spectroscopy.....	113
5.3.2	Solution Phase Studies of Nanomaterial TiO ₂ Previously Reacted with HCOOH	114
5.3.3	Sources of Chemicals.....	114
5.4	Results and Discussion	115
5.4.1	Transmission FTIR Studies of formic Acid Adsorption on TiO ₂ Nanoparticles.....	115
5.4.2	Saturation Coverage and Heterogeneous Reaction Kinetics	124
5.4.3	Photochemistry of Adsorbed Formate under a Range of Environmental Conditions	129
5.4.4	Aqueous Phase Behavior of Formic Acid Reacted Nanomaterial TiO ₂	135
5.5	Conclusions and Atmospheric Implications	137
6.	SURFACE PHOTOCHEMISTRY OF ADSORBED NITRATE: THE ROLE OF ADSORBED WATER IN THE FORMATION OF REDUCED NITROGEN SPECIES ON α -Fe ₂ O ₃ PARTICLE SURFACES	139
6.1	Abstract	139
6.2	Introduction.....	140
6.3	Experimental Methods	142

6.3.1	Surface XPS Analysis Chamber Coupled with Transfer and Reaction Auxiliary Chambers	142
6.3.2	Data Processing of Core Photoelectron Spectra	144
6.3.3	Transmission FTIR Spectroscopy	145
6.3.4	Iron Dissolution Experiments	145
6.3.5	Characterization of α -Fe ₂ O ₃	146
6.3.6	Sources of Chemicals.....	146
6.4	Results and Discussion	147
6.4.1	Characterization of γ -Fe ₂ O ₃	147
6.4.2	XPS of Metal-nitrogen Salt Standards.....	147
6.4.3	XPS of HNO ₃ Acid Reacted α -Fe ₂ O ₃ in the Presence of Environmentally Relevant Pressures of Relative Humidity and Molecular Oxygen	148
6.4.4	Nitrate Photochemistry on α -Fe ₂ O ₃ in the Presence of Environmentally Relevant Pressures of Water Vapor and Molecular Oxygen	151
6.4.5	Aqueous Phase Behavior of HNO ₃ Reacted Hematite Particles.....	163
6.5	Conclusions and Atmospheric Implications	164
7.	CONCLUSIONS AND FUTURE DIRECTIONS	166
	REFERENCES	171

LIST OF TABLES

Table

1.1	Abundance of Major Oxides in the Continental Crust.....	3
1.2	TiO ₂ Distribution within Different Dust Source Regions	10
1.3	Fe ₂ O ₃ Distribution within Different Dust Source Regions.	16
2.1	Source of metal oxide powders with particle and surface area specifications.....	45
3.1	Vibrational assignment of hydroxyl groups, ¹⁶ O-H, O-D and ¹⁸ O-H, on TiO ₂ nanoparticle surfaces	56
3.2	Vibrational frequencies of different adsorbed sulfur-containing species on TiO ₂ nanoparticle surfaces and on other metal oxides surfaces.	65
4.1	Assignment of vibrational frequencies of adsorbed products following the reaction of CO ₂ , SO ₂ and NO ₂ with TiO ₂ nanoparticles	91
4.2	Saturation Surface Coverage for Adsorbed CO ₂ , SO ₂ and NO ₂ on nanomaterial TiO ₂ quantified using QCM at 296 K	94
4.3	Water uptake on TiO ₂ quantified with QCM measurements as a f(%RH) for unreacted and previously reacted with CO ₂ , SO ₂ , and NO ₂	105
5.1	Vibrational Frequencies Assignment of Adsorbed Species after HCOOH Reaction with TiO ₂	119
6.1	Assignment of Binding Energies for N1s, O1s and Fe2p Transitions Observed in this Study.	148
6.2	Percentage Relative Humidity for Water Layer Formation on α-Fe ₂ O ₃ Estimated from Water Adsorption Isotherm Curves Reported in Reference 230	161

LIST OF FIGURES

Figure

1.1	Satellite images of (a) Dust plume is transported off of the west coast of Africa and over the Atlantic Ocean in late September 2011 and (b) Dust from the Gobi desert is transported eastward as shown in late April 2011 raised from both north and south sources of the Mongolia-China border. The images were captured using the Moderate Resolution Imaging Spectroradiometer (MODIS) on NASA's Terra satellite. Reprinted with permission from Visible Earth (http://visibleearth.nasa.gov). Copyright 2011 NASA.....	2
1.2	Cartoon representation of the life cycle of dusts represented in terms of emissions, long-range transport of dust where important yet in some cases poorly understood chemical and physical processes occur and subsequent deposition into aquatic and terrestrial ecosystems. These "aged" dust particles can then undergo deposition into aqueous and terrestrial ecosystems with very different physicochemical properties than the freshly emitted particles. Adapted with permission from Ref. 8. Copyright 2010 American Chemical Society.	4
1.3	Schematic of TiO ₂ photoexcitation to initiate electron-hole pairs (e^-/h^+) and redox chemistry at the TiO ₂ surface. Separated electron-hole pairs at the TiO ₂ surface can result in the reduction of electron acceptors (A) by photogenerated electrons, and the oxidation of electron donors (D) by photogenerated holes. Metal oxide photocatalysis with atmospheric gases has the potential to play an important role in atmospheric chemistry. Adapted with permission from Ref. 7. Copyright 2012 American Chemical Society.	6
1.4	Application of different uses of self-cleaning exterior building materials. (a) The MM Towers, in Yokohama, coated with self-cleaning tiles; (b) The Matsushita Denso building covered with self-cleaning glass; (c) The self-cleaning sound-proof wall; (d) Eco-life-type houses using self-cleaning tiles and glass and; (e) Self-cleaning roof of a train station in Motosumiyoshi. Reprinted from Ref 34, Copyright 2008, with permission from Elsevier	13

1.5	A schematic diagram showing some of the most important processes controlling the speciation of Fe in the atmosphere and its subsequent deposition back to the land and/or ocean. Processes in the source regions include weathering and aging of Fe oxides, which affect the Fe mineralogy of dust, resulting in dust of different potential solubilities. During transport, dust may mix with soot particles from biomass burning and other anthropogenic aerosols. This mixture of particles may also take up sulphate, nitrate and organic ligands. During long range transport, dust undergoes gravitational settling, cloud processing, photo-reduction, and acid uptake/processing. Cycles between dust, particularly aged dust (serving as cloud condensation nuclei, CCN) and clouds through condensation/evaporation processes can occur 5–10 times before the dust is deposited to the ocean. Reprinted from Ref 84, copyright 2008, with permission from Elsevier.....	18
2.1	Schematic of the IR cell used for transmission FTIR studies: 1. A Photoetched tungsten grid held by sample holder jaws (a) the sample side and (b) blank grid side; 2. Infrared incident light; 3. Aluminum screws and holder for the BaF ₂ windows; 4. O-rings to hold the BaF ₂ windows; 5. BaF ₂ window; 6. Stainless steel holder; 7. Stainless steel infrared cube; 8. Holes for clamping the sample holder; 9. Gas inlet/outlet port which is connected to a gas handling system.....	29
2.2	Schematic of the infrared cell and gas handling system used for these studies.	30
2.3	Schematic of the optical path of the light from the mercury arc lamp the infrared cell sitting inside the FTIR spectrometer. The sample is irradiated for certain time intervals after which spectra are then recorded of the gas phase and the oxide surface.....	32
2.4	Irradiance profile of the light source (Hg arc lamp) with and without the broadband UV filter which cutoff wavelength of light below 300 nm.	33
2.5	Schematic of the flow system which allows for simultaneous measurements of quartz crystal microbalance (QCM) and ATR-FTIR spectrometer. Only the QCM portion was used in this dissertation research. Adapted with permission from Ref. 114. Copyright 2012 American Chemical Society.	36
2.6	Schematic of the custom-designed Kratos Axis Ultra XPS. The system consists of four chambers: a transfer antechamber, surface analysis chamber, reaction chamber and Teflon coated HNO ₃ reaction chamber (not shown). Each chamber is equipped with a separate pumping system, pressure gauges and is separated from the other chambers from manual and motorized valves, V2 and V4 respectively. The surface analysis	

	chamber is equipped with X-ray sources, Fe-SEM gun, SE detector, UPS source, ion gun and sample manipulator. See experimental methods section for a more detailed description of this four chamber system. (Note: TMP – turbomolecular pump; CCG – cold cathode gauge; LV – leak valve and V – valve). Adapted from ref. 4 with permission of the PCCP Owner Societies.	40
2.7	Nanoparticle characterization (a) Transmission electron microscopy (TEM) image and (b) X-ray Diffraction (XRD) pattern of TiO ₂	46
2.8	Particle characterization (a) Scanning electron microscope (SEM) image and (b) X-ray diffraction (XRD) pattern of of □-Fe ₂ O ₃	47
3.1	Peak-fitted hydroxyl group region for (a) ¹⁶ O-H stretching vibrations for unlabeled TiO ₂ , (b) ¹⁶ O-D stretching vibrations for deuterated TiO ₂ following D ₂ O exchange, (c) ¹⁸ O-H stretching vibrations for ¹⁸ O labeled TiO ₂ following H ₂ ¹⁸ O exchange. See text for further details.....	55
3.2	Transmission FTIR spectra of TiO ₂ surface as a function of increasing pressure of SO ₂ . Spectra labeled “gas-phase subtracted” were recorded in the presence of the gas phase at initial pressures of 5, 10, 15, 20, 22, 25, 28, 30, 40, and 100 mTorr. The spectra are stacked from lowest initial SO ₂ pressure to highest SO ₂ pressure. The spectrum labeled “gas-phase evacuated” was collected after evacuation of SO ₂ at the highest pressure. These difference spectra show both positive and negative absorptions associated with the formation and loss, respectively of species from the surface. See text for further details.	59
3.3	Peak-fitted hydroxyl group region following reaction with 100 mTorr SO ₂ of (a) ¹⁶ O-H stretching vibrations for unlabeled TiO ₂ , (b) ¹⁶ O-D stretching vibrations for deuterated-TiO ₂ , (c) ¹⁸ O-H stretching vibrations for ¹⁸ O-labeled TiO ₂	60
3.4	Transmission FTIR spectra for TiO ₂ in the presence of gas phase SO ₂ at a pressure of 100 mTorr for (a) SO ₂ adsorbed on TiO ₂ with (b) SO ₂ adsorbed on deuterated-TiO ₂ , and (c) SO ₂ adsorbed on ¹⁸ O-labeled TiO ₂ . Gas-phase absorptions have been subtracted from the spectra.	61
3.5	Transmission FTIR spectra for (a) H ₂ O (b) D ₂ O (c) H ₂ ¹⁸ O adsorption on TiO ₂ surface as a function of increasing relative humidity (0.6, 1.2, 3.1, 10, 26, 56 and 76 %). Spectra were recorded in the presence of gas phase and gas phase was subtracted out.	62
3.6	Transmission FTIR spectra are shown as a function of irradiation time for the TiO ₂ surface containing bisulfite/sulfite species. As discussed in detail in the text, these spectra show the conversion to adsorbed sulfate.	68

3.7	Transmission FTIR spectra of water adsorption as a function of increasing relative humidity on (a) sulfited-TiO ₂ after SO ₂ adsorption and (b) sulfated-TiO ₂ surfaces after irradiation of sulfited-TiO ₂ with light. These spectra show changes with increasing relative humidity of 0.6 to 76 %RH. Following increasing RH, the infrared cell is evacuated to less than 0.6 %RH. These spectra are shown as the top spectra in both (a) and (b).....	70
4.1	FTIR spectra of hydroxyl group region before reaction with gas phase reactants, of TiO ₂ used for this study.....	84
4.2	Hydroxyl region of TiO ₂ surfaces reacted with (a) CO ₂ , (b) SO ₂ and (c) NO ₂	85
4.3	Transmission FTIR spectra of (a) CO ₂ , (b) SO ₂ and (c) NO ₂ adsorption on nanomaterial TiO ₂ surface. The spectra were recorded in the presence of the gas phase with contributions from gas phase subtracted from these spectra	89
4.4	Pictorial representation of CO ₂ , SO ₂ and NO ₂ reaction with hydroxylated TiO ₂ surfaces. Surface species in the presence and after evacuating the gas-phase reactant derived from FTIR spectra are depicted. The amount of adsorbed species is quantified using a QCM flow cell. Coverages are reported in units of molecules cm ⁻²	95
4.5	FTIR spectra of water uptake on TiO ₂ nanoparticles previously reacted with (a) CO ₂ , (b) SO ₂ and (c) NO ₂ with exposure to increasing relative humidity of 0.6, 1.2, 3.1, 10, 26, 56 and 76% RH. Gas-phase water vapor was evacuated for 25 minutes after each exposure before the next higher exposure. After exposed to highest %RH, the infrared cell is evacuated to less than 0.6%RH. These final spectra are shown in (a), (b) and (c)	99
4.6	Transmission FTIR spectra between 800 and 4000 cm ⁻¹ for H ₂ O adsorption on TiO ₂ before (a) and after reaction with: (b) CO ₂ ; (c) SO ₂ ; and (d) NO ₂ These spectra are shown as a function of increasing relative humidity from 0.6, 1.2, 3.1, 10, 26, 56 and 76% RH at T = 296 K	103
4.7	Pictorial cartoon depicting water uptake on TiO ₂ nanoparticles following reaction with CO ₂ , SO ₂ and NO ₂	107
5.1	Transmission FTIR spectra of HCOOH adsorption on nanomaterial TiO ₂ . Spectra were collected as particles were exposed to increasing HCCOH (11, 25, 41, 60, 100, 306 and 491 mTorr) pressure for 25 minutes. The spectra were recorded in the presence of gas-phase and	

	gas-phase spectra have been subtracted. The inset shows the spectrum recorded after evacuation of gas-phase HCOOH following the highest exposure	116
5.2	Formate adsorption structures: (a) Monodentate, (b) bridged bidentate and (c) chelating bidentate	117
5.3	FTIR spectra of water uptake on TiO ₂ nanoparticles previously reacted with formic acid. Water vapor was introduced with increasing relative humidity between 0.3 and 79% (0.3, 1.0, 3.5, 11, 33, 76 and 79) relative humidity at 296 K. Gas-phase water vapor was evacuated for 25 minutes after each exposure before introducing the next exposure. After exposed to the highest relative humidity the infrared cell was evacuated overnight.....	123
5.4	The number of formic acid molecules adsorbed on the TiO ₂ surface at 296 K as a function of P _{exposed} was determined by volumetric measurements.....	125
5.5	Transmission FTIR spectra of formic acid uptake on nanomaterial TiO ₂ as a function of time. For clarity, spectra at 0 s, first 5 spectra and every 10 th spectrum followed by final spectrum are shown. The peak height for the absorption band for formate at 1362 cm ⁻¹ is plotted as a function of time using each of the spectra collected	128
5.6	Surface spectra of adsorbed formate on TiO ₂ particles following UV irradiation as a function of time under different environmental conditions (a) <1% RH and PO ₂ = 0 Torr, (b) <1% RH and PO ₂ = 100 Torr, (c) 40% RH and PO ₂ = 100 Torr and (d) 85% RH and PO ₂ = 100 Torr	131
5.7	Comparison of CO ₂ formation during formate photooxidation. Integrated absorbance of the gas-phase CO ₂ peak was used for the comparison.	132
5.8	FTIR spectra of gas-phase carbon dioxide formation upon irradiation of adsorbed formate in the absence and presence of molecular oxygen under different relative humidity conditions of (a) <1% RH and P(O ₂) = 0 Torr, (b) <1% RH and P(O ₂) = 100 Torr, (c) 40% RH and P(O ₂) = 100 Torr and (b) 85% RH and P(O ₂) = 100 Torr	133
5.9	Intensity normalized aggregate distribution of unreacted and TiO ₂ particles previously reacted with gas-phase formic acid	136
5.10	Schematic representation of formic acid adsorption, phototoxidation and solution phase behavior of TiO ₂ nanoparticles	136

6.1	Schematic of the custom-designed Kratos Axis Ultra XPS system with UV irradiation setup. The system consists of four chambers: a transfer antechamber, surface analysis chamber (not shown), reaction chamber and Teflon coated HNO ₃ reaction chamber. A cross section of the O ₂ /H ₂ O reaction chamber equipped with the UV source and beam optics is shown in the inset. <i>See</i> experimental methods section for a more detailed description of this four chamber system. (<i>Note</i> : TMP – turbomolecular pump; CCG – cold cathode gauge; LV – leak valve and V – valve).....	143
6.2	High-resolution X-ray photoelectron spectra of α -Fe ₂ O ₃ particles in the Fe2p, O1s and N1s binding energy regions (a) prior to and (b) after saturation exposure of HNO ₃	150
6.3	High resolution X-ray photoelectron spectra of α -Fe ₂ O ₃ particles in the N1s binding energy regions following exposure to HNO ₃ to saturation coverages and subsequent UV irradiation for 90 minutes in the presence and absence of water vapor and molecular oxygen. (a) %RH < 1 without O ₂ , (b) %RH < 1 with 100 Torr O ₂ , (c) %RH = 45 without 100 Torr O ₂ , (d) %RH = 45 with 100 Torr O ₂ at T = 296 K. Black and green lines represent the experimental data acquired and the total fit respectively. Surface species obtained by peak fitting are shown in red and blue lines. The fitted curve for nitrate peak overlaps with the total fit	152
6.4	High resolution X-ray photoelectron spectra of α -Fe ₂ O ₃ particles in the N1s binding energy regions following exposure to HNO ₃ to saturation coverages and subsequent UV irradiation for 0, 30 and 90 minutes in the presence of %RH = 45 without O ₂ . All spectra were acquired at 296 K. Black and green lines represent the experimental data acquired and the total fit respectively. Surface species obtained by peak fitting are shown in red and blue lines. The fitted curve for nitrate peak overlaps with the total fit	156
6.5	High resolution X-ray photoelectron spectra of α -Fe ₂ O ₃ particles in the N1s binding energy regions following exposure to HNO ₃ to saturation coverages and subsequent UV irradiation for 90 minutes in the presence of (a) 0 Torr H ₂ O, (b) 5 Torr H ₂ O, (c) 11.5 Torr H ₂ O, (d) 17 Torr H ₂ O at T = 296 K (left panel) and the percentage loss of nitrate after 90 minutes of UV irradiation in the presence of different water vapor pressures (right panel). In the left panel black and green lines represent the experimental data acquired and the total fit respectively. Surface species obtained by peak fitting are shown in red and blue lines. The fitted curve for nitrate peak overlaps with the total fit	158

6.6	Schematic of adsorbed nitrate photochemistry on α -Fe ₂ O ₃ ; (a) in the absence of water vapor, adsorbed nitrates present on the hematite surface in different coordination modes undergo limited nitrate photochemistry due to electron and hole pair recombination, (b) in the presence of 5 and 11.5 Torr water vapor pressure (24 and 55 %RH), there is higher nitrate conversion due to lower electron/hole recombination rates, thus NO ⁻ and N ⁻ form on cationic sites and O vacancy sites, (c) in the presence of 17 Torr (81 %RH) of water vapor pressure, there is high nitrate conversion, similar as in (b), however cationic sites and O vacancy sites are not available to form NO ⁻ and N ⁻ . See text for further details.....	159
6.7	Transmission FTIR spectra of gas-phase product formation from UV illumination of adsorbed nitrate under %RH = 45 without O ₂ at T = 296 K.....	162

CHAPTER 1

INTRODUCTION

1.1 Metal Oxides in the Atmosphere

The main source of metal oxide containing particles suspended in the atmosphere is most likely from windblown mineral dust. As one of the most mass abundant types of aerosols emitted into the atmosphere, windblown mineral dust aerosol accounts for one third to one half of the mass of the total aerosol budget. It is estimated that between 1600 and 2000 Tg of mineral dust is uplifted into the atmosphere annually.¹ Major desert areas like Sahara and Gobi account as major sources of windblown dust. Figure 1.1 shows images of Saharan and Gobi desert regions during dust storm events captured by NASA's Terra satellite. In addition, human activities, such as improper agricultural and grazing practices, contribute to 20-50% of the atmospheric dust loadings.^{2,3} The improper agricultural and grazing practices have resulted in desertification of land throughout the globe. The estimated budget of mineral dust is therefore, likely to increase due to the predicted increase of human activities as well as the expansion of arid regions.⁴

Given that mineral dust aerosol is from windblown eroded soils, the chemical composition is thought to be similar to that of the continental crust which is in part composed of a number of mineral oxide phases. Typical abundances of different major oxides in the continental crust are given in Table 1.1.⁵ As shown in Table 1.1 SiO_2 and Al_2O_3 are the most abundant oxides in continental crust. The exact percentage of each phase will vary and depend on the exact mineral dust source region from which it originates.⁶ Components of mineral dust such as silicon dioxide, aluminium oxide, iron

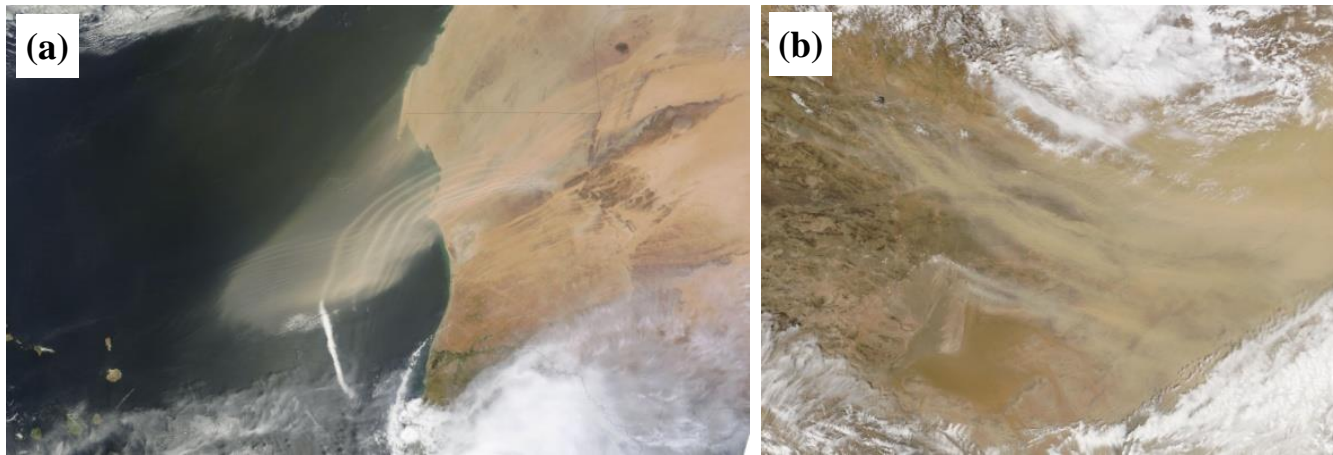


Figure 1.1. Satellite images of (a) Dust plume is transported off of the west coast of Africa and over the Atlantic Ocean in late September 2011 and (b) Dust from the Gobi desert is transported eastward as shown in late April 2011 raised from both north and south sources of the Mongolia-China border. The images were captured using the Moderate Resolution Imaging Spectroradiometer (MODIS) on NASA's Terra satellite. Reprinted with permission from Visible Earth (<http://visibleearth.nasa.gov>). Copyright 2011 NASA.

in experimental studies. Heterogeneous chemistry of trace atmospheric gases on these oxide surfaces has been widely studied using different experimental techniques and summary of those studied can be found in several review articles.^{6,7}

Table 1.1. Abundance of Major Oxides in the Continental Crust

Oxide	SiO ₂	Al ₂ O ₃	Fe ₂ O ₃	CaO	Na ₂ O	MgO	K ₂ O	TiO ₂	BaO	MnO
%	61.5	15.1	6.28	5.5	3.2	3.7	2.4	0.68	0.0584	0.1

In the atmosphere, mineral dust aerosol particles undergo atmospheric processing by reacting with different trace atmospheric gases in the presence of water vapor, molecular oxygen and light before finally deposited onto the earth's surface. Processed particles can also be deposited into the hydrosphere. Figure 1.2 shows a pictorial representation of the life cycle of an atmospheric dust particle, in terms of emission, transport, and deposition into aqueous and terrestrial ecosystems as a modified dust particle.⁸

The focus in this thesis is on the important yet sometimes poorly understood physical and chemical heterogeneous processes, especially the role of heterogeneous chemistry and photochemistry of light adsorbing components. Laboratory studies on the heterogeneous chemistry of mineral dust aerosol have focused mainly on night time chemistry of the metal oxide components of mineral dust. Short wavelength (< 300 nm) radiation is absorbed in the stratosphere and upper troposphere. However, a significant solar actinic flux reaches the Earth's surface. The actinic flux in the troposphere in the near UV region between 300 – 400 nm, is on the order of 10^{13} quanta $\text{cm}^{-2} \text{s}^{-1}$.⁹ Photon

energies corresponding to this wavenumber range are 300 – 400 kJ/mol and are sufficient to initiate a number of direct photochemical processes involving adsorbates on the dust particle surface. Additionally, light adsorbing components of mineral dust can induce new reaction pathways due to electron/hole pair generation and can play a significant role in the troposphere during daytime. In the presence of solar radiation, photochemistry dominates gas phase chemistry of the atmosphere. Although these solar light initiated reactions may be of significance in the atmosphere, little is known about photochemical reactions involving mineral dust aerosol. Additionally, the role of relative humidity and molecular oxygen on heterogeneous photochemical reactions are important to understand.

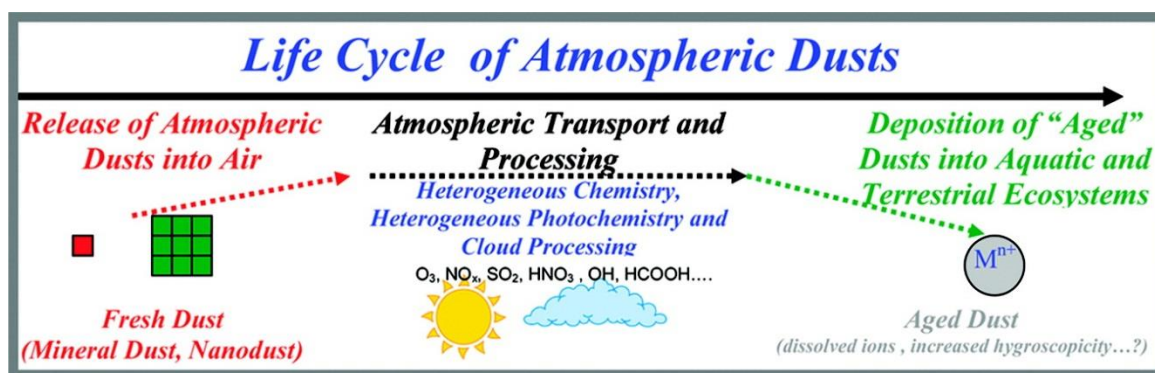
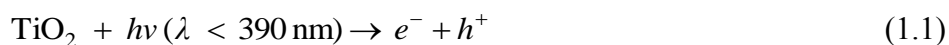


Figure 1.2. Cartoon representation of the life cycle of dusts represented in terms of emissions, long-range transport of dust where important yet in some cases poorly understood chemical and physical processes occur and subsequent deposition into aquatic and terrestrial ecosystems. These "aged" dust particles can then undergo deposition into aqueous and terrestrial ecosystems with very different physicochemical properties than the freshly emitted particles. Adapted with permission from Ref. 8. Copyright 2010 American Chemical Society.

1.2 Semiconductor Metal Oxides

When excited with light at wavelength equal to or greater than the band gap energy, the photocatalytic nature of semiconductors leads to the generation of electron hole pairs in the conduction and valence bands, respectively. The photogenerated electron hole pairs can then follow several pathways: *(i)* recombination of electron and hole on the surface or in the bulk of the semiconductor; *(ii)* reduction of electron acceptors by photogenerated electrons and; *(iii)* oxidation of electron donors by photogenerated holes. Electrons and holes transported to the particle surface can therefore initiate redox chemistry.¹⁰ Some examples of oxidation and reduction processes following reaction with electron acceptors (A) and donors (D) for TiO₂, a well-known photocatalyst are shown in Figure 1.3. Photogenerated electrons and holes, for example, can react with H₂O and O₂ molecules with the formation reactive oxygen species. The reaction mechanism can be depicted as follows in equations (1.1)-(1.3):



The resultant reactive oxygen species can reduce and/or oxidize environmental pollutants, including volatile organic compounds (VOCs), leading to the breakdown of these pollutants into low-molecular weight products. It is a main feature developed as a

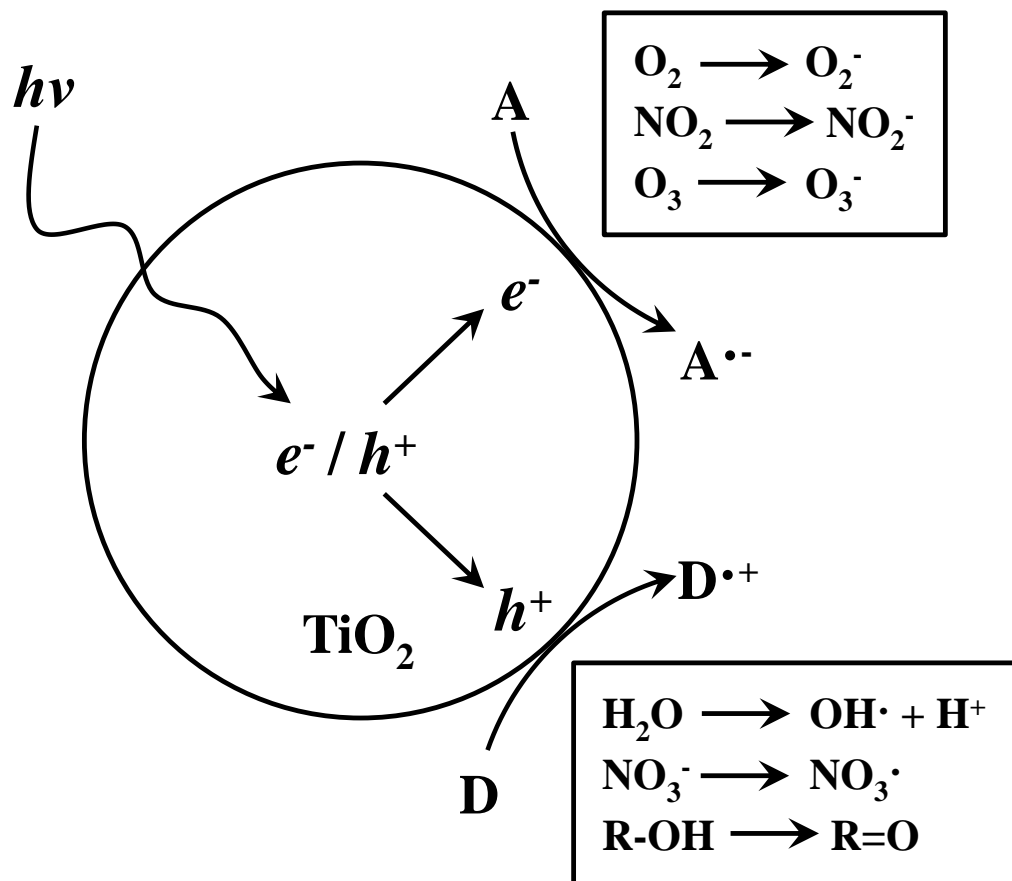


Figure 1.3. Schematic of TiO_2 photoexcitation to initiate electron-hole pairs (e^-/h^+) and redox chemistry at the TiO_2 surface. Separated electron-hole pairs at the TiO_2 surface can result in the reduction of electron acceptors (A) by photogenerated electrons, and the oxidation of electron donors (D) by photogenerated holes. Metal oxide photocatalysis with atmospheric gases has the potential to play an important role in atmospheric chemistry. Adapted with permission from Ref. 7. Copyright 2012 American Chemical Society.

usage of self-cleaning materials by adding semiconductor material such as TiO_2 or applying a coating to the conventional building materials for environmental remediation.¹¹⁻¹³

1.3 Semiconductor Oxides Studied

Under Dissertation Research

1.3.1 Titanium Dioxide

Titanium dioxide (TiO_2) is a relatively inexpensive, non-toxic and easy to handle material, which is of great interest as evidenced by the wide number of applications, as well as the number of publications that have appeared in the past twenty years.¹⁴ Besides reports in the literature related to the utilization of TiO_2 in solar cells,¹⁵ environmental remediation,¹⁶ sensing,^{17,18} and as coatings^{19,20}, recent studies have focused on the role of TiO_2 photocatalysis in atmospheric chemistry. It has been reported that TiO_2 surfaces facilitate interfacial photochemical reactions, and that these reactions have the potential to change the chemical balance of the atmosphere.²¹⁻²⁵

TiO_2 is a semiconductor material with a band gap of ~ 3.2 eV, corresponding to a wavelength of ~ 390 nm. TiO_2 has three major stable polymorphs, namely anatase, rutile and brookite. Among those, anatase has generally shown the highest photocatalytic activity with some crystallographic planes of anatase being particular reactive.^{26,27} The presence of rutile in anatase sample, however, was suggested to increase catalytic activity by introducing mesoporosity and a wider pore size distribution.²⁸⁻³⁰ Degussa P25 TiO_2 is a typical commercially available material composed of 75% anatase and 25% rutile. It is

generally accepted to exhibit better photocatalytic efficiency compared with other forms of TiO_2 , and has been widely used as a reference material in laboratory studies.^{29,31}

TiO_2 surfaces can reduce and/or oxidize environmental pollutants, including volatile organic compounds (VOCs), leading to the breakdown of these pollutants into low-molecular weight products. The ability of TiO_2 surfaces to reduce and/or oxidize environmental pollutants and its potential self-cleaning applications of TiO_2 are related to window materials, cement, tiles, paving stones, paints and other building materials, which stay clean themselves in the presence of sunlight due to their ability to breakdown organic atmospheric species.³²⁻³⁴ TiO_2 surface chemistry and photochemistry and its applications in environmental remediation have been extensively reviewed in several publications.^{10,34-38}

The greatest interest and focus of this dissertation research is the impact of TiO_2 heterogeneous chemistry and photochemistry in the atmospheric environment. Photon energies in the troposphere are sufficient to activate TiO_2 with the formation of separated electron/hole pairs as discussed previously.⁹ TiO_2 can be found as a minor component in Aeolian dust particles. The mass mixing ratio of TiO_2 in atmospheric dust sources are in the range of 0.1 to 10% depending on the source from which they originated prior to uplifting into the atmosphere.³⁹ Additionally, TiO_2 particle surfaces have been recently reported in urban airsheds, suggesting that there may be some anthropogenic release due to its widespread usage.^{40,41} Although TiO_2 is a relatively minor component in the environment, its interaction with solar radiation can initiate a number of photochemical processes, and therefore, potentially play a role in daytime atmospheric chemistry. Understanding the photocatalytic behavior of TiO_2 is expected to fill a gap in our

knowledge of atmospheric chemistry, which previously has not considered TiO_2 photocatalysis to impact the chemical balance of the troposphere to any great extent.

1.3.2 Titanium-Containing Mineral Dust Aerosol

TiO_2 has been widely reported to be present in airborne particulate matter (PM).⁴²⁻
⁵⁴ For example, analysis of total suspended particles (TSP) in the atmosphere in south-east Beijing reported that on average there was 250 to 520 $\mu\text{g m}^{-3}$ of TSP for the different seasons from autumn 2005 to summer 2007 with 0.75 to 1.58 $\mu\text{g m}^{-3}$ of that TSP composed of TiO_2 .⁴² Sources of TiO_2 particles in the atmosphere include both natural processes and human activities, which is discussed in more detail below.

The main source of TiO_2 particles suspended in the atmosphere is from windblown mineral dust. The exact percentage of each phase will vary and depend on the exact mineral dust source region from which it originates.⁶ Approximately 0.7 wt% TiO_2 is found in the continental crust.⁵ However, TiO_2 is not evenly distributed throughout the earth's crust. Table 1.2 shows TiO_2 distributions derived from various dust samples originated from Saharan and Gobi deserts from information provided in several studies.^{39,55-58}

The content of TiO_2 in the atmosphere is also seasonally variable. The median mass concentration of TiO_2 was reported to be 7.3 ng m^{-3} in PM_{10} samples collected during the cold period in a 2006 campaign at K-puszta, Hungary, but samples collected in the warm period at the same site contained significantly higher TiO_2 concentrations with a median mass concentration of 50.0 ng m^{-3} .⁵² The mobilization of TiO_2 during the warm period was explained by the combination of a dried soil and increased agricultural

activities. Additionally, the TiO_2 content in PM_{10} is generally higher than that in $\text{PM}_{2.5}$ as reported in several field studies.^{43,49,50,53,59}

Table 1.2. TiO_2 Distribution within Different Dust Source Regions.

Dust Source	Region	% TiO_2	Ref.
Saharan	Cape Verde Islands	4.5	39
	Ile-Ife, Nigeia	3.33	55
Gobi	Beijing	0.58	56
	Taklimakan desert	0.38	56

Field studies using single particle analysis techniques also revealed TiO_2 -containing particles in aerosol samples.^{44,60,61} TiO_2 was commonly found mixed with other metallic elements including Fe. For example, Kertész et al. carried out quantitative X-ray emission analysis for single particles collected in an urban location in Debrecen and in the Szemlőhegy-cave situated under Budapest in the winter of 1998.⁶⁰ They reported that particles within all different size bins contain titanium, but the abundance of titanium varies from particle to particle. Single particle analysis of dust samples from Africa suggested that the titanium-rich particles account for approximately 0.3% of all particles analyzed, and contained particles greater than 20% Ti.⁶¹ These particles are rare, but occur in both fine and coarse modes, often in small aggregates. Titanium-enriched silicate particles were observed, suggesting that TiO_2 readily aggregated with clay minerals.

Smaller-size fraction of mineral dust, consisting of particles with diameters less than 0.1 μm or less, can be transported over long distances and therefore raise the possibility that TiO_2 in mineral dust aerosol can interact with atmospheric trace gases during transport on a global scale.^{6,62} Compositional analysis of sea aerosol particles (reference⁴⁶ and papers therein) was reported to contain titanium-rich particles originated from continental areas, supporting the long-range transport of mineral dust over the open ocean.

1.3.3 Other Sources of TiO_2 in the Atmosphere

Besides TiO_2 in mineral dust, there are additional sources of airborne particulate matter containing TiO_2 from industrial processes including the nanotechnology industry that could contribute significantly to TiO_2 in the atmosphere.^{44,47,59,63-67} For example, compositional analysis and source identification of PM samples collected at the Pittsburgh Supersite indicated that wood combustion, vegetative detritus, and industrial processes account for significant sources of TiO_2 besides mineral dust.⁵⁹ Titanium contents in food and personal care products were studied recently showing their potential importance as TiO_2 sources in the environment.⁶⁶ Due to the ineffectiveness of aerosol sampling methods in collecting nanoscale particles, atmospheric nanoparticles remain relatively unknown and difficult to detect.⁶⁸⁻⁷⁰ In a study by Bang et al., tetragonal rutile TiO_2 particles around 50 nm in size were identified in atmospheric particles in several outdoor locations in the El Paso, Texas. Larger crystalline-agglomerated particles containing Fe and Ti in a 2:1 ratio with sizes around 100 nm were also found.⁶⁴ Such aggregates may be mixtures of Fe_2O_3 and TiO_2 . Although nanoscale TiO_2 particles

represent only a relative small portion of the mass of $\text{PM}_{2.5}$ or PM_{10} , these particles are expected to display high photocatalytic activity due to their large surface area to volume ratios, potentially playing an important role in atmospheric chemistry as TiO_2 -containing particles from mineral dust.⁶⁵

1.3.4 Sources of TiO_2 Particles in Contact

with the Atmosphere

Since it can save time, cost, and energy for maintenance, self-cleaning materials coated with TiO_2 have been widely applied to building exteriors, cover glass for road lamps, airport roofs, and road bricks to name a few. In the last two decades, the use of commercial TiO_2 -coated surfaces has grown and is currently used in building exteriors, floor tiles, road pavements, and windows.^{11-13,33,34} One reason for this is that TiO_2 coated surface can decompose organic pollutants adhering to the surface and maintain itself clean while exposure to irradiation.^{33,34} Self-cleaning cover glass for tunnel light is one of the typical commercial products using this effect. For example, in most tunnels in Japan, sodium lamps emitting UV-Vis light are used, and the decrease in light intensity due to organic thin film formation from vehicle exhaust compounds is a serious problem. When the lamp is coated with TiO_2 , it can decompose the contaminant, remaining clean and transparent for long-term use.³⁴ Building exteriors coated with TiO_2 are thought to be another successful application and this application is widely used around the world. Several thousand buildings in Japan have been covered with self-cleaning tiles from TOTO, Ltd., one of the pioneers of self-cleaning technology.³⁴ Figure 1.4 contains images of some of these self-cleaning building materials used in cities throughout Japan.

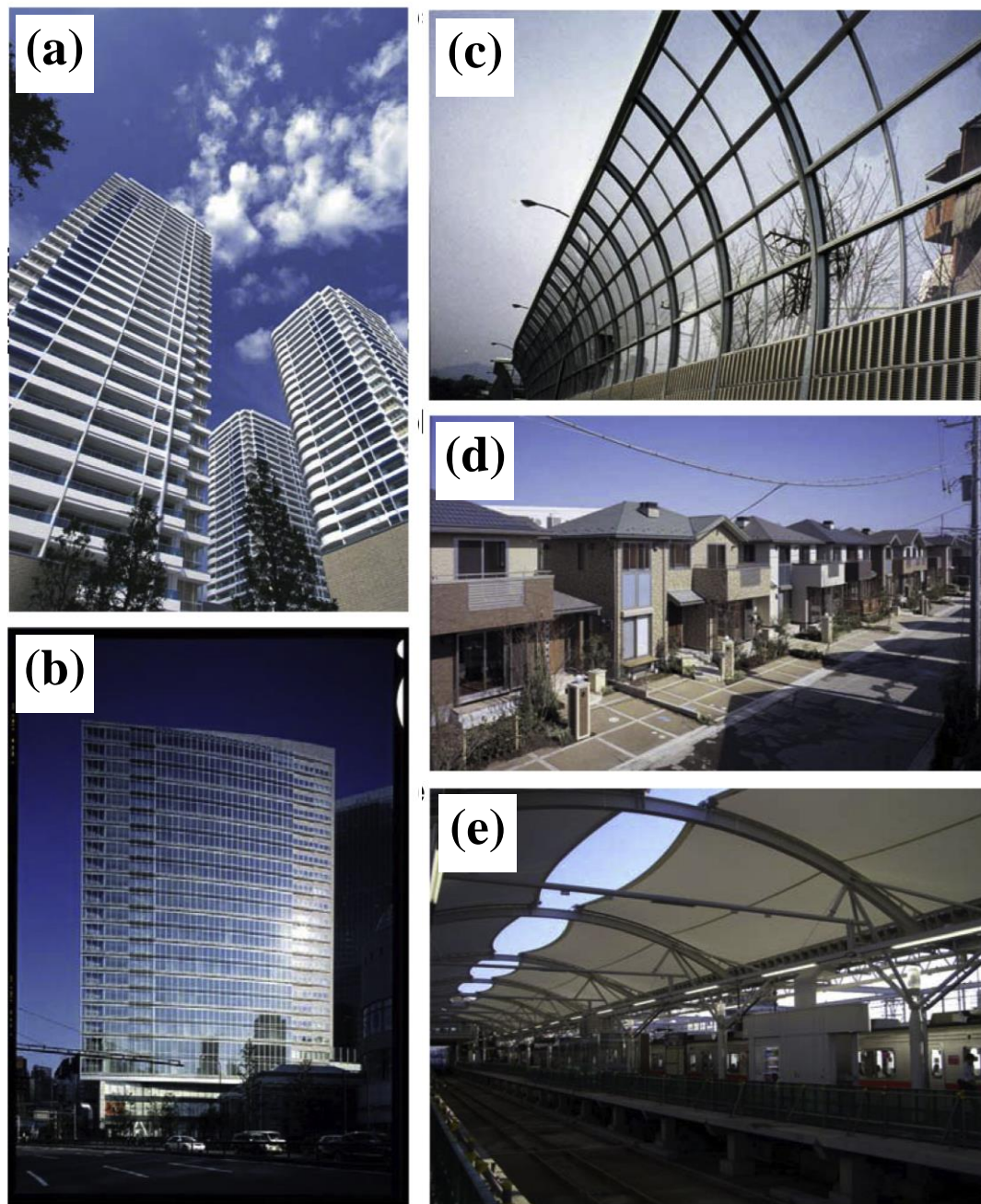


Figure 1.4. Application of different uses of self-cleaning exterior building materials. (a) The MM Towers, in Yokohama, coated with self-cleaning tiles; (b) The Matsushita Denso building covered with self-cleaning glass; (c) The self-cleaning sound-proof wall; (d) Eco-life-type houses using self-cleaning tiles and glass and; (e) Self-cleaning roof of a train station in Motosumiyoshi. Reprinted from ref 34, Copyright 2008, with permission from Elsevier.

The ongoing and continuous development of applications of TiO_2 as a coating material accounts for another significant source of TiO_2 surfaces that can be in contact with atmospheric gases. It is expected that the application of TiO_2 will continue to grow and expand. Thus, TiO_2 -coated materials potentially make more TiO_2 surfaces available for heterogeneous photocatalysis of atmospheric gases.

1.3.5 Iron Oxide

Iron oxides are the third most abundant fraction of the Earth's crust and therefore, a major component of wind-blown mineral dust aerosol in the atmosphere.⁶ In addition, iron oxides are introduced to the atmosphere as fly ash from power plants, combustion exhaust, and from industrial operations. Wet and dry deposition of atmospheric iron-containing aerosols particles act as a main source of iron for ocean waters as iron is an essential nutrient for marine phytoplankton.⁷¹

Because iron ions may exist in different oxidation states, electron transfer reactions are possible on Fe-containing mineral dust particles. Another interesting feature of iron oxide chemistry is the presence of different polymorphs. The major polymorphs include $\alpha\text{-Fe}_2\text{O}_3$ (hematite), Fe_3O_4 (magnetite) and $\gamma\text{-Fe}_2\text{O}_3$ (maghemite).⁷² Among these different polymorphs, $\alpha\text{-Fe}_2\text{O}_3$ (hematite) is the thermodynamically stable phase and therefore, the most common form of iron oxide. Iron hydroxides and oxide-hydroxides are other types of iron containing materials which can also be found in several different polymorphs.⁷² Among iron oxide-hydroxides, $\alpha\text{-FeOOH}$ (goethite) has reported in various mineral dust samples and thought to be the most common iron oxide-hydroxide component of mineral dust.

Hematite ($\alpha\text{-Fe}_2\text{O}_3$) exists as a corundum crystal structure. The band gap energy of $\alpha\text{-Fe}_2\text{O}_3$ is 2.2 eV and the semiconductor nature of iron oxides can influence atmospheric reactions in the troposphere.^{72,73} However, the quantum efficiency of $\alpha\text{-Fe}_2\text{O}_3$ has been reported as low compared to other well-known semiconductors such as TiO_2 and ZnO .⁷⁴ The lower quantum efficiency could be due to both the low band gap energy and energy the gap being the energy for indirect d-d Fe^{3+} crystal field transitions.⁷³ $\alpha\text{-Fe}_2\text{O}_3$ can absorb visible radiation leading to a red coloration of the particles. Therefore, radiative forcing of iron-containing mineral dust may be highly dependent on iron content and type of iron-containing material present.

1.3.6 Iron-Containing Mineral Dust Aerosol

Iron is a major component of mineral dust aerosol, usually found in the form of iron oxides and particularly Fe_2O_3 . Fe_2O_3 composition in continental crust accounts for 6.28%.⁶ Iron oxides in mineral dust aerosols are transferred into the atmosphere as a result of wind and volcanic activity. Iron has been widely reported to be present in airborne particulate matter (PM).⁴³⁻⁵⁴ Studies on total suspended particles (TSP) collected in different dust regions have reported iron in those samples. Analysis of total suspended particles in the atmosphere in two sample collection stations in the Canary Islands reported 45 and 49 $\mu\text{g m}^{-3}$ of average TSP from December 2001 to December 2009 with an average total Fe content from both stations being 2.919 $\mu\text{g m}^{-3}$.⁷⁵ The main source of mineral dust in the Canary Islands is from the Saharan desert region. Higher standard deviations for TSP levels were reported in this study and may be associated with the changes in local weather patterns. TSP collected in 3 stations in Korea reported yearly

average of 2.5736, 0.7552 and 1.2349 $\mu\text{g m}^{-3}$ of Fe.⁷⁶ Iron analysis from TSP at the same sites during mineral dust episodes enhanced Fe content by 4.4 – 9.3 % confirming the effect of dust outbreak on Fe content.

Table 1.3 contains the Fe_2O_3 composition reported in several studies for different dust source regions. As can be seen in Table 1.3 Fe_2O_3 composition can be varying slightly from region to region and study to study. Elemental composition analysis by Lafon et. al. have presented Fe content as Fe_2O_3 mass percentage and reported 6 – 9 % for several samples from Niger, China and Cape Verde.⁷⁷

Table 1.3. Fe_2O_3 Distribution within Different Dust Source Regions

Dust Source	Region	% Fe_2O_3	Ref.
Saharan	Cape Verde Islands	14.7 (FeO)	39
	Ile-Ife, Nigeria	5.6	55
Gobi	Beijing	5.63	57
	Taklimakan desert	2.2	57

1.3.7 Iron from Fly Ash

Iron released from combustion sources is generally referred to as fly ash. These sources include fossil fuel combustion and biomass burning. Field, laboratory, and modeling studies reported fly ash can act as an important source of bioavailable iron. Combustion derived iron account for ~50% of the total deposited iron on ocean surrounding industrial regions.⁷⁸ Luo et al. reported a summary of %Fe found in fine and coarse particulate matter of industrial and combustion sources from various references.⁷⁸

Among these sources industrial coal combustion accounts for being the highest percentage of Fe in both coarse and fine particles with 4.5 – 9.4 % being iron. Iron was reported as a dominant element in wild fire particulate matter samples in Portugal during summer 2010.⁷⁹ Fly ash particles are mostly fine particles and therefore, can be transported to far away locations from their source and deposited into the hydrosphere.⁸⁰

1.3.8 Iron Deposition into Aqueous Environment

In the oceans, iron is a critical nutrient for phytoplankton and several other organisms. Mineral dust and fly ash deposition into the ocean is thought to be the major iron source for these organisms.^{71,81} Therefore, many experimental and modeling studies have focused on the chemistry of iron dissolution from fly ash and iron oxides.⁷¹ Iron dissolution from iron containing materials and natural mineral dust aerosol samples have been extensively studied under various environmentally relevant conditions.^{7,82,83} These studies on iron dissolution from iron containing materials such as fly ash, mineral dust and iron oxides have revealed that the iron deposition and its effects on biogeochemistry greatly depends on source, environmental pH, iron speciation, and solar radiation.⁷¹ Iron solubility data reported in the literature shows highest solubility for oil fly ash followed by coal fly ash with mineral dust being least soluble. Shi et al. have recently reviewed the dissolution of iron from iron containing particles and discussed the necessity of more field and modeling studies to further investigate the complex nature of iron dissolution.⁷¹ Atmospheric processing of iron containing mineral dust can also play a significant role in the solution phase behaviors of mineral dust particles once deposited into hydrosphere. Atmospheric processing by reaction with atmospheric trace gases can either enhance or

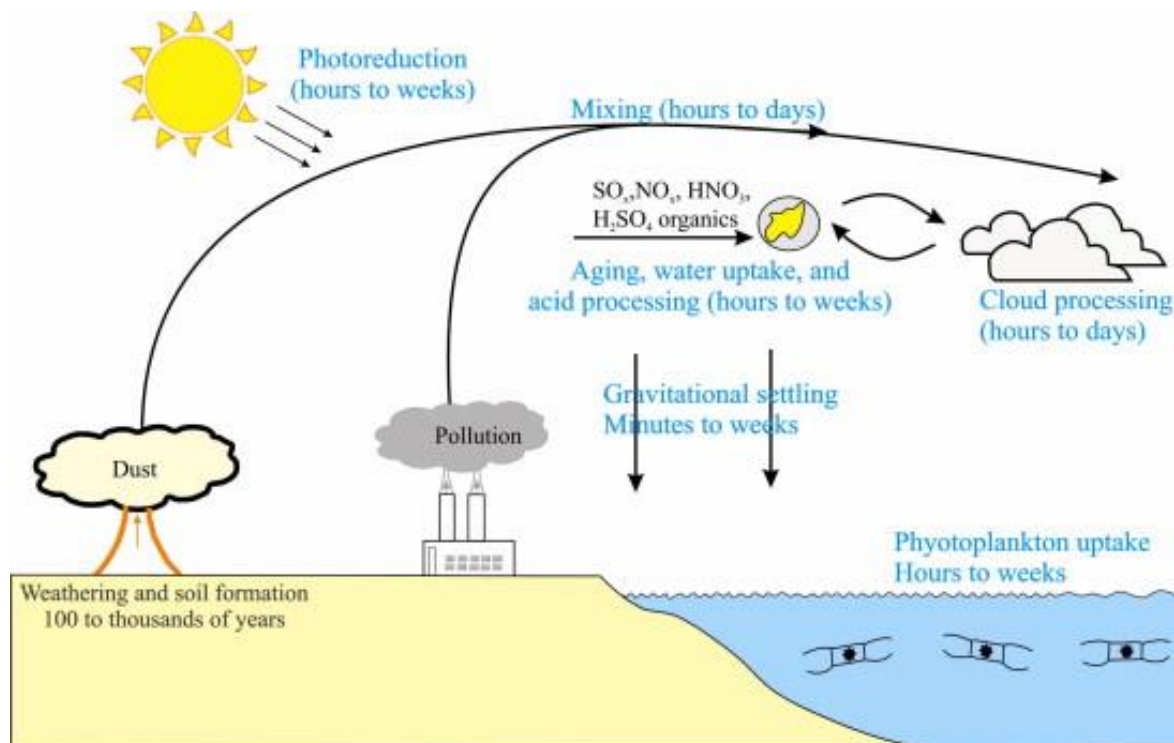


Figure 1.5. A schematic diagram showing some of the most important processes controlling the speciation of Fe in the atmosphere and its subsequent deposition back to the land and/or ocean. Processes in the source regions include weathering and aging of Fe oxides, which affect the Fe mineralogy of dust, resulting in dust of different potential solubilities. During transport, dust may mix with soot particles from biomass burning and other anthropogenic aerosols. This mixture of particles may also take up sulphate, nitrate and organic ligands. During long range transport, dust undergoes gravitational settling, cloud processing, photo-reduction, and acid uptake/processing. Cycles between dust, particularly aged dust (serving as cloud condensation nuclei, CCN) and clouds through condensation/evaporation processes can occur 5–10 times before the dust is deposited to the ocean. Reprinted from Ref 71, copyright 2008, with permission from Elsevier.

hinder the iron solubility. Study of solution phase behavior of iron oxides previously reacted with atmospheric trace gases is important in terms of iron solubility and the biogeochemistry of processed particles. The schematic in Figure 1.5 summarizes some important process in iron cycling.

1.4 Atmospheric Trace Gases

Earth's atmosphere is mainly

composed of 78% nitrogen (N_2), 21% oxygen (O_2), water vapor (H_2O), argon (Ar) and other noble gases. Apart from these gases, the atmosphere contains trace gases which account for less than 1%.⁸⁴ The composition of trace gas abundances have changed rapidly and remarkably since the industrial revolution due to world population growth and increase in industrial activities. The trace atmospheric species include carbon dioxide, nitrogen oxides, nitric acid, sulfur dioxide, ozone, hydrogen peroxide and volatile organic compounds (VOCs). A brief overview of the atmospheric trace gases studied in dissertation research will be presented here.

Atmospheric trace gas composition and their reactions leading to secondary products in the atmosphere are vital to life on earth.⁸⁴ For example, greenhouse gases, including CO_2 , are important in terms of keeping the earth's surface warm enough to sustain life on earth. However, atmospheric CO_2 concentration has increased over the last few hundred years continuously. Ice core records have revealed the pre-industrial revolution CO_2 level was about 280 ppm. The current level in December 2013 was 396.81 ppm as measured at Scripps Institute of Oceanography at Mauna Loa, Hawaii. This increase in CO_2 levels can result in a global temperature increase leading to global

warming and global climate changes. Therefore, surface reactions of carbon dioxide are of much importance and interest in terms of increased interest in carbon dioxide capture, storage and transformation in the scientific community. Carbon dioxide adsorption on oxide surfaces mainly results in adsorbed carbonate and bicarbonate.^{85,86} Carbon dioxide transformation to more useful products using photocatalysis has been widely investigated in bare and doped semiconductor oxide materials.^{87,88}

Sulfur dioxide is another trace atmospheric gas. In the atmosphere, the main source of sulfur dioxide is from coal power plant emissions. Once in the atmosphere, SO_2 can be oxidized to sulfate leading to cloud condensation nuclei formation and acid rain.^{89,90} Mechanisms that convert SO_2 to sulfate leading to acid rain on mineral dust surfaces are poorly understood. SO_2 uptake on Saharan dust, where TiO_2 is a measurable but minor component, has shown an irreversible uptake with uptake coefficients on the order of 10^{-5} at a temperature of 298 K.⁹¹ Components of mineral dust aerosol have been shown to play an important role in the heterogeneous conversion of sulfur dioxide to sulfate. Sulfur dioxide adsorption on metal oxide surfaces, including titanium dioxide and iron oxides, have been shown to form adsorbed sulfite and bisulfite.⁹²⁻⁹⁷ Details of the sulfur dioxide adsorption and conversion to adsorbed sulfate on oxide surfaces have been investigated in several studies.^{92-95,97}

Nitrogen oxides (NO_x , $x = 1, 2$) are mainly emitted from the combustion of fossil fuels.⁹⁸ Car exhausts emit 0.015-0.8 g NO_x per kilometer, and diesel engines exhaust contributes 35-70% NO_x in urban areas. NO_x concentration during intense photochemical pollution events in urban environments is around several hundred ppbv.⁸⁴ NO_x can cause a wide range of health and environmental effects, from adverse respiratory problems to

acid rain. Tropospheric ozone is mainly produced through a series of nonlinear reactions between NO_x and VOCs.⁸⁴ The World Health Organization has suggested that the maximum NO_x concentration should not exceed 23 ppb as an annual mean concentration. With the increased interest towards removal of NO_x (de NO_x), the possibility of applying metal oxides in de NO_x processes has been widely studied. TiO_2 has been reported as an effective NO_x removal material by oxidizing NO and NO_2 into nitrate. NO_2 reacted on metal oxide surfaces mainly forms adsorbed nitrate species with different coordination modes.⁹⁹ Furthermore, NO_2 reactions on TiO_2 in the presence of solar irradiation have been shown to form more harmful products such as HONO.^{25,100}

NO_x oxidation in the atmosphere leads to gas phase HNO_3 , a stable product that is thought to be removed from the atmosphere via wet or dry deposition. Nitrate formation on dust particles has long been thought to be a sink for atmospheric NO_x and HNO_3 . Similar to NO_2 , reaction between HNO_3 and oxide surfaces results in adsorbed nitrate with several coordination modes.¹⁰¹ However, recent studies on the photochemistry of adsorbed nitrate on Al_2O_3 , TiO_2 and Fe_2O_3 have shown the potential renoxification with NO, NO_2 and N_2O formation, under different environmental conditions pertinent to the troposphere.¹⁰²⁻¹⁰⁴ Furthermore, estimations have shown the produced NO has a range of 0.02-13 pptv after 10 hours travel time which has implications on higher NO_x levels in remote and clean areas.¹⁰³

In addition to the ubiquitous presence of inorganic trace gases in the atmosphere, there are also numerous volatile organic compounds (VOCs) present as atmospheric trace pollutants.⁸⁴ Sources of VOCs contain both biogenic processes and human activities.⁸⁴ Natural biogenic processes give rise to substantial ambient levels of organic compounds

and include the emissions from plants, wild animals, natural forest fires, and anaerobic processes in bogs and marshes. Human activities also release a variety of organic matters directly into the atmosphere through, for example, automobile emissions, leaf abrasion, wood smoke, gas combustion and petrol evaporation, increasing levels of atmospheric VOCs. The presence of VOCs is of great environmental concern due to its role in the production of tropospheric ozone and secondary organic aerosols. Once emitted into the atmosphere, VOCs undergo a number of physical and chemical processes leading to their removal or transformation in the atmosphere.¹⁰⁵ Adsorption and subsequent reactions of VOCs on oxide surfaces act as a potential removal pathway. Among the class of VOCs, volatile organic acids, including formic acid and acetic acid, have been found to be one of the most abundant species in VOCs.⁸⁴ Organic acids originate from both anthropogenic and biogenic sources on the ground as well as photochemical oxidation of organic compounds in the atmosphere.⁸⁴ Studies of precipitation chemistry have shown that organic acids may account for a large fraction, up to 64%, of the total acidity in non-urban environments.¹⁰⁶ Removal pathways of organic acids in the atmosphere principally include wet and dry deposition and, to a smaller extent, reaction with OH radicals.

Trace atmospheric gases, such as CO₂, SO₂, NO₂, HNO₃, and HCOOH, can react with mineral oxide surfaces in the atmosphere by forming gaseous and/or surface adsorbed species. These surface species can undergo various transformations in the presence of light. Most of the major dust storms originate in remote regions, but mineral oxide particles can be transported by wind activity to other regions where they could encounter atmospheric trace gases. Additionally, engineered oxide materials released into

the environment can act as a source of atmospheric oxide surfaces and undergo chemical reactions as well.

1.4.1 Roles of Water Vapor and Molecular Oxygen

Both water vapor and molecular oxygen are abundant in the troposphere. Their interactions with oxide surfaces play a critical role in the chemistry and photochemistry of atmospheric oxide particles. The adsorption of these is certainly one of the most extensive areas of study in the surface science of metal oxides. Water vapor plays an important role on adsorption and reaction chemistry on metal oxide surfaces.¹⁰⁷ Water adsorption on oxide surfaces has been widely investigated using various techniques.^{101,108-110} Adsorbed water can play multiple roles on adsorbed surface species by changing the oxide coordinated adsorbed products to water solvated products, as well as affecting the stability of tightly adsorbed species on oxide surfaces.¹⁰⁷ Furthermore, hygroscopic behavior can be greatly affected by the adsorbed species on metal oxide surfaces. For example, alumina particles reacted with formic acid have shown to be hydrophobic compare to unreacted.¹¹¹ However, water uptake on Arizona test dust reacted with co-dosed SO₂, O₂ and H₂O did not show changes in hygroscopic behavior.¹¹² Therefore, it is important to study the water uptake on oxide particles previously reacted with trace atmospheric gases. In semiconductor metal oxide surfaces, H₂O molecules can react with holes (h⁺) and increasing RH increases the OH radical formation. Hole scavenging by water molecules minimize electron hole recombination leaving excess electrons on the surface.

Molecular oxygen is the second most abundant gas in the atmosphere and it plays an important role in atmospheric photocatalysis. It assists in charge separation by acting as an electron scavenger to form O_2^- as shown in equation 1.3. It can also generate other active species, like H_2O_2 and OH that participate in subsequent photocatalyzed reactions.⁷ The presence of molecular oxygen can greatly influence the product formation by the reactions involving adsorbates on oxide surfaces.¹⁰² Fundamental studies of the photochemistry of atmospheric trace gases with oxide surfaces in the presence of molecular oxygen are therefore critical in understanding atmospheric photocatalysis of oxides.

1.4.2 Atmospherically Processed Particles in Aqueous Environment

Atmospherically processed particles can deposit on aqueous systems resulting in aqueous suspensions. Depending on the atmospheric processing, dissolution and solution phase behavior can be changed significantly, such as enhanced dissolution of metal ions of the oxides or making stable suspensions. Studies have shown NO_2 reacted PbO particles display higher lead release to aqueous phase and nitric acid reacted goethite particles form more stable suspension compared to unreacted.^{113,114} Therefore, solution phase behavior of oxide particles reacted with trace gas was investigated in some of this dissertation research.

1.5 Thesis Overview and Objectives

The research presented herein focuses on understanding the heterogeneous chemistry and photochemistry of light adsorbing atmospherically relevant metal oxides

using various experimental methods. Furthermore, aqueous phase behavior of the processed metal oxide particles has also been investigated.

Multiple experimental techniques were involved in the investigation of the reactions of trace atmospheric gases with titanium dioxide and iron oxide. These experimental methods include FT-IR spectroscopy, X-ray Photoelectron Spectroscopy (XPS), as well as the use of a quartz crystal microbalance (QCM). Oxide samples used for these studies were characterized using Transmission Electron Microscopy (TEM), Scanning Electron Microscopy (SEM), X-ray diffraction (XRD), and BET surface area measurements. In addition to these techniques, several other techniques were used to study the solution phase behavior of oxide particles previously reacted with trace gases. The experimental methods that were used for the dissertation research discussed in this thesis are described in detail in Chapter 2.

In Chapter 3, understanding the mechanistic aspects of sulfur dioxide surface chemistry and photochemistry on TiO_2 nanoparticle surface is the major focus. Vibrational frequencies of adsorbed SO_2 to yield adsorbed sulfite as well as sulfate formation on TiO_2 are reported. Isotope labeling was used to get additional insight into the reaction chemistry of SO_2 on TiO_2 nanoparticle surfaces. Furthermore, the relative stability of adsorbed sulfite compared to adsorbed sulfate on TiO_2 particle surfaces as a function of relative humidity is investigated for the first time to the best of our knowledge. Loss of sulfur from the surface as a function of relative humidity is quantified using X-ray photoelectron spectroscopy.

In Chapter 4, the surface chemistry of three pollutant triatomic gases CO_2 , SO_2 and NO_2 on TiO_2 nanoparticle surfaces is discussed. Reactivity of different surface

hydroxyl groups with these three gases and product formation have been examined. We show here that there are large and important differences in the chemistry of these three atmospheric gases with surface hydroxyl groups. Furthermore, water uptake and effect of water vapor on adsorbed carbonate, sulfite and nitrate on TiO_2 surfaces was investigated.

In Chapter 5, formic acid adsorption on nanoparticle TiO_2 and the effect of relative humidity on photooxidation of adsorbed formate is discussed. In this study transmission FTIR spectroscopy was used for studying the surface and gas-phase products. Vibrational frequencies of adsorbed species are reported. Aqueous phase behavior of formic acid reacted TiO_2 particles examined.

In Chapter 6, a detailed spectroscopic study of the photochemistry of adsorbed nitrate on hematite, $\alpha\text{-Fe}_2\text{O}_3$, surface under environmentally relevant relative humidity and molecular oxygen by XPS and FTIR spectroscopic techniques is presented. The formation of reduced nitrogen surface species was presented as a function of relative humidity. The impact that HNO_3 reaction has on iron dissolution is also investigated.

The conclusions and future directions for research are given in Chapter 7 including future directions for better understanding of the light adsorbing components in the troposphere. The results presented here provide insight into the heterogeneous chemistry and photochemistry of atmospherically relevant light absorbing metal oxides under different environmental conditions.

CHAPTER 2

EXPERIMENTAL METHODS

The scope of the research presented in the following chapters used a number of different experimental methods to investigate atmospheric trace gas adsorption on oxide surfaces. In this chapter, a description of multiple experimental techniques and methods utilized in dissertation research are discussed in detail. These techniques include Transmission Fourier Transform Infrared (FTIR) spectroscopy, X-ray Photoelectron Spectroscopy (XPS) and Quartz Crystal Microbalance (QCM) measurements. In addition to these techniques, several other characterization methods such as X-Ray diffraction (XRD), scanning electron microscopy (SEM) as well as methods used to study the aqueous phase behavior of oxide particles previously reacted with trace gases will be briefly discussed. The specifics of each study are discussed in more detail in the respective chapters.

2.1 Fourier Transform Infrared (FTIR)

Spectroscopy

Infrared (IR) spectroscopy provides data on the structure of surface adsorbates, the nature of bonds formed between adsorbed molecules and the surface, and the existence of various types of surface and gas phase compounds. A vibrational spectrum reflects both the properties of molecules and characteristic features of chemical bonds within the molecule. Vibrational spectroscopy provides information on changes in

molecule experiences as it comes into contact with the solid surface and thus gives us information about the relationship between the surface and the adsorbate.

2.1.1 Transmission FTIR Spectroscopy:

Experimental Setup

Transmission FTIR spectroscopy was used in a number of experiments to investigate formation of new surface and gas phase species when in contact with different metal oxide surfaces in equilibrium with atmospherically relevant gases. Infrared spectra were collected using a single beam FTIR spectrometer, Mattson Infinity Gold, equipped with a liquid nitrogen-cooled narrowband mercury cadmium telluride (MCT) detector. A commercially available air dryer (Balston 75-62) was used to purge the spectrometer and the internal compartment to minimize and to stabilize H₂O and CO₂ concentrations in the purge air. A custom designed infrared cell made from a stainless steel cube was placed in the internal sample compartment of the spectrometer. A schematic of the sample holder and infra-red cell are shown in Figure 2.1. The sample holder contains a tungsten grid (3 cm × 2 cm, 100 mesh/in., 0.002" wire dia., Accumet Materials Co.) held in position by nickel jaws. Thermocouple wires are spot welded to the tungsten grid to measure the temperature of the sample. In a typical experiment, one half of the tungsten grid is coated with the particular solid sample. Infrared cell is equipped with two BaF₂ windows for infrared measurements which were sealed by O-rings in the cell. The infra-red cell is a cube of 7 cm in all dimensions along the outside, with a total inner volume (V) of 310 ± 3 mL. A stage on which the infra-red cell sits is placed on equipped with a linear translator to allow either the gas phase or the surface to

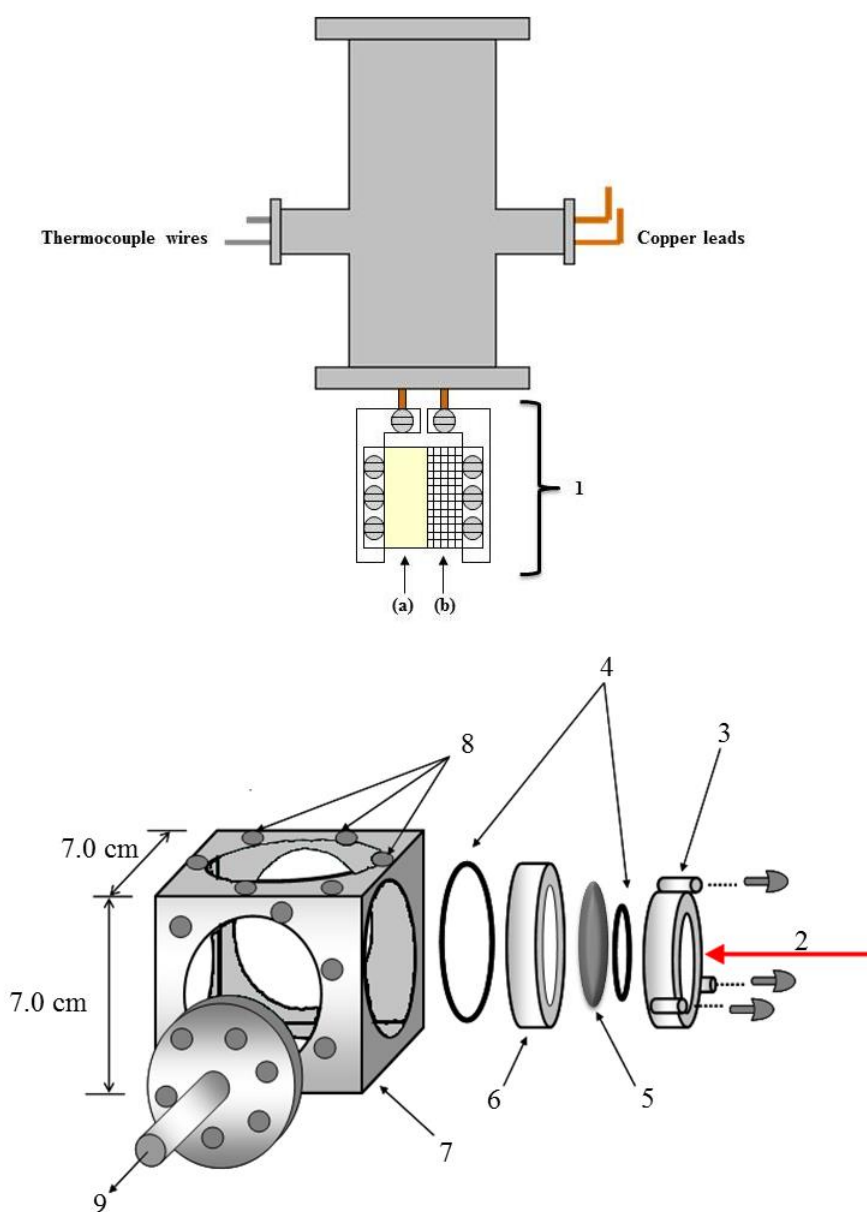


Figure 2.1. Schematic of the IR cell used for transmission FT-IR studies: 1. A Photoetched tungsten grid held by sample holder jaws (a) the sample side and (b) blank grid side; 2. Infrared incident light; 3. Aluminum screws and holder for the BaF₂ windows; 4. O-rings to hold the BaF₂ windows; 5. BaF₂ window; 6. Stainless steel holder; 7. Stainless steel infrared cube; 8. Holes for clamping the sample holder; 9. Gas inlet/outlet port which is connected to a gas handling system.

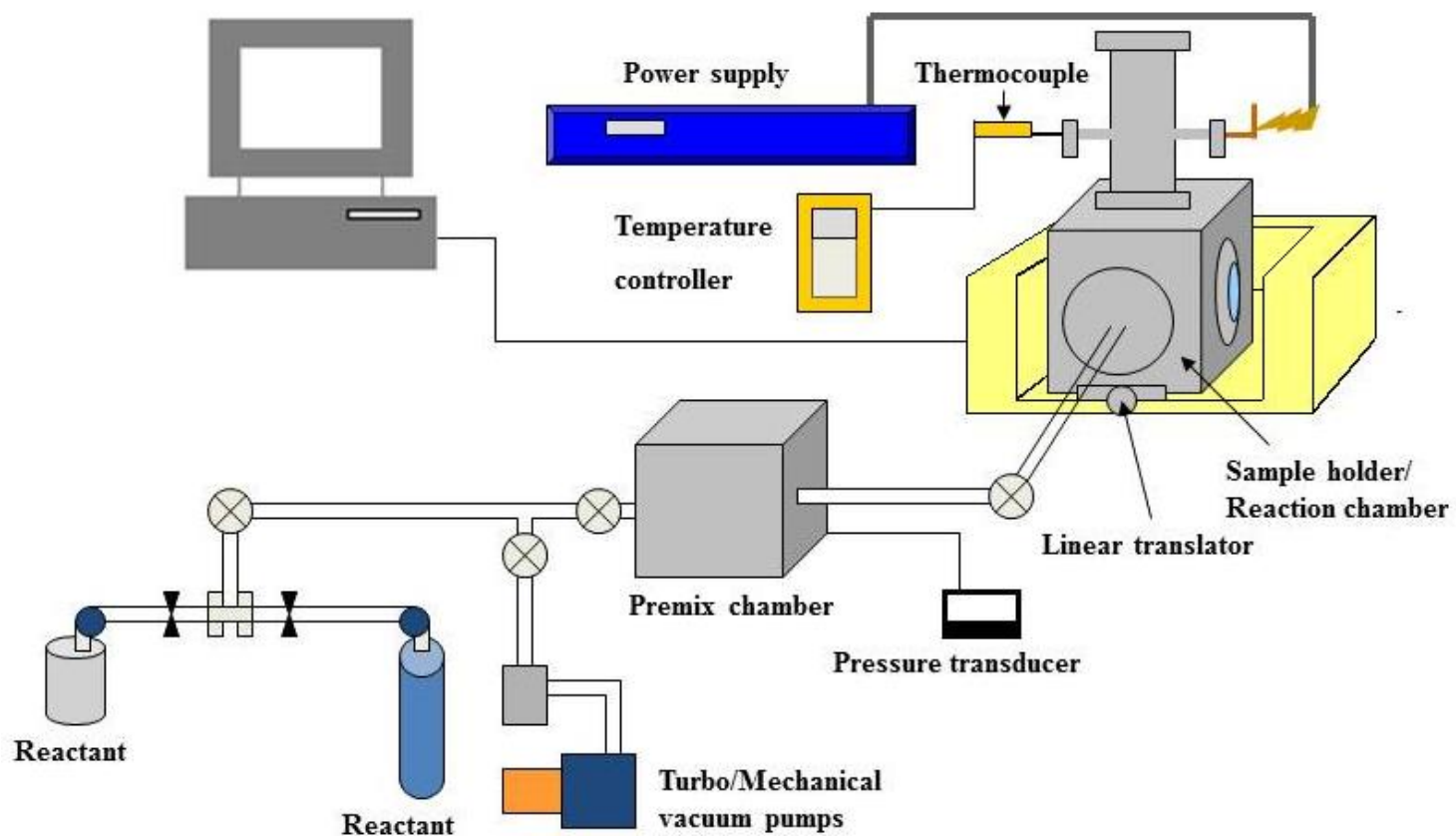


Figure 2.2. Schematic of the infrared cell and gas handling system used for these studies.

be placed in the path of the FTIR beam. The reaction chamber was connected to a power supply and vacuum/gas handling system (Figure 2.2). The infrared cell was connected to a premix chamber ($V = 565 \pm 9$ mL). The pre-mix chamber contains valves and gas supply lines connected to reagent gas containers, a two-stage vacuum system and two absolute pressure transducers (MKS instruments) that operate in two different pressure regimes from 0.001 to 10.00 Torr and from 0.1 to 1000 Torr. A schematic of this setup is shown in Figure 2.2. The experimental apparatus has been previously described in detail.¹¹⁵ The vacuum system consists of a turbo molecular pump and a mechanical pump that is used to evacuate the system down to a final pressure of around 1×10^{-7} Torr. Data acquisition was carried out using Winfirst software. Typically, spectra were recorded using a resolution of 4 cm^{-1} with 250 averaged scans from 800 to 4000 cm^{-1} .

2.1.2 Experimental Method

Solid samples (~ 10 mg) were dissolved in optima water at room temperature to produce a hydrosol. The hydrosol was sonicated for 10 min and transferred to one half of a tungsten grid using a pipette. Water evaporated at room temperature to create a uniform thin film. The sample holder was placed in the infrared cell. The sample was then evacuated overnight at room temperature or specific temperature for the oxide sample prior to introduce gas-phase reactants.

For absorbance spectra of surface species resulting from adsorption of gas-phase reactant, the gas was allowed into the reaction chamber at a desired pressure and then allowed to equilibrate until a constant pressure was measured. The coated half of the grid is associated with the spectral features of the surface and gas-phase whereas the other half

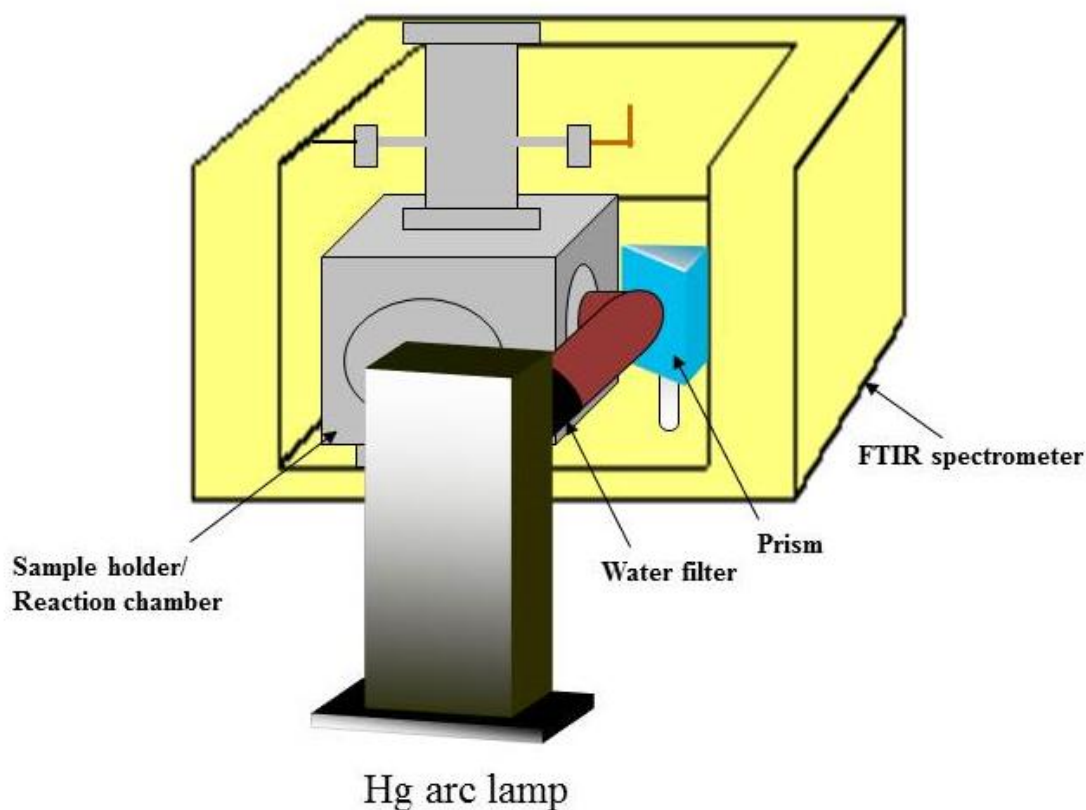


Figure 2.3. Schematic of the optical path of the light from the mercury arc lamp the infrared cell sitting inside the FTIR spectrometer. The sample is irradiated for certain time intervals after which spectra are then recorded of the gas phase and the oxide surface.

of the grid only contains spectral features of the gas-phase. Single beam spectra were referenced to the initial surface or gas phase to identify adsorbed and gas phase species. Spectra of adsorbed products were obtained by subtracting gas-phase spectra under similar conditions. All IR spectra were recorded at 296 K unless otherwise indicated.

2.1.3 Transmission FTIR Spectroscopy:

Photochemical Studies

The transmission FTIR experiments described in Section 2.1.1 was slightly modified for photochemical experiments. A 500 Watt mercury arc lamp (Oriel, model no. 66033) was used as a broadband light source that contained ultra-violet, visible, and infrared light. The optical path of the light from the arc lamp to the infrared cell and a graphical representation of these modifications are shown in Figure 2.3.

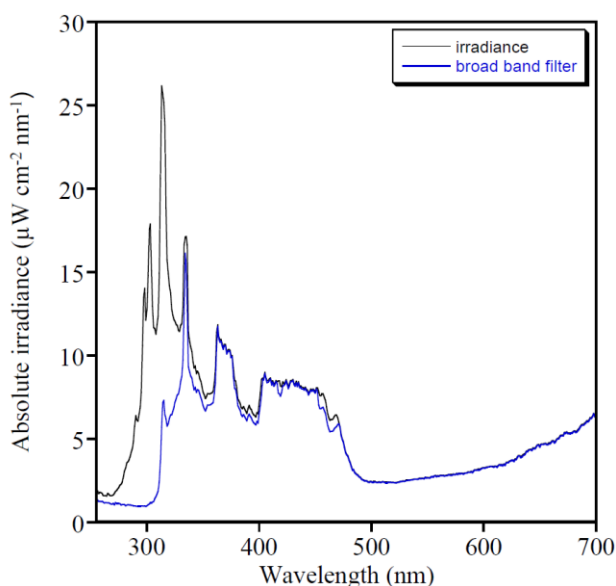


Figure 2.4. Irradiance profile of the light source (Hg arc lamp) with and without the broadband UV filter which cutoff wavelength of light below 300 nm.

Following sample preparation and reactive gas introduction, the valve connecting the FTIR cell to the mixing chamber was closed, letting the gas-phase products accumulate inside the cell as the surface was irradiated. The infrared light from the broadband source was removed with a water-filled filter. Samples were irradiated with

either the full broadband irradiation (without infrared light) or with the use of long-pass filters ($\lambda < 300$ nm, Oriel filter no. 59425) to cut off some of the higher energy wavelengths of light. Figure 2.4 shows the Irradiance of the lamp output measured using a spectroradiometer (model RPS900-R, International Light Technologies).

During the photolysis, infrared spectra of both gas phase and surface were recorded with the FTIR spectrometer in a similar fashion described in section 2.1.1. To acquire the infra-red spectra of surface-mediated and gas-phase post irradiation processes, the light source was blocked using a plastic shutter and spectra were recorded.

2.2 Quartz Crystal Microbalance (QCM)

Measurements

2.2.1 Flow cell for QCM Measurements

A custom built flow system was used to study CO₂, SO₂, NO₂ and water uptake on TiO₂ surfaces. The details of the flow system can be found elsewhere.^{113,116} Flow system consist a Thermo Nicolette 6700 FTIR spectrophotometer and a QCM200, 5 MHz quartz crystal microbalance. The amount of water and reactive gas uptake on oxide surfaces was measured with the QCM. An ATR-FTIR system is in parallel to QCM can be simultaneously used to get the spectroscopic information of the adsorption (Figure 2.5). The QCM portion of this system was used in dissertation research to quantify the uptake of reactive gases and water vapor.

2.2.2 QCM Analysis and the Sauerbrey Equation

The QCM measures the frequency of vibration at piezoelectric point for the

crystal in the instrument as humid air flows over the sample. The change in the frequency can be related to the mass of water or reactive gas uptake from the air passing through the sample when the mass loading is less than 2% of the crystal frequency by the Sauerbrey equation,

$$\Delta f = -C_f \times \Delta m \quad (2.1)$$

where Δf is the change in frequency (Hz), Δm is the change in mass ($\mu\text{g}/\text{cm}^2$) related to the change in frequency, and $-C_f$ is the sensitivity factor which is a constant for a 5 MHz AT-cut quartz crystal ($56.6 \text{ Hz } \mu\text{g}^{-1}\text{cm}^2$). Water and reactive gas adsorption on oxide particle surfaces were quantified using a commercial 5 MHz quartz crystal microbalance flow cell with a 1" inch diameter gold/Cr polished quartz crystal (QCM200, Stanford Research Systems). The QCM measurements yield important quantitative data for a better understanding of adsorbed species quantitatively on atmospherically relevant particles.^{113,116}

2.2.3 Experimental Method

In sample preparation, oxide power, approximately 10 mg, was first suspended in water and then the suspension was sprayed onto the QCM crystal using a glass atomizer. This method created a uniform thin film of particles covering the entire active area of the gold-coated quartz balance. The entire QCM system was placed inside a custom-made box constructed from Teflon that was designed to protect the flow cell from air currents which could affect the stability of these measurements.

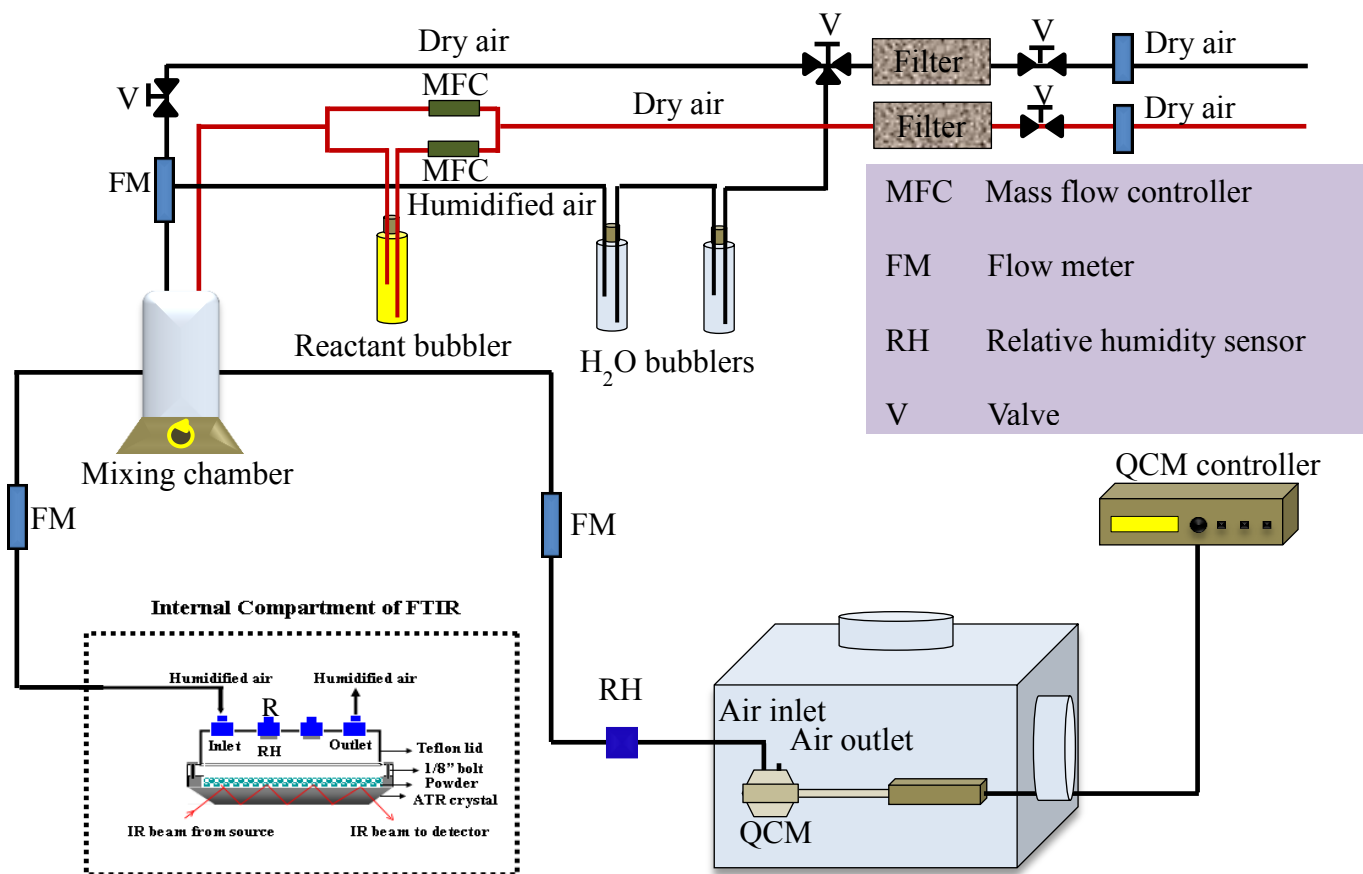


Figure 2.5. Schematic of the flow system which allows for simultaneous measurements of quartz crystal microbalance (QCM) and ATR-FTIR spectrometer. Only the QCM portion was used in this dissertation research. Adapted with permission from Ref. ¹¹³. Copyright 2012 American Chemical Society.

The frequency of the coated QCM was then recorded and subtracted from the baseline frequency (5 ± 0.1 MHz) with no sample present. This gave the exact mass of the sample before starting gas uptake measurements. After the sample was dried overnight ($< 1\%$ RH), the QCM was zeroed to $\Delta f = 0$ so that the change in mass measured was only due to the mass of water or reactive gas taken up by the sample. The relative humidity or reactive gas was allowed to stabilize and equilibrate for approximately 30 minutes, depending on the sample. Uptake experiments were carried out in triplicate measurements.

Gas uptake was studied by using a steady flow rate of 250 SCCM of the gas of interest over the sample deposited onto the QCM. Uptake was monitored using change in frequency of the QCM. The water uptake was carried out using two water bubblers and dry air flow. The dry air flow was sent through the two water bubblers producing humidified air. This humidified air was mixed with dry air to get the desired relative humidity. Both dry and humidified air flows equilibrated inside a mixing chamber before being directed towards the sample deposited on QCM. The relative humidity was controlled by changing the dry air flow through the water bubblers. The water uptake at each relative humidity was monitored using QCM. The relative humidity of the flow was read using a (Honeywell) humidity sensor and a custom-built digital readout.

2.3 X-ray Photoelectron Spectroscopy

X-ray photoelectron spectroscopy (XPS) is a powerful surface analysis technique which uses X-rays to eject core electrons from the surface region. An electron from a higher energy level then relaxes down to a lower energy state and simultaneously releases

a photoelectron which has a characteristic binding energy of the element and its chemical environment. Since the mean free path of electrons in the solid usually on the order of several nanometers, XPS inherently probes the surface and near-surface regions of the material.

The sample is irradiated with X-rays with energy $h\nu$. Kinetic energy (KE) of the emitted photoelectrons is measured. Then binding energy (BE) of emitted photoelectrons is calculated using the work function of the instrument (Φ). This relationship is given by:

$$BE = h\nu - KE - \Phi \quad (2.2)$$

where BE is the binding energy referenced to vacuum level and KE is the kinetic energy of the electron. Furthermore, the binding energy can shift up to a several eVs depending on the chemical environment of the atom. Thus, XPS can yield information about the elements present on the surface, the oxidation state of the elements, surface functional groups, and surface adsorbates present. A Kratos Axis Ultra X-ray photoelectron spectroscopy system (Manchester, UK) was used to investigate the bare and reacted surfaces of the metal oxide particles as described below.

2.3.1 XPS Experimental Setup

The custom-designed Kratos Axis Ultra X-ray photoelectron spectroscopy system for reactions and analysis has been described in detail before.^{117,118} The experimental setup has capabilities for reacting samples with gas-phase reactants and evacuating the gas-phase and surface product analysis with four different chambers that include: (i) an

ultra-high vacuum (UHV) surface analysis chamber, (ii) a sample transfer antechamber, (iii) a stainless steel reaction chamber (Figure 2.6) and (iv) a Teflon coated reaction chamber. The transfer antechamber is connected to the analysis chamber, steel reaction chamber and Teflon coated reaction chamber. With this configuration, the transfer antechamber is used to introduce samples into the analysis chamber, and also allows for samples to be transferred directly from the surface analysis chamber to the reaction chambers vice versa.

The details of the stainless steel reaction chamber have been described before.¹¹⁸ Teflon coated reaction chamber was used to react corrosive gases such as HNO_3 to react with solid samples during experiments. Additionally, UV light source consisting a 500 W Hg lamp (Oriel Instruments model number 66033) was used to irradiate the samples. A water filter (Oriel Instruments) was used in line with the lamp output to minimize infrared damage and heating of the sample. The light from the lamp was reflected using a 90° turning mirror (Oriel Instruments, Model: 66215 Beam Turning Mirror, Full Reflector, 200 nm – 30 μm Primary Range, 1.5 Inch Series) into the reaction chamber via the Pyrex window. The transmissivity of the Pyrex window was ~80% at the wavelengths above ~320 nm with a 0.72 W/cm^2 measured light intensity at the sample.

The surface analysis chamber is equipped with monochromatic radiation at 1486.6 eV from an aluminum K_α source using a 500 mm Rowland circle silicon single crystal monochromator. The X-ray gun was operated using a 15 mA emission current at an accelerating voltage of 15 kV. Low energy electrons were used for charge compensation to neutralize the sample. Survey scans were collected using the following instrument parameters: energy scan range of 1200 to -5 eV; pass energy of 160 eV; step

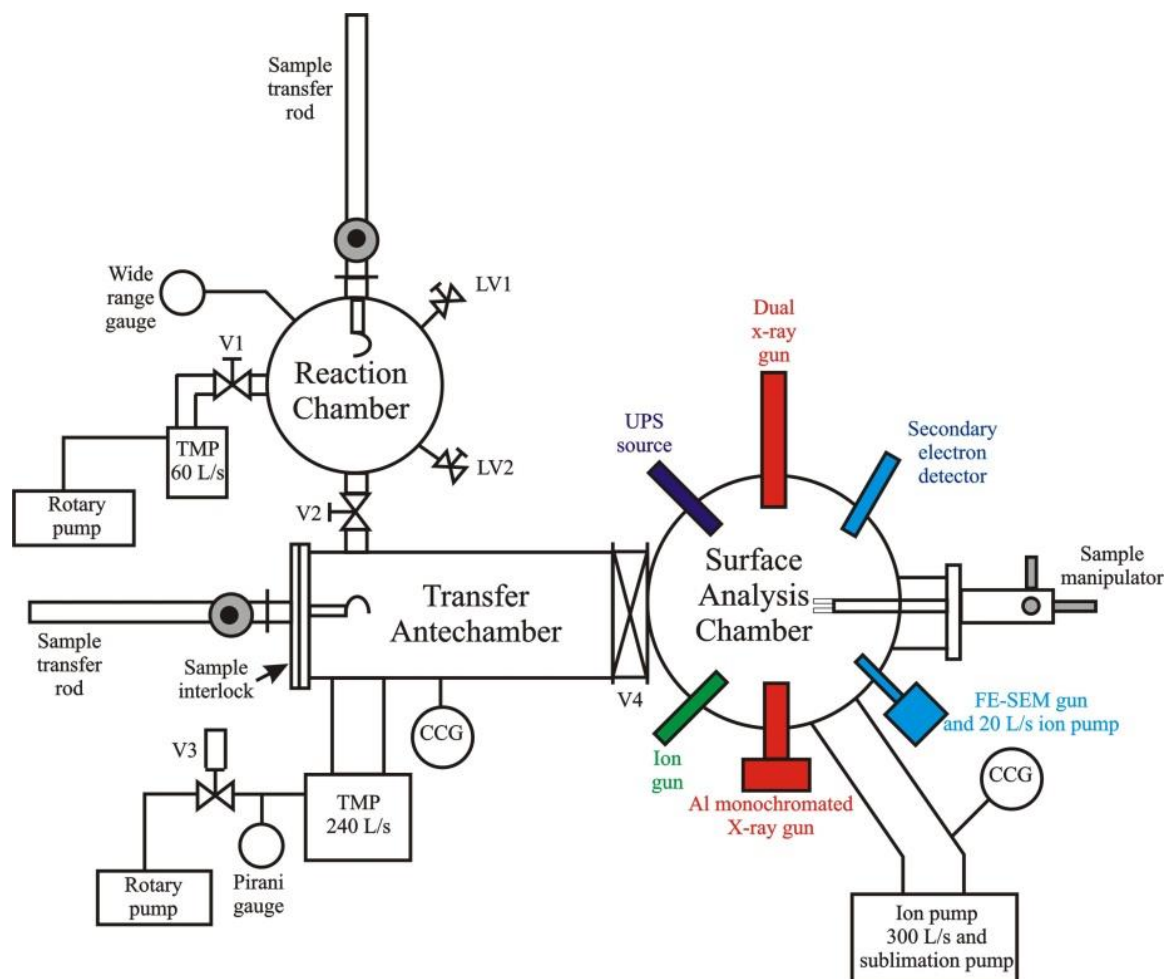


Figure 2.6. Schematic of the custom-designed Kratos Axis Ultra XPS. The system consists of four chambers: a transfer antechamber, surface analysis chamber, reaction chamber and Teflon coated HNO_3 reaction chamber (not shown). Each chamber is equipped with a separate pumping system, pressure gauges and is separated from the other chambers from manual and motorized valves, V2 and V4 respectively. The surface analysis chamber is equipped with X-ray sources, Fe-SEM gun, SE detector, UPS source, ion gun and sample manipulator. See experimental methods section for a more detailed description of this four chamber system. (Note: TMP – turbomolecular pump; CCG – cold cathode gauge; LV – leak valve and V – valve). Adapted from ref. 117 with permission of the PCCP Owner Societies.

size of 1 eV; dwell time of 200 ms and an X-ray spot size of $700 \times 300 \mu\text{m}$. High resolution spectra were acquired in the region of interest using the following experimental parameters: 20 to 40 eV energy window; pass energy of 20 eV; step size of 0.1 eV and dwell time of 1000 ms. The absolute energy scale was calibrated to the $\text{Cu}2p_{2/3}$ peak binding energy of 932.6 eV using an etched copper plate.

2.3.2 Data Processing of Core Photoelectron Spectra

All spectra were calibrated using the adventitious C1s peak at 285.0 eV. For TiO_2 samples, spectra were calibrated using a well-defined Ti^{4+} binding energy of 459.3 eV. A Shirley-type background was subtracted from each spectrum to account for inelastically scattered electrons that contribute to the broad background. CasaXPS software was used to process the XPS data.¹¹⁹ Details of the binding energies and full-width-at-the-half-maximum (FWHM) of the bands observed in high resolution XPS spectra will be discussed in detail in following chapters where necessary. An error of ± 0.2 eV is reported for all peak binding energies.

2.3.3 Experimental Method

For typical XPS analysis, powdered samples were pressed onto indium foil. The indium foil was then placed on either a stainless steel bar or copper stub for analysis. The samples were placed into the transfer antechamber and evacuated to 5×10^{-7} Torr and transferred to the XPS analysis chamber, which had a pressure that was maintained in the 10^{-9} Torr range during analysis. After acquiring the initial scans at the surface analysis

chamber, the sample was transferred to either steel or Teflon coated chamber via the transfer antechamber by means of sample transfer rods depending on the reactive gas. The sample was then reacted with gas-phase reactants followed by evacuation to remove gas-phase and transferred to the sample analysis chamber for scans. The evacuation step removes any weakly adsorbed species. After acquiring the initial scans, samples were transferred to the steel reaction chamber for reactions under environmentally relevant conditions of (1) H_2O , (2) O_2 , (3) $\text{H}_2\text{O}/\text{O}_2$ and UV light. H_2O or O_2 was introduced in approximately 15 seconds. The resulting gas mixture was allowed to equilibrate with the sample for at least 30 minutes. The reacted sample was then evacuated and transferred back to the analysis chamber for post-reaction surface analysis.

2.4 Aqueous Phase Studies of Oxide Particles

Reacted with Trace Gases

2.4.1 Solution Phase Behavior of Metal Oxide

Particles Reacted with Trace Atmospheric Gases

Reacted and unreacted particles were suspended in optima water (Fisher). The suspension was sonicated for 10 minutes. The stabilities of unreacted and reacted particle suspensions were measured using sedimentation plots created by measuring the extinction with a Perkin-Elmer Lambda 20 UV-visible spectrometer. Hydrodynamic radii, Zeta potential and pH of the suspension were measured as necessary.

2.4.2 Iron Dissolution Experiments

HNO₃ reacted α -Fe₂O₃ particles were prepared in a Teflon coated reaction chamber by reacting with gas-phase HNO₃ to investigate the effect of reaction on iron dissolution. Reacted particles were suspended in optima water (Fisher). The suspension was stirred for 24 h. Metal ion dissolution was studied for both reacted and unreacted particles. Aliquot from the supernatant suspension was passed through a 0.2 μ m PTFE filter to remove particles. The concentration of metal ions was measured using Varian 720-ES inductively coupled plasma-optical emission spectrometer (ICP-OES). Dissolution of unreacted sample was also conducted under the same conditions for comparison. All experiments were conducted in triplicate.

2.5 Complementary Physical and Chemical

Characterization Techniques

2.5.1 Transmission Electron Microscopy (TEM)

The size and the morphology of metal oxide nanoparticles were determined by JEOL JEM-1230 Transmission Electron Microscope (TEM). Sample preparation for the TEM analysis is as follows. A dilute suspension of nanoparticles in water was prepared and sonicated for 10 minutes. A drop of the sample was transferred to the TEM grid and was allowed to dry. Once dried the TEM analysis was performed. The TEM grids were carbon coated Cu grids (CF150-Cu) purchased from Electron Microscopy Sciences. The oxide particle size was given as the average diameter of 200 particles.

2.5.2 Scanning Electron Microscopy (SEM)

A Hitachi S-4000 SEM-EDX system was used to collect scanning electron microscopy (SEM) images. Particles were sprinkled onto tape that was attached to an aluminum stub. An accelerating voltage of 15 kV was used to obtain the images shown. Particles were sprinkled onto carbon tape. The tape was attached to a carbon stub. An accelerating voltage of 15 kV was used to obtain bulk elemental compositions with a limit of detection of 1 wt% of the bulk. The oxide particle size was determined as the average diameter of at least 200 particles.

2.5.3 X-ray Diffraction (XRD)

Crystalline structure and composition of bulk powder samples were determined using (XRD) analysis. Dry powder samples were placed in the XRD sample holder, and the surface of the powder was smoothed with a razor until flush with the rim of the holder. A Siemens D5000 X-ray diffractometer with Cu K α target and nickel filter was used to collect the XRD powder patterns between angles of 2θ from 10° and 90°.

2.5.4 Brunauer, Emmett and Teller (BET)

Surface Area Measurements

The surface area of the mineral oxide powders were measured by BET surface area analysis. Relative pressures, (P/P_0) , of inert gases are introduced into a calibrated sample cell that allows the adsorption of the inert gas, N₂ in the current studies, to be measured, W . The cross section of the N₂ molecule is known and total surface area can be calculated. The total surface area is divided by the sample mass to give a surface area per

unit mass. The specific surface area of each nanoparticle was determined from seven-point N₂-BET adsorption isotherm measurements performed on a Quantachrome 4200e surface area analyzer by the following equation (2.3) in the limited linear range of the BET isotherm,

$$\frac{1}{W((P_o / P)-1)} = \frac{1}{W_m C} + \frac{C-1}{W_m C} \left(\frac{P}{P_o} \right) \quad (2.3)$$

where W_m is the weight of adsorbate constituting one monolayer of coverage and C is a constant. Plotting $1/W((P_o/P)-1)$ versus (P/P_o) allows for determination of W_m and C by the slope and intercept of the linear fit. The sample preparation for surface area analysis is minimal. Prior to analysis, samples were degassed overnight at temperatures that would not change the properties of the oxide. Typically temperature between 150 – 300 °C depending on the sample.

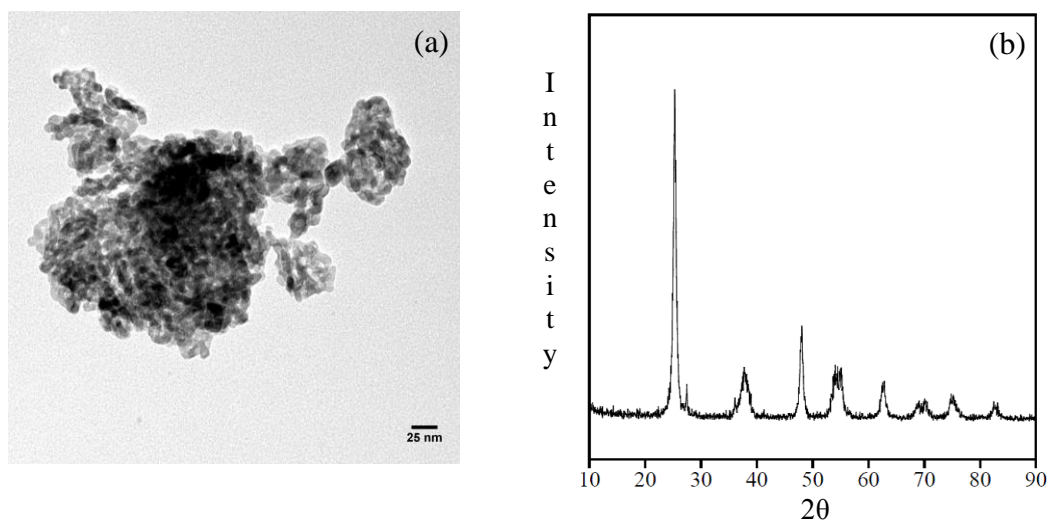
2.6 Materials and Reagents

2.6.1 Oxide Powders

Commercially available TiO₂ and α -Fe₂O₃ powder samples were used in this dissertation research. The source of all metal oxides used in the research, with their measured particle size and specific surface area measurements, are listed in Table 2.1. All surface areas were measured using a Quantachrome Nova 1200 Multipoint BET apparatus. X-ray diffraction of the powders confirmed the crystalline phases of the metal

Table 2.1. Source of metal oxide powders with particle and surface area specifications.

Oxide Sample	Commercial Source	Purity	Average Particle size (nm)	Surface area (m ² /g)
TiO ₂	Nanostructures and Amorphous Inc.	anatase (~94%)	10 (± 3)	128 (± 5)
α-Fe ₂ O ₃	Alfa Aesar	hematite	310 (± 22)	23 (± 2)

Figure 2.7. Nanoparticle characterization (a) Transmission electron microscopy (TEM) image and (b) X-ray Diffraction (XRD) pattern of TiO₂.

oxides presented here. TEM and SEM were used to acquire images of TiO₂ and α-Fe₂O₃ particles respectively.

2.6.2 Liquid and Gas Reagents

For relative humidity studies and aqueous phase studies optima water (Fisher) and distilled H₂O (Milli-Q) were used. Dry gaseous nitric acid was taken from the vapor of a

1:3 mixture of concentrated HNO_3 (70.6% HNO_3 , Mallinckrodt) and 95.9% H_2SO_4 (Mallinckrodt). Formic acid (Alfa Aesar) was used as received. Prior to use, liquid phase reactants were degassed several times with consecutive freeze-pump-thaw cycles. Oxygen (UPC grade) was obtained from Airgas and Praxair. CO_2 (UPC grade) was purchased from Airgas Inc. SO_2 (99.98% purity) and NO_2 (99.95% purity) were purchased from Matheson gas.

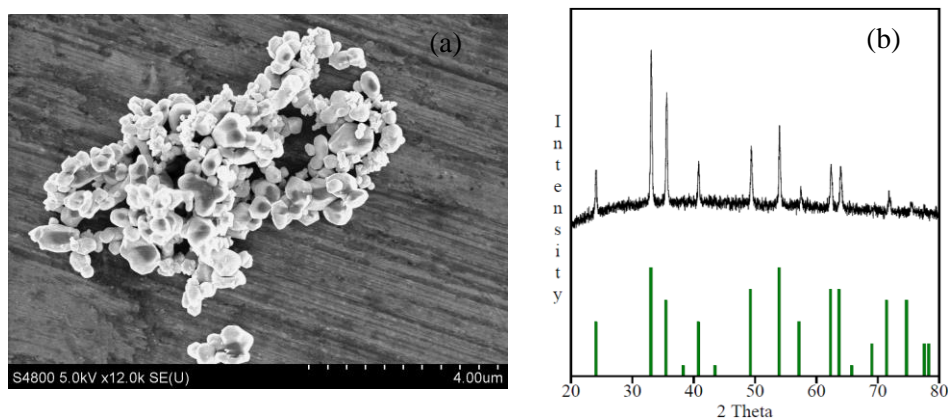


Figure 2.8. Particle characterization (a) Scanning electron microscope (SEM) image and (b) X-ray diffraction (XRD) pattern of $\alpha\text{-Fe}_2\text{O}_3$.

CHAPTER 3

SULFUR DIOXIDE ADSORPTION AND PHOOTOOXIDATION ON
ISOTOPICALLY-LABELLED TITANIUM DIOXIDE NANOPARTICLE SURFACES:
ROLES OF SURFACE HYDROXYL GROUPS AND ADSORBED WATER IN THE
FORMATION AND STABILITY OF ADSORBED SULFITE AND SULFATE

3.1 Abstract

Transmission FTIR spectroscopy and X-ray photoelectron spectroscopy (XPS) are used to probe the details of sulfur dioxide adsorption and photooxidation on titanium dioxide nanoparticle surfaces. Adsorption sites, surface speciation and photooxidation chemistry have been determined from analysis of FTIR spectra in conjunction with isotope labeling experiments. These data show that surface hydroxyl groups are involved in the adsorption of sulfur dioxide, and in particular, sulfur dioxide reacts with either one surface O–H group to yield adsorbed bisulfite or two surface O–H groups to yield adsorbed sulfite and water. Using ^{16}O –H, ^{16}O –D and ^{18}O –H labeled surface O–H groups, additional insights into the adsorption mechanism as well as shifts in the vibrational modes of adsorbed sulfite have been determined. Upon irradiation, adsorbed sulfite/bisulfite converts to adsorbed sulfate. The relative stability of adsorbed sulfite to adsorbed sulfate on TiO_2 nanoparticle surfaces was also examined in the presence of increasing relative humidity (RH). It is shown here that adsorbed water can more easily displace sulfite compared to sulfate by forming a stable sulfur dioxide water complex in the presence of adsorbed water. These differences in the RH-dependent stability of adsorbed species that form as a

result of surface heterogeneous reactions on oxide particles surfaces has important implications in the heterogeneous chemistry of mineral dust aerosol in the atmosphere.

3.2 Introduction

There is increasing evidence that mineral dust aerosol plays an important role in the Earth's atmosphere.^{8,120} Among the components of mineral dust aerosol, there has been some recent interest in titanium dioxide due to the fact that it is a semiconductor material and a well-known photocatalyst.^{8,97} Additionally, with the widespread use and production of nanoscale TiO₂, there is a possibility that these engineered nanomaterials can get into atmospheric environment.^{40,41} Thus, for these reasons, there is interest in the atmospheric chemistry of TiO₂.

UV light irradiation of TiO₂ with photon energies above the band gap, i.e. $E > 3.2$ eV with $\lambda < 390$ nm, generates electron-hole (e^-/h^+) pairs on TiO₂ particle surfaces which can lead to redox processes.^{10,32,38,121} These photocatalytic properties of TiO₂ have been used in a wide range of applications including the destruction of volatile organic compounds.^{38,121} For example, TiO₂ coated self-cleaning window glasses are widely used thin films for removing organic pollutants.³² Additionally, as an atmospheric component of mineral dust aerosol, it has been proposed that TiO₂ can photochemically convert nitrogen dioxide in urban environments to HONO.^{25,122}

Here we investigate reactions of sulfur dioxide, which has several atmospheric sources including as a product of the burning of sulfur-containing fuels and coal, on the surface of TiO₂.^{8,94} Earlier studies of SO₂ adsorption on metal oxides have clearly shown that Lewis acid sites, hydroxyl groups and oxygen vacancies can all play a role in the

surface chemistry.^{8,96,123} In the case of titanium dioxide, there have been several infrared and theoretical studies on SO₂ heterogeneous interactions with anatase and rutile TiO₂ surfaces.^{8,124,125} More recently, attention has been focused on these heterogeneous interactions and their dependence on environmental conditions.⁸ In a recent study on heterogeneous reactions of SO₂ on nanoscale titanium dioxide particles using XPS, Baltrusaitis *et. al.* showed the formation of a variety of sulfur-containing surface products, including adsorbed sulfite and sulfate.⁸ The coverage of these different surface products was found to depend on sample pre-treatment and particle size as well as several environmental factors including the presence of molecular oxygen, water vapor and/or UV light.

Although both sulfite and sulfate have been detected on metal oxide particles as well as other components of mineral dust aerosol,^{8,94,95,117} little is known about the relative stabilities of adsorbed sulfite and sulfate, especially as a function of relative humidity and in the presence of adsorbed water. Studies at the adsorbed water-oxide interfaces have shown that ions such as nitrate and carbonate can be readily solvated by adsorbed water molecules under ambient conditions.^{101,126} For example, previous FTIR studies have shown that there are changes in the infrared spectrum of adsorbed nitrate as a function of relative humidity as a result of changes in the bonding of nitrate on the surface of aluminum oxide particle surfaces.¹⁰¹ In the absence of adsorbed water, nitrate forms different coordination modes to the oxide surface but in the presence of adsorbed water these oxide coordinated nitrate ions can be solvated by water molecules forming stable inner and outer sphere solvated complexes. Furthermore, this process is reversible for the nitrate ion, i.e. upon decreasing relative humidity the conversion back to oxide-

coordinated nitrate is observed upon decreasing relative humidity with the concurrence of water desorption from the surface.¹⁰¹ In contrast, previous studies have suggested that the vibrational bands of sulfate groups on sulfated TiO₂ change very little in the presence and absence of adsorbed water.¹²⁷ Therefore, it is important to further understand the interactions between adsorbed species such as sulfite and sulfate on particle surfaces under different relative humidity conditions.

In this study, we investigate mechanistic aspects of sulfur dioxide surface chemistry and photochemistry on TiO₂ nanoparticle surfaces. Vibrational frequencies of adsorbed SO₂ to yield adsorbed sulfite as well as sulfate formation on TiO₂ are reported. Isotope labeling provides additional insights into the reaction chemistry of SO₂ on TiO₂ nanoparticle surfaces. Furthermore, the relative stability of adsorbed sulfite compared to adsorbed sulfate on TiO₂ particle surfaces as a function of relative humidity is investigated for the first time to the best of our knowledge. Loss of sulfur from the surface as a function of relative humidity is quantified using X-ray photoelectron spectroscopy.

3.3 Experimental Methods

3.3.1 Sources and Purity of Gases

D₂O, H₂¹⁸O (Sigma Aldrich) and distilled H₂O (Fisher, Optima grade) were degassed with several freeze-pump-thaw cycles prior to use. SO₂ (99.98 wt % min purity) was purchased from Matheson gas and O₂ (UPC grade) was obtained from Airgas Inc.

3.3.2 Source of TiO₂ and Nanoparticle Characterization

TiO₂ nanoparticles purchased from Nanostructures and Amorphous Materials Inc. were used as received. The bulk crystalline phase of TiO₂ sample was analyzed using a Siemens D5000 diffractometer with a Cu K α source. Transmission electron microscopy (TEM) images were acquired using a JEOL 1230 Transmission Electron Microscope. Brunauer-Emmet-Teller (BET) adsorption isotherm measurements were carried out using a Quantachrome Nova 4200e multipoint surface area analyzer. TiO₂ particles were degassed for 4 h at 473 K prior to the surface area analysis to remove any impurities.

3.3.3 Transmission FTIR Spectroscopy

Transmission FTIR spectroscopy was used to investigate SO₂ adsorption on TiO₂ nanoparticles, in an experimental apparatus that has been previously described in detail.^{101,128} FTIR spectra were collected using a Mattson Galaxy 6000 spectrometer equipped with a liquid nitrogen cooled mercury cadmium telluride detector (MCT). TiO₂ samples (8–10 mg) were dissolved in optima water at room temperature to produce a hydrosol. The hydrosol was sonicated for 10 min and transferred to one half of a tungsten grid (3 cm \times 2 cm, 100 mesh/in., 0.002" wire dia., Accumet Materials Co.) held in position by nickel jaws using a pipette. Water evaporated at room temperature to create a uniform thin film. Thermocouple wires were attached to the tungsten grid to allow resistive heating. The sample holder was placed in a stainless steel reaction chamber equipped with a linear translator to allow either the gas phase or the TiO₂ sample to be placed in the path of the FTIR beam. The reaction chamber was connected to a power supply and vacuum/gas handling system. Data acquisition was carried out using Winfirst

software and spectra were recorded using a resolution of 4 cm^{-1} with 264 averaged scans from 800 to 4000 cm^{-1} . For absorbance spectra of surface species resulting from adsorption of SO_2 , the gas was allowed into the reaction chamber at a desired pressure and then allowed to equilibrate until a constant pressure was measured. The coated half of the grid is associated with the spectral features of the surface and gas-phase whereas the other half of the grid only contains spectral features of the gas phase. Single beam spectra were referenced to the initial surface or gas phase to identify adsorbed and gas phase species. Spectra of adsorbed products were obtained by subtracting gas-phase spectra under similar conditions.

A pretreatment process was carried out for cleaning TiO_2 nanoparticles as these particles contain an obvious impurity potentially from the manufacturing process (*vide infra*). This begins with overnight heating and evacuation at 10^{-7} Torr. The sample was then allowed to cool to room temperature before gases were admitted into the reaction chamber. All spectra were recorded at 296 K . For photochemical experiments, irradiation was carried out using a 500 W broadband Hg arc lamp (Oriel, model no. 66033), followed by a water filter, to remove IR radiation, and a UV filter to remove shorter wavelengths ($\lambda < 300\text{ nm}$, Oriel filter no. 59425), was used to distinguish the effect of UV light.

3.3.4 X-ray Photoelectron Spectroscopy (XPS)

XPS was used to quantify the amount of adsorbed sulfur species on the surface. A custom-designed Kratos Axis Ultra spectrometer that was used for these measurements and data analysis has been previously described in detail.¹¹⁷

3.4 Results and Discussion

3.4.1 Characterization of TiO₂ Nanoparticles

Transmission electron microscopy images show primary particles with an average particle size of 10 ± 3 nm (200 particles counted). The image in Figure 2.1 shows these smaller particles appearing quite aggregated. Only the primary particles were used to calculate the average particle size. A primary particle size histogram is shown along with the TEM image in Figure 2.1. XRD reveals that the TiO₂ particles are primarily anatase with small amount of rutile (~6%). Surface area measurements using a seven-point BET analysis results in an average value and standard deviation of 128 ± 5 m²/g from three replicate measurements.

3.4.2 Surface Hydroxyl Groups and Adsorbed

Water on TiO₂ Nanoparticles

An FTIR spectrum of TiO₂ nanoparticle surfaces placed in the infrared cell and evacuated initially contained surface adsorbed water with a broad band of H-bonded hydroxyls at 3300 cm⁻¹ and water bending mode at 1620 cm⁻¹ as well as the presence of a band at 1361 cm⁻¹ that appeared to be an impurity (spectra not shown). Surface-bound water was completely desorbed by 200 °C and the particles were further heated to 400 °C for 12 hours to remove impurities left on the particle surface most likely a result of the synthesis process. During the 400 °C heat treatment, all hydroxyl groups were removed leading to dehydroxylated TiO₂ nanoparticle surfaces. Hydroxyl groups on TiO₂ surfaces have been shown to play a role in sulfur dioxide adsorption.⁸ Therefore, after heating, samples were exposed to water vapor at room temperature to regenerate hydroxyl groups

followed by evacuation at 200 °C to remove weakly adsorbed water. Samples were then allowed to cool to room temperature prior to gas adsorption.

The hydroxyl group region following heating and subsequent re-hydroxylation shows absorption bands between 3600 and 3800 cm^{-1} with at least two prominent features at 3672 cm^{-1} and 3717 cm^{-1} respectively. FTIR spectra, which contain features due to surface species present on the surface, are peak fitted to more clearly resolve absorptions due to different vibrational frequencies for the different hydroxyl groups present on the surface. Peak-fitting results in five absorption bands at 3733, 3717, 3691, 3672 and 3642 cm^{-1} as seen in Figure 3.1(a). There is some controversy in the literature on the exact assignment of these bands. In general, it is accepted that the different bands are due to the O–H stretching motion mostly associated with hydroxyl groups present as isolated

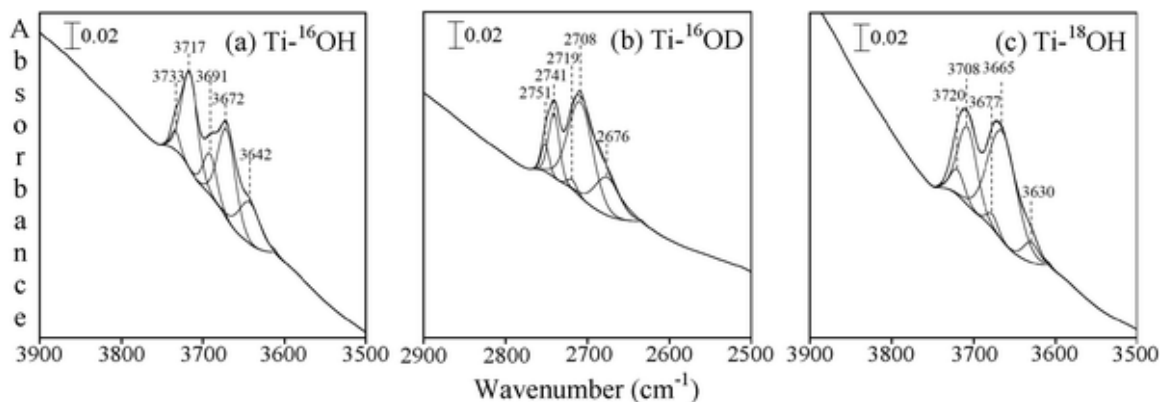


Figure 3.1. Peak-fitted hydroxyl group region for (a) ^{16}O -H stretching vibrations for unlabeled TiO_2 , (b) ^{16}O -D stretching vibrations for deuterated TiO_2 following D_2O exchange, (c) ^{18}O -H stretching vibrations for ^{18}O labeled TiO_2 following H_2^{18}O exchange. See text for further details.

and bridge bonded moieties.¹²⁹ In another study, Dizwigaj et. al. combined experimental data and theoretical calculations to assign the vibrational bands of TiO_2 hydroxyl groups

as isolated hydroxyl groups and O-H associated with chemisorbed water on different surface crystallographic planes¹³⁰ Deiana et. al. have discussed the hydroxyl groups and defect sites of P25 TiO₂ in more detail proposing that absorption bands higher than 3680 cm⁻¹ assigned to isolated hydroxyls and bands below 3680 cm⁻¹ be assigned to bridged hydroxyls.¹²⁹ Due to these differences in assignments, further studies are needed to confirm the presence of chemisorbed water on TiO₂ surface. In this study we follow the assignment of Deiana et al. as being due to isolated and bridged hydroxyl groups on TiO₂ nanoparticle surfaces as summarized in Table 3.1.

Table 3.1. Vibrational assignment of hydroxyl groups, ¹⁶O-H, O-D and ¹⁸O-H, on TiO₂ nanoparticle surfaces.

Assignment	This Study			Literature
	Ti- ¹⁶ OH	Ti- ¹⁶ O-D	Ti- ¹⁸ O-H	Ti- ¹⁶ OH
Ti – OH isolated	3733	2751	3720	3736
	3717	2741	3708	3717
	3691	2719	3677	3688
Ti – OH bridged	3672	2708	3665	3672
	3642	2676	3630	3642

Isotope studies were conducted to provide insights into SO₂ adsorption (*vide infra*). TiO₂ nanoparticles were exposed to 10 Torr of D₂O for 30 minutes followed by evacuation. This process was repeated several times until all surface O-H groups were found to exchange to O-D.⁸⁵ To investigate ¹⁸O-H labeled groups, TiO₂ nanoparticles were exposed to H₂¹⁸O for 12 hours under UV irradiation to exchange surface ¹⁶O-H for ¹⁸O-H groups.¹³¹ After these isotope labeling treatments, samples were evacuated at 200 °C for 12 hours to remove physisorbed water. Infrared spectra of these two isotopically-

labeled surface hydroxyl groups, O–D and ^{18}O –H, are shown in Figure 3.1(b) and (c), respectively. Assignments for these are also given in Table 3.1 along with the ^{16}O –H assignments.¹²⁹

3.4.3 SO_2 Adsorption on TiO_2 Particles

TiO_2 nanoparticle surfaces were exposed to known pressures of SO_2 and, after 25 minutes, an infrared spectrum was recorded. For the surface adsorbed species, each spectrum was obtained by referencing to the initial TiO_2 spectrum prior to SO_2 introduction and then subtracting out gas-phase absorptions. These difference spectra are shown in Figure 3.2 and are recorded following exposure of TiO_2 nanoparticles to SO_2 as a function of increasing initial pressures between 5 mTorr to 100 mTorr (5, 10, 15, 20, 22, 25, 28, 30, 40, and 100 mTorr). As can be seen in Figure 3.2, these difference spectra are quite rich with several spectral features apparent. In particular, multiple absorption bands are observed between 800 and 1200 cm^{-1} and more isolated bands are seen at 1325 and 1620 cm^{-1} . Additionally, there is another broad absorption band between 2500 and 3500 cm^{-1} . Furthermore, these spectra show negative features between 3600 and 3900 cm^{-1} associated with the loss of surface hydroxyl groups from the surface upon adsorption of SO_2 .

The broad absorption between 800 and 1200 cm^{-1} of Figure 3.2 is composed of several components that can be identified at the highest coverage at 886, 923, 971, 1006, 1057 and 1139 cm^{-1} . After evacuation of gas-phase SO_2 , the absorption band at 1139 cm^{-1} disappears from the spectrum as does the absorption band at 1325 cm^{-1} . This can be seen in the inset of Figure 3.2. This behavior suggest that the 1139 and 1325 cm^{-1} bands

are associated with a more weakly, reversibly adsorbed species on the surface whereas absorption bands between 800 and 1200 cm^{-1} are not removed upon evacuation of gas-phase SO_2 suggesting a more strongly bound chemisorbed species on the surface. Assignment of the weakly adsorbed species can be made to physisorbed SO_2 with symmetric (ν_1) and asymmetric (ν_3) stretching modes at 1139 and 1325 cm^{-1} , respectively, which are close in frequency to the gas-phase values. This assignment agrees well with previous studies of SO_2 physisorbed on different metal oxides.¹²³

In analyzing these spectra, the role of the hydroxyl groups in the adsorption and surface chemistry of SO_2 on TiO_2 nanoparticles can be addressed by viewing the O-H stretching region not as difference spectra as shown in Figure 3.1 but instead as absorption features that are due to O-H groups remaining on the surface. Figure 3.3 shows the O-H region for all three isotopes after adsorption of SO_2 at the highest exposed initial pressures (100 mTorr). It can be seen that the intensity of some hydroxyl groups decrease significantly after the adsorption of SO_2 . In particular, for $\text{Ti-}^{16}\text{OH}$ absorption bands at 3717 cm^{-1} and 3691 cm^{-1} are nearly gone while absorptions at 3733 and 3642 cm^{-1} remain in the spectrum. The band at 3672 cm^{-1} is also visible but less intense after reaction. From the vibrational assignment of O-H absorptions, it can be concluded that SO_2 prefers reaction of isolated hydroxyl groups followed by reaction with bridged hydroxyl groups. The hydroxyl groups at 3733 cm^{-1} and 3642 cm^{-1} , the hydroxyl groups with the highest and lowest frequencies for isolated and bridging O-H groups, respectively, appear to be much less reactive and remain on the surface. Similar changes

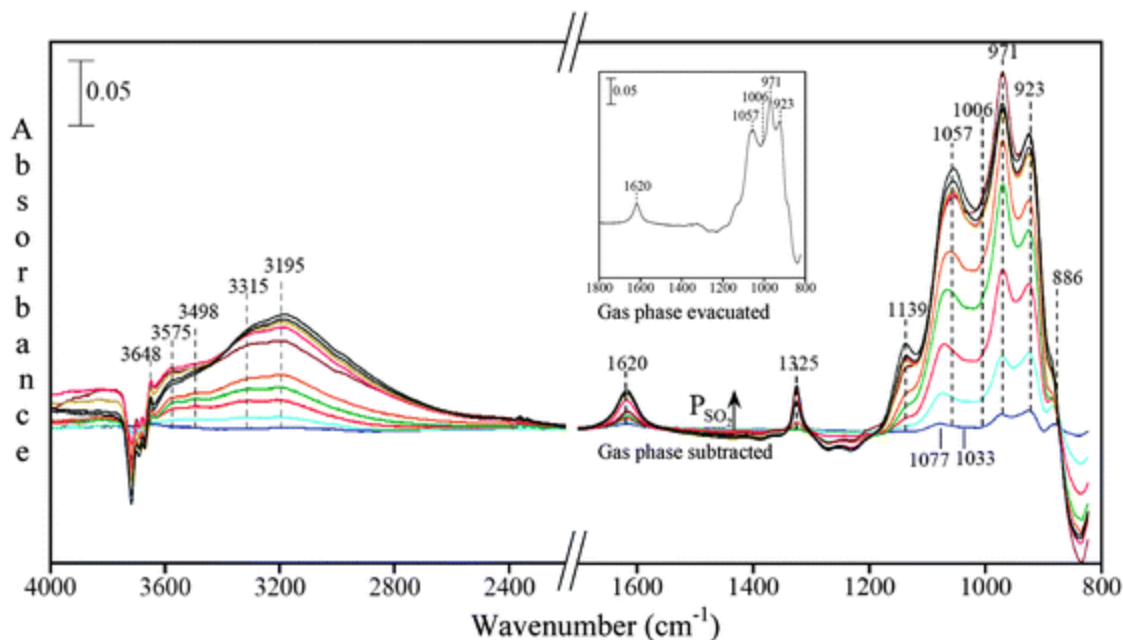


Figure 3.2. Transmission FTIR spectra of TiO_2 surface as a function of increasing pressure of SO_2 . Spectra labeled “gas-phase subtracted” were recorded in the presence of the gas phase at initial pressures of 5, 10, 15, 20, 22, 25, 28, 30, 40, and 100 mTorr. The spectra are stacked from lowest initial SO_2 pressure to highest SO_2 pressure. The spectrum labeled “gas-phase evacuated” was collected after evacuation of SO_2 at the highest pressure. These difference spectra show both positive and negative absorptions associated with the formation and loss, respectively of species from the surface. See text for further details.

are seen for the other two isotopes $\text{Ti-}^{16}\text{OD}$ and $\text{Ti-}^{18}\text{OH}$. These remaining absorption bands in the spectra may be associated with a particular crystallographic plane that may in fact be less reactive. Additionally, experiments on dehydroxylated surfaces show much less reactivity with little product formation (data not shown) consistent with XPS results recently reported suggesting that surface oxygen atoms are less reactive compared to O–H groups toward SO_2 .

Before an assignment of all remaining bands in Figure 3.2 is made, additional spectra are shown for SO_2 adsorption on $\text{Ti-}^{16}\text{O-D}$ and $\text{Ti-}^{18}\text{O-H}$ labeled surfaces. The

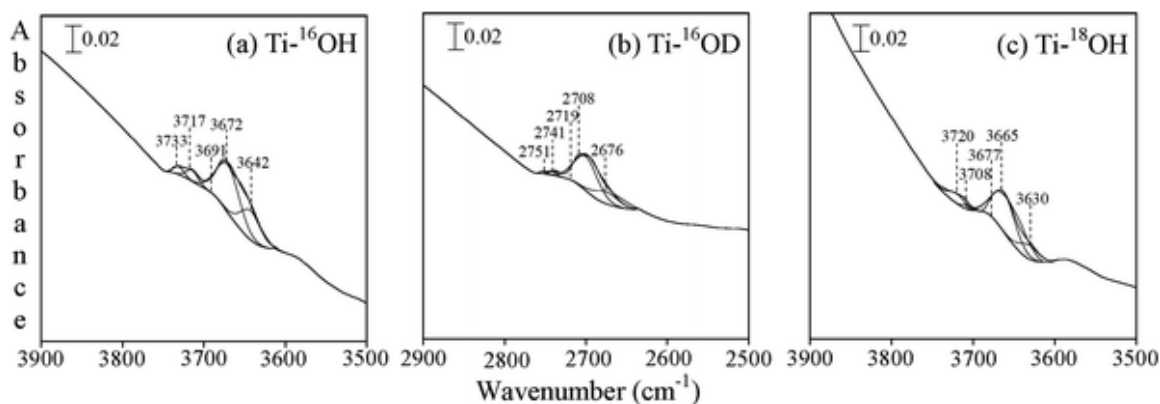


Figure 3.3. Peak-fitted hydroxyl group region following reaction with 100 mTorr SO_2 of (a) $^{16}\text{O-H}$ stretching vibrations for unlabeled TiO_2 , (b) $^{16}\text{O-D}$ stretching vibrations for deuterated- TiO_2 , (c) $^{18}\text{O-H}$ stretching vibrations for ^{18}O -labeled TiO_2 .

IR spectra of labeled and unlabeled TiO_2 surfaces in the presence of 100 mTorr SO_2 are shown in Figure 3.4. Absorption band frequencies in the 800 to 1800 cm^{-1} spectral region are similar for the SO_2 adsorption on both $\text{Ti-}^{16}\text{O-H}$ and $\text{Ti-}^{16}\text{O-D}$ surfaces. SO_2 adsorption on $\text{Ti-}^{18}\text{O-H}$ shows frequency shifts for some bands due to ^{18}O incorporation into the adsorbed sulfur species. Negative features seen in the $^{16}\text{O-D}$ (between 2500 – 2900 cm^{-1}) and $^{18}\text{O-H}$ (between 3500 – 3900 cm^{-1}) stretching region are similar to what is observed for $\text{Ti-}^{16}\text{O-H}$ indicating the involvement of surface hydroxyl groups. Additionally, instead of a band at 1620 cm^{-1} , there is a band seen at 1194 cm^{-1} following SO_2 adsorption on $\text{Ti-}^{16}\text{O-D}$ surface in Figure 3.4. This shift confirms the assignment of this vibration to the water-bending mode for adsorbed water formed in the reaction. Furthermore, the broad band between 2300 – 2600 cm^{-1} is consistent with the formation of D_2O . Most interestingly, in the case of SO_2 adsorption on $\text{Ti-}^{18}\text{O-H}$ labeled surfaces, is the fact that the band at 1620 cm^{-1} associated with the water bending mode does not shift to lower frequency suggesting that the H_2O formation does not involve ^{18}O surface

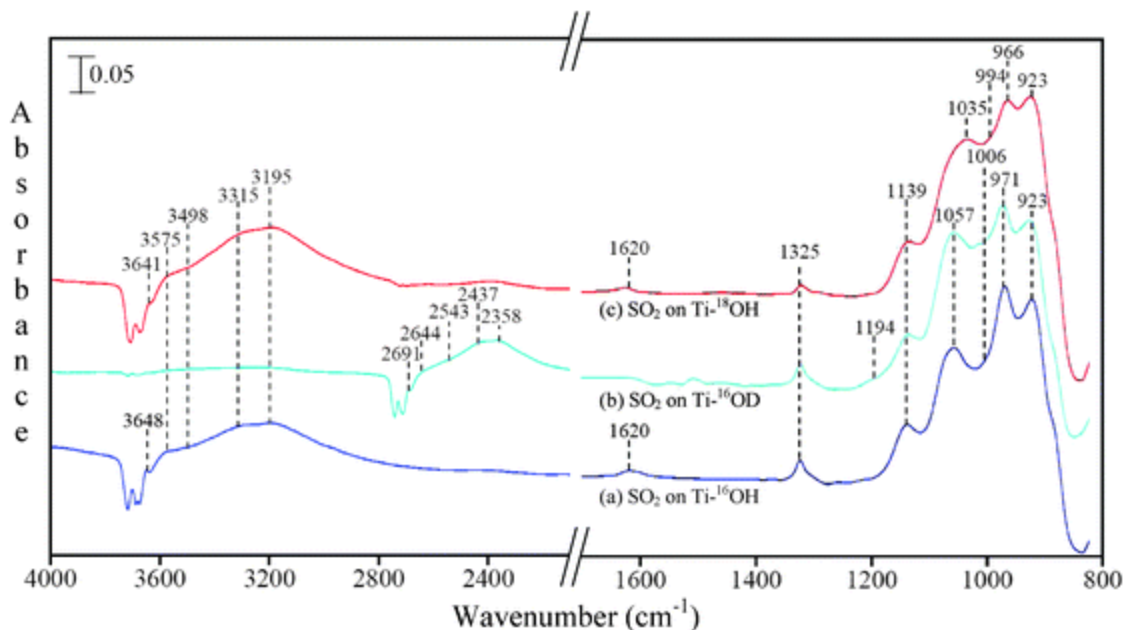


Figure 3.4. Transmission FTIR spectra for TiO_2 in the presence of gas phase SO_2 at a pressure of 100 mTorr for (a) SO_2 adsorbed on TiO_2 with (b) SO_2 adsorbed on deuterated- TiO_2 , and (c) SO_2 adsorbed on ^{18}O -labeled TiO_2 . Gas-phase absorptions have been subtracted from the spectra.

atoms. Additionally, the $2400 - 3600 \text{ cm}^{-1}$ region for the SO_2 adsorption on both Ti-O-H and $\text{Ti-}^{18}\text{O-H}$ show similar features at the same frequencies indicating that the ^{18}O -label does not end up in the water product. The data in Figure 3.5 shows water adsorption on TiO_2 nanoparticles surfaces as a function of increasing relative humidity for all three isotopes, H_2O , D_2O and H_2^{18}O , on different isotopically labeled surfaces, O-H , O-D and $^{18}\text{O-H}$, respectively, as a comparison as these spectra show how the vibrational frequency do change for these three isotopes due to the change in the reduced mass. This important point here for SO_2 adsorption and the water product that forms in this reaction is that the ^{18}O label from surface $\text{Ti-}^{18}\text{O-H}$ does not get into the water product. Any mechanism

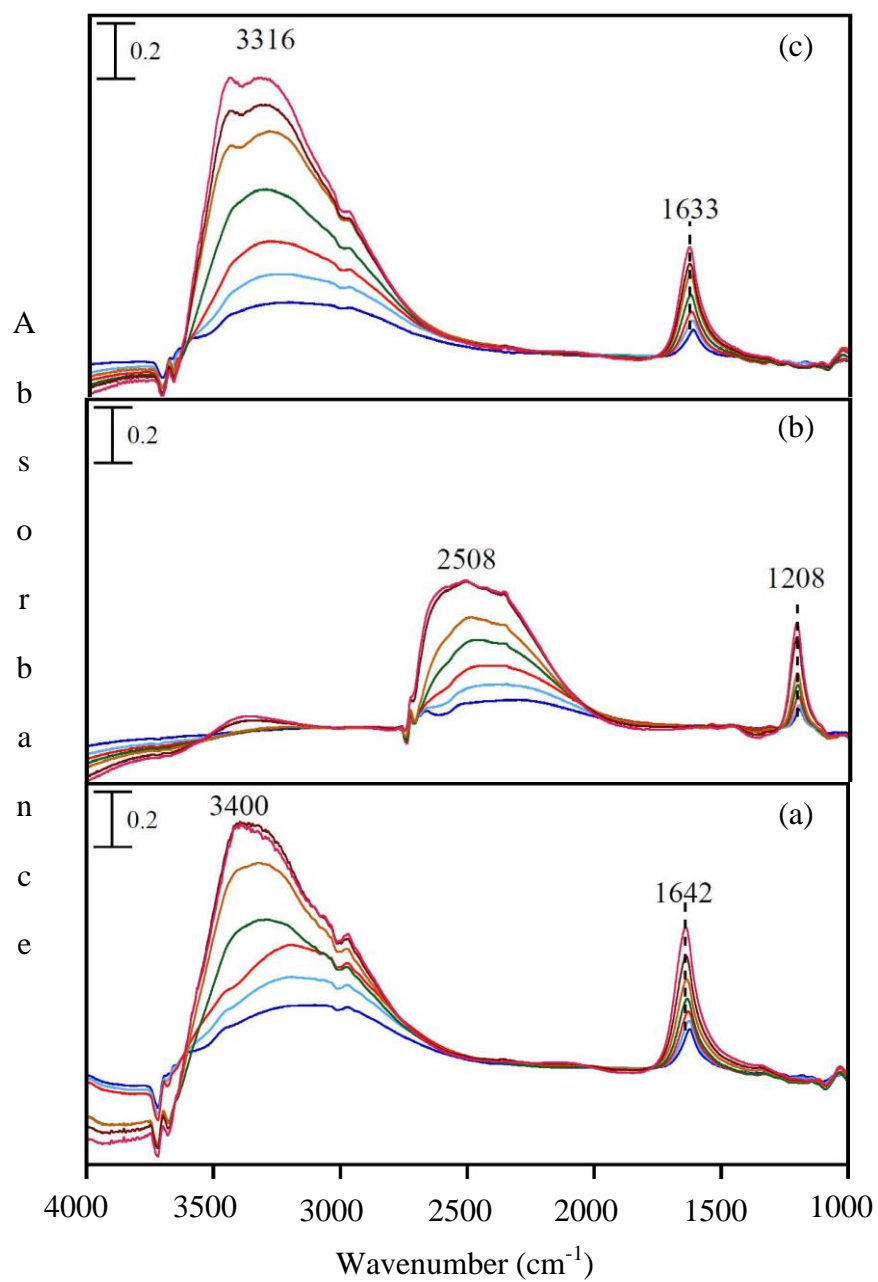


Figure 3.5. Transmission FT-IR spectra for (a) H₂O (b) D₂O (c) H₂¹⁸O adsorption on TiO₂ surface as a function of increasing relative humidity (0.6, 1.2, 3.1, 10, 26, 56 and 76 %). Spectra were recorded in the presence of gas phase and gas phase was subtracted out.

proposed for this reaction will need to account for this fact (*vide infra*). Furthermore, although ^{18}O label is not in the water product, it does get into the more strongly bound sulfur-containing products that form as seen in the shifts of the absorption bands in the 800 to 1200 cm^{-1} spectral region.

The vibrational assignment of the features observed in the 800 to 1200 cm^{-1} region and the mechanism for the formation of different species can be interpreted based on assignments in the literature for SO_2 adsorption on different metal oxide surfaces that have been previously reported,^{95,123,132-135} In fact the features in the 800 to 1200 cm^{-1} of Figure 3.2 can be made to two surface adsorbed sulfur species, sulfite and bisulfite, as result of SO_2 adsorption.¹²³ It has been proposed that adsorbed SO_2 on metal oxides surfaces can lead to form monodentate and bidentate sulfite.¹³⁶ Datta et al. investigated SO_2 adsorption on $\gamma\text{-Al}_2\text{O}_3$ and suggested sulfite formation based on a band observed 1050 cm^{-1} . Recently, this assignment was confirmed by calculations for SO_2 adsorption on $\gamma\text{-Al}_2\text{O}_3$.¹³⁷ Additionally, in another recent study of SO_2 adsorption on ferrihydrite nanoparticles by Liu et. al., bands at 1070, 1030, 966 and 910 cm^{-1} have been assigned to the oxygen coordinated monodentate sulfite whereas bands at 1005, 820 and 875 cm^{-1} for bidentate bridging sulfite. At lower pressures of SO_2 , there are two distinct bands apparent in the spectrum shown in Figure 3.2 at 1077 cm^{-1} and 1033 cm^{-1} . As the pressure increases, the peaks broaden and there is a broader band centered at 1057 cm^{-1} . Adsorbed HSO_3^- on TiO_2 surfaces has been reported between 1070 and 1090 cm^{-1} .¹²⁸

Additionally, the band at 3648 cm^{-1} of Figure 3.2 is most likely associated with the OH stretching vibration of adsorbed bisulfite.¹³⁸ However, it should be noted that the band at 1006 cm^{-1} could also belong to a bidentate sulfite according to the Liu et. al.

Furthermore, calculated and experimental vibrational frequencies of SO₂ adsorption on ferrihydrite nanoparticles by Liu et al. have shown that the vibrational frequency of symmetric stretching mode of monodentate sulfite strongly depends on the hydrogen bonding to neighboring hydroxyl groups. In the present study, highly hydroxylated TiO₂ surfaces could be expected to have similar behavior with different vibrational frequencies for the symmetric stretching mode of adsorbed monodentate sulfite.

Taking all of these data from earlier studies and the data presented here – FTIR spectra, literature assignments and isotope data – the broad band between 800 and 1200 cm⁻¹ is suggested to be a combination of sulfite and bisulfite absorptions. The band centered at 1057 cm⁻¹ at high coverage is most likely a combination of asymmetric stretching mode of sulfite (1033 cm⁻¹) and bisulfite (1077 cm⁻¹) bands. Furthermore O–H stretching vibration of HSO₃⁻ is seen at 3648 cm⁻¹. The bands at 971 and 923 cm⁻¹ are assigned to the symmetric stretching vibration of monodentate sulfite and 1006 and 886 cm⁻¹ for bidentate sulfite. A summary of the band assignments for absorptions observed in this study along with frequencies reported in earlier studies are given in Table 3.2.

Several mechanisms for SO₂ adsorption on hydroxylated metal oxide surfaces have been proposed in these earlier studies. From the data shown in Figures 3.1-3.5, several different surface reactions are proposed for strongly bound sulfur species following exposure of SO₂ to TiO₂ nanoparticle surfaces. In the current study, experimental results confirm that the reaction shown in reaction (3.1) is occurring and there is water formation following reaction of SO₂. Second the formation of bisulfite from reaction of SO₂ molecules with O-H groups reaction (3.2) is also occurring as discussed previously. A third reaction to yield sulfite involving O atoms and SO₂ has

Table 3.2. Vibrational frequencies of different adsorbed sulfur-containing species on TiO₂ nanoparticle surfaces and on other metal oxides surfaces.

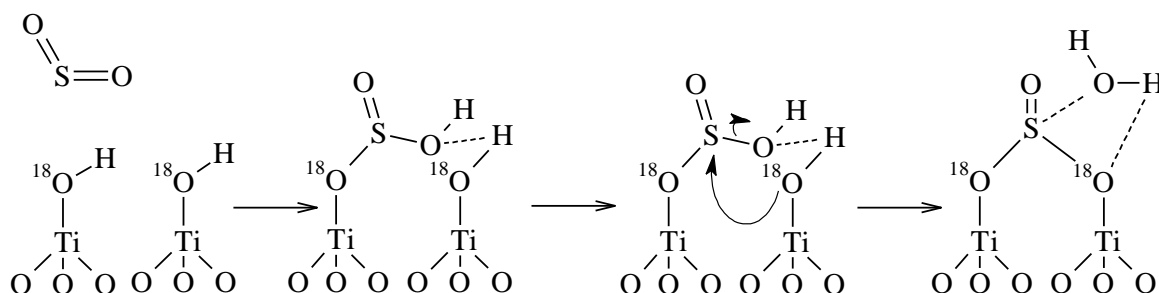
Molecular species	This Study	TiO ₂	Al ₂ O ₃	SO ₄ ²⁻ / TiO ₂	α-Fe ₂ O ₃	Ferrihydrite	Water-Air interface
SO ₂	1325 and 1139	1330	1330 and 1149		1400	1330 and 1144	
HSO ₃ ⁻	1077 and 3648	1070 - 1090	1200 – 900 1100 – 850				
SO ₃ ²⁻		1050-1060	1060				
Monodentate	1033, 971, 923		1041 and 956			1074, 1028, 966, 913	
Bidentate	1006, 886		1062 and 954			1005, 875, 820	
SO ₄ ²⁻ (several coordination modes)	1361, 1297, 1172, 1116, 1050, 1000	1161, 1111, 1070	1100 – 1300 1176 and 1350	1372, 1211, 1043 1370	1000 – 1300 ^h		
Solvated SO ₃ ²⁻ /HSO ₃ ⁻	1050						
Solvated SO ₄ ²⁻	1168, 1129	1161, 1111					
SO ₂ ·H ₂ O complex O–H region	3498, 3211						3460, 3200

Source: Assignments from reference 92

also been suggested in the literature and is shown in reaction (3.3).⁸



Scheme 3.1. Reaction of SO_2 and surface hydroxyl groups to form adsorbed sulfite and water



Although reactions shown in eqs (3.2) and (3.3) may occur in a single step, clearly the reaction shown in eq. (3.1) must involve multiple steps. Scheme I suggests a mechanism for sulfite and water formation that is in agreement with the experimental results for the different isotopes. The mechanism involves two neighboring O-H groups and the insertion of SO_2 into one of the O-H bonds. This is followed by nucleophilic attack of the neighboring O-H group and proton transfer followed by the elimination of water.

3.4.4 Photooxidation of Adsorbed Sulfite/bisulfite

XPS studies have previously shown conversion of S(IV) species to S(VI) species on TiO₂ nanoparticle surfaces in the presence of UV light and in the presence or absence of an external source of oxygen (e.g. O₂ or H₂O).⁸ Transmission FTIR spectra of SO₂ reacted TiO₂ surface collected with increasing irradiation are shown in Figure 3.6. Absorptions at 1361, 1297, 1172, 1116, 1050 and 1000 cm⁻¹ clearly grow in as a function of irradiation time. These can be assigned to adsorbed sulfate species.¹³⁹ Vibrational modes for different protonation states and adsorption coordination modes have different frequencies across the frequency range from ca. 900 to 1400 cm⁻¹. Molecular sulfuric acid shows four adsorption bands at 1350 – 1440, 1150 – 1230, 960 -1000 and around 910 cm⁻¹.¹⁴⁰ Attenuated total reflectance Fourier transform infrared (ATR-FTIR) spectroscopy studies on solution phase sulfate adsorption on TiO₂ surface have shown bands at 1070, 1111 and 1161 cm⁻¹.¹⁴¹ Studies on SO₄²⁻/TiO₂ catalyst preparation and characterization provide important information on the vibrational frequency assignment of adsorbed sulfate. Yang et. al. observe infrared absorption bands at 1384, 1211, and 1043 cm⁻¹ for the SO₄²⁻/TiO₂ catalyst surfaces, which were assigned to a catalytically active sulfate species. In addition, an absorption band at 1142 cm⁻¹ has been also assigned to a sulfate species.¹⁴² Lange et. al. observed a band at 1370 cm⁻¹ for a tridentate sulfate groups on SO₄²⁻/TiO₂ that forms under dry conditions. Ma et. al. investigated the sulfate formation on γ -alumina and assigned peaks at 1176 cm⁻¹ and 1350 cm⁻¹ to the symmetric and asymmetric stretching vibrations, respectively, of adsorbed sulfate.¹⁴³ Experimental results combined with the early studies have shown the presence of tridentate sulfate

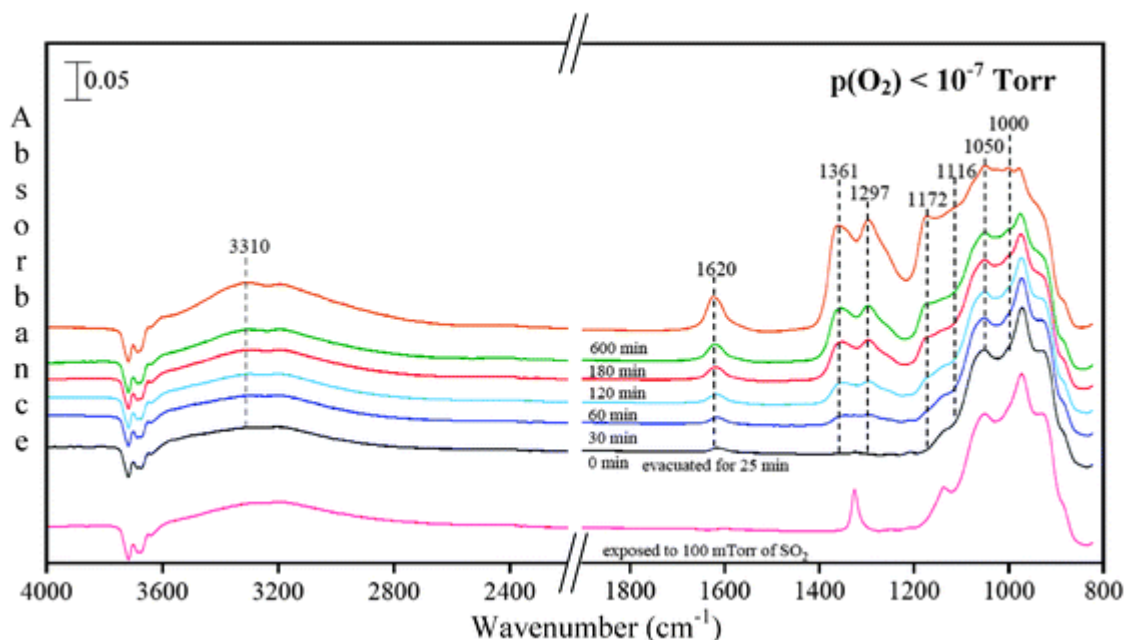


Figure 3.6. Transmission FTIR spectra are shown as a function of irradiation time for the TiO_2 surface containing bisulfite/sulfite species. As discussed in detail in the text, these spectra show the conversion to adsorbed sulfate.

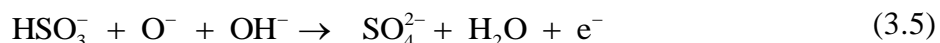
bands. Based on these literature data, an assignment for the sulfate bands are given in Table 3.2.

A reaction for sulfate formation has been proposed previously and is shown in eq. (3.4).⁹⁴



Apart from the adsorbed sulfate peaks, there is the growth of the band at 1620 cm^{-1} and a broadband in the range of $3300 \sim 3500 \text{ cm}^{-1}$ with the increasing irradiation time that is clearly observed. The band at 1620 cm^{-1} is again assigned to the bending mode of the adsorbed H_2O . This indicates the formation of surface water with the sulfate

formation which agrees with the mechanism (3.5) proposed by Zhang et al. that involves both surface OH and O.⁹⁵



3.4.5 Effect of Water Vapor on Adsorbed Sulfite and Sulfate on TiO₂ Particles.

Surface adsorbed water plays an important role in the heterogeneous chemistry of trace atmospheric gases, however, little is known about the role of adsorbed water in the stability of various adsorbates on oxide surfaces. Therefore, water adsorption on TiO₂ nanoparticles with adsorbed sulfite and sulfate was further examined by FTIR spectroscopy. Sulfite coated TiO₂ nanoparticles were prepared by reacting 100 mTorr of SO₂ for 25 minutes to saturate the surface followed by 25 minute evacuation to remove physisorbed SO₂. Sulfate coated TiO₂ nanoparticles were obtained by irradiating the adsorbed sulfite for 600 minutes. A known pressure of water vapor was then introduced to the TiO₂ surface coated with either sulfite or sulfate for 25 minutes and IR spectra were collected. The cell was evacuated for 25 minutes and the second relative humidity was introduced. Water adsorption on both surfaces was carried out as a function of increasing relative humidity from 0.6 to 76% RH (from water pressures of 150 mTorr to 18 Torr at 296 K). Adsorbed sulfite and sulfate show very different behaviors in the presence of water vapor.

An increase in intensity as well as a shift in frequency to 1633 cm⁻¹ is seen for the water bending mode as the relative humidity is increased for both sulfite coated and

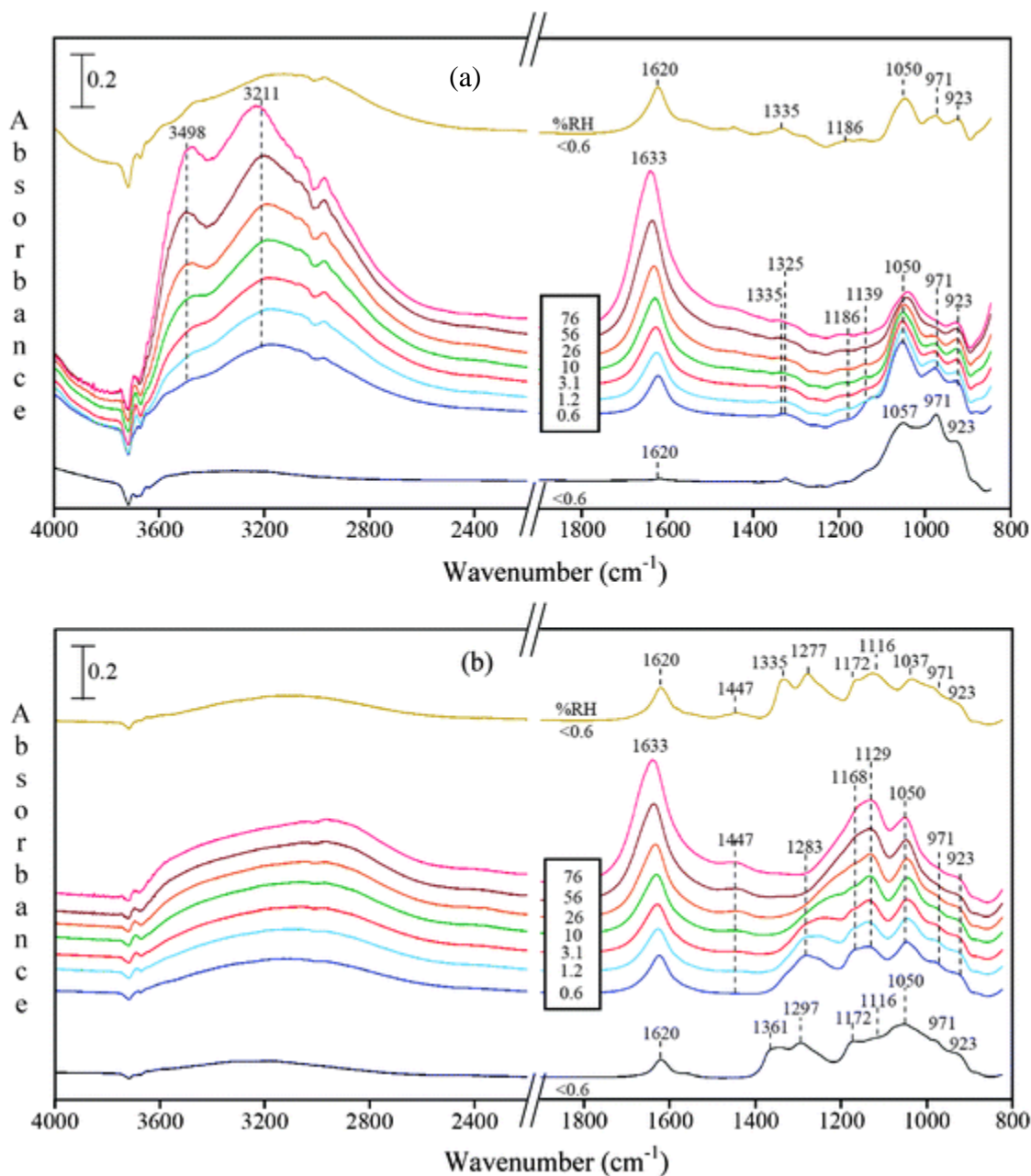
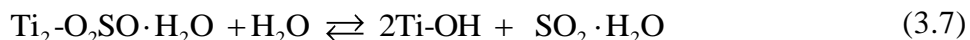


Figure 3.7. Transmission FTIR spectra of water adsorption as a function of increasing relative humidity on (a) sulfited-TiO₂ after SO₂ adsorption and (b) sulfated-TiO₂ surfaces after irradiation of sulfited-TiO₂ with light. These spectra show changes with increasing relative humidity of 0.6 to 76 %RH. Following increasing RH, the infrared cell is evacuated to less than 0.6 %RH. These spectra are shown as the top spectra in both (a) and (b).

sulfate coated TiO_2 nanoparticle surfaces (Figure 3.7). Upon addition of increasing relative humidity, sulfite-coated particles show changes in the relative intensities of several bands in the $800\text{--}1200\text{ cm}^{-1}$ region in Figure 3.7(a). Upon water adsorption, there is a large enhancement in the O–H stretching region with distinct features at 3211 and 3498 cm^{-1} that are quite visible for water adsorbed on hydroxylated TiO_2 surfaces that have been exposed to SO_2 . These bands are characteristic of absorptions seen at the liquid water air interface using sum frequency generation in the presence of SO_2 and provide evidence for the formation of $\text{SO}_2\cdot\text{H}_2\text{O}$ complex at the oxide water interface.¹⁴⁴ The characteristic bands for molecularly adsorbed SO_2 were also observed, albeit very weakly; in the presence of water vapor further confirming the formation of this solvated complex. Sulfur dioxide water complexes have been observed at the air water interface and at the surface of a crystalline sulfuric acid solid film but never hitherto at the oxide-adsorbed water interface.^{144,145}

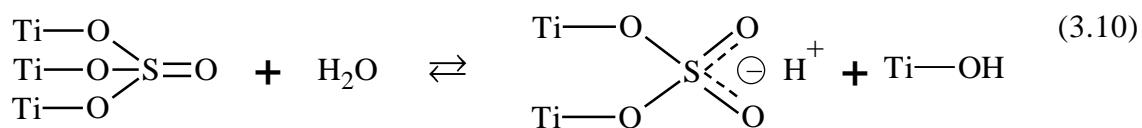
Additionally, the intensity of the band at 1050 cm^{-1} decreases with increasing relative humidity suggesting loss of this species and an overall lower stability of adsorbed sulfite in the presence of water vapor. After exposing the surface to the highest relative humidity, the infrared cell was evacuated overnight. Upon evacuation, water solvated sulfite converts back to the chemisorbed sulfite. However, the intensity of the absorption broads between $800 - 1200\text{ cm}^{-1}$ has considerably decreased suggesting loss of sulfur species from the surface. Thus, indicating desorption of sulfur oxide species, most likely as SO_2 during evacuation after exposure to water. The two bands at 1335 and 1186 cm^{-1} after overnight evacuation are most likely due to the formation of small amount of sulfate in the presence of water vapor. Sulfate formation by water vapor was previously reported

in XPS studies on SO₂ and H₂O adsorption on TiO₂ surfaces.⁸ It has been reported that the adsorbed SO₂ becomes solvated in the presence of water vapor followed by hydrolysis forming a surface complex which then becomes fully solvated in the bulk phase.¹⁴⁵ This process can be proposed to a set of reactions of solvation of adsorbed sulfite and bisulfite according to the reaction (3.6), (3.7) and (3.8). This is similar to what happens at the air-liquid interface as it has been proposed that the complex between SO₂ and H₂O is in equilibrium with bisulfite according to the reaction (3.9).



Water adsorption on sulfate coated TiO₂ particles are shown in the panel (b) of the Figure 3.7. The increase in the intensity of the bands at 1283, 1186, 1168 and 1129 cm⁻¹ can be clearly seen leading to a broad band centered at 1129 cm⁻¹ at higher relative humidity. This can be due to the formation of water solvated sulfate at the higher relative humidity and these bands can be assigned to solvated sulfate. Bisulfate formation is observed with the new band growing at 1447 cm⁻¹ with the increasing relative humidity by solvating the adsorbed sulfate. Increasing intensity of H bonded hydroxyl region has shown a broad band between 2500 - 3600 cm⁻¹. The decrease in vibrational frequency of sulfate S=O bond due to water solvation has previously observed and it was suggested that this was due to a weakening of SO bond on sulfated titania.¹²⁷ Overnight evacuation

following the water uptake regenerated a surface spectrum for adsorbed sulfate, which differs some from the initial spectrum. In particular, the infrared absorptions for surface adsorbed sulfate showed a red shift before and after the water uptake experiment. Adsorbed water on TiO₂ surface could not be completely removed with the evacuation; hence the remaining water molecules on the surface can affect the bonding of adsorbed sulfate. Lange *et. al.* has observed a band at 1318 cm⁻¹ for the tridentate sulfate groups on sulfated TiO₂ which shifts to 1370 cm⁻¹ upon evacuation at 720 K. The results of the present study agree well with the observations of Lange et al. and according to the reaction (3.10) proposed by Saur et al., where they have suggested a bridged tri-dentate



sulfate structure is formed which is assumed to interact with H₂O by breaking one Ti-O bond resulting a bridged solvated sulfate complex.¹⁴⁶ The water solvated sulfate complex is bridged to the surface leading to a tight interaction with the surface making it difficult to remove by evacuation.

Finally, the amount of sulfur species desorbed from the surface following exposure to SO₂ was quantified with XPS. The S(2p):Ti(2p) ratio decreased by 31 and 9%, for adsorbed sulfite/bisulfite and sulfate, respectively, following exposure to water vapor corresponding to 8% RH (data not shown). Following additional water exposures corresponding to 34 and then 75 %RH, the S(2p):Ti(2p) ratio decreased by 50 and 25%, respectively, for adsorbed sulfite/bisulfite and sulfate. These XPS data quantitatively

shows that adsorbed sulfite is less stable compared to adsorbed sulfate on titanium dioxide surfaces in the presence of relative humidity and adsorbed water. These data further suggest that adsorbed water in equilibrium with water vapor plays a role in the stability of secondary species associated with oxide particle surfaces, important components of mineral dust aerosol.

3.5 Conclusions and Environmental Implications

The current study provides detailed analysis of FTIR data for SO₂ adsorption on TiO₂ nanoparticle surfaces on isotopically labeled surfaces. The data show that for hydroxylated surfaces, O-H groups are involved in the surface chemistry to yield sulfite and bisulfite on the surface and those O-H groups on some surface sites react more readily. These data also provide information on the mechanism for different products formed in the reaction. S(IV) species readily oxidize upon irradiation at solar wavelengths to form S(VI) species, namely sulfate, on the surface. A comparison of the relative stability of these different adsorbed sulfur species in the presence of water vapor gave some interesting results. Under humid conditions, there was a greater loss of S(IV) species from the surface relative to S(VI) suggesting that under atmospheric conditions of temperature and relative humidity that adsorbed sulfite is less stable than sulfate as a result of the formation of a SO₂•H₂O complexes that can play a role in the desorption of sulfur species from the surface.

Acknowledgement

The material is based on the work supported by the National Science Foundation under grant number CHE-0952605. Any opinions, findings and conclusions or recommendations expressed in this material are those of the authors and do not necessarily reflect the views of the National Science Foundation. The results of this work are presented in the publication under authorship of Charith E. Nanayakkara, John Pettibone and Vicki H. Grassian, *Physical Chemistry and Chemical Physics*, 2012, 14, 6957-6966.

CHAPTER 4

TITANIUM DIOXIDE NANOPARTICLE REACTIVITY WITH CO₂, SO₂ AND NO₂: ROLES OF SURFACE HYDROXYL GROUPS AND ADSORBED WATER IN THE FORMATION AND STABILITY OF ADSORBED PRODUCTS

4.1 Abstract

The reactivity of O–H groups on titanium dioxide nanoparticle surfaces with gas-phase carbon dioxide, sulfur dioxide and nitrogen dioxide is compared. As shown here, the surface reactivity of O–H groups with these three triatomic gases differs considerably due to different reaction mechanisms for adsorption and surface chemistry. Carbon dioxide, sulfur dioxide and nitrogen dioxide react with ca. 5, 50 and nearly 100%, respectively, of all hydroxyl groups on the surface. In addition to investigating O–H group reactivity, the role of adsorbed water in the stability of different surface species that form from adsorption of carbon dioxide, nitrogen dioxide and sulfur dioxide on hydroxylated TiO₂ nanoparticles is probed as a function of relative humidity as is quantitative measurements of water uptake on TiO₂ nanoparticles before and after surface reaction. These water uptake studies provide insights into the stability of adsorbed species on oxide surfaces under atmospherically relevant conditions as well as changes in particle hygroscopicity following reaction with atmospheric gases.

4.2 Introduction

There is a great deal of interest in the chemistry of atmospheric gases with solid surfaces and metal oxide surfaces being of particular interest.⁶ This attention comes from a number of perspectives including heterogeneous catalysis, environmental remediation and heterogeneous atmospheric chemistry.⁷ Adsorption and photochemistry of small molecules on TiO_2 surfaces has been received a lot of attention due to its industrial and environmental applications as well as atmospheric importance as has been discussed in several recent review articles.^{7,34,121,147-150} Titanium dioxide (TiO_2) is a semiconductor metal oxide with band gap around 3.2 eV. TiO_2 coated or mixed materials break down pollutants into less harmful products while retaining photocatalytic activity.⁷ These self-cleaning materials act as surfaces for reaction with atmospheric gases. Mineral dust aerosol is another source of TiO_2 in the atmosphere. As a component of mineral dust aerosol, TiO_2 can facilitate atmospheric trace gas adsorption, heterogeneous reactions and photochemical reactions.⁷

Hydroxyl groups often play a role in the reaction chemistry of metal oxide surfaces. From hydrogen bonding to insertion reactions to OH radical chemistry, the different types of reactivity for surface O–H groups are quite large and depend on the particular metal oxide, surface crystallography and coordination mode. TiO_2 surfaces have several different kinds of hydroxyl groups including isolated and bridged hydroxyls on different sites that depends on the specific crystal planes.¹²⁹ It is therefore important to gain an understanding of reactivity of these hydroxyl groups on TiO_2 with common atmospheric gases.

In this study, the reactivity of O–H groups on titanium dioxide nanoparticle surfaces with gas-phase carbon dioxide, sulfur dioxide and nitrogen dioxide is compared. Surface reactions of carbon dioxide are of much importance and interest in many aspects. It is the most abundant greenhouse gas after water vapor and has a higher warming capacity. The increasing concentration of atmospheric carbon dioxide since the industrial revolution has greatly impacted the earth's climate and because of this, there has been increased interest in carbon dioxide capture, storage and transformation in the scientific community. In several studies, carbon dioxide adsorption on TiO_2 has shown the formation of adsorbed carbonate species and bicarbonate.¹⁵¹⁻¹⁵⁴ However, these studies have not shown the details of surface hydroxyl group reactivity with CO_2 quantitatively.

The main source of sulfur dioxide is from coal power plant emissions. The conversion of sulfur dioxide to sulfate in the troposphere leads to acid rain and aerosol particle formation. Various components of mineral dust aerosol have shown to play an important role in heterogeneous conversion of sulfur dioxide to sulfate.⁷ In addition, sulfur dioxide adsorption on metal oxide surfaces including TiO_2 have shown to form adsorbed sulfite and bisulfite.⁹² The reactions of sulfur dioxide with hydroxyl groups' results adsorbed bisulfite, sulfite and water. Details of the sulfur dioxide adsorption on TiO_2 have been investigated in several studies.^{92,93,97}

Reactions with nitrogen dioxide lead to acid rains and photochemical smog with combustion of fossil fuels as the main source of NO_2 emissions. NO_2 reacted on TiO_2 surfaces mainly forms adsorbed nitrate species on different coordination modes.⁹⁹ Although nitrate is assumed to be final product of atmospheric NO_x , studies have shown the potential renoxification of adsorbed nitrate in the presence of ultra violet light on

TiO₂ surfaces leading to the production of gas phase products of NO and NO₂.^{23,103} Furthermore, NO₂ reactions on TiO₂ in the presence of solar irradiation have shown to form more harmful products such as HONO.^{25,100}

It is clear that adsorbed water plays an important role in surface adsorption and surface chemistry of metal oxides.¹⁰⁷ In fact, adsorbed water can play multiple roles in the reaction chemistry of oxide surfaces with atmospheric gases as recently reviewed by Rubasinghege and Grassian.¹⁰⁷ Water adsorption on TiO₂ surfaces has been widely investigated using various techniques but few studies have addressed how water uptake on TiO₂ changes in the presence of adsorbates.^{101,108-110} The hygroscopic behavior and the uptake of water can be greatly affected by the presence of adsorbed species.¹¹¹ For an example, alumina particles reacted with formic acid have shown low water uptake¹¹¹ whereas water uptake on Arizona test dust reacted with co-dosed SO₂, O₂ and H₂O did not show any change in hygroscopic behavior.¹¹² Thus, further investigations of gas-phase water adsorption on surfaces with different adsorbates is warranted.

As discussed below, the surface chemistry of three triatomic gases CO₂, SO₂ and NO₂ on TiO₂ nanoparticle surfaces has been investigated and compared. In particular, the reactivity of different surface hydroxyl groups with these three gases and product formation is examined. It is shown here that there are large and important differences in the chemistry of these three atmospheric gases with surface hydroxyl groups. Furthermore, the effect of water vapor on the adsorbed product stability – carbonate, sulfite and nitrate – on TiO₂ surfaces is compared and the possible change in adsorbed water dynamics is discussed.

4.3 Experimental Methods

4.3.1 Sources and Purity of Gases

CO₂ (UPC grade) was purchased from Airgas Inc. SO₂ (99.98% purity) and NO₂ (99.95% purity) were purchased from Matheson gas. Distilled H₂O (Fisher, Optima grade) were degassed with several freeze-pump-thaw cycles prior to use.

4.3.2 Source of TiO₂ Nanoparticles and Nanoparticle Characterization

TiO₂ sample was purchased from Nanostructures and Amorphous Materials Inc. TiO₂ particles were characterized using Siemens D5000 diffractometer with a Cu-K α source, JEOL 1230 transmission electron microscope (TEM) and Quantachrome Nova 4200e multipoint Brunauer-Emmet-Teller (BET) surface area analyzer. TiO₂ particles were degassed for 4 h at 473 K prior to the surface area analysis to remove any impurities.

4.3.3 Adsorption and Surface Chemistry

Monitored by Transmission FTIR

Spectroscopy

Transmission FTIR spectroscopy was used to investigate gas adsorption on TiO₂ nanoparticles and the surface chemistry of O–H groups. The experimental setup has been previously described in detail.¹¹⁵ FTIR spectra were collected using a Mattson Galaxy 6000 spectrometer equipped with a liquid nitrogen cooled mercury cadmium telluride detector (MCT). TiO₂ samples (8–10 mg) were dissolved in optima water at room

temperature to produce a hydrosol. The hydrosol was sonicated for 10 minutes to break any agglomerates and transferred to one half of a tungsten grid (3 cm \times 2 cm, 100 mesh/in., 0.002" wire dia., Accumet Materials Co.) held in position by nickel jaws using a pipette. Water evaporated at room temperature to create a uniform thin film. Thermocouple wires were attached to the tungsten grid to allow resistive heating. The sample holder was placed in a stainless steel reaction chamber equipped with a linear translator to allow either the gas phase or the TiO₂ sample to be placed in the path of the FTIR beam. The reaction chamber was connected to a power supply and a vacuum/gas handling system. Data acquisition was carried out using Winfirst software and spectra were recorded using a resolution of 4 cm⁻¹ with 264 averaged scans from 800 to 4000 cm⁻¹. For absorbance spectra of surface species resulting from gas adsorption, the gas was allowed into the reaction chamber at a desired pressure and then allowed to equilibrate until a constant pressure was measured. The coated half of the grid is associated with the spectral features of the surface and gas-phase whereas the other half of the grid only contains spectral features of the gas phase. Single beam spectra were referenced to the initial surface or to gas phase to identify adsorbed and gas phase species. Spectra of adsorbed products were obtained by subtracting gas-phase spectra under similar conditions.

A pretreatment process was carried out for cleaning TiO₂ nanoparticles. The TiO₂ thin film held by nickel jaws was heated at 400 °C and evacuated at 10⁻⁷ Torr for 4 hours. During the 400 °C heat treatment, all hydroxyl groups were removed leading to dehydroxylated TiO₂ nanoparticle surfaces. After heating, samples were exposed to water vapor at room temperature to regenerate hydroxyl groups followed by evacuation at 200

^0C overnight to remove weakly adsorbed water. Samples were then allowed to cool to room temperature prior to gas adsorption.

4.3.4 Quantitative Uptake Measurements

Using a Quartz Crystal Microbalance

Flow Cell

A custom-built flow system was used to study CO_2 , SO_2 , NO_2 and water uptake on TiO_2 surfaces. The details of the flow system can be found elsewhere.¹¹⁶ The flow system consist a Thermo Nicolette 6700 FTIR spectrophotometer and a QCM200, 5 MHz quartz crystal microbalance. The QCM portion only was used for the current study. Gas uptake was studied by using a steady flow rate of 250 SCCM of the gas of interest over the sample in the QCM. Uptake was monitored using QCM measurements.

In order to control relative humidity, two water bubblers and dry air flow was used. The dry air flow was sent through the two water bubblers producing humidified air. This humidified air was mixed with purely dry air stream to get the desired relative humidity. Both dry and humidified air flows equilibrated inside a mixing chamber before flowing to the sample contained in the QCM. The relative humidity was controlled by changing the dry air flow through the water bubblers. The water uptake at each relative humidity was monitored using QCM. The relative humidity of the flow was read using the humidity sensor and a custom-built digital readout.

4.4 Results and Discussions

4.4.1 Characterization of TiO₂ Nanoparticles

Transmission electron microscopy (TEM) image of TiO₂ show (Figure 2.1) primary particles with an average particle size of 10 ± 3 nm (200 primary particles counted). X-ray Diffraction (XRD) patterns reveal that the TiO₂ particles are primarily anatase with small amount of rutile (~6%). Surface area measurements using BET analysis results in an average value and standard deviation of 128 ± 5 m²/g.

4.4.2 Reactivity of Surface Hydroxyl Groups on TiO₂ Nanoparticles

The hydroxyl group region of TiO₂ particles following heating and subsequent re-hydroxylation shows absorption bands between 3600 and 3800 cm⁻¹. The same band envelope has been observed in previous studies for nanomaterial P25 (rutile content ~ 25%) TiO₂.^{69,129} FTIR spectra were peak fitted to more clearly identify and resolve the infrared absorptions of different hydroxyl groups. Peak-fitting results in five absorption bands at 3733, 3717, 3691, 3672 and 3642 cm⁻¹. The peak fitted hydroxyl region is shown in Figure 4.1. Bands at 3733, 3717 and 3691 cm⁻¹ are assigned to isolated hydroxyl groups and bands at 3672 and 3642 cm⁻¹ were assigned to bridged hydroxyl groups using the literature references.¹²⁹ The multiplicity of the bands can be attributed to different planes, edges and corner sites on the TiO₂ nanoparticle surface. Additionally, CO adsorption studies have previously shown the presence of variety of Ti⁴⁺ sites on P25 TiO₂ in different planes and which may be responsible for the same multiplicity of OH groups as well.^{129,155}

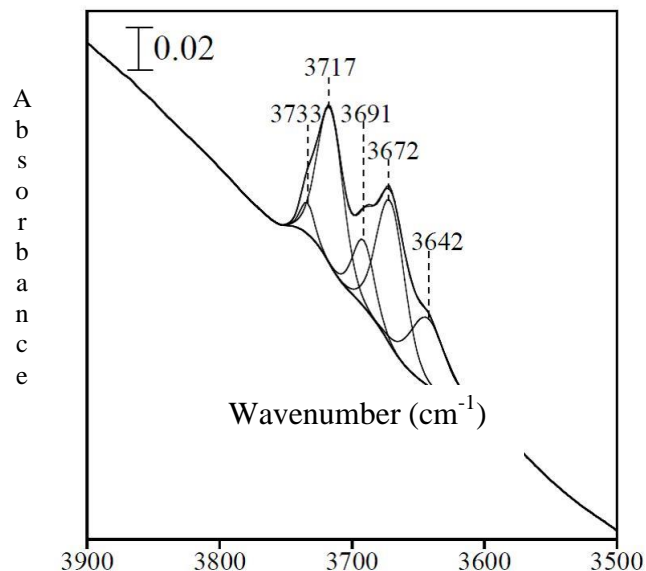


Figure 4.1. FTIR spectra of hydroxyl group region before reaction with gas phase reactants, of TiO_2 used for this study.

The differences in reactivity of surface hydroxyl groups can be seen in the FTIR spectra presented in Figure 4.2 which shows the hydroxyl spectral region following reaction with each atmospheric gas CO_2 , SO_2 and NO_2 as a function of pressure. The spectra in Figure 4.2 are for the O-H region before and after exposed to the highest gas-phase pressure. Figure 4.2(a) shows the spectra recorded in the presence of gas phase CO_2 at initial pressure of 33500 mTorr. Figure 4.2(b) shows the spectra recorded in the presence of gas phase SO_2 at initial pressure of 100 mTorr. Figure 4.2(c) shows the spectra recorded in the presence of gas phase NO_2 at initial pressure of 2343 mTorr. These data show quite convincingly that there is minimal reactivity of surface hydroxyl groups with CO_2 , some reactivity of surface hydroxyl groups with SO_2 and nearly complete reactivity of surface hydroxyl groups with NO_2 . Quantitatively, through

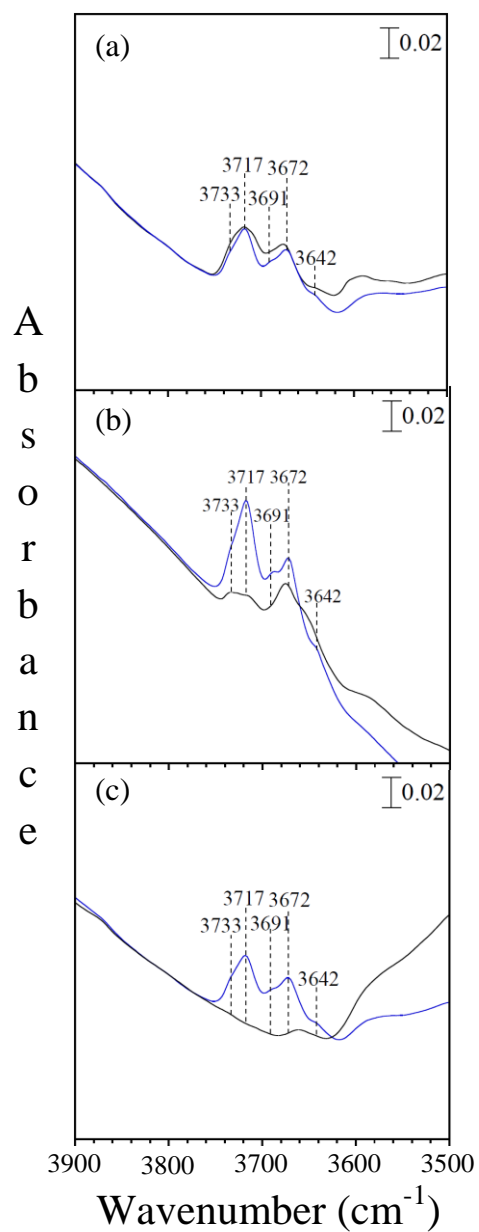


Figure 4.2. Hydroxyl region of TiO_2 surfaces reacted with (a) CO_2 , (b) SO_2 and (c) NO_2 .

integration of the O-H stretching region, it is determined that there is loss of 6, 51 and 96% of the integrated intensity of the O-H stretch due to surface O-H groups, following gas uptake of carbon dioxide, sulfur dioxide and nitrogen dioxide, respectively. This determination is done by integrating the intensity of the absorption band from 3620 to 3750 cm^{-1} in the O-H stretching region at the highest pressures used in these studies.

Although CO_2 is often used to measure the basicity of surface hydroxyls,¹⁵⁶ these findings suggest the inability to study hydroxyls group basicity of TiO_2 using CO_2 due to minimal reactivity as shown in Figure 4.2(a). There is some observed growth of bands between 3600 – 3800 cm^{-1} that can be attributed to the formation of adsorbed HCO_3^- in the presence of gas-phase CO_2 . Previous studies have shown that the reaction between CO_2 and hydroxyl groups on other oxides in equilibrium with HCO_3^- in the presence of gas-phase CO_2 .⁸⁵ Bicarbonate formation was lowest for CO_2 adsorption on TiO_2 compared to other oxides such as Fe_2O_3 , $\gamma\text{-Al}_2\text{O}_3$ suggesting lower reactivity.^{151,157} The results of this current study show minimal adsorbed bicarbonate formation compared to adsorbed carbonate, as discussed below.

For SO_2 , there is significant decrease in some intensity in the O-H region as shown in Figure 4.2(b). Bands at 3717 and 3691 cm^{-1} are completely reacting while the band at 3672 cm^{-1} shows less reactivity compared to the previous two. The bands at 3733 and 3642 cm^{-1} remain in the spectrum indicating low reactivity with respect to SO_2 . Therefore, SO_2 prefers reaction with isolated hydroxyl groups and only certain bridged hydroxyl groups. SO_2 adsorption on TiO_2 suggests less basicity of hydroxyl groups with frequencies at 3733 cm^{-1} and 3642 cm^{-1} . Interestingly, there is complete reaction with O-

H groups and NO₂, as seen in the hydroxyl stretching region. This is in agreement with previous studies.¹⁵⁸

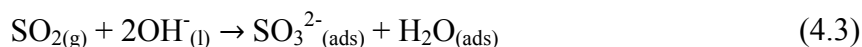
Recent experimental studies on toluene adsorption and photooxidation on P25 TiO₂ have suggested the hydroxyl groups at 3733 cm⁻¹ and 3717 cm⁻¹ are a source of OH radicals, while the remaining acting as adsorption sites.⁶⁹ However, in the present study, the hydroxyl group at 3717 cm⁻¹ act as an adsorption site for both SO₂ and NO₂, suggesting the importance of the nature of the adsorbate on hydroxyl group reactivity. Apart from the basicity of O-H groups, recent study of P25 and nanoanatase TiO₂ reactivity with CO claimed higher Bronsted acidity of bridged OH groups compared to terminal ones.¹⁵⁵ However, since CO₂ showed minimal and NO₂ showed complete reactivity only SO₂ reaction can be used to get an idea about the Bronsted acidity of OH groups in the present study.

In order to gain additional information about the reactivity of these three triatomic gases, it is important to look at the surface products that form. FTIR spectra following the formation of adsorbed products from the reaction of these three triatomic gases are shown in Figure 4.3. Figure 4.3(a) shows the spectra recorded in the presence of gas phase CO₂ at initial pressures of 89, 339, 636, 1261, 6684, 15900 and 33500 mTorr. Figure 4.3(b) shows the spectra recorded in the presence of gas phase SO₂ at initial pressures of 5, 10, 15, 20, 22, 25, 28, 30, 40, and 100 mTorr. Figure 4.3(c) shows the spectra recorded in the presence of gas phase NO₂ at initial pressures of 25, 55, 85, 216, 1136 and 2343 mTorr. Adsorbed carbonate, sulfite and nitrate are observed following reaction of CO₂, SO₂ and NO₂ at the exposed pressures previously stated. The vibrational bands observed in the spectra can be assigned based on previous studies and these assignments are given in

Table 4.1. In the case of CO₂, it can be seen that the spectrum is dominated by adsorbed carbonate that is a result of the reaction of surface oxygen atoms according to reaction (4.1). In particular adsorbed monodentate and bidentate carbonate was observed from this reaction. CO₂ reaction with small amounts of hydroxyls has shown small amount of bicarbonate formation as evident by the 1623, 1433 and 1222 cm⁻¹ bands in Figure 4.3(a). Formation of a band for molecularly adsorbed CO₂ was observed at 2350 cm⁻¹ (not shown), only present in the presence of gas-phase CO₂ and disappeared with gas-phase evacuation.



For SO₂, spectra are assigned to primarily adsorbed sulfite and bisulfite and can be shown to react with O-H groups according to the following reactions.



The HSO₃⁻ band can initially be seen at 1077 cm⁻¹, but overlaps with the sulfite band at 1033 cm⁻¹ with increasing exposure pressure. Evidence for the sulfite formation via reaction (4.3) is evident by the formation of water as seen by the band at 1620 cm⁻¹ in Figure 4.3(b). SO₂ reaction with O²⁻ sites also forms adsorbed sulfite but have shown minimal contribution in sulfite formation in previous studies.⁹² Hydroxyl group reactivity shows mostly isolated and some bridged hydroxyl groups react with SO₂. Reaction (4.2)

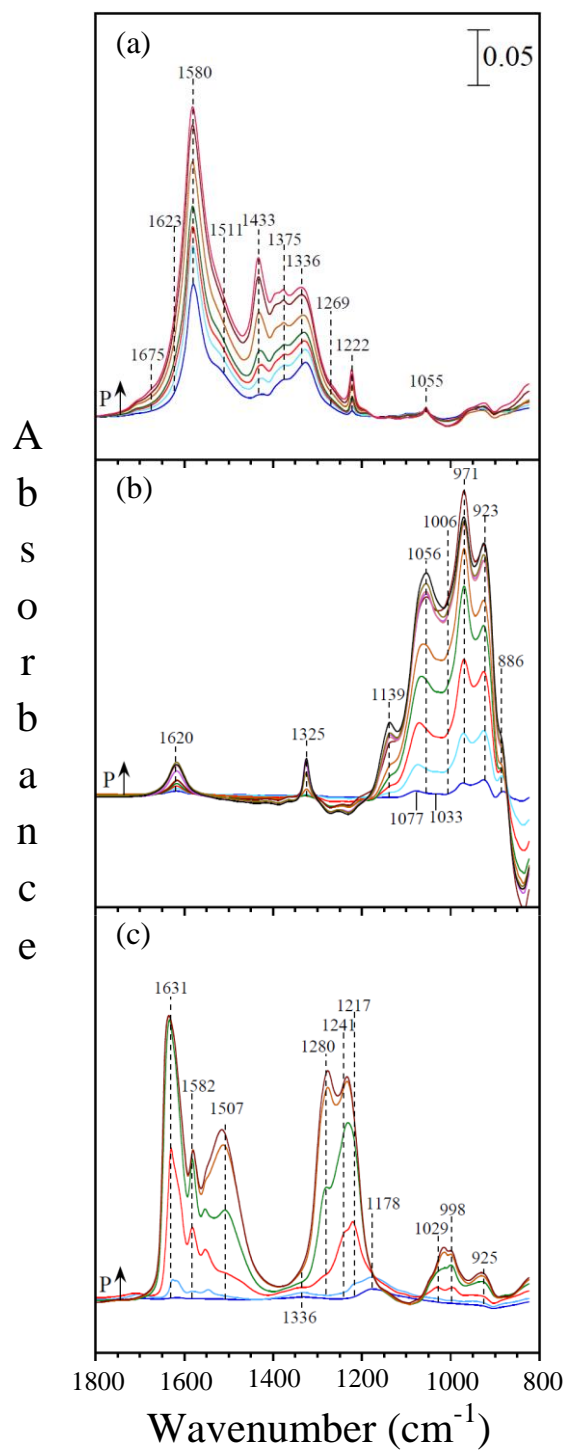
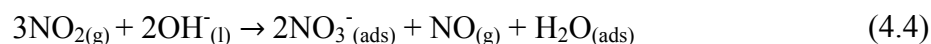


Figure 4.3. Transmission FTIR spectra of (a) CO_2 , (b) SO_2 and (c) NO_2 adsorption on nanomaterial TiO_2 surface. The spectra were recorded in the presence of the gas phase with contributions from gas phase subtracted from these spectra.

forms stable bisulfite indicating higher Bronsted acidity of isolated OH in comparison to bridged. However, it should be noted that there is a contribution from reaction (4.3) for the O-H group reactivity as well. Similar to CO₂, bands for molecularly adsorbed SO₂ was observed. These bands disappeared upon gas phase evacuation. This suggests the presence of available Ti⁴⁺ centers for physisorption of gas phase reactants even after hydroxylation.

NO₂ reactions with hydroxyl groups are more complex as the mechanism is quite different. The overall reaction that has been previously proposed involves three NO₂ molecules reacting with two hydroxyl groups forming nitrate, nitric oxide and water according to reaction (4.4).^{158,159}



Bands for adsorbed nitrate with different coordination modes are observed in the 1000 – 1700 cm⁻¹ region. The water bending mode was not easily observed as it might overlap with some of the nitrate bands. Additionally, the NO₂ dimer, N₂O₄, can react on the surface to yield NO⁺NO₃⁻ on O²⁻Ti⁴⁺O²⁻ sites to form nitrate and nitrite.¹⁶⁰ NO₂ adsorption results in nitrate as the major surface species in different coordination modes of monodentate, bidentate and bridged as shown in Figure 4.3(c). Vibrational frequency assignments for these different nitrate species are presented in table 4.1. The band for the adsorbed nitrite at 1178 cm⁻¹ appears only at the low NO₂ pressures as the increasing NO₂ dosage oxidizes nitrite to nitrate forming complete nitrate coating and gas phase NO.^{99,160,161} At higher NO₂ pressures NO⁺ accumulates on the surface as evident by the

Table 4.1. Assignment of vibrational frequencies of adsorbed products following the reaction of CO₂, SO₂ and NO₂ with TiO₂ nanoparticles.

Surface species			Vibrational	Frequency	Refs ^a
description			mode	(cm-1)	
			assignment		
CO ₂	Carbonate	Monodentate	v ₃ (low)	1375	151
			v ₃ (high)	1511	151
			v ₁	1055	151
		Bidentate	v ₃ (low)	1336	151
			v ₃ (high)	1580	151
			v ₁	n.o.b	151
	Carboxylate	v ₃ (low)		1269	151
			v ₃ (high)	1675	151
		Bicarbonate	v ₁ (OH)	3606	151
			v ₂ (O-C-O)	1623	151
			v ₃ ((O-C-O))	1433	151
			δ ₄ (COH)	1222	151
SO ₂	Molecular		v ₁	1139	92
			v ₃	1325	92
	Sulfite	Monodentate	v ₁	923	92
			v ₁	971	92
			v ₃	1033	92
		Bidentate	v ₁	886	92

			ν_3	1006	92
	bisulfite		ν (SO)	1077	92,128
			ν_1 (OH)	3648	92,138
	Solvated sulfite			1050	92,138
NO ₂	Nitrate	Monodentate	ν_3 (low)	1280	99
			ν_3 (high)	1507	99
			ν_1	925	162
		Bidentate	ν_3 (low)	1240	99
			ν_3 (high)	1582	99
			ν_1	998	162
		Bridged	ν_3 (low)	1216	99
			ν_3 (high)	1631	99
			ν_1	1029	99
	Nitrite		ν_3	1178	99
	NO ⁺			2218	21,158
	N ₂ O ₃		ν (N=O)	1911	21
	N ₂ O ₂ ²⁻			1328	21
	Solvated Nitrate		ν_3 (low)	1338	99
			ν_3 (high)	1409	99
			ν_1	1044	162

Note. ^a Literature references on TiO₂ and Al₂O₃ surfaces and references therein, ^b n.o.: not observed

band at 2218 cm^{-1} which goes away upon evacuation of the gas phase.²¹ Small amounts of adsorbed N_2O_3 formation is observed as evident by a weak band at 1911 cm^{-1} .

The stability of these different species agreed with the previously reported literature. That is, upon evacuation, molecularly adsorbed CO_2 , bicarbonate and most of the carbonate desorbs from the surface, molecularly adsorbed SO_2 leaves the surface, leaving adsorbed sulfite and bisulfite, and nitrate strongly adsorbs to the surface while small amount of nitrate (mainly monodentate) and all NO^+ desorbs from the surface. Therefore, it can be concluded that evacuation of the gas phase removes more weakly bonded species.

Uptake of these reactive gases by TiO_2 was further quantified using a flow system attached to a QCM cell. The change in frequency of the QCM resonator can be related to the increase in mass on the crystal. This relation is given by the Sauerbrey equation.

$$\Delta f = -Cf\Delta m \quad (4.6)$$

In equation 4.6, Δf is the change in frequency of the resonator, Δm is the change in mass related to the change in frequency ($\mu\text{g}/\text{cm}^2$), and Cf is the sensitivity factor, which is a constant of $56.6\text{ Hz cm}^2/\mu\text{g}$ for a 5 MHz AT-cut quartz crystal. In a typical experiment, a hydrosol was made from the solid TiO_2 sample and applied to the QCM crystal using a custom designed atomizer. Dry air was passed through the QCM cell overnight to allow the sample to dry completely. Details of the sample preparation can be found elsewhere. The following day, the sample was reacted with the gas of interest using the flow system. The dry air flow was switched to a 250 SCCM reactive gas flow using

MKS type flow controller. The adsorption was allowed to reach equilibrium, which was determined by monitoring the change in frequency. Once the change in frequency became constant, which was after about 15 to 30 minutes, the flow was switched back to dry air flow to remove reversibly adsorbed products. Adsorption and desorption of the reactants on the TiO₂ thin film resulted in changes in mass and therefore, changes in the frequency. Using the Sauerbrey equation the change can be quantified. Table 4.2 shows the irreversible, reversible and total uptake of CO₂, SO₂ and NO₂.

Table 4.2. Saturation Surface Coverage for Adsorbed CO₂, SO₂ and NO₂ on nanomaterial TiO₂ quantified using QCM at 296 K

Reactive gas	Surface coverage (molecules cm ⁻²)		
	reversible	irreversible	total uptake
CO ₂	$1.1 \pm 0.1 \times 10^{13}$	$0.4 \pm 0.5 \times 10^{13}$	$1.5 \pm 0.5 \times 10^{13}$
SO ₂	$3.6 \pm 0.3 \times 10^{13}$	$1.5 \pm 1.1 \times 10^{13}$	$5.0 \pm 1.3 \times 10^{13}$
NO ₂	$3.9 \pm 1.7 \times 10^{14}$	$1.7 \pm 1.2 \times 10^{14}$	$5.5 \pm 2.4 \times 10^{14}$

The QCM data showed highest coverage for NO₂ adsorption and lowest for CO₂ adsorption. SO₂ adsorption showed moderate coverage. CO₂ showed the lowest total coverage of 1.5×10^{13} molecules cm⁻² with 1.1×10^{13} molecules cm⁻² of reversible and 0.4×10^{13} molecules cm⁻² of irreversible coverage. This lower irreversible coverage agrees with desorption of most adsorbed carbonate and bicarbonate under evacuation shown in FTIR experiments. Total uptake of SO₂ was determined to be 5.0×10^{13} molecules cm⁻² with 1.5×10^{13} molecules cm⁻² of irreversible coverage. The observed coverage values are lower than the coverage found using volumetric measurements in previous studies where FTIR studies showed SO₂ reaction on Al₂O₃ and MgO forming adsorbed sulfite and

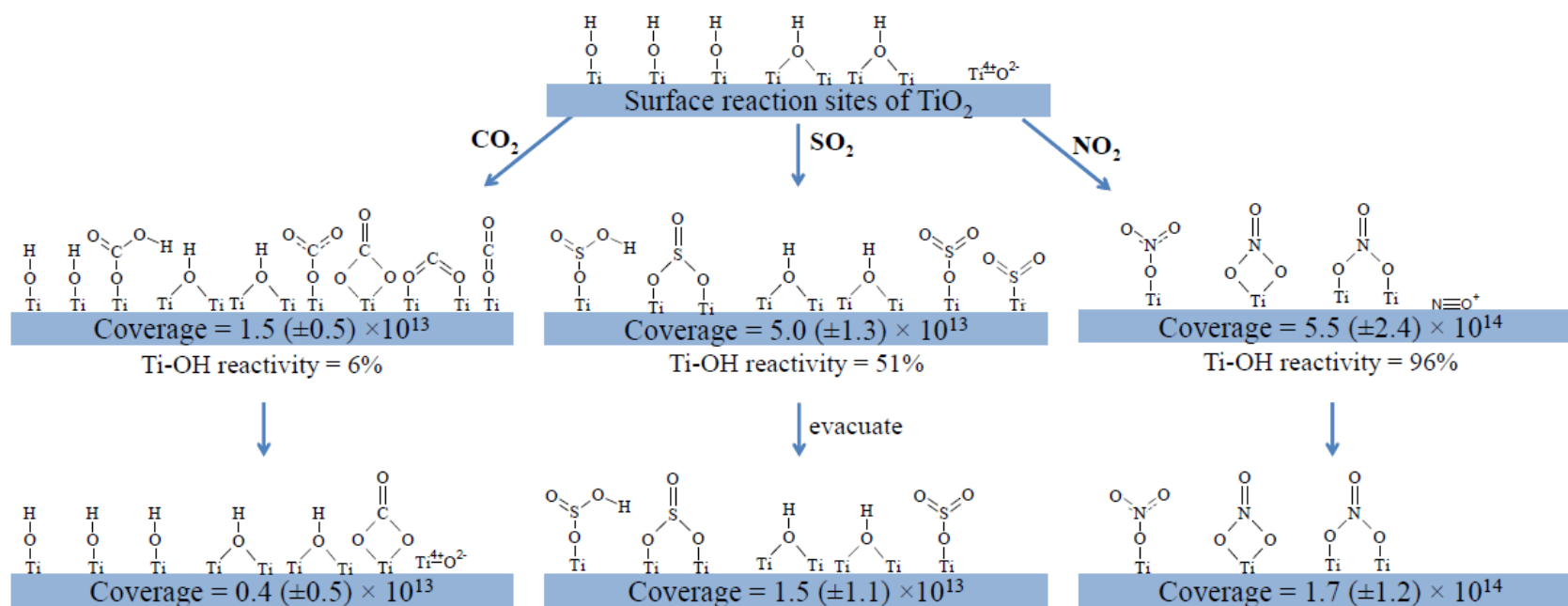


Figure 4.4. Pictorial representation of CO_2 , SO_2 and NO_2 reaction with hydroxylated TiO_2 surfaces. Surface species in the presence and after evacuating the gas-phase reactant derived from FTIR spectra are depicted. The amount of adsorbed species is quantified using a QCM flow cell. Coverages are reported in units of molecules cm^{-2} .

bisulfite with saturation coverage of $2 \pm 1 \times 10^{14}$ molecules cm^{-2} . Adams and coworkers have studied SO_2 uptake on Saharan dusts using a flow tube and reported $\sim 8 \times 10^{13}$ molecule cm^{-2} of highest irreversible coverage.⁹¹ In the present study reversible coverage was higher than the irreversible coverage. This suggests higher molecular SO_2 adsorption in the flow system. Irreversible coverage found for NO_2 was 1.7×10^{14} molecules cm^{-2} and agreed well with that previously reported for TiO_2 , $(1.5-2) \times 10^{14}$ molecules cm^{-2} .¹⁰¹ The total coverage including reversible coverage of 5.5×10^{14} molecules cm^{-2} found in this study is higher than the previously reported saturation coverage using volumetric measurements. Similar to the reversible coverage of CO_2 and SO_2 gases the reversible uptake of NO_2 showed a higher coverage. Combining spectroscopic data and QCM measurements, the schematic in Figure 4.4 represents the overall surface species speciation and coverages in the presence of gas-phase reactant and after evacuation.

The schematic in Figure 4.4 summarizes the discussion of surface species formed by TiO_2 particles reaction with CO_2 , SO_2 and NO_2 . Coverages of surface species resulting from the reaction with gas-phase reactants in the presence of gas-phase and after evacuation quantified using QCM are presented as well.

4.4.3 Water Uptake on Particles Reacted with

CO_2 , SO_2 and NO_2

Water vapor has been shown to play an important role in the reaction chemistry of adsorbed species on metal oxide surfaces. Water vapor can enhance or suppress adsorption and change the speciation of adsorbed products to water solvated products. In turn, adsorbed species can enhance or suppress the water uptake by changing the surface

sites and hygroscopic behavior. Ambient pressure X-ray photoelectron spectroscopy studies have shown the bridged hydroxyl groups as a nucleation site for water uptake.¹⁰⁸ Therefore, the study of water uptake on metal oxides such as TiO_2 previously reacted with CO_2 , SO_2 and NO_2 is important since the reaction with those gases change the surface O-H group speciation. In the present work, water uptake on nanoparticle TiO_2 previously reacted with CO_2 , SO_2 and NO_2 was studied using both FTIR spectroscopy to gather molecular level information and QCM to quantify the water uptake. Firstly, the FTIR experimental setup described under experimental methods was used to study water adsorption. The TiO_2 surface was saturated with the gaseous species of interest followed by an evacuation to remove any weakly bound species. Water vapor was introduced with increasing relative humidity and exposure for 25 minutes, to reach equilibrium. The FTIR spectra were then recorded, and the surface was evacuated for another 25 minutes before introducing the next relative humidity.

Figure 4.5(a) shows the FTIR spectra of water adsorption on TiO_2 nanoparticles previously reacted with CO_2 . The bottom spectrum shows the spectrum for TiO_2 particles reacted with CO_2 for 25 minutes and evacuated for another 25 minutes. The bands for the adsorbed carbonate and bicarbonate in Figure 4.5(a) before water introduction show less intensity compared to the adsorption spectra in Figure 4.3(a) due to carbonate and bicarbonate desorption upon evacuation. Among the remaining bands, bidentate carbonate bands show the highest intensity and bands for monodentate carbonate and bicarbonate show the lowest intensity. Intensity of the band at 1640 cm^{-1} increases with exposure to increasing relative humidity. Furthermore, intensity of the bands for carbonate and bicarbonate decrease with exposure to water vapor. Bands for water

solvated carbonate at 1428 cm^{-1} and 1324 cm^{-1} on TiO_2 have been previously observed when CO_2 and H_2O were co-dosed¹⁵¹, but were very low in intensity. Here we did not see any new band growth at 1428 cm^{-1} and 1324 cm^{-1} . The band at 1336 cm^{-1} for the symmetric stretching mode of bidentate carbonate remained in very low intensity even at the highest water exposure suggesting a higher stability for water vapor. The band at 1580 cm^{-1} for the asymmetric stretching mode of the bidentate carbonate appeared only at low water vapor exposures and was not seen at higher exposures. This could be due to overlap with water bending mode at higher water vapor exposures. The top spectra of Figure 4.5(a) show the spectra after overnight evacuation after the highest water vapor exposure. It shows very low intensity of the water bending mode and bidentate carbonate bands with very low intensity. Overall, both carbonate and solvated carbonate species desorption from the surface upon evacuation after exposed to water vapor due to being more weakly adsorbed to the surface.

Figure 4.5(b) shows the effect of relative humidity on adsorbed sulfite/bisulfite. TiO_2 sample was reacted with 100 mTorr of SO_2 for 25 minutes and evacuated another 25 minutes. The adsorbed sulfite and bisulfite were then exposed to water vapor, where a band centered at 1050 cm^{-1} grows initially with increasing relative humidity. The intensity of sulfite and bisulfite band envelope decreases with increasing relative humidity. This observation was previously explained by the formation of water solvated sulfite in the presence of water vapor, leading to a more liquid like reaction and desorption from the surface upon evacuation.⁹² Therefore, adsorbed water decreases the stability of sulfite and bisulfite.

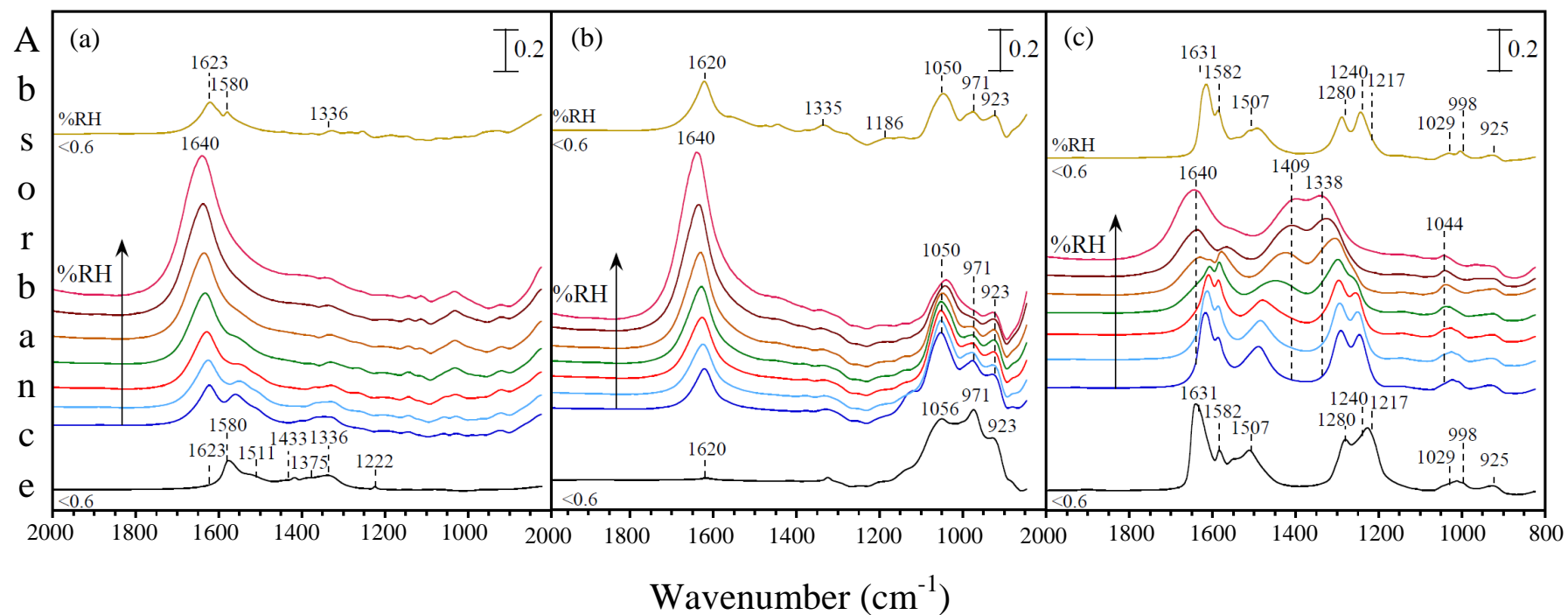


Figure 4.5. FTIR spectra of water uptake on TiO_2 nanoparticles previously reacted with (a) CO_2 , (b) SO_2 and (c) NO_2 with exposure to increasing relative humidity of 0.6, 1.2, 3.1, 10, 26, 56 and 76% RH. Gas-phase water vapor was evacuated for 25 minutes after each exposure before the next higher exposure. After exposed to highest %RH, the infrared cell is evacuated to less than 0.6%RH. These final spectra are shown in (a), (b) and (c).

Figure 4.5(c) shows the formation of water solvated nitrate with exposure to increasing relative humidity, with the growth of bands at 1409 cm^{-1} and 1338 cm^{-1} . At the highest exposure, all of the nitrate ions are solvated by co-adsorbed water as evident by dominance of water solvated nitrate bands in the spectrum. Adsorbed nitrate in different geometries resulted from NO_2 reaction conversion to water solvated nitrate on oxide surfaces after exposed to water vapor has been previously observed.^{160,162,163} The intensity of the band at 1640 cm^{-1} for bending mode of adsorbed water started increasing with exposure to water vapor. This feature started appearing as a shoulder at the 10% RH exposure and appeared with the highest intensity at the highest exposure. This suggests low water adsorption at low water exposures and higher water adsorption at higher exposures. The intensity of the adsorbed nitrate band envelope has decreased after exposure to different relative humidities and evacuation cycles as seen from the top spectra of Figure 4.5(c). Oxide coordinated nitrate conversion to water solvated nitrate conversion and the reverse reaction are thought to be reversible processes. In our experimental method, we evacuate the introduced water vapor down to 1×10^{-7} before introducing the next higher relative humidity. It is proposed on clay surfaces as water pushing bridged and bidentate nitrate to comparatively less tightly bound monodentate nitrate.¹⁶⁴ This also can lead to possible desorption of some of monodentate nitrate under evacuation. Therefore, during water vapor exposure and evacuation cycles, some of the nitrate molecules which are going through the conversion from oxide coordinated to water solvated and vice versa can be desorbed.

The broad O-H stretching absorption band of H bonded OH groups of adsorbed water resulted from water adsorption on unreacted and reacted TiO_2 particles as a

function of increasing water vapor pressure between 0.6 and 76% relative humidity is shown in Figure 4.6. The broad band adsorbed water between 2500 and 4000 cm^{-1} and is centered at 3551 cm^{-1} with water bending mode is centered at 1640 cm^{-1} . Water adsorption on unreacted TiO_2 particles and TiO_2 particles previously reacted with CO_2 as a function of increasing water vapor pressure is shown in Figure 4.6 (a) and (b) and they show no difference suggesting no effect from initial CO_2 reaction on water uptake of TiO_2 . Surface hydroxyl groups are acting as the water adsorption sites on oxide surfaces.¹⁰⁷ The negative bands appeared between 3600 – 3900 cm^{-1} in Figure 4.6 (a) and (b) confirms that adsorbed water by interacting with the surface hydroxyl groups. Water adsorption on TiO_2 particles reacted with SO_2 in Figure 4.6(c) shows growth of broad band between 4000 – 2500 cm^{-1} with two features at 3498 cm^{-1} and 3211 cm^{-1} that has been previously assigned to $\text{SO}_2 \cdot \text{H}_2\text{O}$ complex. Figure 4.6(d) contains the FTIR spectra between 800 and 4000 cm^{-1} for water uptake on nitrogen dioxide reacted TiO_2 surface. The bending mode for adsorbed water grows in intensity similar to others. The intensity of broad band between 2500 and 4000 cm^{-1} shows lower growth for H bonded OH of adsorbed water with increasing relative humidity compare to the Figure 4.6(a), (b) and (c). This suggests the adsorbed water is used to solvate the adsorbed nitrate while not forming much of H bonds with other water molecules. Negative bands resulted between 3600 and 3900 cm^{-1} from NO_2 reaction with surface hydroxyl groups of TiO_2 particles prior to exposure to water vapor in Figure 4.6(d) did not show changes after exposure to water vapor. This suggests water adsorption has not regenerated hydroxyl groups on the surface in the presence of these adsorbates. However, as discussed earlier exposure to water vapor solvates the adsorbed nitrate completely. Therefore, during the solvation of

adsorbed nitrate, the surface Ti sites which were initially coordinated to nitrate molecules can be expected to be occupied by adsorbed water molecules.

Changes in the H bonded O-H group region for adsorbed water in Figure 4.6 (d) compared to the other three scenarios can be possibly due to the changes in dynamics of adsorbed water in the adsorbed water layer. Experimental studies of neutral vs ionic interfaces have shown changes in hydrogen bond rearrangement in the ionic interfaces compare to neutral interfaces and bulk water.^{165,166} The dynamics of adsorbed water can be significantly different in these confined space environments compared to liquid water. This can be seen in the FTIR spectra for adsorbed water on TiO₂ nanoparticle surfaces before reaction (Figure 4.6(a)) compared to following reaction with CO₂, SO₂ and NO₂ (Figure 4.6(b), (c), (d)). Furthermore, water dynamics will be greatly influenced by the species present and the nature of the interface.⁴⁵ TiO₂ nanoparticle surfaces exposed to water vapor results in several layers of adsorbed water on the surface. These adsorbed water layers can be considered as being in confined space environments. Therefore, solvated ions on the adsorbed water layer of TiO₂ particles previously reacted with trace atmospheric gases can change the dynamics of adsorbed water resulting changes in the intensity of the broad vibrational band for the H bonded OH groups that can not be simply explained by the transmission FTIR spectroscopy. Therefore, further studies using different techniques are useful in terms of understanding the dynamics of adsorbed water in these environmentally relevant and confined adsorbed water layers of reacted oxide surfaces.

The mass of water taken up on TiO₂ particles reacted with CO₂, SO₂, and NO₂ was quantified using QCM. Quantification of water uptake using FTIR data was not

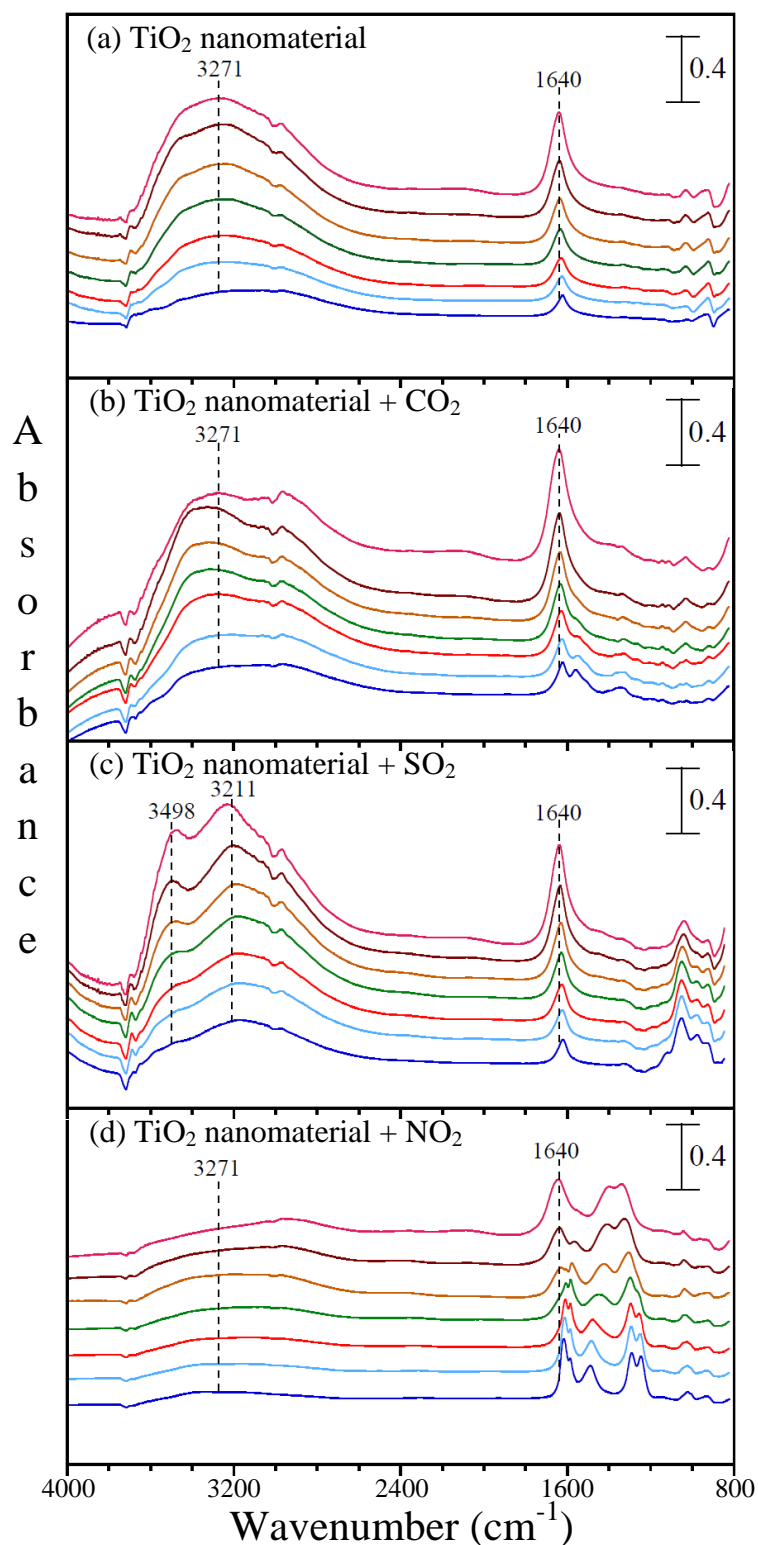


Figure 4.6. Transmission FTIR spectra between 800 and 4000 cm^{-1} for H_2O adsorption on TiO_2 before (a) and after reaction with: (b) CO_2 ; (c) SO_2 ; and (d) NO_2 . These spectra are shown as a function of increasing relative humidity from 0.6, 1.2, 3.1, 10, 26, 56 and 76% RH at $T = 296$ K.

feasible due to several reasons. First, the bending mode of adsorbed water overlaps with the bidentate carbonate and bridged nitrate bands. This made curve fitting unfeasible due to the uncertainty of the contribution from the overlapping peaks. Quantification of adsorbed water using the H-bonded hydroxyl region of adsorbed water between 2500 – 3600 cm^{-1} was not possible due to water uptake on NO_2 reacted TiO_2 was not showing much growth in H-bonded hydroxyl region while conversely showing an increase in intensity of the band for bending mode of adsorbed water vapor (Figure 4.6(d)). Therefore, quantitative comparison of water uptake was carried out using QCM technique.

Table 4.3 contains the amount of water uptake quantified by QCM for unreacted TiO_2 particles and TiO_2 particles previously reacted with CO_2 , SO_2 and NO_2 . In these experiments the TiO_2 sample was reacted with the reactant gas for about 15 minutes until the QCM showed a maximum uptake, determined by monitoring relative frequency until it remained constant, followed by passing dry air for another 15 minutes to remove weakly bound species. Water vapor was then introduced in increasing relative humidity, allowing approximately 15 minutes for the relative frequency to stabilize before increasing relative humidity. The data is presented as total water uptake between 0-30% RH, 30-60% RH and 60-100%RH in Table 4.3. All the uptake experiments were repeated 3 or more times to collect more data points. The data does not show much difference in water uptake on unreacted TiO_2 and TiO_2 reacted with CO_2 and SO_2 . This suggests the lower impact of CO_2 and SO_2 reaction on hygroscopic behavior of TiO_2 . For CO_2 reacted TiO_2 particles, most of the adsorbed CO_2 are removed from the surface during evacuation of the QCM sample (dry air passing) due to less stability. Additionally, the O-H groups

are available for water adsorption; therefore, water uptake is similar to unreacted TiO_2 . Some of the remaining bidentate carbonate leaving the surface during water vapor flow can also add a negative contribution to the total mass uptake. For SO_2 reacted, most of the

Table 4.3. Water uptake on TiO_2 quantified with QCM measurements as a f(%RH) for unreacted and previously reacted with CO_2 , SO_2 , and NO_2

TiO_2 sample	Surface coverage of water (Mass H_2O /Mass TiO_2)		
	%RH Range		
	0 - 30	30 - 60	60 - 100
Unreacted	0.006 (± 0.0032)	0.0184 (± 0.0045)	0.0328 (± 0.0093)
Reacted with CO_2	0.0071 (± 0.0029)	0.0206 (± 0.0056)	0.0340 (± 0.0058)
Reacted with SO_2	0.0036 (± 0.0021)	0.0175 (± 0.0055)	0.0331 (± 0.0085)
Reacted with NO_2	0.0057 (± 0.0048)	0.0161 (± 0.0005)	0.1136 (± 0.0307)

bridged O-H and some of the isolated O-H are available on TiO_2 surface after reaction with SO_2 . Availability of these sites enables water adsorption. Water uptake measurements were similar to the unreacted TiO_2 . Thus it appears that SO_2 did not change of amount of adsorbed water on TiO_2 particle surfaces. Additionally, weakly bound $\text{SO}_2 \cdot \text{H}_2\text{O}$ complex in the presence of water vapor which showed less stability during evacuation has been proposed in previous studies.⁹² Similar to CO_2 reacted TiO_2 , it is possible that this complex formed and was removed from the surface with water vapor flow adding negative contribution to the water uptake measurements. Ma and coworkers have studied water uptake on Arizona test dust with a different experimental method where samples were co-dosed with SO_2 , O_2 and water, and reported no impact of the presence of SO_2 on hygroscopic behavior agreeing with our QCM results.¹¹² For the water uptake on NO_2 reacted TiO_2 lower water uptake was observed at 0-30% and 30-

60% RH regions. After that, at the highest relative humidity range the water uptake was significantly higher compared to the unreacted TiO_2 and reacted with CO_2 and SO_2 . For the water uptake on TiO_2 particles previously reacted with NO_2 , the experiment was repeated 3 times and results from one of those trials were excluded due to significant difference from other two trials. The data suggests adsorbed NO_3^- complete solvation has more water associated with it compared to other adsorbates. In the literature there have been several studies on water uptake measurements on nitrated TiO_2 . Water uptake calculated using volumetric measurements on TiO_2 particles previously reacted with HNO_3 using a reaction system attached to transmission FTIR spectrometer did not show an enhancement in water uptake.¹⁰¹ Ma and co-workers have observed enhancement in water uptake on Degussa TiO_2 (known as P25) particles previously reacted with $\text{NO} + \text{O}_2$ to generate adsorbed nitrate using DRIFTS system attached to a flow system.¹⁶⁷ They have seen continuous enhancement in water uptake for 0-100% RH and used the integrated absorbance of $2600\text{-}3800\text{ cm}^{-1}$ region of DRIFT spectra of adsorbed water to compare the water uptake. The differences in their observations from the spectroscopy and QCM results shown here were they have observed continuous enhancement in water uptake and growth in H-bonded O-H groups of adsorbed water of nitrate covered TiO_2 . These observations could be due to several factors. They have used a 100 SCCM flow rate that might have left some O-H groups available for water uptake. Another possibility is the NO and O_2 co adsorption mechanism shows that they produce surface NO_2 .⁸² This newly formed NO_2 should then react with O-H groups to remove O-H groups completely. Since NO_2 production is a secondary product, O-H groups might not have completely reacted. The observed increase in intensity for H bonded hydroxyl region for

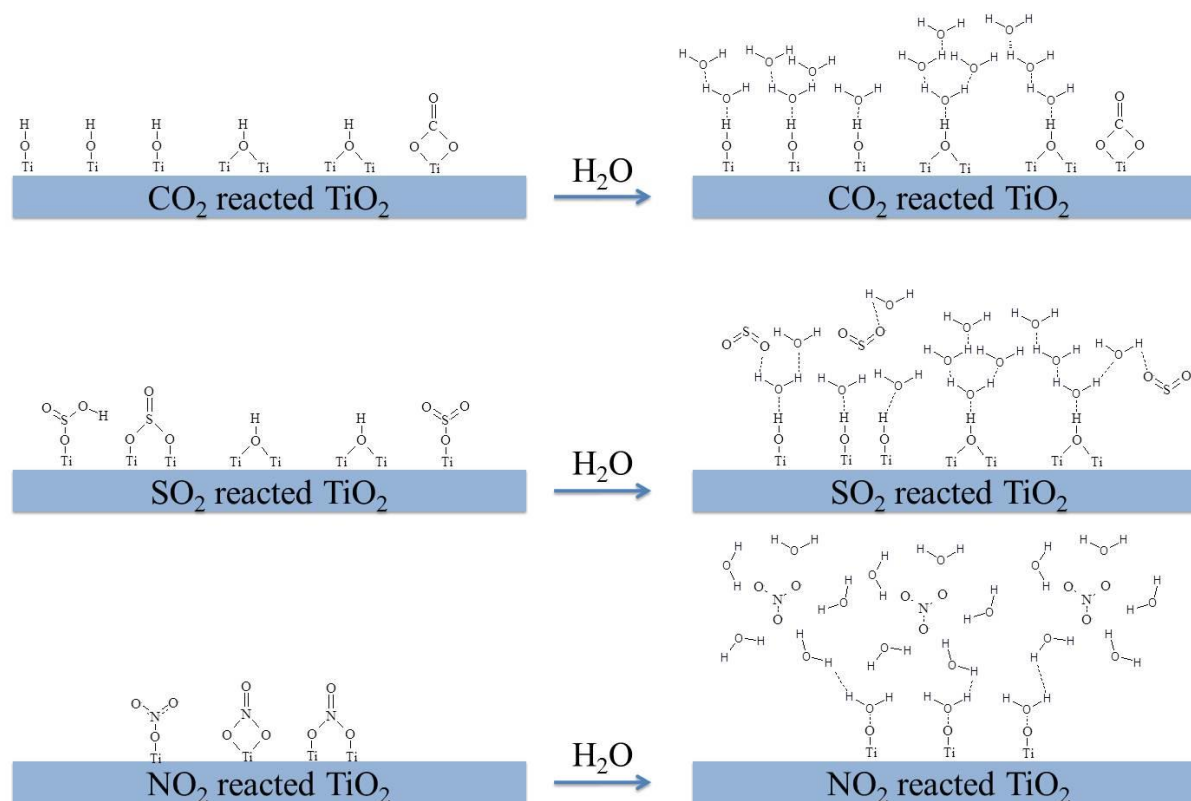


Figure 4.7. Pictorial cartoon depicting water uptake on TiO_2 nanoparticles following reaction with CO_2 , SO_2 and NO_2 .

adsorbed water could be due to the combined effect from the availability of some O-H groups for water uptake after reaction with $\text{NO}+\text{O}_2$ and adsorbed nitrate solvation. However, agreeing with the results discussed here they observed an increase in water uptake with increasing relative humidity. The observed higher water uptake could be due to higher water uptake by solvated nitrate. Experimental studies have shown the conversion of oxide coordinated nitrate formed by NO_2 reacting with water solvated nitrate after exposure to water vapor on several different metal oxide surfaces including TiO_2 .^{162,163,168} The structure of solvated nitrate or nitrate water clusters ($\text{NO}_3^-\cdot(\text{H}_2\text{O})_n$) has been studied using experimental and computational methods in several studies for $n=1-6$ and $n=15-500$ and the importance in nitrate heterogeneous photochemistry on surfaces has been discussed.^{162,169,170} Our QCM results suggest complete nitrate solvation of oxide coordinated nitrate of TiO_2 requires more water. Therefore, TiO_2 previously reacted with NO_2 appears to be more hygroscopic at higher %RH.

Figure 4.7 summarizes the water adsorption on TiO_2 particles previously reacted with CO_2 , SO_2 and NO_2 . TiO_2 particles reacted with CO_2 and SO_2 contains surface hydroxyl groups for H_2O adsorption and water adsorbs forming multilayers. Water adsorption on TiO_2 particles reacted with SO_2 also forms $\text{SO}_2\cdot\text{H}_2\text{O}$ complex in the presence of water vapor. Water adsorption on TiO_2 particles reacted with NO_2 , changes the oxide coordinated nitrate to water solvated nitrate.

4.5 Conclusions

The reactivity of three triatomic gases on TiO_2 surface is discussed here. The results show the difference in surface hydroxyl group reactivity with trace gas adsorption.

Specifically, nitrogen dioxide is highly reactive with nearly complete reaction occurring with all hydroxyl groups, whereas carbon dioxide on the other end shows the least reactivity. However, understanding the orbitals involved and the dynamics of the reactivity of different hydroxyl groups is currently a challenge due to controversies in the literature on the exact assignment of different hydroxyl groups. Therefore, further experimental and computational investigations are needed to elaborate the bonding of hydroxyl groups on TiO_2 nanoparticle surfaces. The effect of water vapor on the stability of surface species is demonstrated here as well as the role of solvation. Upon evacuation, solvated sulfite/bisulfite desorbs from the surface but this does not occur for adsorbed nitrate. QCM studies revealed that the adsorbed nitrate enhance the hygroscopic properties of TiO_2 , potentially due to the formation of solvated nitrate.

Acknowledgement

This work was supported by the NSF under grant CHE-1305723. Any opinions, findings, and conclusions or recommendations expressed in this material are those of the authors and do not necessarily reflect the views of National Science Foundation.

CHAPTER 5

SURFACE ADSORPTION AND PHOTOCHEMISTRY OF FORMIC ACID ON TiO₂
NANOPARTICLES: THE ROLE OF ADSORBED WATER IN THE ADSORPTION
KINETICS, SURFACE COORDINATION MODE AND RATE OF PHOTOPRODUCT
FORMATION**5.1 Abstract**

Formic acid adsorption and photochemistry have been investigated on TiO₂ nanoparticle surfaces using transmission FTIR spectroscopy. The results show that gas-phase formic acid adsorbs on the surface at low exposures to yield adsorbed bridged bidentate formate and, at higher exposures, molecularly adsorbed formic acid as well. Upon exposure to water vapor, adsorbed formate becomes solvated by co-adsorbed water molecules and the bonding configuration changes as indicated by shifts in the vibrational mode frequencies for adsorbed formate. Adsorbed water also impacts the adsorption kinetics for formic acid on TiO₂ by providing a medium for facile dissociation. Ultraviolet irradiation of adsorbed formate on TiO₂ in the presence of molecular oxygen results in the formation of gas-phase carbon dioxide. Although carbon dioxide forms under the different environmental conditions investigated, carbon dioxide formation increases in the presence of adsorbed water. Additionally, the dispersion of TiO₂ nanoparticles in water suspensions is found to change following exposure to formic acid. The environmental implications of all these results are discussed.

5.2 Introduction

TiO₂ is a component of mineral dust aerosol and the amount of TiO₂ present depends on the dust source.^{6,7} Typically, the composition of TiO₂ in mineral dust is reported to be in the range of 1 to 10% by mass.⁷ These dust particles can react with trace atmospheric gases as the dust is transported away from the source region.¹⁷¹ Additionally, stationary surfaces of TiO₂ or TiO₂ composite mixed materials, which are mainly used as self-cleaning coatings mainly to eliminate organic pollutants due to its high photocatalytic activity, can also act as surfaces for atmospheric trace gas adsorption and reaction.³⁴

Volatile organic compounds (VOCs) are important constituents of the troposphere and emit from both biogenic and anthropogenic sources.¹⁷² Volatile organic compound degradation as well as direct biogenic and anthropogenic emissions generate atmospheric formic acid. Among the class of atmospheric acids, formic acid is the most abundant organic acid in the troposphere.¹⁷³ A recent modeling study revealed that around 30% contribution of emissions are directly by vehicles in northern hemisphere (mid-high latitudes).¹⁷⁴ In another study, formic and acetic acids were identified as the main constituents of cloud and rain water samples in a mountainous region in southern China.¹⁷⁵ Formic acid concentrations have been reported to be in the range from 3 to 20 ppbv and have shown changes in both urban and remote regions.¹⁷⁶ Formic acid emissions measured during Winter ClearfLo Campaign in London, January 2012 have shown maximum concentrations of 6.7 ppm with mean concentrations a factor of ten less near 610 ppt.¹⁷⁴ Furthermore, studies have shown adsorbed mineral dust particles can adsorb organic acids.^{171,177}

Formic acid uptake on components of mineral dust such as clays, carbonates and oxides that include SiO_2 , Al_2O_3 , Fe_2O_3 , and TiO_2 has been studied using experimental and computational methods.^{111,178-187} These studies have investigated formic acid adsorption, uptake coefficients, stability of adsorbed products and hygroscopic behavior of reacted particles. In fact, heterogeneous chemistry and photochemistry of volatile organic compounds including organic acids on oxide surfaces have received some attention in scientific community and have been discussed in several recent review articles.^{7,172,188}

Formic acid adsorption on anatase and rutile TiO_2 has been studied using gas-phase and aqueous phase formic acid in several studies.^{181,183,189-191} Studies of formic acid heterogeneous reaction on metal oxides revealed that formic acid can dissociatively adsorb on oxide surfaces resulting in adsorbed formate. Adsorbed formate in a bridged bidentate geometry was the main coordination mode found under dry conditions.¹⁸¹ Additionally, physisorbed and chemisorbed molecular formic acid are found to be present on the surface in smaller, but measurable, quantities.^{181,183}

Furthermore, light absorbing components of mineral dust aerosol such as TiO_2 can initiate photocatalytic decomposition of adsorbed formate in the presence of solar light. Surface reactions in the presence of UV light can be initiated due to the formation of electron and hole (e^-/h^+) pair generation which diffuse to the particle surface.^{10,36} Molecularly adsorbed formic acid can photocatalytically decompose to formate and adsorbed formate photooxidizes to yield CO_2 and H_2O .¹⁸³ Additionally, adsorbed methanol photooxidation on rutile TiO_2 particle surfaces have shown bridged bidentate formate production.¹⁹²

The focus of the current study is to further understand the details of formic acid adsorption on TiO₂ nanoparticles and the effect of relative humidity on photooxidation of adsorbed formate. Transmission FTIR spectroscopy has been used for studying the surface and gas-phase products. Furthermore, the aqueous phase behavior of formic acid reacted TiO₂ particles has also been examined.

5.3 Experimental Methods

5.3.1 Transmission FTIR Spectroscopy

The experimental system used to study the HCOOH acid adsorption on nanoparticle TiO₂ has been described in detail elsewhere.¹¹⁵ Briefly, the sample holder contains two nickel jaws to hold the tungsten grid (3 cm × 2 cm, 100 mesh/in., 0.002" wire dia., Accumet Materials Co.). Two thermocouple wires were attached to the tungsten grid to monitor the temperature of the sample during any resistive heating procedures. A TiO₂ sample (~10 mg) was dissolved in a small amount of water and sonicated for 10 minutes to decrease particle aggregation. One half of the tungsten grid was then coated with the hydrosol to get the surface information and other half remained uncoated to get the gas phase information. After coated the sample was allowed to dry at the room temperature. Then, the sample holder is connected to the reaction chamber. The reaction chamber was connected to a premix chamber and was pumped down to 10⁻⁷ Torr using a turbomolecular/mechanical pump system. The reaction chamber acts as the infrared cell with two BaF₂ windows. Reaction chamber was moved using a linear translator, allowing both halves of the grid to be scanned for surface and gas-phase information. Infrared spectra were recorded with a Mattson Galaxy 6000 spectrometer

equipped with a MCT detector. In a typical experiment, an instrument resolution of 4 cm^{-1} was used and 250 scans were co-added and further processed to give the absorbance spectra shown here. Single beam spectra for the surface and gas phase were referenced to the initial spectra in order to obtain the absorbance spectra. UV irradiation experiments were carried out using a 500 W broadband Hg arc lamp (Oriel, model no. 66033). A water filter was used to remove IR radiation.

5.3.2 Solution Phase Studies of Nanomaterial

TiO₂ Previously Reacted with HCOOH

TiO₂ particles reacted with HCOOH in the reaction chamber described earlier. Reacted and unreacted particles were suspended in optima water (Fisher) at a mass loading of 0.7 mg/20 mL. The suspension was sonicated for 10 minutes. The size distribution of aggregates of unreacted and reacted particles was obtained using a commercial dynamic light scattering (DLS) instrument (Delsa Nano C particle analyzer) equipped with a green laser at 532 nm.

5.3.3 Sources of Chemicals

Formic acid (Alfa Aesar) and optima H₂O (Fisher) was used as received. Prior to use, both the distilled water and HCOOH were degassed several times with consecutive freeze-pump-thaw cycles. Oxygen (UPC grade) was obtained from Praxair. TiO₂ sample was purchased from Nanostructures and Amorphous Inc.

5.4 Results and Discussions

5.4.1 Transmission FTIR Studies of Formic Acid

Adsorption on TiO₂ Nanoparticles

Titanium dioxide nanoparticles used in the current study have been previously characterized by a variety of techniques. The sample is composed of nanoparticles with an average particle size determined from transmission electron microscopy to be 10 ± 3 nm (200 particles counted). BET analysis gives a surface area of $128 \pm 5 \text{ m}^2 \text{ g}^{-1}$, with the standard deviation determined from three replicate measurements. Powder X-ray diffraction patterns from this sample show that the TiO₂ nanoparticles are primarily anatase with a small amount of rutile (~6%).

Formic acid adsorption was carried out by exposing the TiO₂ nanoparticles to a known pressure for 25 minutes. After 25 minutes, single beam spectra for the surface and gas phase were collected. The single beam spectra were referenced to the initial single beam spectra to get the absorbance spectra. Gas-phase absorbance spectra were subtracted from the surface spectra to remove them from the surface spectra. Figure 5.1 shows the FTIR spectra of adsorbed species after exposure to increasing pressures of formic acid, 11, 25, 41, 60, 100, 306, and 491 mTorr.

The gas phase subtracted spectra show the surface species formed by formic acid adsorption and the inset shows the surface spectrum collected following overnight evacuation following exposure at the highest formic acid pressure. The spectra show the growth of adsorption bands at 1208, 1252, 1322, 1362, 1385, 1412, 1562, 1620, 1675, 1725, 2591, 2735, 2872, 2923 and 2951 cm^{-1} . These bands can be assigned to two surface

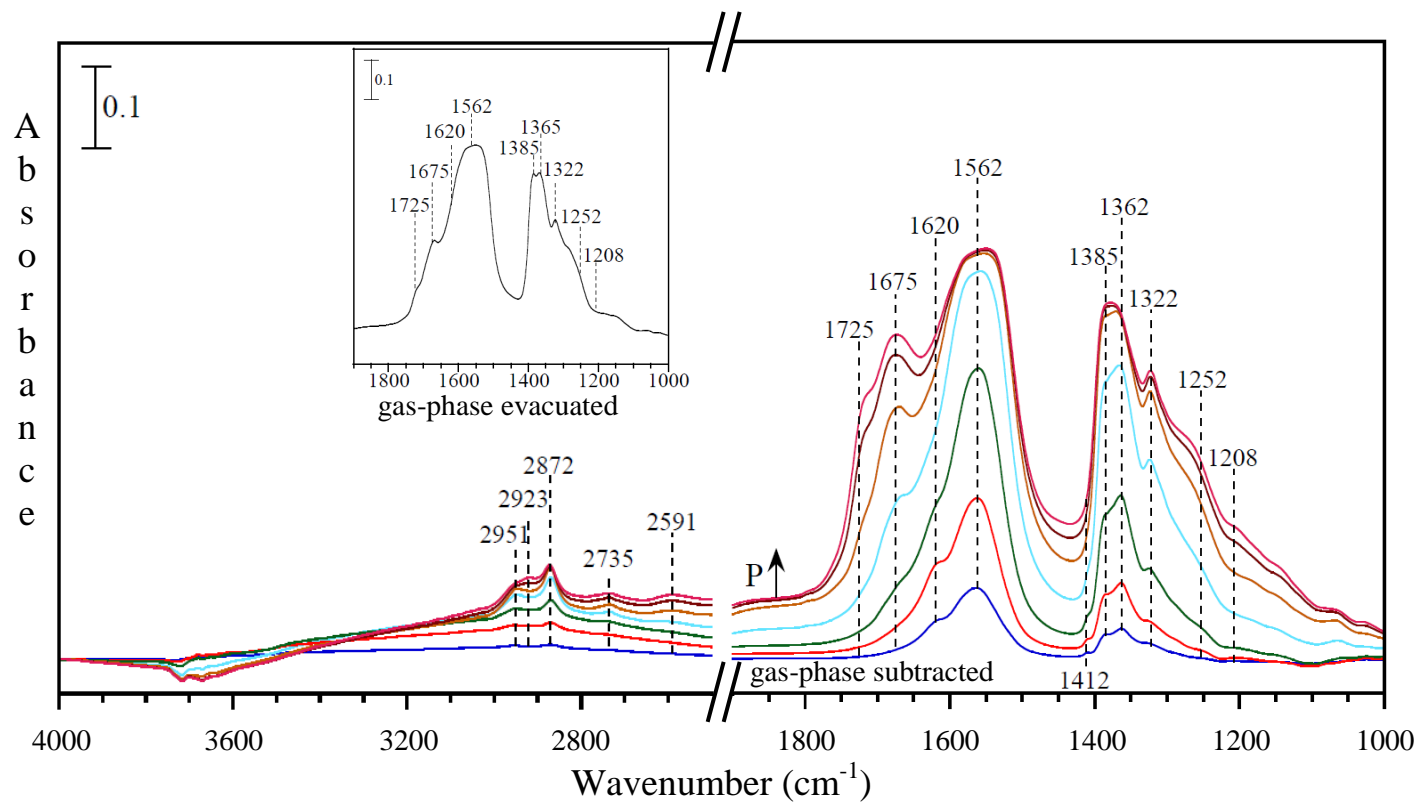


Figure 5.1. Transmission FTIR spectra of HCOOH adsorption on nanomaterial TiO_2 . Spectra were collected as particles were exposed to increasing HCCOH (11, 25, 41, 60, 100, 306 and 491 mTorr) pressure for 25 minutes. The spectra were recorded in the presence of gas-phase and gas-phase spectra have been subtracted. The inset shows the spectrum recorded after evacuation of gas-phase HCOOH following the highest exposure.

species: (i) adsorbed formate resulting from dissociative formic acid adsorption and; (ii) molecularly adsorbed formic acid.

Earlier studies have shown that formic acid can dissociatively adsorb on metal oxide surfaces forming adsorbed formate according to reaction (5.1). Formic acid can also react with surface hydroxyl groups to form adsorbed formate and water as shown in reaction (5.2). Reactivity of surface hydroxyl groups on TiO₂ nanoparticles can be seen with the negative peaks observed between 3600 and 3900 cm⁻¹ in Figure 5.1. Evidence for water formation can also be seen by the absorption band at 1620 cm⁻¹ characteristic for the bending mode of adsorbed water. This band is only apparent at initial, low pressures of formic acid. At higher pressures, this band is more difficult to discern due to the growth and overlap of other absorption bands in the spectrum.

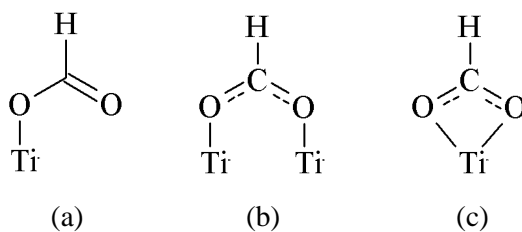


Figure 5.2. Formate adsorption structures: (a) Monodentate, (b) bridged bidentate and (c) chelating bidentate.

Adsorbed formate can coordinate to the surface in different modes including monodentate, bridged bidentate and chelating bidentate (Figure 5.2). The frequency difference between the asymmetric and symmetric modes of the $\nu(\text{COO})$ stretch is often used to distinguish between these different bonding modes. This analysis has been previously described in detail for adsorbed formate on P25 TiO_2 .¹⁸¹ The vibrational energy difference ($\Delta\nu(\text{COO})$) for the asymmetric and symmetric COO stretching for sodium formate is 201 cm^{-1} ($\nu_{\text{as}}(\text{OCO})$ and $\nu_{\text{s}}(\text{OCO})$ at 1567 and 1366 cm^{-1}).¹⁹³ A wavenumber difference lower than or close to that of sodium formate can be assigned to bridged bidentate formate.¹⁹⁴ In this current study, absorptions are seen at 1562 cm^{-1} and 1362 cm^{-1} which gives a wavenumber difference of 197 cm^{-1} that is very close to that of the sodium salt. Therefore, these bands are assigned to bridged bidentate formate. Bridged bidentate formate is the major surface species resulted from formic acid adsorption on 10 nm TiO_2 particle surfaces. A wavenumber difference higher than that of sodium formate was used to assign the bands for monodentate formate. The band at 1322 cm^{-1} which grows in along with bridged bidentate formate bands can be assigned to $\nu(\text{COO})$ symmetric stretching mode of monodentate formate. The lower intensity of this band suggests less monodentate formate formation, assuming the absorptivity for this mode does not differ too much between these different coordination modes. The higher wavenumber asymmetric stretch may have some overlap with the band at 1562 cm^{-1} making it difficult to distinguish. The vibrational band assignments for adsorbed species are summarized in Table 5.1.^{181,183,190,191,195,196 179}

Table 5.1. Vibrational Frequencies Assignment of Adsorbed Species after HCOOH Reaction with TiO₂.

Adsorbed Species	Assignment	This study	Literature Reference Frequencies						
			TiO ₂				α -Al ₂ O ₃		
			P25 Liao et al.	P25 Miller et al.	Rutile Rotzinger et al.	P25 El-Maazawi et al.	Anatase (101) Xu et al.	Wu et al.	Tong et al.
Bridged bidentate formate	$\nu_{as}(\text{OCO})$	1562	1557	1550	1533	1575	1598	1590	1600
	$\nu_s(\text{OCO})$	1362	1371	1378	1355	1358	1362	1393	1393
	δCH	1385	1385	1323	1377	1323	1386	1378	1378
	νCH	2872		2867		2873		2867	2866
	$\nu_{as}(\text{OCO})+\delta\text{CH}$	2951		2945		2957			2985
	$\nu_s(\text{OCO})+\delta\text{CH}$	2735						2750	2750
Monodentate formate	$\nu_{as}(\text{OCO})$	n.o.		1565			1647		
	$\nu_s(\text{OCO})$	1322		1360			1315		
Formic acid physisorbed	$\nu\text{C=O}$	1725		1787	1716			1706	
	νCO	1208		1105	1204				
Formic acid chemisorbed	$\nu\text{C=O}$	1675	1682	1675					
	νCO	1252	1277	1263					
	δCH	n.o.	1325						
	νCH	2923		2921				2921	
	νOH	2591						2562	
Dioxymethylene		1412				1407			
Solvated formate (monodentate)	$\nu_{as}(\text{OCO})$	1583		1565					
	$\nu_s(\text{OCO})$	1338		1360					

Density functional theory studies have previously shown the bridged bidentate orientation to be more favored on anatase (101) over monodentate which further confirms our observation and assignment to the formation of bridged bidentate formate on the surface of TiO₂ nanoparticles.¹⁹⁷ The anatase sample used in this study is dominated by the (101) plane as revealed by XRD. Thus theory agrees with the experimental data presented here.

Absorption bands for molecularly adsorbed formic acid at 1725, 1208, 1675 and 1252 cm⁻¹ become visible as the pressure is increased and become increasingly dominant at exposure higher than 100 mTorr. Another set of bands are seen between 2500 and 3200 cm⁻¹ for C-H stretching of adsorbed formate, combination bands of C-H bending with symmetric and asymmetric stretching of $\nu(\text{COO})$ of adsorbed formate, and C-H and O-H stretching of chemisorbed formic acid. Assignments of these bands are presented in Table 5.1. Additionally, a weak feature at 1412 cm⁻¹ which has been previously assigned to the dioxymethylene is also observed. In some studies, this band has been assigned to $\delta\text{C-H}$ bending mode of adsorbed formate. Dioxymethylene can be formed by the protonation of bridged bidentate formate.

There is some controversy on some of the band assignments for adsorbed formic acid on oxide particles in the literature. Liao et al. and Rotzinger et al. observed bands at 1385 and 1377 cm⁻¹ and assigned to $\delta\text{C-H}$ of adsorbed formate.^{183,190} Miller et al. and El-Maazawi et al. have assigned this vibration to band at 1323 cm⁻¹.^{181,195} Liao et al. have observed a band at 1323 cm⁻¹ and assigned it to molecularly adsorbed formic acid.¹⁸³ The reason for the controversy can be possibly due to the lower intensity of some of the bands resulting from formic acid adsorption and their multiplicity. Sodium formate solid has a

$\delta\text{C-H}$ band at 1377 cm^{-1} ,¹⁹³ whereas the band for aqueous formate is observed at 1383 cm^{-1} at pH 6.3.¹⁹⁰ Formate adsorption from solution phase to a rutile coating did not show changes in the same band for adsorbed formate.¹⁹⁰ Therefore we assigned band observed at 1385 cm^{-1} to $\delta\text{C-H}$ of adsorbed formate. The band at 1322 cm^{-1} grows simultaneously with the growth of bands for adsorbed bridged bidentate formate (1562 cm^{-1} and 1362 cm^{-1}) and all saturate simultaneously in intensity. That gives an indication that the band at 1322 cm^{-1} is not associated with molecularly adsorbed formic acid. Furthermore, the band at 1322 cm^{-1} does not grow with the bands at 1725 and 1675 which are the most intense bands associated with molecularly adsorbed formic acid. Therefore the band at 1322 cm^{-1} could be related to an adsorbed formate species. Since the bands for bridged bidentate formate are already assigned, this feature could be responsible for a small amount of monodentate formate on the surface.

Following exposure to the highest formic acid pressure, the sample was evacuated at 10^{-7} Torr overnight. The inset of Figure 5.1 shows the spectra obtained after overnight evacuation. The bands for adsorbed formate remained on the surface whereas other bands decrease in intensity indicating higher stability for adsorbed formate after the evacuation relative to other surface species. For example, the intensity of molecularly adsorbed formic acid bands decreases upon evacuation of the gas phase. However, small amounts of molecularly adsorbed formic acid still remain even after the overnight evacuation potentially coordinate to Ti^{4+} sites.

These formic acid reacted nanoparticle surfaces were then exposed to water vapor in increments of increasing relative humidity. Figure 5.3 shows changes in the surface spectra with increasing relative humidity across the percentage relative humidity range

from 0.3 to 79. In these experiments, water vapor was introduced and spectra were recorded after 25 minutes equilibrium. Then water vapor was evacuated for another 25 minutes before introducing the next higher water pressure. These spectra clearly show growth of a band at 1640 cm^{-1} representing the water bending mode associated with adsorbed water as well as a shift in the frequency of absorption bands at 1562 and 1362 cm^{-1} to 1583 and 1338 cm^{-1} for bidentate bridged formate. The wavenumber difference between these two bands is 245 cm^{-1} . This value could differ slightly from the actual value due to the band at 1583 cm^{-1} overlapping with water bending mode at 1640 cm^{-1} and the band at 1338 cm^{-1} overlap with 1322 cm^{-1} . Miller and co-workers observed a 205 cm^{-1} wavenumber difference for monodentate formate after exposing adsorbed bridged bidentate formate to water vapor.¹⁸¹ However, the difference observed in the current study is seen to be much larger. The wavenumber difference observed for aqueous formate at pH 6.3 is 230 cm^{-1} (bands at 1580 and 1350 cm^{-1}).¹⁹⁰ Therefore, the large splitting observed for adsorbed formate in the presence of adsorbed water suggests the adsorbed bridged bidentate formate has both changed its coordination and is also solvated by water molecules. Furthermore, this process is reversible and bridged bidentate formate appears again after water vapor evacuation. This equilibrium behavior with water has been previously observed by Medin and co-workers. They have exposed TiO_2 surface that contained adsorbed formic acid and formate to water saturation pressure and observed the change in adsorbed geometry from bidentate to monodentate.¹⁸¹ Additionally, they have observed that adsorbed formic acid is displaced after exposure to the saturation water vapor pressure. In the current study, we introduced water vapor in increasing relative humidity in order to understand the behavior as a function of relative

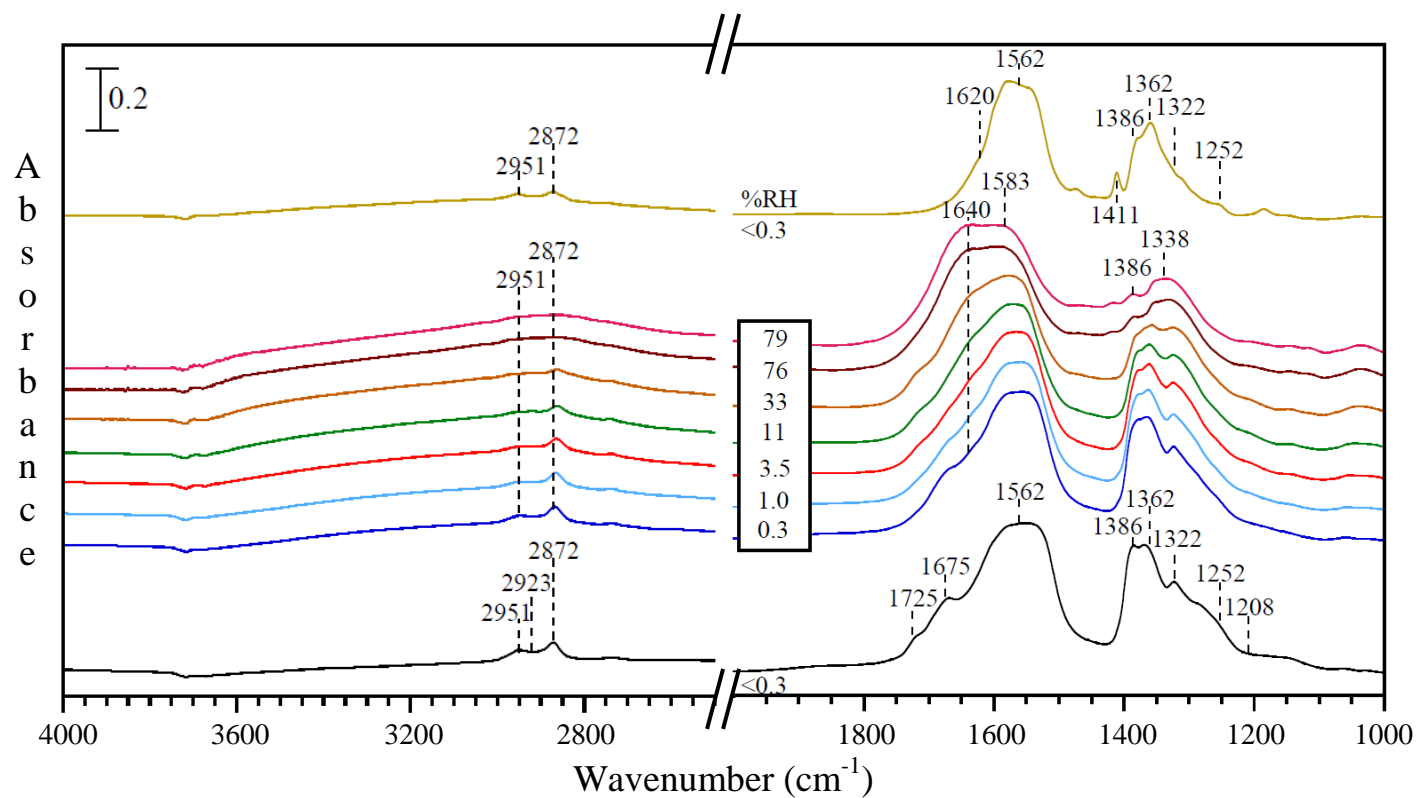


Figure 5.3. FTIR spectra of water uptake on TiO_2 nanoparticles previously reacted with formic acid. Water vapor was introduced with increasing relative humidity between 0.3 and 79% (0.3, 1.0, 3.5, 11, 33, 76 and 79) relative humidity at 296 K. Gas-phase water vapor was evacuated for 25 minutes after each exposure before introducing the next exposure. After exposed to the highest relative humidity the infrared cell was evacuated overnight.

humidity. Absorption bands for molecularly adsorbed formic acid at 2923, 1675, 1257, 1725 and 1208 cm^{-1} are present at lower relative humidity exposures suggesting their stability at low relative humidity environments. However, these bands disappear with increasing relative humidity and do not appear again after water vapor was evacuated. The band at 1412 cm^{-1} became more prominent after exposure to water vapor pressures followed by overnight evacuation, which could be due to the abstraction of protons from water molecules by bidentate formate to form dioxymethylene.

5.4.2 Saturation Coverage and Heterogeneous

Reaction Kinetics

Formic acid saturation coverage was determined using volumetric measurements. The adsorbed volume of the gas was calculated using the equilibrium pressure difference with and without sample after exposure to gas-phase HCOOH . Then the pressure difference was converted to the adsorbed molecules. A plot of adsorbed cumulative molecules vs exposed pressure (P_{exposed}) is shown in Figure 5.4, but a plot of adsorbed molecules vs equilibrium pressure (P_{eq}) was not possible due to overlap of equilibrium pressure for the first three exposures. Figure 5.4 clearly shows the increase in HCOOH adsorption leading to a plateau for adsorbed formate saturation and further molecular adsorption. FTIR spectra discussed above agree with these results and show a saturation

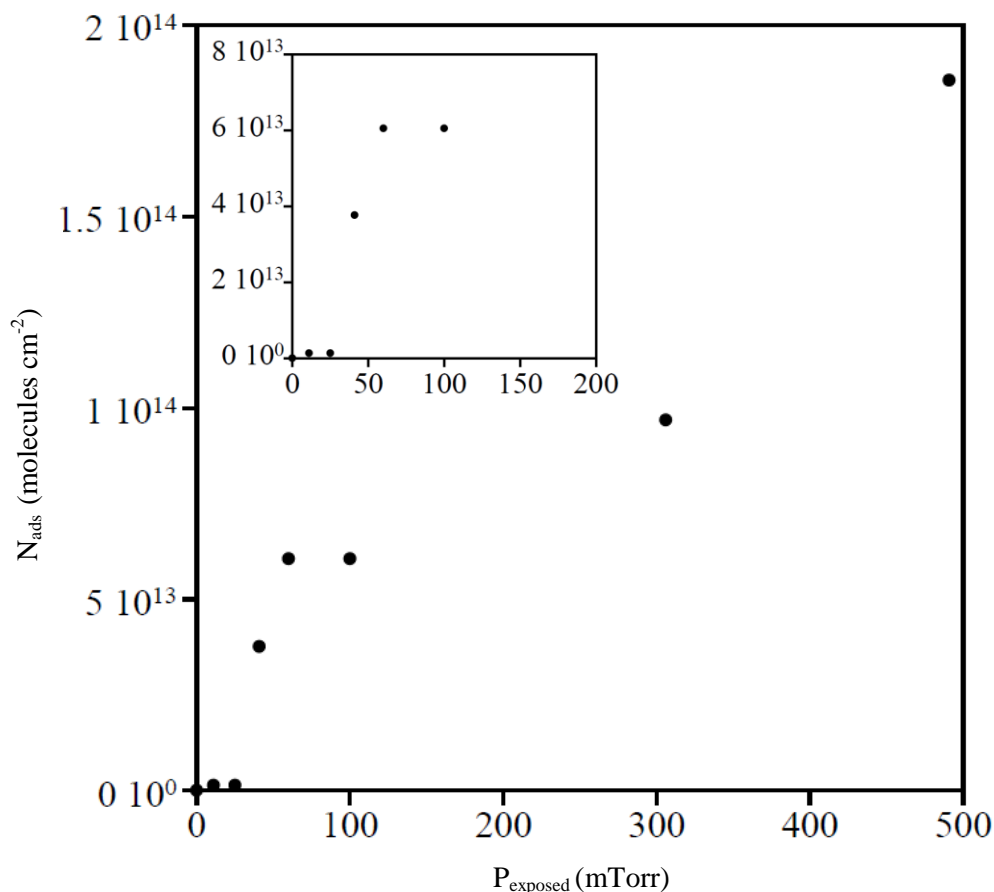


Figure 5.4. The number of formic acid molecules adsorbed on the TiO_2 surface at 296 K as a function of P_{exposed} was determined by volumetric measurements.

of adsorbed formate after exposed to 100 mTorr of gas-phase formic acid. Formic acid exposures higher than 100 mTorr did not show an increase in the intensity of adsorbed formate bands but did show an increase in bands for molecularly adsorbed formic acid. The formate saturation coverage estimated from the Figure 5.4 is ca. 6×10^{14} molecules cm^{-2} . Coverage calculations using volumetric measurements have a higher uncertainty and reported error in previous studies is about 50% due to the gas affinity to the reactor walls. However, this is a good method to get an approximate value for the the coverage and uptake coefficient. Formic acid saturation coverage reported for CaCO_3 was $3 \pm 1 \times 10^{14}$ molecules cm^{-2} using volumetric measurements.¹⁸² Irreversible HCOOH uptake

reported for both alumina and kaolinite using a flow system attached to a quartz crystal microbalance is $3 \pm 1 \times 10^{14}$ molecules cm^{-2} .¹¹¹ Reported formic acid saturation coverage for P25 TiO_2 quantified using temperature programmed desorption was 52 $\mu\text{mol/g}$ and 355 $\mu\text{mol/g}$ corresponding to 6.3×10^{13} molecules cm^{-2} and 4.3×10^{14} molecules cm^{-2} in two separate studies.^{181,198} The value obtained in the current study is close to that of Ref. 111.

The rate of HCOOH uptake on TiO_2 particles was determined by time course experiments. TiO_2 particles were exposed to 11 mTorr of gas phase HCOOH leading to equilibrium pressure of 9 ± 2 mTorr (corresponding to $3.3 \pm 0.7 \times 10^{14}$ molecules cm^{-3}) after 25 minute of exposure. Equilibrium pressure after 25 minutes of exposure without the sample was recorded to determine the adsorbed pressure of the gas. In these experiments, FTIR spectra were recorded with four scans per spectrum at an instrument resolution of 4 cm^{-1} for 1494 total seconds. Spectra collected for HCOOH uptake on TiO_2 as a function of time are shown in Figure 5.5. Formic acid uptake on TiO_2 particles was determined by taking the peak height of band at 1362 cm^{-1} and plotting the peak height versus time as shown in the inset of Figure 5.5. The peak height after 25 minutes was then related to the pressure drop from blank experiments, and this relationship was used to convert the integrated absorbance into the number of adsorbed molecules per surface area.

The heterogeneous uptake of a gas on a solid is most often expressed in terms of an uptake coefficient, γ . Equation 5.3 shows γ as the rate of adsorption divided by rate of gas-surface collisions.

$$\gamma = \frac{\frac{dNa}{dt}}{\text{Flux}} \quad (5.3)$$

$$\text{Flux} = \frac{PN}{(2\pi MRT)^{1/2}} \quad (5.4)$$

The numerator of equation (5.3) is the rate of formation of surface-bound species on the oxide particles upon reaction with HCOOH vapor (units of molecules $\text{cm}^{-2} \text{s}^{-1}$). The denominator is the flux or collision rate per unit area of HCOOH vapor with the oxide particles (units of molecules $\text{cm}^{-2} \text{s}^{-1}$). The flux is calculated according to the kinetic gas theory using equation (5.4), where P is the pressure of HCOOH, N is the Avogadro's number, M is the molecular weight of the gas, R is the gas constant, and T is the temperature.

The rate of formation of surface-bound products was calculated using the slope of the first 120 seconds of the inset in Figure 5.5. The rate calculated was 4.4×10^{-5} peak height s^{-1} which, upon conversion from the calibration, results in a rate of 1.7×10^9 molecules $\text{s}^{-1} \text{cm}^{-2}$. The flux of formic acid calculated using equation (5.4) at exposed pressure of 11 mTorr is 3.3×10^{18} molecules $\text{s}^{-1} \text{cm}^{-2}$. From this, the average uptake coefficient was determined to be $0.5 \pm 2.6 \times 10^{-9}$. Previous studies on formic acid uptake on $\alpha\text{-Al}_2\text{O}_3$ have reported uptake coefficients of $2.37 \pm 0.30 \times 10^{-7}$ and $2.07 \pm 0.26 \times 10^{-3}$ from DRIFTS using BET and geometric surface areas respectively.¹⁹⁶ The two values resulted from BET and geometric surface area have been proposed as lower and upper limits for the uptake coefficient of formic acid.^{196,199} This was explained by the reactive gas molecules being larger in size compared to the nitrogen molecules used for BET surface area measurements and thereby the area accessed by formic acid molecules may be lower than the BET area.

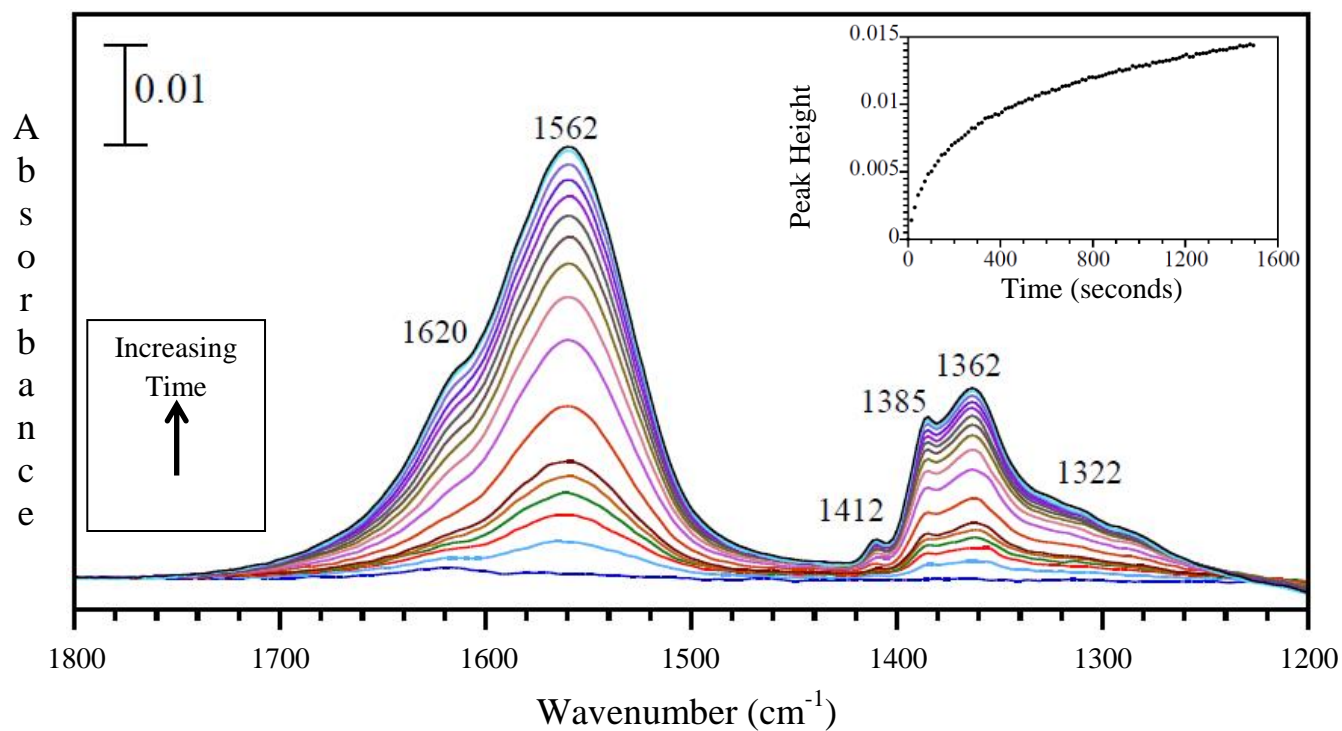


Figure 5.5. Transmission FTIR spectra of formic acid uptake on nanomaterial TiO_2 as a function of time. For clarity, spectra at 0 s, first 5 spectra and every 10th spectrum followed by final spectrum are shown. The peak height for the absorption band for formate at 1362 cm^{-1} is plotted as a function of time using each of the spectra collected.

Formic acid uptake coefficient under dry conditions for CaCO_3 found using Knudsen cell was $3 \pm 1 \times 10^{-3}$. This is orders of magnitude lower than the value obtained here.¹⁸² Ullerstam et al. have studied SO_2 uptake on mineral dust in the presence of NO_2 and found the uptake coefficient (BET) derived using Knudsen cell is $\sim 10^4$ times higher compare to the same from DRIFTS.¹⁹⁹ This has been explained by differences in measured values with the uptake coefficient obtained by Knudsen cell being an initial uptake coefficient whereas from the DRIFTS experiments an overall average reactive uptake coefficients.^{196,199} Similarly, HNO_3 , another acid present in the atmosphere with a similar adsorption mechanism to HCOOH , with uptake coefficients (BET) calculated for CaO , MgO and SiO_2 using Knudsen cell and FTIR system have shown a difference of $\sim 10^4$.²⁰⁰ Hence, the uptake coefficient we report here agrees with the previous findings and can be considered as an average and not an initial reactive uptake coefficient.

5.4.3 Photochemistry of Adsorbed

Formate under a Range of Environmental Conditions

Photochemistry of adsorbed formate was studied under a range of environmental conditions. TiO_2 sample was exposed to 100 mTorr of gaseous formic acid to form adsorbed formate to saturate the surface with adsorbed formate. Additionally, molecularly adsorbed formic acid has shown very fast photocatalytic decomposition in previous studies.¹⁸³ After reaction with formic acid, the sample was evacuated for 25 minutes and the valve of the reaction chamber was closed before irradiation began. Formate coated TiO_2 was irradiated for 6 hours under different environmental conditions.

Figure 5.6 shows the surface spectra of adsorbed formate on TiO_2 particles under different environmental conditions (a) <1% RH and $\text{PO}_2 = 0$ Torr, (b) <1% RH and $\text{PO}_2 = 100$ Torr, (c) 40% RH and $\text{PO}_2 = 100$ Torr and (d) 85% RH and $\text{PO}_2 = 100$ Torr, of water vapor and molecular oxygen. In the absence of water vapor, monodentate formate bands were prominent at time = 0 minute and the intensity of these bands decrease with increasing irradiation time indicating photooxidation of adsorbed formate in Figure 5.6 (a) and (b). Bands for molecularly adsorbed formic acid in Figure 5.6 (a) and (b) disappear more quickly, after 30 minutes of irradiation, agreeing with higher photocatalytic decomposition of molecularly adsorbed formic acid. The presence of molecular oxygen shows further increases the rate of loss of adsorbed formate bands (Figure 5.6 (b)). Band position at 1562 cm^{-1} shift slightly at longer irradiation time that might have resulted due to the decrease in formate band intensity and its overlapping with band at 1620 cm^{-1} resulted from water formed during the formic acid adsorption. In Figure 5.6 (c) and (d), bands for bridged bidentate formate are prominent at time = 0 minutes before irradiation. The intensity of absorption bands associated with bridged bidentate formate decreases significantly in Figure 5.6 (c) and (d) with increasing irradiation time suggesting further enhancement of adsorbed formate photooxidation by water vapor in the presence of oxygen.

Irradiation resulted in gas-phase CO_2 as the main product. Figure 5.7 shows the integrated absorbance of the CO_2 peak with irradiation time in three different relative humidities of <1%, 40% and 85% in the presence of 100 Torr molecular oxygen. Figure 5.8 contains the FTIR spectra of gas-phase carbon dioxide formation upon irradiation under these conditions. Figure 5.7 contains the carbon dioxide formation without

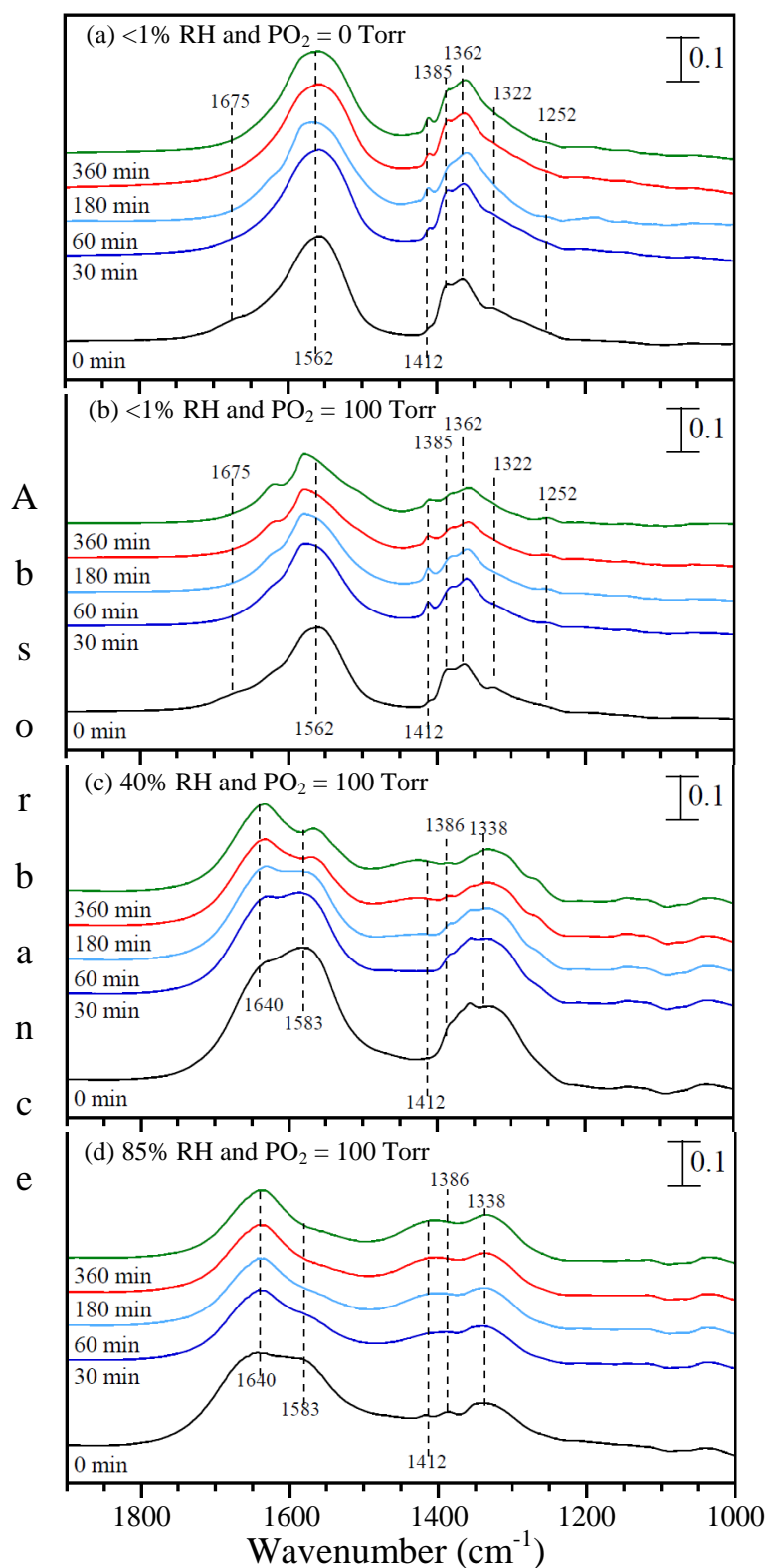


Figure 5.6. Surface spectra of adsorbed formate on TiO_2 particles following UV irradiation as a function of time under different environmental conditions (a) <1% RH and $\text{PO}_2 = 0$ Torr, (b) <1% RH and $\text{PO}_2 = 100$ Torr, (c) 40% RH and $\text{PO}_2 = 100$ Torr and (d) 85% RH and $\text{PO}_2 = 100$ Torr.

molecular oxygen and water vapor under irradiation for comparison. UV irradiation of TiO_2 forms electron/hole pairs in the conduction and valence bands according to reaction (5.5). It has been proposed that formate photooxidation is initiated by reaction with photogenerated holes as reported by several studies leading to several reactions producing carbon dioxide and water.^{186,201,202} Figure 5.7 shows an increase in CO_2 production in the presence of molecular oxygen, with a ~ 3.5 increase in the presence of 100 Torr of molecular oxygen. This could be due to the reaction of photogenerated electrons with O_2 molecules, thereby decreasing the electron hole recombination which leads to more formate photooxidation according to reaction (5.6), (5.7) and (5.8).

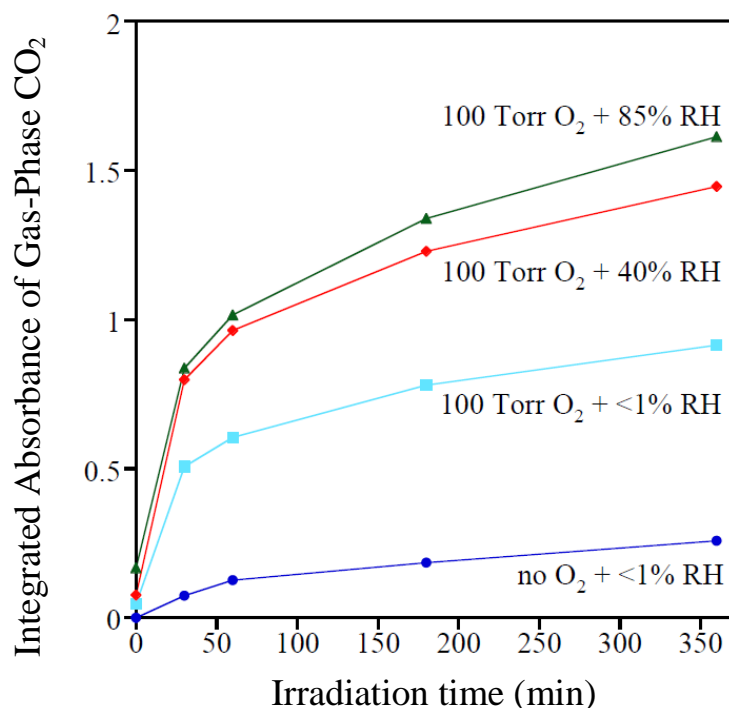


Figure 5.7. Comparison of CO_2 formation during formate photooxidation. Integrated absorbance between $2280 - 2400 \text{ cm}^{-1}$ of the gas-phase CO_2 peak was used for the comparison.

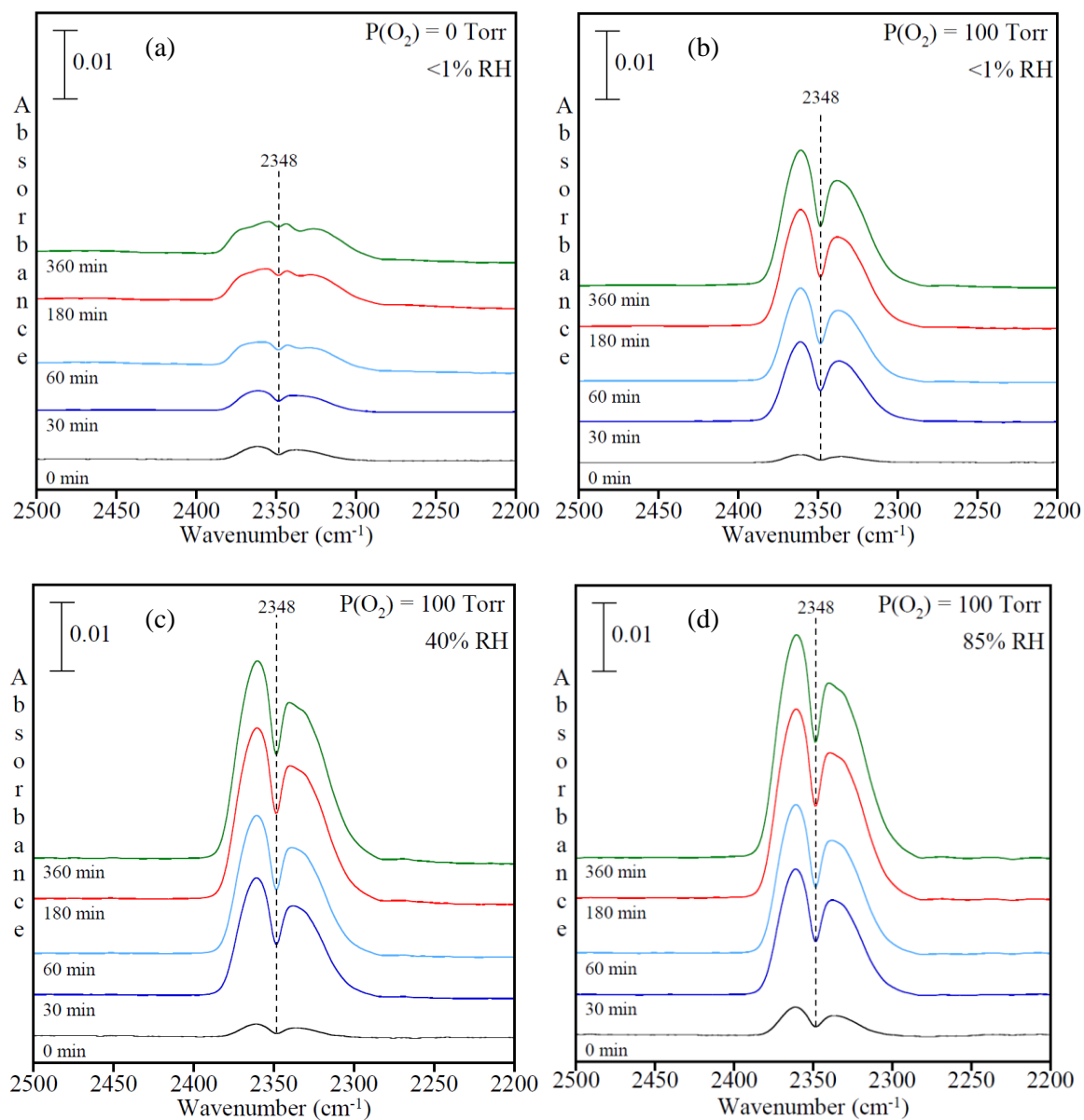
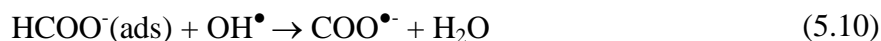


Figure 5.8. FTIR spectra of gas-phase carbon dioxide formation upon irradiation of adsorbed formate in the absence and presence of molecular oxygen under different relative humidity conditions of (a) $<1\%$ RH and $P(\text{O}_2) = 0$ Torr, (b) $<1\%$ RH and $P(\text{O}_2) = 100$ Torr, (c) 40% RH and $P(\text{O}_2) = 100$ Torr and (b) 85% RH and $P(\text{O}_2) = 100$ Torr.

Carbon dioxide production increased an additional ~1.6 times in the presence of 40% and 1.8 times at 85% RH compared to <1% RH all in the presence of 100 Torr of oxygen. Agreeing with these results, Liao et al. observed a doubling of the CO₂ production with 1 Torr water vapor pressure in the presence of 10 Torr molecular oxygen.¹⁸³ In the present study, the focus was on the change in gas phase water vapor pressure on photooxidation of formate in order to better understand the behavior of adsorbed organic acids under atmospherically relevant conditions. The results show that under atmospherically relevant conditions, CO₂ formation increases with increasing relative humidity from 40% to 85%. The increase in gas phase CO₂ formation can be explained by series of reactions. In the presence of water vapor, H₂O molecules react with holes generating H⁺ and OH[•] radicals according to reaction (5.9) and OH[•] can further react with adsorbed formate enhancing the overall carbon dioxide production (5.10). Newly formed H⁺ can react with O₂⁻, scavenging more electrons, resulting in adsorbed water according to reaction (5.11). Our experimental results and previous studies showed the bridged bidentate to solvated monodentate transformation of adsorbed formate in the presence of water vapor. Miller et al. computationally showed presence of monodentate formate and adsorbed water increases the conduction band minimum enough to favor reaction (5.6).¹⁸⁶ This will make carbon dioxide formation favorable in the presence of water vapor.

To summarize the above discussion, gas-phase CO₂ can be formed according to reactions (5.5) – (5.10) under environmentally relevant conditions.



5.4.4 Aqueous Phase Behavior of Formic

Acid Reacted Nanomaterial TiO_2

As discussed in the Introduction, unreacted and formate coated TiO_2 samples were introduced to water to investigate the possible changes on aqueous phase behavior of TiO_2 nanoparticles upon reaction with gas-phase formic acid. Formate coated samples were prepared by reacting TiO_2 particles with gas-phase formic acid followed by gas-phase evacuation. Reacted sample was then removed from the tungsten grid and suspension was prepared with a 0.035 g/L (0.7 mg/20 ml) solid loading. Dynamic light scattering (DLS) of the reacted and unreacted suspensions were measured. The DLS plot in Figure 5.9 shows smaller aggregate size for formate coated compare to unreacted TiO_2 . This can be due to the adsorbed bridged bidentate formate solvation resulting solvated monodentate formate that increases surface charge resulting smaller TiO_2 aggregates.

Schematic in Figure 5.10 summarizes the findings of the current study. In summary formic acid adsorption results mainly adsorbed bridged bidentate formate. Adsorbed

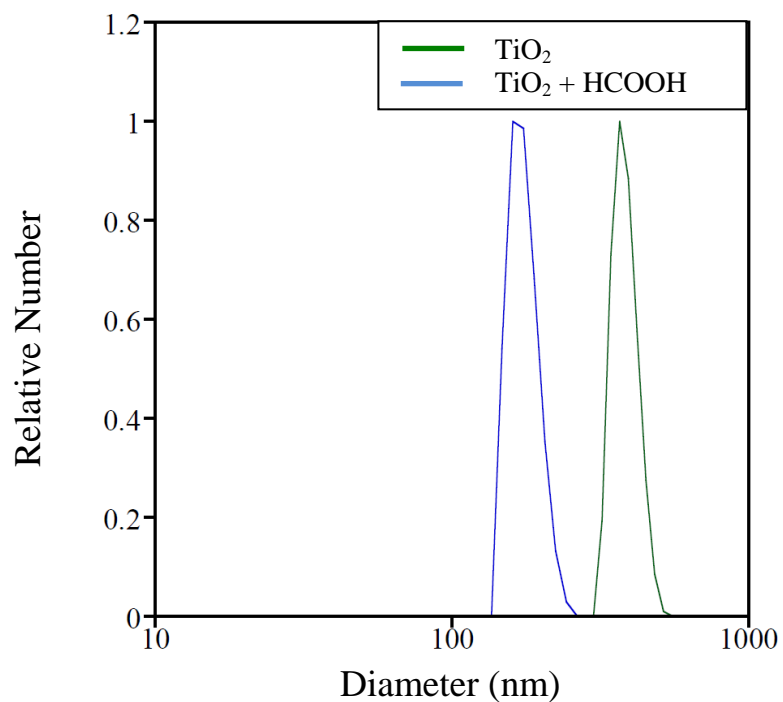


Figure 5.9. Intensity normalized aggregate distribution of unreacted and TiO_2 particles previously reacted with gas-phase formic acid.

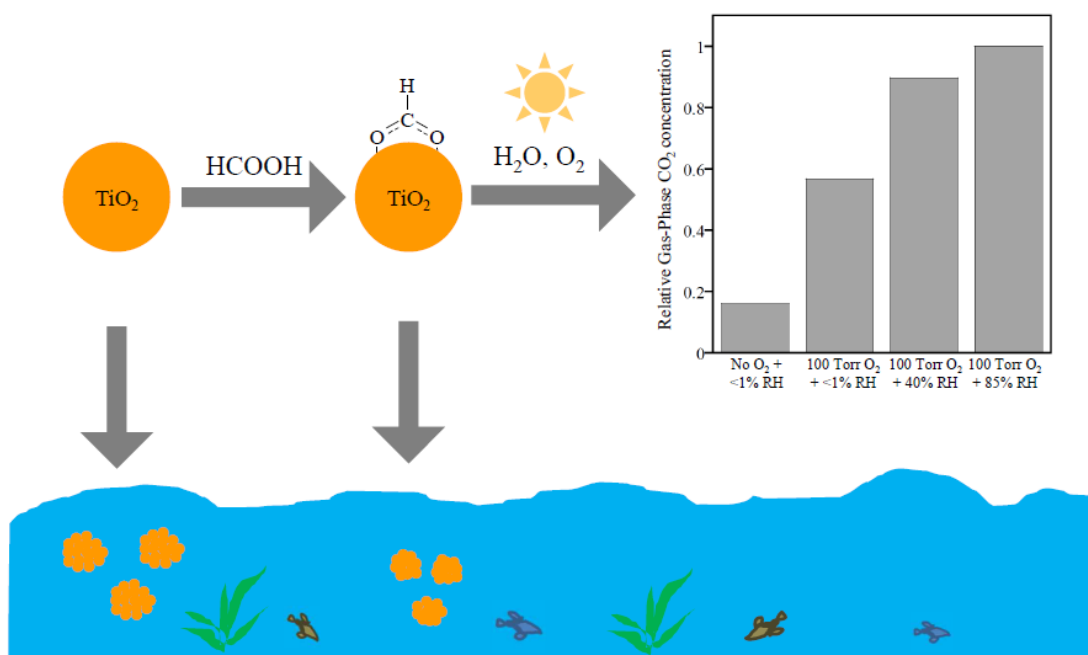


Figure 5.10. Schematic representation of formic acid adsorption, phototoxidation and solution phase behavior of TiO_2 nanoparticles.

formate photooxidize to gas-phase carbon dioxide in the presence of water vapor and molecular oxygen. Additionally, reaction with formic acid changes the solution phase aggregate formation of TiO_2 nanoparticles.

5.5 Conclusions and Atmospheric Implications

The adsorption of formic acid with TiO_2 nanoparticles, 10 nm in diameter, and the photooxidation of the resultant adsorbed formate were investigated. These results showed gas-phase formic acid adsorbs dissociatively on TiO_2 forming adsorbed formate mainly in bridged bidentate coordination. Co-adsorbed water changes the coordination of formate to solvated, monodentate formate. The calculated reactive uptake coefficient agrees with the previously reported values for other atmospherically relevant surfaces. Coadsorbed water have shown an enhance in formic acid uptake. Higher relative humidity conditions in the presence of molecular oxygen showed enhanced formate photooxidation. According to these findings, more formate conversion under tropospheric conditions can be expected during daytime. Furthermore, solution phase behavior of formic acid reacted TiO_2 was investigated. These results show that TiO_2 nanoparticle dispersion into aqueous suspensions differ upon reaction with formic acid. These oxide nanoparticles with formate coatings can be more readily dispersed into water systems.

Acknowledgment

This material is based on the work supported by the National Science Foundation under grant CHE-1305723. Any opinions, findings and conclusions or recommendations

expressed in this material are those of the authors and do not necessarily reflect the views of the National Science Foundation.

CHAPTER 6

SURFACE PHOTOCHEMISTRY OF ADSORBED NITRATE: THE ROLE OF
ADSORBED WATER IN THE FORMATION OF REDUCED NITROGEN SPECIES
ON α -Fe₂O₃ PARTICLE SURFACES

6.1 Abstract

The surface photochemistry of nitrate, formed from nitric acid adsorption, on hematite (α -Fe₂O₃) particle surfaces under different environmental conditions is investigated using X-ray photoelectron spectroscopy (XPS). Following exposure of α -Fe₂O₃ particle surfaces to gas-phase nitric acid, a peak in the N1s region is seen at 407.4 eV; this binding energy is indicative of adsorbed nitrate. Upon broadband irradiation with light ($\lambda > 300$ nm), the nitrate peak decreases in intensity as a result of a decrease in adsorbed nitrate on the surface. Concomitant with this decrease in the nitrate coverage, there is the appearance of two lower binding energy peaks in the N1s region at 401.7 and 400.3 eV, due to reduced nitrogen species. The formations as well as the stability of these reduced nitrogen species, identified as NO⁻ and N⁻, are further investigated as a function of water vapor pressure. Additionally, irradiation of adsorbed nitrate on α -Fe₂O₃ generates three nitrogen gas-phase products including NO₂, NO, and N₂O. As shown here, different environmental conditions of water vapor pressure and the presence of molecular oxygen greatly influence the relative photoproduct distribution from nitrate surface photochemistry. The atmospheric implications of these results are discussed.

6.2 Introduction

Nitrate ion is an important chromophore and can undergo photochemical reactions on the surface of atmospheric aerosols,¹²⁰ deliquesced thin films,²⁰³ ice/snow²⁰⁴⁻²⁰⁷ and in solution.²⁰⁸⁻²¹⁰ Nitrate ion has an absorption maximum at 302 nm ($\epsilon=7.2 \text{ mol dm}^{-3} \text{ cm}^{-1}$) in aqueous solution.²¹¹ In the atmosphere, gas-phase nitrogen oxides readily react with particulate matter (e.g., mineral dust) to yield adsorbed nitrate. Atmospheric nitric acid is the main reservoir species in the NO_x cycle. Heterogeneous reactions and possible renoxification mechanisms of tropospheric HNO₃ acid have been widely studied on different environmental interfaces and surfaces.²¹²⁻²¹⁷ Mineral dust aerosols act as a reactive surface for atmospheric nitric acid adsorption and photochemical reactions of adsorbed nitrate.

The photochemistry of adsorbed nitrate, formed by either exposure to NO₂ or HNO₃ has been widely studied on the surface of components of mineral dust aerosol.^{23,100,102,218} Photoexcitation of adsorbed nitrates forms several gas-phase products like N₂O, NO and NO₂ and HONO.^{100,102,219} For example, transmission FTIR studies of HNO₃ reacted γ -Al₂O₃ particles observed gas-phase NO and NO₂ formation as the main gas-phase products upon irradiation with $\lambda > 300 \text{ nm}$ light.¹⁰² Irradiation of HNO₃ reacted in NaY zeolite showed formation of nitrite thought to be stabilized in the zeolite cage due to interactions with the charge compensating cation.²¹⁸ Additionally, some recent studies on NO₂ adsorption and photochemistry on semiconductor metal oxides such as Cr₂O₃ and TiO₂ have shown conversion of adsorbed nitrate to gas-phase NO_x species under irradiation conditions.^{23,100,168} These studies used chemiluminescence, mass spectrometry and infrared spectroscopy as tools to detect gas-phase photoproducts and infrared

spectroscopy and X-ray photoelectron spectroscopy to detect adsorbed photoproducts as well. For adsorbed species, it is sometimes difficult to differentiate products due to the fact that there are overlapping absorption bands for different species that contain N-O functional groups.^{21,158} X-ray photoelectron spectroscopy (XPS), however can detect adsorbate which differ in the oxidation state of nitrogen atom. In this study XPS is used to investigate the surface photochemistry of nitrate adsorbed on hematite particle surfaces.

Hematite is one of the most common iron oxide polymorphs present in the earth's crust. Iron-containing particles are transferred to the atmosphere from both wind and volcanic activities in the form of iron containing mineral dust and volcanic ash aerosols.⁶ Hematite is a semiconductor material with a lower band gap of 2.2 eV that can absorb solar radiation and has the potential to alter nitrate photochemistry pathways.²²⁰ Therefore, understanding both gas-phase and surface processes that occur on nitrate adsorbed on hematite is important to further understand atmospheric processes. Fe dissolution from iron-containing atmospheric particles has received much attention recently due to atmospheric aging is thought to play a role.¹⁶⁸ In this study, photochemistry of adsorbed nitrate on hematite, α -Fe₂O₃ surface is investigated under environmentally relevant relative humidity and molecular oxygen by XPS and FTIR spectroscopic techniques. The impact that this reaction has on iron dissolution is also investigated.

6.3 Experimental Methods

6.3.1 Surface XPS Analysis Chamber Coupled with

Transfer and Reaction Auxiliary Chambers

The custom-designed Kratos Axis Ultra X-ray photoelectron spectroscopy system for reactions and analysis has been described in detail before.¹¹⁸ For these experiments it was modified to accommodate an additional Teflon coated reaction chamber for HNO₃ reaction experiments and UV source for photochemistry experiments.^{94,117,118} The experimental setup has capabilities for reacting samples with gas-phase reactants and evacuating the gas-phase and surface product analysis with four different chambers that include: (i) an ultra high vacuum (UHV) surface analysis chamber, (ii) a sample transfer antechamber, (iii) a stainless steel reaction chamber and (iv) a Teflon coated reaction chamber (Figure 6.1). The transfer antechamber is connected to the analysis chamber, steel reaction chamber and Teflon coated reaction chamber. With this configuration, the transfer antechamber is used to introduce samples into the analysis chamber, and also allows for samples to be transferred directly from the surface analysis chamber to the reaction chambers vice versa.

The Teflon coated reaction chamber is connected to the transfer antechamber. The details of the stainless steel reaction chamber have been described before.¹¹⁸ Additionally, a 500 W Hg lamp (Oriel Instruments model number 66033) was used to irradiate the samples in the steel reaction chamber. A water filter (Oriel Instruments) was used in line with the lamp output to minimize infrared damage and heating of the sample. The light from the lamp was reflected using a 90° turning mirror (Oriel Instruments, Model: 66215 Beam Turning Mirror, Full Reflector, 200 nm – 30 μm

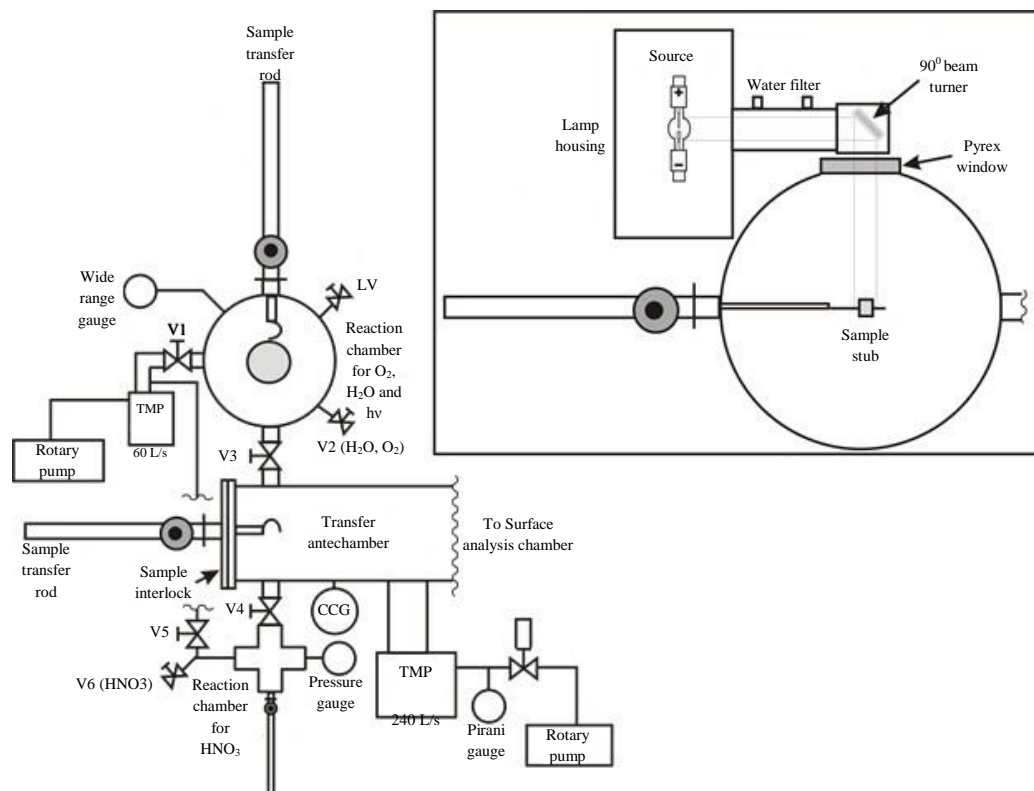


Figure 6.1. Schematic of the custom-designed Kratos Axis Ultra XPS system with UV irradiation setup. The system consists of four chambers: a transfer antechamber, surface analysis chamber (not shown), reaction chamber and Teflon coated HNO_3 reaction chamber. A cross section of the $\text{O}_2/\text{H}_2\text{O}$ reaction chamber equipped with the UV source and beam optics is shown in the inset. See experimental methods section for a more detailed description of this four chamber system. (Note: TMP – turbomolecular pump; CCG – cold cathode gauge; LV – leak valve and V – valve).

Primary Range, 1.5 Inch Series) into the reaction chamber via the Pyrex window. The transmissivity of the Pyrex window was ~80% at the wavelengths above ~320 nm with a 0.72 W/cm^2 measured light intensity at the sample.

For typical XPS analysis, powdered samples were pressed into indium foil and mounted onto a copper stub. After acquiring the initial scans at the surface analysis chamber, the sample was transferred to the Teflon coated chamber via the transfer antechamber by means of sample transfer rod and a hand valve. The sample was then reacted with HNO_3 . HNO_3 reacted $\alpha\text{-Fe}_2\text{O}_3$ surfaces were evacuated and transferred to the sample analysis chamber for initial scans. The evacuation removes molecularly adsorbed HNO_3 . After the initial scans, samples were transferred to the steel reaction chamber for reactions under environmentally relevant conditions of (1) H_2O , (2) O_2 , (3) $\text{H}_2\text{O/O}_2$ and UV light. No gas phase HNO_3 was present in the chamber during those reactions. Reactant gas was introduced in approximately 15 seconds. The resulting gas mixture was allowed to equilibrate with the sample for at least 30 minutes. The reacted sample was then evacuated and transferred back to the analysis chamber for post-reaction surface characterization.

6.3.2 Data Processing of Core Photoelectron Spectra

All spectra were calibrated using the adventitious C1s peak at 285.0 eV. A Shirley-type background was subtracted from each spectrum to account for inelastically scattered electrons that contribute to the broad background. CasaXPS software was used to process the XPS data.¹¹⁹ The N1s transition was fit to one peak with a fixed full-width-at-the-half-maximum (FWHM) value of 1.4 eV that of HNO_3 . The components of the

peaks contain a Gaussian/Lorentzian product with 30% Lorentzian and 70% Gaussian character. An error of ± 0.2 eV is reported for all peak binding energies.

6.3.3 Transmission FTIR Spectroscopy

For FTIR measurements, the α -Fe₂O₃ particles were prepared by pressing onto half of a tungsten grid (Buckbee Mears, 100 lines per inch tungsten mesh wire widths of ~ 0.0015 in. and thickness of ~ 0.002 in.). The other half of the grid was left blank for gas-phase measurements. The grid half coated with the oxide powder was placed inside the infrared cell. The inside of the stainless steel cube is coated with Teflon in order to avoid HNO₃ decomposition on the walls of the infrared cell. The oxide samples prepared on the tungsten grid are secured inside the infrared cell by Teflon coated sample holder jaws. The infrared cell is connected to a vacuum chamber through a Teflon tube and two consecutive glass gas manifolds with ports for gas introduction and two absolute pressure transducers. Details of the experimental system have been described before.¹⁰¹ Typically, 250 scans were collected with an instrument resolution of 4 cm^{-1} in the spectral range from 4000 to 750 cm^{-1} . Absorbance spectra for gas and adsorbed species were obtained by referencing single beam spectra of the blank grid and the oxide coated grid to single beam spectra collected prior to gas exposure.

6.3.4 Iron Dissolution Experiments

Iron Dissolution Experiments. HNO₃ reacted α -Fe₂O₃ particles were prepared in a Teflon coated reaction chamber by reacting with HNO₃ to investigate the effect of HNO₃ on Fe dissolution. Reacted particles were suspended in optima water (Sigma Aldrich) at a

mass loading of 30 mg/50 mL. The suspension was stirred for 24 h. The stability of unreacted and reacted particle suspensions were measured using the sedimentation plots by measuring the extinction with a Perkin-Elmer Lambda 20 UV-visible spectrometer at 510 nm. Iron dissolution was studied for both unreacted and HNO₃ reacted α -Fe₂O₃. Aliquot from the supernatant suspension was passed through a 0.2 μ m PTFE filter to remove particles. The concentration of iron was measured using Varian 720-ES inductively coupled plasma-optical emission spectrometer (ICP-OES). Dissolution of unreacted α -Fe₂O₃ was also conducted under the same conditions for comparison. All experiments were conducted in triplicate.

6.3.5 Characterization of α -Fe₂O₃

X-ray diffraction (XRD), scanning electron microscopy (SEM) and BET surface area analyzer were used to characterize the α -Fe₂O₃ samples.

6.3.6 Sources of Chemicals

Dry gaseous nitric acid was taken from the vapor of a 1:3 mixture of concentrated HNO₃ (70.6% HNO₃, Mallinckrodt) and 95.9% H₂SO₄, (Mallinckrodt). For relative humidity studies, distilled H₂O (Milli-Q) was used. Prior to use, both the distilled water and HNO₃ were degassed several times with consecutive freeze-pump-thaw cycles. Oxygen (UPC grade) was obtained from Airgas. Hematite (α -Fe₂O₃, Alfa Aesar, α -phase, 99% metal basis) was used as received.

6.4 Results and Discussions

6.4.1 Characterization of α -Fe₂O₃

The average particle size of α -Fe₂O₃ was determined by scanning electron microscopy (SEM) and shows particles with diameter of 310 ± 22 nm (200 particles counted). Figure 2.8(a) shows an SEM image of the α -Fe₂O₃ particles used. Surface area measurements using BET analysis showed a specific surface area of 23 ± 2 m²/g. X-ray diffraction pattern of α -Fe₂O₃ shown in Figure 2.8(b) agrees well with the standard pattern for hematite.

6.4.2 XPS of Metal-nitrogen Salt Standards

In order to establish characteristic binding energies that may help to identify surface species generated from HNO₃ adsorption on α -Fe₂O₃ surfaces, the results of previously measured N1s binding energies for nitrogen containing salts were used here. In particular, a single peak at 407.4 eV was observed for NaNO₃ and was assigned to the N1s transition in nitrate ion (NO₃⁻) and similarly a single peak was observed in N1s region for NaNO₂ at 403.6 eV, assigned to N1s transition in adsorbed nitrite (NO₂⁻).¹¹⁸ Torres et al. has reported that N1s peak of iron nitride (FeN) appeared at 397.4 eV.²²¹ These three reference compounds encompass a full range of N1s binding energies for HNO₃ reaction product related compounds, as nitrogen oxidation state changes from +5 on NaNO₃ to -3 in FeN thus accounting for all possible nitrogen oxidation states. The binding energy decreases with the decrease in the nitrogen oxidation state due to the increase in number of electrons as well as the electron-electron repulsion.

6.4.3 XPS of HNO₃ Acid Reacted α -Fe₂O₃ in the Presence of Environmentally Relevant Pressures of Relative Humidity and Molecular Oxygen

The high-resolution spectra of Fe2p, O1s and N1s binding energy regions of unreacted and α -Fe₂O₃ reacted with HNO₃ for 25 minutes are shown in Figure 6.2. Assignments of the observed peaks in the different binding energy regions are given in Table 6.1 with values reported for reference compounds and previous literature assignments. Photoelectrons emitted within the Fe2p region of unreacted α -Fe₂O₃ are at

Table 6.1. Assignment of Binding Energies for N1s, O1s and Fe2p Transitions Observed in this Study.

Region	Assigned species	Binding Energy, eV	
		This work	Literature reference
N1s	NO ₃ ⁻	407.4	407.4 (NaNO ₃) Baltrusaitis et al.; 407.6 (NO ₃ ⁻) Aduru et al. and references therein
	NO ₂ ⁻	not observed	403.6 (NaNO ₂) Baltrusaitis et al. and 403.7 (NO ₂ ⁻) Bandis et al.
	NO ⁻	401.7	401.7 (NO ⁻) Baltrusaitis et al.; 402.6 (NO ⁻) Overbury et al.
	atomic N ⁻ on defect sites	400.3	400.3 (N ⁻) Baltrusaitis et al.; 400.5 (anionic N at defects) Overbury et al.; 400.8 (atomic N) Rosseler et al.;
	N ³⁻	not observed	397.3 (FeN) Taylor et al.; 397.4 Torres <i>et al.</i>
O1s	lattice O in α -Fe ₂ O ₃	530.0	529.8 Baltrusaitis et al.
	Chemisorbed NO ₃ ⁻	532.5	531.3 Rodriguez et al.
Fe2p	lattice Fe in α -Fe ₂ O ₃	Fe2 _{p3/2} : 711.2 and Fe 2 _{p1/2} : 724.7	Fe 2 _{p3/2} : 710.8 and Fe 2 _{p1/2} : 724.4 Baltrusaitis et al.

Note: Calibrated to the C1s peak at 285.0 eV, Source: Assignments from 105

binding energies of 711.2 and 724.7 eV which correspond to $\text{Fe}2_{\text{p}3/2}$ and $\text{Fe}2_{\text{p}1/2}$. In the O1s region, photoelectrons at 530.0 and 531.6 eV were observed for the unreacted surface. These are assigned to Fe-O in $\alpha\text{-Fe}_2\text{O}_3$ lattice structure and surface hydroxyl groups, respectively. Upon reaction with HNO_3 , formation of adsorbed nitrate is observed as well as seen by a new peak in the N1s region. Additionally, there are observed shifts in the O1s and Fe2p levels by ~ 0.5 eV and ~ 0.7 eV, respectively as a result of strong electrostatic interaction between nitrate and the hematite surface. The peak appearing at 532.5 eV in the O1s region after reacting with HNO_3 can be assigned to the oxygen atoms in adsorbed nitrate. A similar peak has been assigned to the chemisorbed nitrate by Rodriguez et al. for NO_2 reacted $\text{TiO}_2(110)$ surface.²²² The high resolution N1s spectrum of HNO_3 reacted $\alpha\text{-Fe}_2\text{O}_3$ can be curve fit with one component corresponding to the 407.4 eV peak that is assigned to nitrate ion (NO_3^-), adsorbed on the surface. The binding energy of this peak can be confirmed by the binding energy of NaNO_3 .¹¹⁸ The formation of adsorbed NO_3^- species can be written as follows;



Nitrate formation is governed by dissociative HNO_3 adsorption with NO_3^- occupying Fe sites and dissociated proton on lattice oxygen sites according to Reaction (6.1). Another possible adsorption mechanism is surface hydroxyl groups react with HNO_3 forming adsorbed nitrate and water. Bands for newly formed water or hydroxyl groups were not readily apparent due to overlap with oxygen band of adsorbed nitrate in O1s

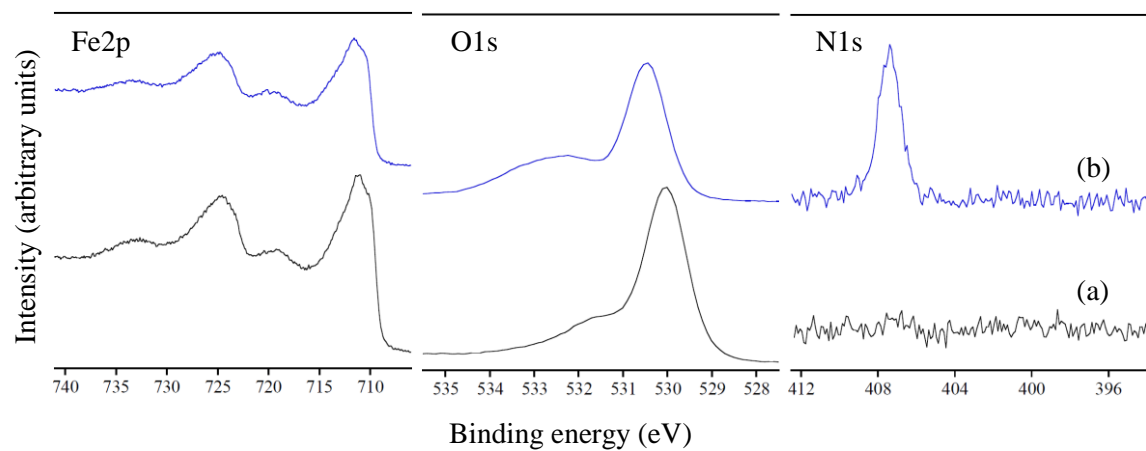


Figure 6.2. High-resolution X-ray photoelectron spectra of α -Fe₂O₃ particles in the Fe2p, O1s and N1s binding energy regions (a) prior to and (b) after saturation exposure of HNO₃.

region of HNO_3 reacted $\alpha\text{-Fe}_2\text{O}_3$ as shown in Figure 6.2. The dissociative adsorption of HNO_3 acid is presumably an exothermic process and thus thermodynamically favorable process on hematite surface. Upon HNO_3 adsorption no features were observed around 403 eV or 406 eV region to surface nitrite (NO_2^-) or molecularly adsorbed NO_2 species. Formation of such species have been observed in various oxide surfaces including hematite when reacted with NO_2 .^{23,118,161,223}

Further experiments were performed by adsorbing HNO_3 on $\alpha\text{-Fe}_2\text{O}_3$ particles and then subsequently exposing this reacted surface to various conditions, i.e. under dry conditions %RH<1 and without O_2 and with 100 Torr of O_2 as well as 45 %RH without and with 100 Torr of O_2 . Upon post-analysis with XPS, no new peaks or change in the binding energy observed in the N1s upon subjecting HNO_3 reacted $\alpha\text{-Fe}_2\text{O}_3$ particles for 30 minutes under each of these different environmental conditions.

6.4.4 Nitrate Photochemistry on $\alpha\text{-Fe}_2\text{O}_3$ in the Presence of Environmentally Relevant Pressures of Water Vapor and Molecular Oxygen

In order to understand the photochemistry of adsorbed nitrate on $\alpha\text{-Fe}_2\text{O}_3$ particle surfaces following reaction with nitric acid, the surface was irradiated and high resolution XPS analysis was performed. The high-resolution spectra in the N1s binding energy region of $\alpha\text{-Fe}_2\text{O}_3$ reacted with HNO_3 and then irradiated with UV light ($\lambda > 300$ nm) for 90 minutes are shown in Figure 6.3. These experiments were performed under different levels of molecular oxygen and water vapor. XPS in the N1s showed only the binding energy peak corresponding to surface nitrate at 407. 4 eV, but with a decreased intensity

following UV exposure time indicating loss of surface bound nitrate. However, when nitrate was irradiated with UV radiation in the presence of water vapor a broad feature appeared at low binding energy region of Figure 6.3 (c) and (d) and there is also a more significant decrease in the intensity of nitrate peak (*vide infra*). This broad low binding energy feature was fit to two components, a peak centered at 401.7 and another 400.3 eV.

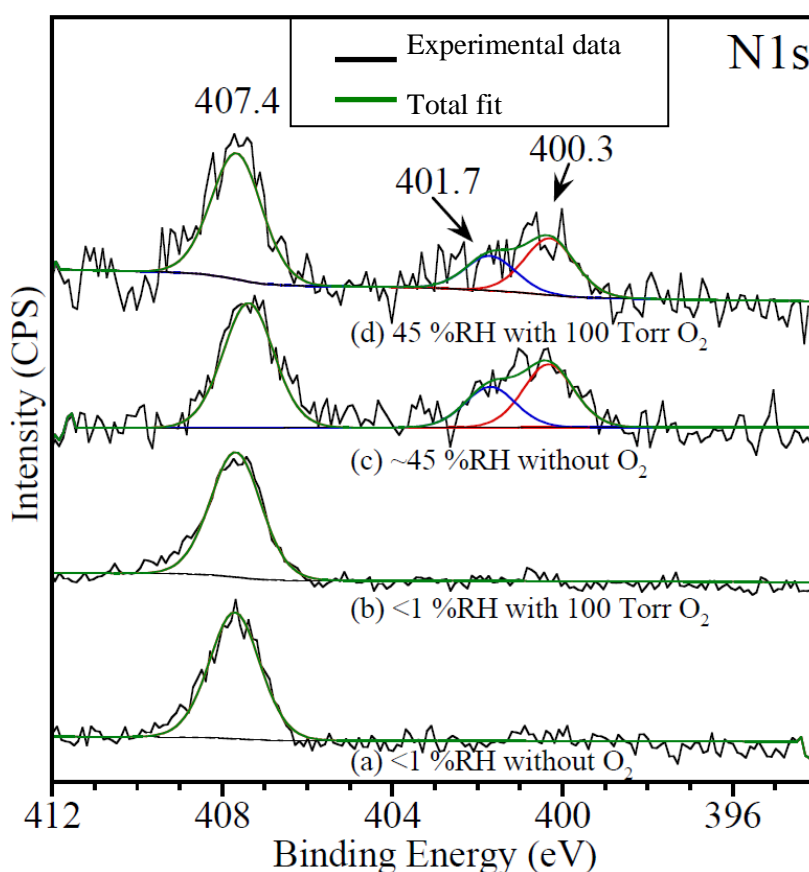
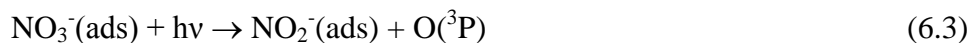
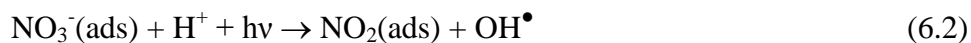


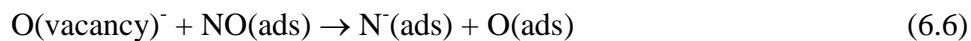
Figure 6.3. High resolution X-ray photoelectron spectra of α -Fe₂O₃ particles in the N1s binding energy regions following exposure to HNO₃ to saturation coverages and subsequent UV irradiation for 90 minutes in the presence and absence of water vapor and molecular oxygen. (a) %RH < 1 without O₂, (b) %RH < 1 with 100 Torr O₂, (c) %RH = 45 without 100 Torr O₂, (d) %RH = 45 with 100 Torr O₂ at T = 296 K. Black and green lines represent the experimental data acquired and the total fit respectively. Surface species obtained by peak fitting are shown in red and blue lines. The fitted curve for nitrate peak overlaps with the total fit.

The exact binding energy assignment of reduced nitrogen species between 402 – 399 eV has been controversial as the surface binding sites can change the binding energy slightly. Baltrusaitis and co-workers have discussed these differences in detail and used computational analysis to assign these two features at 401.7 and 400.3 eV to NO^- and N^- , respectively.¹¹⁸

In previous studies, the photochemistry of adsorbed nitrate and formation of NO has been observed using FTIR spectroscopy in the presence of UV light via short lived NO_2 and/or NO_2^- species according to the reactions (6.2) to (6.4).¹⁰²



The newly formed adsorbed NO and NO_2 can desorb into the gas phase. Photolysis of adsorbed nitrate on alumina reported NO and NO_2 as the major gas phase species.¹⁰² It has also been shown that NO has a relatively high electron affinity and can easily trap free electron thus forming a negatively charged NO^- anion adsorbed on metal cationic sites on the surface according to reaction (6.5) resulting band at 401.7 eV.¹¹⁸



In addition, adsorbed NO can decompose on some surfaces to produce atomic N and O on the surface as reported by NO₂ adsorption studies on Mo(110) by Jirsak et al.²²⁴. In another study, adsorbed NO conversion to N₂O through an atomic N intermediate has reported by Yates and co-workers on TiO₂ surfaces.²²⁵ Rosseler et al. have observed a band at 400.8 eV for NO₂ adsorption on TiO₂ studies and have assigned to reduced N. Overbury et al. have observed a band at 400.5 eV that they have claimed to anionic N species that have resulted from NO decomposition which then had charge transferred to nitrogen atom leading to N⁻.²²⁶ Iron oxide surfaces have been reported as materials rich with oxygen vacancies. Higher population of point defects have been reported for hematite surface compared to the bulk.²²⁷ Furthermore, oxygen vacancies on other semiconductor surfaces like TiO₂ have shown negative charge associated with trapped electrons and similar sites has been proposed on iron oxide surfaces in previous studies.^{94,228} The electrons generated from band gap excitations of hematite can be trapped in oxygen vacancy sites and increase the availability of negatively charged oxygen vacancy sites. Therefore, in the current study, newly formed NO decomposition on negatively charged O vacancy can be expected resulting N⁻ according to the reaction (6.6).

More reaction pathways according to reaction (6.7) – (6.9) are available for nitrate photolysis on a semiconductor surface as evident by the nitrate photochemistry studies on TiO₂.¹⁰⁰ Nitrate photolysis via a nitrate radical intermediate forming reduced NO and NO₂ was reported for TiO₂ surfaces.¹⁰³ These reactions, initiated by electron-hole (e⁻/h⁺) pairs, can also play a significant role on hematite surface.



Newly formed $\text{NO}_2(\text{ads})$ from reaction (6.9) can either react with photogenerated electrons forming adsorbed NO_2^- which undergoes continued photoreactions to yield adsorbed NO according to reaction (6.4) or desorb to the gas phase. However, from these studies, we have no evidence for $\text{NO}_2(\text{ads})$ or $\text{NO}_2^-(\text{ads})$. Therefore, $\text{NO}_2(\text{ads})$ conversion to $\text{NO}(\text{ads})$ via NO_2^- may be a very fast reaction. Additionally, the electron attachment, reaction (6.10), is more feasible on hematite surface due to the availability of photogenerated electrons.

Figure 6.4 shows the high resolution spectra in the N1s region for $\alpha\text{-Fe}_2\text{O}_3$ surface exposed to gas-phase HNO_3 and then irradiated with UV light for 0, 30 and 90 minutes time periods in the presence of 45%RH. Spectra clearly show the loss of surface-bound nitrate and the appearance of low binding energy features corresponding to reduced nitrogen species with increasing irradiation time. Reduced-nitrogen, surface-species formation did not show any difference in the presence of molecular oxygen (spectra not shown). In the presence of water vapor, hydroxyl radicals formed on hematite surface upon UV irradiation, reaction (6.11) can initiate following reactions in competition with the nitrate photolysis reactions leading to secondary pathways.

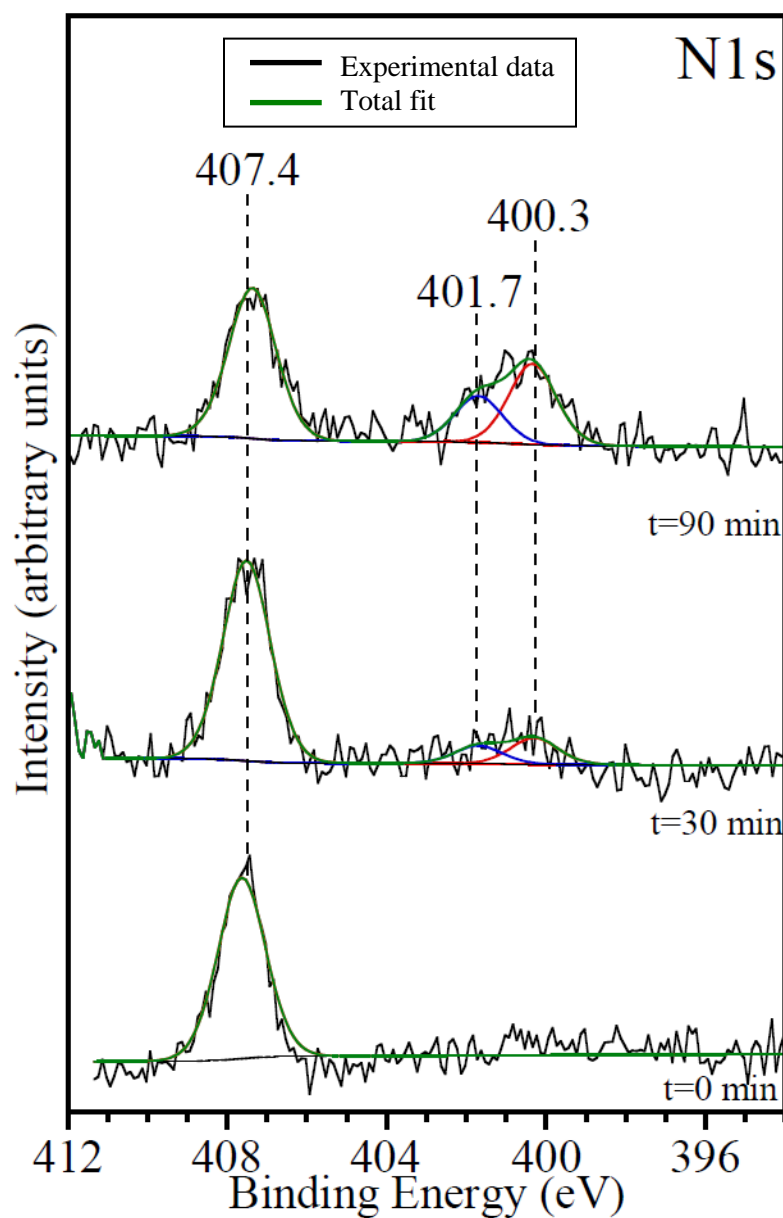


Figure 6.4. High resolution X-ray photoelectron spectra of $\alpha\text{-Fe}_2\text{O}_3$ particles in the N1s binding energy regions following exposure to HNO_3 to saturation coverages and subsequent UV irradiation for 0, 30 and 90 minutes in the presence of %RH = 45 without O_2 . All spectra were acquired at 296 K. Black and green lines represent the experimental data acquired and the total fit respectively. Surface species obtained by peak fitting are shown in red and blue lines. The fitted curve for nitrate peak overlaps with the total fit.



These alternative pathways can dominate in the presence of relative humidity according to the reactions (6.12) and (6.13) converting NO_2^- intermediate to the gas phase HONO and NO_2 and converting NO_3^- (ads) to nitrate radical according to reaction (6.14).¹⁰⁰ In HONO uptake studies on Fe_2O_3 , Bedjanian and co-workers have reported the HONO decomposition to gas phase NO and NO_2 .²²⁹ This decomposition is also possible under the experimental conditions used in the current study.

Surface product formation under irradiation was investigated as a function of water vapor pressure. It can be seen that the formation of surface-bound reduced nitrogen species changes significantly with water vapor pressure. Left panel of Figure 6.5 shows the N1s region of HNO_3 reacted $\alpha\text{-Fe}_2\text{O}_3$ after 90 minute UV irradiation at different water vapor pressures. UV irradiation in the presence of different water vapor pressures showed changes in the presence of reduced nitrogen surface species. The right panel of Figure 6.5 shows the total nitrate loss after 90 minute UV irradiation calculated from initial and final N1s:Fe2p speciation ratio using the adsorbed nitrate N1s peak at 407.4 eV. In the absence of water vapor, reduced nitrogen species were not observed. This can be due to the low nitrate loss under irradiation in the absence of water vapor and low availability of electrons due to higher electron hole recombination. As shown in the right panel the total nitrate loss is ~3 times higher in the presence of water vapor. This confirms the important

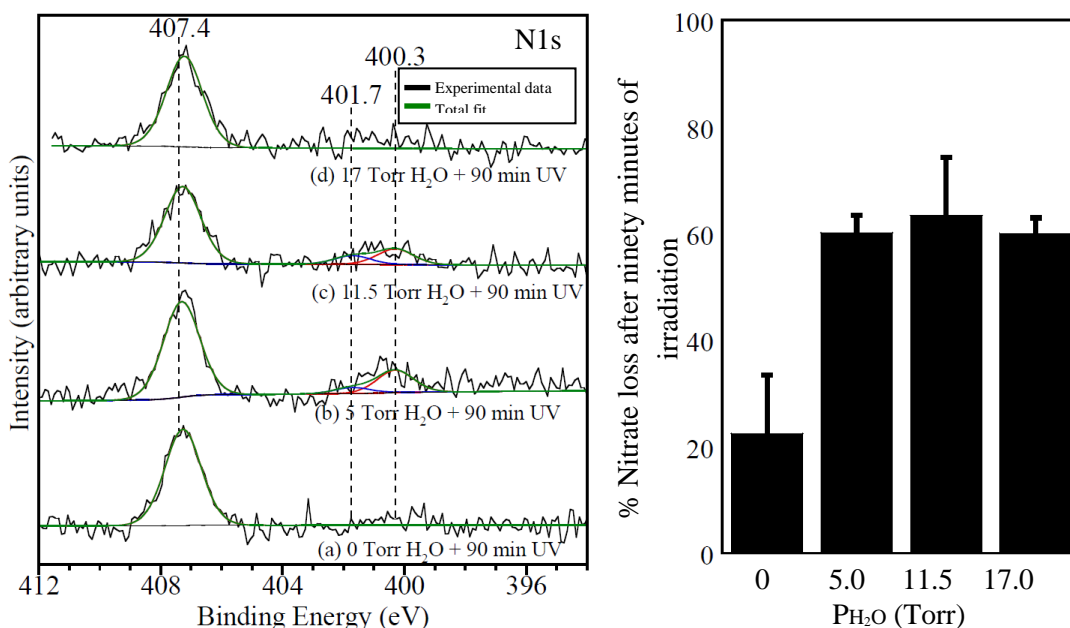


Figure 6.5. High resolution X-ray photoelectron spectra of $\alpha\text{-Fe}_2\text{O}_3$ particles in the N1s binding energy regions following exposure to HNO_3 to saturation coverages and subsequent UV irradiation for 90 minutes in the presence of (a) 0 Torr H_2O , (b) 5 Torr H_2O , (c) 11.5 Torr H_2O , (d) 17 Torr H_2O at $T = 296$ K (left panel) and the percentage loss of nitrate after 90 minutes of UV irradiation in the presence of different water vapor pressures (right panel). In the left panel black and green lines represent the experimental data acquired and the total fit respectively. Surface species obtained by peak fitting are shown in red and blue lines. The fitted curve for nitrate peak overlaps with the total fit.

role of water in nitrate photolysis on hematite and the increase in nitrate loss due to increase ability to react and new mechanisms available for reactions giving rise to a significantly greater loss of nitrate and the observed increase in surface-bound products at 5 and 11.5 Torr water exposures. Additionally, in the presence of water vapor photo-generated holes react with water molecules and that decreases the e^-/h^+ recombination leaving more electrons to form reduced nitrogen surface species. In the presence of water vapor, around 60% nitrate loss was observed for all three %RH experiments. However, reduced-nitrogen, surface-species were not observed at the highest water vapor exposure. This may suggest that surface sites for NO^- and N^- adsorption are available only at 5 and

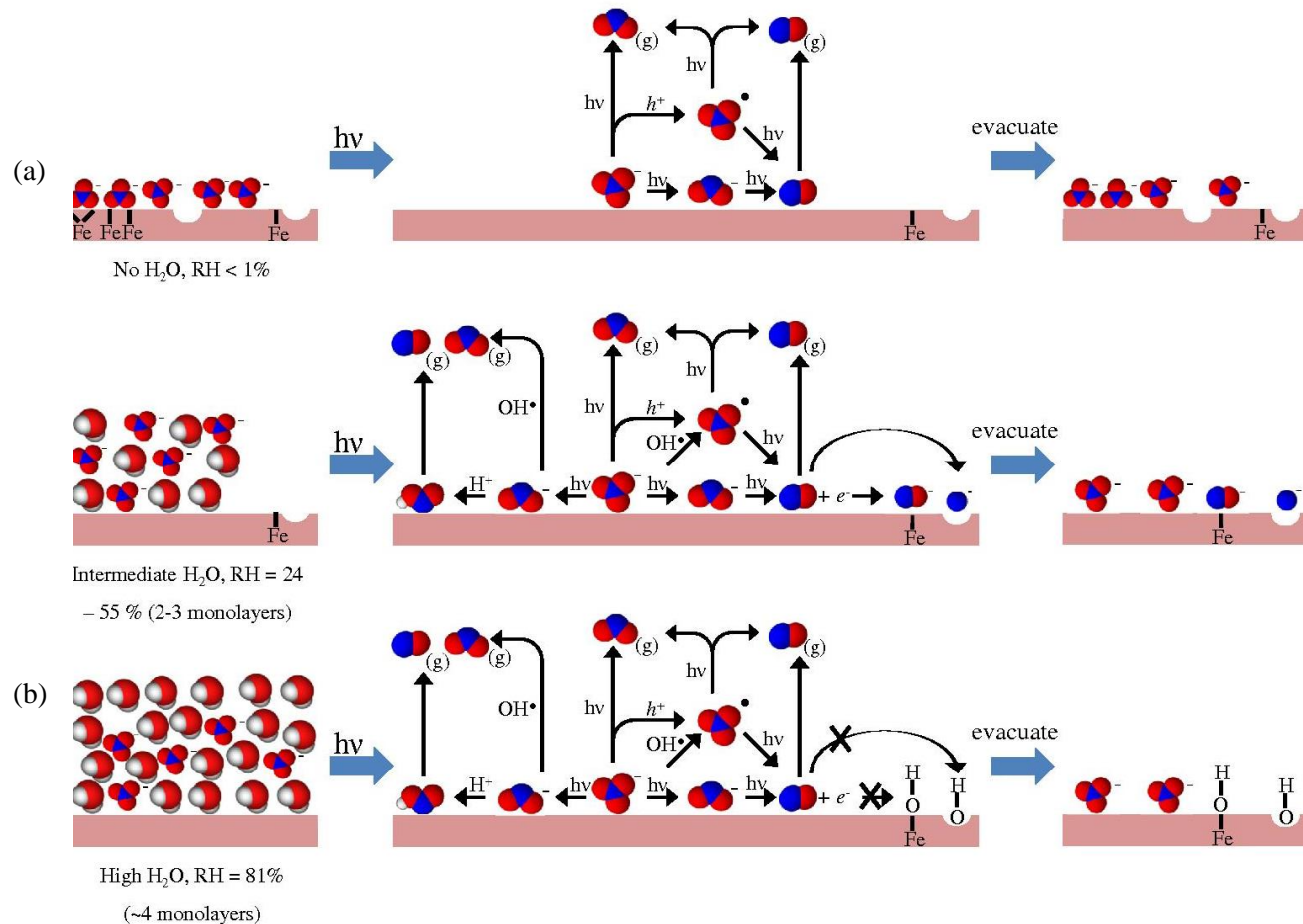


Figure 6.6. Schematic of adsorbed nitrate photochemistry on $\alpha\text{-Fe}_2\text{O}_3$; (a) in the absence of water vapor, adsorbed nitrates present on the hematite surface in different coordination modes undergo limited nitrate photochemistry due to electron and hole pair recombination, (b) in the presence of 5 and 11.5 Torr water vapor pressure (24 and 55 %RH), there is higher nitrate conversion due to lower electron/hole recombination rates, thus NO^- and N^- form on cationic sites and O vacancy sites, (c) in the presence of 17 Torr (81 %RH) of water vapor pressure, there is high nitrate conversion, similar as in (b), however cationic sites and O vacancy sites are not available to form NO^- and N^- . See text for further details.

11.5 Torr water exposures (24 and 55% RH) and potentially covered at the highest water vapor pressure of 17 Torr (81% RH). Mogili and co-workers have previously reported that the water adsorption is not uniform on hematite surfaces and water adsorption results water patches leaving some of the surface sites available up to 60% RH water vapor exposure.²³⁰ This uneven water adsorption on hematite has been reported previously in several studies.^{24,107,230} Since the percentage nitrate loss did not show much difference for three water vapor pressures the disappearance of NO^- and atomic N^- species at the highest water vapor exposure can be possibly due to the occupation of water molecules on adsorption sites at the highest relative humidity that are then blocked for further reactions.

Figure 6.6 shows schematics of the summary of reactions for nitrate photochemistry on hematite and reduced nitrogen surface species and gas-phase NO , NO_2 formation under different water vapor exposures. Table 6.2 contains percentage relative humidity for adsorbed water layers formation taken from the water adsorption isotherms reported in Mogili et al. for $\alpha\text{-Fe}_2\text{O}_3$.²³⁰ In the absence of water vapor, low nitrate loss and higher e^-/h^+ recombination does not facilitate reduced nitrogen surface species formation. At the intermediate and higher water vapor pressures higher nitrate loss results due to the available new mechanisms in the presence of water molecules. In the presence of water vapor oxide coordinated nitrate converts to water solvated nitrate and degree of solvation depends on amount of water vapor equilibrium with the surface. At the intermediate water vapor exposures of 5 and 11.5 Torr (24 and 55 %RH) ~2 and ~3 water layers are formed. In these intermediate water vapor exposures less electron hole

Table 6.2. Percentage Relative Humidity for Water Layer Formation on α -Fe₂O₃ Estimated from Water Adsorption Isotherm Curves Reported in Reference 230

%RH	Number of layers formed
8	1
27	2
58	3
77	4

recombination due to water molecules reaction with photo-generated holes and availability of adsorption sites results reduced nitrogen surface species. At the highest water vapor pressure the surface is covered with ~4 layers of water and adsorption sites are not available for the formation of reduced nitrogen surface species.

The gas-phase products formed during photolysis of nitrate adsorbed on α -Fe₂O₃ particles were also monitored using the FTIR system described under experimental methods. Adsorption of HNO₃ on α -Fe₂O₃ particles produced absorption bands for monodentate, bidentate and bridged nitrate in the FTIR spectrum under dry conditions. Adsorbed nitrate exposed to water vapor showed the formation of solvated nitrate. Surface FTIR spectra were consistent with data reported for HNO₃ adsorption on α -Fe₂O₃ under dry and wet conditions. Adsorbed nitrates on nanoparticle surfaces such as γ -Fe₂O₃, γ -Al₂O₃, α -Al₂O₃ have been reported in previous publications.^{101,162,231} Figure 6.7 show the gas-phase product formation recorded as a function of UV exposure time in presence of 45% RH of water vapor. Three peaks appeared at 1616, 1874 and 2223 cm⁻¹. These vibrational modes can be attributed to the gas-phase NO₂, NO and N₂O species respectively. The mechanisms for N₂O formation will be discussed later in the text. The bands for gas-phase NO and N₂O appeared after 30minutes UV irradiation and grow continuously for 420 minutes. Gas-phase NO₂ was not observed after 30 minute

irradiation and can be due to the NO_2 reaction with H_2O according to the reaction (6.15) under acidic conditions. Another possible reaction is NO_2 react with H_2O forming HONO and HNO_3 according to the reaction (6.16).²³² Gas phase HONO was not observed possibly due to the decomposition on Fe_2O_3 surface. Gas phase NO_2 appeared at longer irradiation times 120 and 420 minutes. The dominant gas-phase species in the presence of water vapor was NO at all the irradiation times agreeing with the presence of adsorbed NO^- on the surface. Identical experiments performed to monitor the gas-phase products under wet condition, in the presence of molecular oxygen showed higher gas phase NO_2 amounts (data not shown). Presence of molecular oxygen has shown NO_2 dominance in

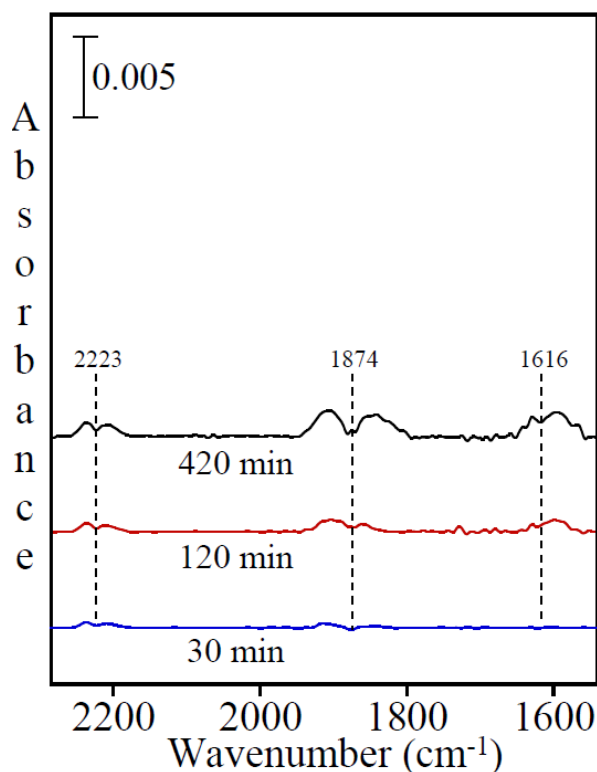
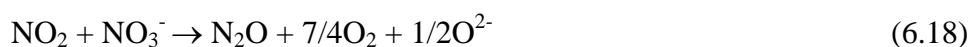
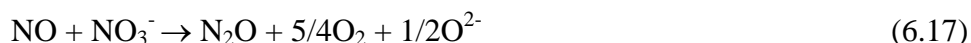


Figure 6.7. Transmission FTIR spectra of gas-phase product formation from UV illumination of adsorbed nitrate under %RH = 45 without O_2 at $T = 296$ K.

the gas phase on UV irradiation of nitrated Al_2O_3 and TiO_2 surfaces.^{231,233} This has been explained by two NO molecules react with molecular oxygen to form two NO_2 molecules.

These infrared spectra clearly indicate that only NO and NO_2 as the major gas-phase products and small amount of N_2O present in the system even after irradiating HNO_3 reacted surface for 420 minutes. The N_2O formation in the presence of 45% RH that can be due to secondary pathway according to the reaction (6.15) under acidic conditions in the presence of water vapor.²³⁴ Furthermore, reactions (6.17) and (6.18) can be sources for N_2O as well.²³⁵



6.4.5 Aqueous Phase Behavior of HNO_3

Reacted Hematite Particles

Aqueous Phase Behavior of HNO_3 Reacted Hematite Particles. HNO_3 reacted $\alpha\text{-Fe}_2\text{O}_3$ particles were introduced to water to investigate the possible enhancements in Fe dissolution due to the HNO_3 reactivity. Studies have shown HNO_3 reacted $\alpha\text{-FeOOH}$ formed stable suspension compared to $\alpha\text{-FeOOH}$ that was not reacted.¹¹³ Sedimentation plots of HNO_3 reacted and unreacted $\alpha\text{-Fe}_2\text{O}_3$ showed fast settling down with no

difference between the two. Dissolved Fe concentration was below the limit of detection of ICP(OES). The data explains HNO_3 reaction does not change particle aggregation or enhance Fe dissolution from $\alpha\text{-Fe}_2\text{O}_3$ particles.

6.5 Conclusions and Atmospheric Implications

HNO_3 adsorption on hematite surface under different environmental conditions of relative humidity and molecular oxygen was explored in the presence and absence of UV irradiation. Ex and in-situ analyses were used to follow the surface and gas-phase species that form in these reactions. Surface nitrate was found to be the predominant species in the absence of UV irradiation. Irradiation with UV light resulted in the formation of surface-bound, reduced-nitrogen species. Furthermore, XPS analysis indicates that reduced species are observed only with the presence of co-adsorbed water except at the highest pressures of water vapor, and thus highest coverage, during the UV irradiation. Thus, these data show a relative humidity dependent extent of reaction and the stability of reduced surface species that form. Transmission FTIR studies confirm that irradiation with the UV light resulted the reduction of the adsorbed nitrate to form gas-phase N_2O , NO and NO_2 species. The distribution of surface-bound and gas-phase products depends on the presence of water vapor. Additionally, HNO_3 acid adsorption does not change the dissolution and solution phase behavior of these $\alpha\text{-Fe}_2\text{O}_3$ particles.

The data presented here support the role that iron-containing aerosol surfaces in the atmosphere can facilitate the conversion of adsorbed nitrate to gas-phase NO_2 , NO and N_2O as well as adsorbed NO^- and N^- during heterogeneous photochemistry. The effect of relative humidity in the formation of highly reduced nitrogen species on iron

oxides has not been shown previously and represents another role of adsorbed water in the reaction chemistry of environmental interfaces.

Acknowledgment

This material is based on the work supported by the National Science Foundation under grants CHE-0952605. Any opinions, findings and conclusions or recommendations expressed in this material are those of the authors and do not necessarily reflect the views of the National Science Foundation. The results of this work are presented in the publication under authorship of Charith E. Nanayakkara, Pradeep M. Jayaweera, Gayan Rubasinghege, Jonas Baltrusaitis, and Vicki H. Grassian, *Journal of Physical Chemistry A*, 2014, 118, 158–166

CHAPTER 7

CONCLUSIONS AND FUTURE DIRECTIONS

Oxide surfaces in the atmosphere as mineral dust particles and stationery surfaces in contact with the atmosphere can alter the chemical balance of the atmosphere via heterogeneous and photochemical processes. This dissertation research focuses on studying the details of heterogeneous chemistry and photochemistry of atmospheric trace gases on light absorbing components of mineral dust. Water vapor and molecular oxygen present in the atmosphere can affect these reactions and can alter reaction mechanisms and product formation. Thus, the role of adsorbed water as a function of relative humidity on the stability and speciation of adsorbates resulted from atmospheric trace gas adsorption is important to study in order to better understand the relative humidity dependence of the stability and speciation.

In Chapter 2, the details of spectroscopic techniques used in investigating heterogeneous chemistry and photochemistry, oxide sample characterization techniques, and solution phase analytical techniques were outlined. The main spectroscopic techniques are combined with reaction chambers designed to study adsorption and photochemical reactions.

Sulfur dioxide adsorption and photooxidation on titanium dioxide nanoparticle surfaces were discussed in Chapter 3. FTIR spectroscopy and isotope labelling experiments were carried out in order to determine adsorption sites, surface speciation and photooxidation chemistry. Sulfur dioxide reacts with either one surface O-H group to yield adsorbed bisulfite or two surface O-H groups to yield adsorbed sulfite and water.

Surface O-H groups were labelled in order to get additional insights into the adsorption mechanism. Adsorbed sulfite/bisulfite conversion to adsorbed sulfate was observed upon irradiation. The stability of adsorbed sulfite/bisulfite and sulfate was examined in the presence of water vapor. Adsorbed water more easily displaces adsorbed sulfite/bisulfite compared to sulfate by forming a sulfur dioxide water complex in the presence of adsorbed water. Therefore, these differences in the stability of adsorbed species that form as a result of surface heterogeneous reactions on oxide particles surfaces has important implications in the heterogeneous chemistry of mineral dust aerosol in the atmosphere.

Chapter 4 contains a comparison of the reactivity of O-H groups on titanium dioxide nanoparticle surfaces with gas-phase carbon dioxide, sulfur dioxide and nitrogen dioxide. The surface reactivity of O-H groups with these three triatomic pollutant gases differs considerably. We show there are considerably different reaction mechanisms for adsorption and surface chemistry that occurs for these three gases. Role of adsorbed water in the stability of surface species that form from adsorption of carbon dioxide, nitrogen dioxide and sulfur dioxide on hydroxylated TiO₂ nanoparticles is probed as a function of relative humidity and provides insights into the stability of adsorbed species on oxide surfaces under atmospherically relevant conditions. Additionally, water uptake on TiO₂ particles previously reacted with CO₂, SO₂ and NO₂ was quantified using quartz crystal microbalance.

In Chapter 5, heterogeneous reactions of HCOOH with nanomaterial TiO₂ and photooxidation of adsorbed formate was investigated. HCOOH adsorbs dissociatively on TiO₂ forming adsorbed formate mainly in bridged bidentate orientation. Adsorbed formate exposed to water vapor changed the coordination from bridged bidentate to

solvated formate. The solvated formate is assumed to be in the monodentate coordination. Uptake coefficient for HCOOH reaction on TiO₂ surface agrees with the previously reported values. Formate photooxidation was studied in the presence of different environmental conditions. Higher relative humidity conditions in the presence of molecular oxygen showed enhanced formate photooxidation. These studies suggest enhanced formate conversion under daytime tropospheric conditions. Solution phase behavior of HCOOH reacted TiO₂ showed the smaller aggregate formation once these particles are coated with formate.

HNO₃ adsorption on hematite surface under different environmental conditions of relative humidity and molecular oxygen was explored using XPS in the presence and absence of UV irradiation in chapter 6. HNO₃ adsorption resulted in adsorbed nitrate in the absence of UV irradiation. Irradiation with UV light resulted in the formation of surface-bound, reduced nitrogen species when the irradiation was carried out in the presence of water vapor. These reduced species are not observed at the highest pressures of water vapor, and thus highest coverage, during the UV irradiation. Thus, these data clearly show a relative humidity dependent surface reduced nitrogen species formation. FTIR results of adsorbed nitrate irradiation with the UV light showed adsorbed nitrate renitrosification to form gas-phase N₂O, NO and NO₂ species. The distribution of surface-bound and gas-phase products depends on relative humidity. Additionally, HNO₃ acid adsorption does not change the dissolution and solution phase behavior of these α -Fe₂O₃ particles. Effect of HNO₃ reaction on iron dissolution from nitrated hematite did not show change in particle aggregation or enhance in Fe dissolution.

The atmospheric abundance of TiO_2 has the potential to significantly increase due to the expected increase in the loading of mineral dust aerosol in the atmosphere and the expanding industrial production and applications of nanom TiO_2 . Additionally, given that TiO_2 composite materials are being used as surface coatings for both indoor and outdoor applications, there is the potential for heterogeneous reactions with atmospheric gases that have the potential to impact indoor and outdoor air quality. Given that solar radiation can provide sufficient energy to initiate photocatalysis on TiO_2 surfaces, heterogeneous photochemistry of TiO_2 has the potential to become increasingly important in impacting the chemical balance of the atmosphere. The abundance of airborne $\alpha\text{-Fe}_2\text{O}_3$ also has the potential to increase due to the increase in mineral dust loading increase results due to desertification and improper agriculture practices. Atmospheric Fe-containing mineral dust can also contain other forms of iron oxides and hydroxides. Therefore, further research is needed in order to fully understand the different roles play by these different iron-containing particles. Additionally, solution phase behavior of Fe-containing oxides and hydroxide has received much attention recently and research related to that has been increasing.

Although the dissertation research provides an important contribution for our understanding, there remain questions as to the role of light absorbing oxide assisted photochemical processes as they relate to atmospheric chemistry. These questions can be answered through a combined effort of laboratory studies, field studies, and modeling analysis. Some future directions include the following:

- (1) Photocatalysis carried out under atmospherically relevant conditions of gas phase concentrations, relative humidity, and solar flux.

- (2) Photocatalytic studies that probe both surface and gas phase species *in situ* under relevant environmental conditions, as these are best suited for mechanistic studies of these reactions.
- (3) Further exploration of the effects of the physicochemical properties of TiO_2 and $\alpha\text{-Fe}_2\text{O}_3$ on heterogeneous photochemistry that include size, shape, coatings, and use as composite materials.
- (4) Experimental studies on solution phase photochemistry studies of oxide particles reacted with atmospheric trace gases can be carried out in order to better understand the photooxidation of atmospherically processed particles in hydrosphere.
- (5) Combined use of model surrogate systems and authentic samples to best understand mechanistic aspects and factors that are important as well as to validate that these occur in multicomponent, complex mixtures.
- (6) Development of instruments of particle characterization to provide information on the size and phase of Ti-containing and Fe-containing particles in aerosols.
- (7) Field measurements that validate the importance of these reactions in atmospheric chemistry.
- (8) Modeling analysis to obtain a better understanding of the relative impact of semiconductor oxide photocatalysis compared to other heterogeneous reactions in atmospheric chemistry.

With research in this area these questions and issues can be further resolved so our understanding of the Earth's atmosphere can be increased.

REFERENCES

1. Ginoux, P.; Chin, M.; Tegen, I.; Prospero, J. M.; Holben, B.; Dubovik, O.; Lin, S. J. Sources and Distributions of Dust Aerosols Simulated with the GOCART Model. *Journal of Geophysical Research: Atmospheres* **2001**, *106*, 20255-20273.
2. Tegen, I.; Fung, I. Modeling of Mineral Dust in the Atmosphere: Sources, Transport, and Optical Thickness. *Journal of Geophysical Research: Atmospheres* **1994**, *99*, 22897-22914.
3. Sokolik, I. N.; Toon, O. B. Direct Radiative Forcing by Anthropogenic Airborne Mineral Aerosols. *Nature* **1996**, *381*, 681-683.
4. Sheehy, D. P. A Perspective on Desertification of Grazingland Ecosystems in North China. *Ambio* **1992**, *21*, 303-307.
5. Hans Wedepohl, K. The Composition of the Continental Crust. *Geochimica et Cosmochimica Acta* **1995**, *59*, 1217-1232.
6. Usher, C. R.; Michel, A. E.; Grassian, V. H. Reactions on Mineral Dust. *Chemical Reviews* **2003**, *103*, 4883-4940.
7. Chen, H.; Nanayakkara, C. E.; Grassian, V. H. Titanium Dioxide Photocatalysis in Atmospheric Chemistry. *Chemical Reviews* **2012**, *112*, 5919-5948.
8. Rubasinghege, G.; Elzey, S.; Baltrusaitis, J.; Jayaweera, P. M.; Grassian, V. H. Reactions on Atmospheric Dust Particles: Surface Photochemistry and Size-dependent Nanoscale Redox Chemistry. *The Journal of Physical Chemistry Letters* **2010**, *1*, 1729-1737.
9. Parmon, V. N.; Zakharenko, V. S. Photocatalysis and Photosorption in the Earth's Atmosphere. *CATTECH* **2001**, *5*, 96-115.
10. Linsebigler, A. L.; Lu, G.; Yates, J. T. Photocatalysis on TiO₂ Surfaces: Principles, Mechanisms, and Selected results. *Chemical Reviews* **1995**, *95*, 735-758.
11. Ballari, M. M.; Hunger, M.; Hüsken, G.; Brouwers, H. J. H. NO_x Photocatalytic Degradation Employing Concrete Pavement Containing Titanium Dioxide. *Applied Catalysis B: Environmental* **2010**, *95*, 245-254.
12. Ballari, M. M.; Yu, Q. L.; Brouwers, H. J. H. Experimental Study of the NO and NO₂ Degradation by Photocatalytically Active Concrete. *Catalysis Today* **2011**, *161*, 175-180.

13. Guo, M. Z.; Poon, C. S. Photocatalytic NO Removal of Concrete Surface Layers Intermixed with TiO₂. *Building and Environment* **2013**, *70*, 102-109.
14. Kamat, P. V. Dominance of Metal Oxides in the Era of Nanotechnology. *The Journal of Physical Chemistry Letters* **2011**, *2*, 839-840.
15. O'Regan, B.; Gratzel, M. A Low-cost, High-efficiency Solar Cell Based on Dye-sensitized Colloidal TiO₂ Films. *Nature* **1991**, *353*, 737-740.
16. Mills, A.; Davies, R. H.; Worsley, D. Water Purification by Semiconductor Photocatalysis. *Chemical Society Reviews* **1993**, *22*, 417-425.
17. Dutta, P. K.; Ginwalla, A.; Hogg, B.; Patton, B. R.; Chwieroth, B.; Liang, Z.; Gouma, P.; Mills, M.; Akbar, S. Interaction of Carbon Monoxide with Anatase Surfaces at High Temperatures: Optimization of a Carbon Monoxide Sensor. *The Journal of Physical Chemistry B* **1999**, *103*, 4412-4422.
18. Birkefeld, L. D.; Azad, A. M.; Akbar, S. A. Carbon Monoxide and Hydrogen Detection by Anatase Modification of Titanium Dioxide. *Journal of the American Ceramic Society* **1992**, *75*, 2964-2968.
19. Zhang, X.-T.; Sato, O.; Taguchi, M.; Einaga, Y.; Murakami, T.; Fujishima, A. Self-cleaning Particle Coating with Antireflection Properties. *Chemistry of Materials* **2005**, *17*, 696-700.
20. Kasanen, J.; Suvanto, M.; Pakkanen, T. T. Self-cleaning, Titanium Dioxide Based, Multilayer Coating Fabricated on Polymer and Glass Surfaces. *Journal of Applied Polymer Science* **2009**, *111*, 2597-2606.
21. Hadjiivanov, K.; Knozinger, H. Species Formed After NO Adsorption and NO+O₂ Co-adsorption on TiO₂: An FTIR Spectroscopic Study. *Physical Chemistry Chemical Physics* **2000**, *2*, 2803-2806.
22. Kebede, M. A.; Varner, M. E.; Scharko, N. K.; Gerber, R. B.; Raff, J. D. Photooxidation of Ammonia on TiO₂ as a Source of NO and NO₂ Under Atmospheric Conditions. *Journal of the American Chemical Society* **2013**, *135*, 8606-8615.
23. Rosseler, O.; Sleiman, M.; Montesinos, V. N.; Shavorskiy, A.; Keller, V.; Keller, N.; Litter, M. I.; Bluhm, H.; Salmeron, M.; Destailats, H. Chemistry of NO_x on TiO₂ Surfaces Studied by Ambient Pressure XPS: Products, Effect of UV Irradiation, Water, and Coadsorbed K⁺. *The Journal of Physical Chemistry Letters* **2013**, *4*, 536-541.
24. Chen, H.; Stanier, C. O.; Young, M. A.; Grassian, V. H. A Kinetic Study of Ozone Decomposition on Illuminated Oxide Surfaces. *The Journal of Physical Chemistry A* **2011**, *115*, 11979-11987.

25. Gustafsson, R. J.; Orlov, A.; Griffiths, P. T.; Cox, R. A.; Lambert, R. M. Reduction of NO₂ to Nitrous Acid on Illuminated Titanium Dioxide Aerosol Surfaces: Implications for Photocatalysis and Atmospheric Chemistry. *Chemical Communications* **2006**, 3936-3938.
26. Augustynski, J. The Role of the Surface Intermediates in the Photoelectrochemical Behaviour of Anatase and Rutile TiO₂. *Electrochimica Acta* **1993**, 38, 43-46.
27. Fang, W. Q.; Gong, X. Q.; Yang, H. G. On the Unusual Properties of Anatase TiO₂ Exposed by Highly Reactive Facets. *The Journal of Physical Chemistry Letters* **2011**, 2, 725-734.
28. Bickley, R. I.; Gonzalez-Carreno, T.; Lees, J. S.; Palmisano, L.; Tilley, R. J. D. A Structural Investigation of Titanium Dioxide Photocatalysts. *Journal of Solid State Chemistry* **1991**, 92, 178-190.
29. Reeves, P.; Ohlhausen, R.; Sloan, D.; Pamplin, K.; Scoggins, T.; Clark, C.; Hutchinson, B.; Green, D. Photocatalytic Destruction of Organic Dyes in Aqueous TiO₂ Suspensions using Concentrated Simulated and Natural Solar Energy. *Solar Energy* **1992**, 48, 413-420.
30. Bacsa, R. R.; Kiwi, J. Effect of Rutile Phase on the Photocatalytic Properties of Nanocrystalline Titania during the Degradation of p-coumaric Acid. *Applied Catalysis B: Environmental* **1998**, 16, 19-29.
31. Yamazaki, S.; Matsunaga, S.; Hori, K. Photocatalytic Degradation of Trichloroethylene in Water using TiO₂ Pellets. *Water Research* **2001**, 35, 1022-1028.
32. Frazer, L. Titanium Dioxide: Environmental White Knight. *Environ Health Perspect* **2001**, 109, A174-A177.
33. Parkin, I. P.; Palgrave, R. G. Self-cleaning Coatings. *Journal of Materials Chemistry* **2005**, 15, 1689-1695.
34. Fujishima, A.; Zhang, X.; Tryk, D. A. TiO₂ Photocatalysis and Related Surface Phenomena. *Surface Science Reports* **2008**, 63, 515-582.
35. Hoffmann, M. R.; Martin, S. T.; Choi, W.; Bahnemann, D. W. Environmental Applications of Semiconductor Photocatalysis. *Chemical Reviews* **1995**, 95, 69-96.
36. Diebold, U. The Surface Science of Titanium Dioxide. *Surface Science Reports* **2003**, 48, 53-229.

37. Henderson, M. A. A Surface Science Perspective on TiO₂ Photocatalysis. *Surface Science Reports* **2011**, 66, 185-297.
38. Yates Jr, J. T. Photochemistry on TiO₂: Mechanisms Behind the Surface Chemistry. *Surface Science* **2009**, 603, 1605-1612.
39. Hanisch, F.; Crowley, J. N. Ozone Decomposition on Saharan Dust: An Experimental Investigation. *Atmospheric Chemistry and Physics* **2003**, 3, 119-130.
40. Kaegi, R.; Ulrich, A.; Sinnet, B.; Vonbank, R.; Wichser, A.; Zuleeg, S.; Simmler, H.; Brunner, S.; Vonmont, H.; Burkhardt, M.; Boller, M. Synthetic TiO₂ Nanoparticle Emission From Exterior Facades Into the Aquatic Environment. *Environmental Pollution* **2008**, 156, 233-239.
41. Zheng, N.; Wang, H. J. Discovery of anatase in Atmospheric Inhalable Particles and Its Significance. *Spectroscopy and Spectral Analysis* **2009**, 29, 1570-1572.
42. Schleicher, N.; Norra, S.; Chai, F.; Chen, Y.; Wang, S.; Stüben, D. Anthropogenic Versus Geogenic Contribution to Total Suspended Atmospheric Particulate Matter and Its Variations During a Two-year Sampling Period in Beijing, China. *Journal of Environmental Monitoring* **2010**, 12, 434-441.
43. Cornille, P.; Maenhaut, W.; Pacyna, J. M. PIXE Analysis of Size-fractionated Aerosol Samples Collected at Birkenes, Norway, during Spring 1987. *Nuclear Instruments and Methods in Physics Research Section B: Beam Interactions with Materials and Atoms* **1990**, 49, 376-382.
44. Xhoffer, C.; Bernard, P.; Van Grieken, R.; Van der Auwera, L. Chemical Characterization and Source Apportionment of Individual Aerosol Particles Over the North Sea and the English Channel using Multivariate Techniques. *Environmental Science & Technology* **1991**, 25, 1470-1478.
45. Chow, J. C.; Chung Shing, L.; Cassmassi, J.; Watson, J. G.; Lu, Z.; Pritchett, L. C. A Neighborhood-scale Study of PM₁₀ Source Contributions in Rubidoux, California. *Atmospheric Environment. Part A. General Topics* **1992**, 26, 693-706.
46. Ebert, M.; Weinbruch, S.; Hoffmann, P.; Ortner, H. M. Chemical Characterization of North Sea Aerosol Particles. *Journal of Aerosol Science* **2000**, 31, 613-632.
47. Weber, S.; Hoffmann, P.; Ensling, J.; Dedik, A. N.; Weinbruch, S.; Miehe, G.; Gütlich, P.; Ortner, H. M. Characterization of Iron Compounds from Urban and Rural Aerosol Sources. *Journal of Aerosol Science* **2000**, 31, 987-997.
48. Ariola, V.; Campajola, L.; D'Alessandro, A.; Del Carmine, P.; Gagliardi, F.; Lucarelli, F.; Mandò, P. A.; Marcazzan, G.; Moro, R.; Nava, S.; Prati, P.; Valli, G.; Vecchi, R.; Zucchiatti, A. Aerosol Characterisation in Italian Towns by IBA

Techniques. *Nuclear Instruments and Methods in Physics Research Section B: Beam Interactions with Materials and Atoms* **2002**, 190, 471-476.

49. Smolik, J.; Zdimal, V.; Schwarz, J.; Lazaridis, M.; Havárnek, V.; Eleftheriadis, K.; Mihalopoulos, N.; Bryant, C.; Colbeck, I. Size Resolved Mass Concentration and Elemental Composition of Atmospheric Aerosols over the Eastern Mediterranean Area. *Atmos. Chem. Phys.* **2003**, 3, 2207-2216.
50. Sillanpää, M.; Saarikoski, S.; Hillamo, R.; Pennanen, A.; Makkonen, U.; Spolnik, Z.; Van Grieken, R.; Koskentalo, T.; Salonen, R. O. Chemical Composition, Mass Size Distribution and Source Analysis of Long-range Transported Wildfire Smokes in Helsinki. *Science of The Total Environment* **2005**, 350, 119-135.
51. Avila, A.; Alarcón, M.; Castillo, S.; Escudero, M.; García Orellana, J.; Masqué, P.; Querol, X. Variation of Soluble and Insoluble Calcium in Red Rains Related to Dust Sources and Transport Patterns from North Africa to Northeastern Spain. *Journal of Geophysical Research: Atmospheres* **2007**, 112, D05210.
52. Maenhaut, W.; Raes, N.; Chi, X.; Cafmeyer, J.; Wang, W. Chemical Composition and Mass Closure for PM_{2.5} and PM₁₀ Aerosols at K-pusztá, Hungary, in Summer 2006. *X-Ray Spectrometry* **2008**, 37, 193-197.
53. Maenhaut, W.; Nava, S.; Lucarelli, F.; Wang, W.; Chi, X.; Kulmala, M. Chemical Composition, Impact from Biomass Burning, and Mass Closure for PM_{2.5} and PM₁₀ Aerosols at Hyytiälä, Finland, in Summer 2007. *X-Ray Spectrometry* **2011**, 40, 168-171.
54. Hsieh, Y. K.; Chen, L. K.; Hsieh, H. F.; Huang, C. H.; Wang, C. F. Elemental Analysis of Airborne Particulate Matter Using an Electrical Low-pressure Impactor and Laser ablation/inductively Coupled Plasma Mass Spectrometry. *Journal of Analytical Atomic Spectrometry* **2011**, 26, 1502-1508.
55. Adedokun, J. A.; Emofurieta, W. O.; Adediji, O. A. Physical, Mineralogical and Chemical Properties of Harmattan Dust at Ile-Ife, Nigeria. *Theoretical and Applied Climatology* **1989**, 40, 161-169.
56. Ta, W.; Xiao, Z.; Qu, J.; Yang, G.; Wang, T. Characteristics of Dust Particles from the Desert/Gobi Area of Northwestern China during Dust-storm Periods. *Environmental Geology* **2003**, 43, 667-679.
57. Wei, L.; Qi, F.; Tao, W.; Yanwu, Z.; Jianhua, S. Physicochemistry and Mineralogy of Storm Dust and Dust Sediment in Northern China. *Advances in Atmospheric Sciences* **2004**, 21, 775-783.
58. Linke, C.; Möhler, O.; Veres, A.; Mohácsi, Á.; Bozóki, Z.; Szabó, G.; Schnaiter, M. Optical Properties and Mineralogical Composition of Different Saharan

- Mineral Dust Samples: A Laboratory Study. *Atmos. Chem. Phys.* **2006**, *6*, 3315-3323.
59. Pekney, N. J.; Davidson, C. I.; Bein, K. J.; Wexler, A. S.; Johnston, M. V. Identification of Sources of Atmospheric PM at the Pittsburgh Supersite, Part I: Single Particle Analysis and Filter-based Positive Matrix Factorization. *Atmospheric Environment* **2006**, *40*, Supplement 2, 411-423.
 60. Kertész, Z.; Borbély-Kiss, I.; Rajta, I.; Uzonyi, I.; Kiss, Á. Z. Analysis of Single Aerosol Particles Collected in Urban and Cave Environment by Proton Microprobe. *Nuclear Instruments and Methods in Physics Research Section B: Beam Interactions with Materials and Atoms* **2000**, *161-163*, 808-813.
 61. Reid, E. A.; Reid, J. S.; Meier, M. M.; Dunlap, M. R.; Cliff, S. S.; Broumas, A.; Perry, K.; Maring, H. Characterization of African Dust Transported to Puerto Rico by Individual Particle and Size Segregated Bulk Analysis. *Journal of Geophysical Research: Atmospheres* **2003**, *108*, 8591.
 62. Dentener, F. J.; Carmichael, G. R.; Zhang, Y.; Lelieveld, J.; Crutzen, P. J. Role of Mineral Aerosol as a Reactive Surface in the Global Troposphere. *Journal of Geophysical Research: Atmospheres* **1996**, *101*, 22869-22889.
 63. Bang, J. J.; Murr, L. E. Collecting and Characterizing Atmospheric Nanoparticles. *The Journal of The Minerals, Metals & Materials Society* **2002**, *54*, 28-30.
 64. Bang, J. J.; Murr, L. E. Atmospheric Nanoparticles: Preliminary Studies and Potential Respiratory Health Risks for Emerging Nanotechnologies. *Journal of Materials Science Letters* **2002**, *21*, 361-366.
 65. Buseck, P. R.; Adachi, K. Nanoparticles in the Atmosphere. *Elements* **2008**, *4*, 389-394.
 66. Weir, A.; Westerhoff, P.; Fabricius, L.; Hristovski, K.; von Goetz, N. Titanium Dioxide Nanoparticles in Food and Personal Care Products. *Environmental Science & Technology* **2012**, *46*, 2242-2250.
 67. Gottschalk, F.; Sun, T.; Nowack, B. Environmental Concentrations of Engineered Nanomaterials: Review of Modeling and Analytical Studies. *Environmental Pollution* **2013**, *181*, 287-300.
 68. Öktem, B.; Tolocka, M. P.; Johnston, M. V. On-line Analysis of Organic Components in Fine and Ultrafine Particles by Photoionization Aerosol Mass Spectrometry. *Analytical Chemistry* **2003**, *76*, 253-261.
 69. Lin, H.; Long, J.; Gu, Q.; Zhang, W.; Ruan, R.; Li, Z.; Wang, X. In Situ IR Study of Surface Hydroxyl Species of Dehydrated TiO₂: Towards Understanding Pivotal

Surface Processes of TiO₂ Photocatalytic Oxidation of Toluene. *Physical Chemistry Chemical Physics* **2012**, *14*, 9468-9474.

70. Prather, K. A.; Hatch, C. D.; Grassian, V. H. Analysis of Atmospheric Aerosols. *Annual Review of Analytical Chemistry* **2008**, *1*, 485-514.
71. Shi, Z.; Krom, M. D.; Jickells, T. D.; Bonneville, S.; Carslaw, K. S.; Mihalopoulos, N.; Baker, A. R.; Benning, L. G. Impacts on Iron Solubility in the Mineral Dust by Processes in the Source Region and the Atmosphere: A Review. *Aeolian Research* **2012**, *5*, 21-42.
72. Schwertmann, U.; Cornell, R. M.: *Iron oxides : Structure, Properties, Reactions, Occurrences and Uses* 2ed.; Wiley-VCH: Hoboken, NJ, USA, 2007.
73. Penpolcharoen, M.; Amal, R.; Brungs, M. Degradation of Sucrose and Nitrate over Titania Coated Nano-hematite Photocatalysts. *Journal of Nanoparticle Research* **2001**, *3*, 289-302.
74. Kormann, C.; Bahnemann, D. W.; Hoffmann, M. R. Environmental Photochemistry: Is Iron Oxide (hematite) An Active Photocatalyst? A Comparative Study: α -Fe₂O₃, ZnO, TiO₂. *Journal of Photochemistry and Photobiology A: Chemistry* **1989**, *48*, 161-169.
75. Gelado-Caballero, M. D.; López-García, P.; Prieto, S.; Patey, M. D.; Collado, C.; Hernández-Brito, J. J. Long-term Aerosol Measurements in Gran Canaria, Canary Islands: Particle concentration, Sources and Elemental Composition. *Journal of Geophysical Research: Atmospheres* **2012**, *117*, D03304.
76. Lee, B. K.; Lee, H. K.; Jun, N. Y. Analysis of Regional and Temporal Characteristics of PM₁₀ during an Asian Dust Episode in Korea. *Chemosphere* **2006**, *63*, 1106-1115.
77. Lafon, S.; Sokolik, I. N.; Rajot, J. L.; Caquineau, S.; Gaudichet, A. Characterization of Iron Oxides in Mineral Dust Aerosols: Implications for Light Absorption. *Journal of Geophysical Research: Atmospheres* **2006**, *111*, D21207.
78. Luo, C.; Mahowald, N.; Bond, T.; Chuang, P. Y.; Artaxo, P.; Siefert, R.; Chen, Y.; Schauer, J. Combustion Iron Distribution and Deposition. *Global Biogeochemical Cycles* **2008**, *22*, GB1012.
79. Vicente, A.; Alves, C. I.; Calvo, A. I.; Fernandes, A. P.; Nunes, T.; Monteiro, C.; Almeida, S. M.; Pio, C. Emission Factors and Detailed Chemical Composition of Smoke Particles from the 2010 Wildfire Season. *Atmospheric Environment* **2013**, *71*, 295-303.

80. Li, W.; Shao, L. Transmission Electron Microscopy Study of Aerosol Particles from the Brown Hazes in Northern China. *Journal of Geophysical Research: Atmospheres* **2009**, *114*, D09302.
81. Schulz, M.; Prospero, J. M.; Baker, A. R.; Dentener, F.; Ickes, L.; Liss, P. S.; Mahowald, N. M.; Nickovic, S.; García-Pando, C. P.; Rodríguez, S.; Sarin, M.; Tegen, I.; Duce, R. A. Atmospheric Transport and Deposition of Mineral Dust to the Ocean: Implications for Research Needs. *Environmental Science & Technology* **2012**, *46*, 10390-10404.
82. Mikhaylov, R. V.; Lisachenko, A. A.; Shelimov, B. N.; Kazansky, V. B.; Martra, G.; Coluccia, S. FTIR and TPD Study of the Room Temperature Interaction of a NO-Oxygen Mixture and of NO₂ with Titanium Dioxide. *The Journal of Physical Chemistry C* **2013**, *117*, 10345-10352.
83. Fu, H.; Lin, J.; Shang, G.; Dong, W.; Grassian, V. H.; Carmichael, G. R.; Li, Y.; Chen, J. Solubility of Iron from Combustion Source Particles in Acidic Media Linked to Iron Speciation. *Environmental Science & Technology* **2012**, *46*, 11119-11127.
84. Seinfeld, J. H.; Pandis, S. N.: *Atmospheric Chemistry and Physics: From Air Pollution to Climate Change*; 2 ed.; John Wiley: New York, 2006.
85. Baltrusaitis, J.; Grassian, V. H. Surface Reactions of Carbon Dioxide at the Adsorbed Water-Iron Oxide Interface. *The Journal of Physical Chemistry B* **2005**, *109*, 12227-12230.
86. Baltrusaitis, J.; Schuttlefield, J.; Zeitler, E.; Grassian, V. H. Carbon Dioxide Adsorption on Oxide Nanoparticle Surfaces. *Chemical Engineering Journal* **2011**, *170*, 471-481.
87. Kondratenko, E. V.; Mul, G.; Baltrusaitis, J.; Larrazabal, G. O.; Perez-Ramirez, J. Status and Perspectives of CO₂ Conversion Into Fuels and Chemicals by Catalytic, Photocatalytic and Electrocatalytic Processes. *Energy & Environmental Science* **2013**, *6*, 3112-3135.
88. Roy, S. C.; Varghese, O. K.; Paulose, M.; Grimes, C. A. Toward Solar Fuels: Photocatalytic Conversion of Carbon Dioxide to Hydrocarbons. *ACS Nano* **2010**, *4*, 1259-1278.
89. Luria, M.; Sievering, H. Heterogeneous and Homogeneous Oxidation of SO₂ in the Remote Marine Atmosphere. *Atmospheric Environment. Part A. General Topics* **1991**, *25*, 1489-1496.
90. Kerminen, V.-M.; Pirjola, L.; Boy, M.; Eskola, A.; Teinilä, K.; Laakso, L.; Asmi, A.; Hienola, J.; Lauri, A.; Vainio, V.; Lehtinen, K.; Kulmala, M. Interaction

- Between SO₂ and Submicron Atmospheric Particles. *Atmospheric Research* **2000**, *54*, 41-57.
91. Adams, J. W.; Rodriguez, D.; Cox, R. A. The Uptake of SO₂ on Saharan Dust: A Flow Tube Study. *Atmospheric Chemistry and Physics* **2005**, *5*, 2679-2689.
 92. Nanayakkara, C. E.; Pettibone, J.; Grassian, V. H. Sulfur Dioxide Adsorption and Photooxidation on Isotopically-labeled Titanium Dioxide Nanoparticle Surfaces: Roles of Surface Hydroxyl Groups and Adsorbed Water in the Formation and Stability of Adsorbed Sulfite and Sulfate. *Physical Chemistry Chemical Physics* **2012**, *14*, 6957-6966.
 93. Baltrusaitis, J.; Jayaweera, P. M.; Grassian, V. H. Sulfur Dioxide Adsorption on TiO₂ Nanoparticles: Influence of Particle Size, Coadsorbates, Sample Pretreatment, and Light on Surface Speciation and Surface Coverage. *The Journal of Physical Chemistry C* **2011**, *115*, 492-500.
 94. Baltrusaitis, J.; Cwiertny, D. M.; Grassian, V. H. Adsorption of Sulfur Dioxide on Hematite and Goethite Particle Surfaces. *Physical Chemistry Chemical Physics* **2007**, *9*, 5542-5554.
 95. Zhang, X.; Zhuang, G.; Chen, J.; Wang, Y.; Wang, X.; An, Z.; Zhang, P. Heterogeneous Reactions of Sulfur Dioxide on Typical Mineral Particles. *The Journal of Physical Chemistry B* **2006**, *110*, 12588-12596.
 96. Fu, H.; Wang, X.; Wu, H.; Yin, Y.; Chen, J. Heterogeneous Uptake and Oxidation of SO₂ on Iron Oxides. *The Journal of Physical Chemistry C* **2007**, *111*, 6077-6085.
 97. Shang, J.; Li, J.; Zhu, T. Heterogeneous Reaction of SO₂ on TiO₂ Particles. *Science China Chemistry* **2010**, *53*, 2637-2643.
 98. Garin, F. Mechanism of NO_x Decomposition. *Applied Catalysis A: General* **2001**, *222*, 183-219.
 99. Underwood, G. M.; Miller, T. M.; Grassian, V. H. Transmission FT-IR and Knudsen Cell Study of the Heterogeneous Reactivity of Gaseous Nitrogen Dioxide on Mineral Oxide Particles. *The Journal of Physical Chemistry A* **1999**, *103*, 6184-6190.
 100. Bedjanian, Y.; El Zein, A. Interaction of NO₂ with TiO₂ Surface under UV Irradiation: Products Study. *The Journal of Physical Chemistry A* **2012**, *116*, 1758-1764.
 101. Goodman, A. L.; Bernard, E. T.; Grassian, V. H. Spectroscopic Study of Nitric Acid and Water Adsorption on Oxide Particles: Enhanced Nitric Acid Uptake

- Kinetics in the Presence of Adsorbed Water. *Journal of Physical Chemistry A* **2001**, *105*, 6443-6457.
102. Rubasinghege, G.; Grassian, V. H. Photochemistry of Adsorbed Nitrate on Aluminum Oxide Particle Surfaces. *The Journal of Physical Chemistry A* **2009**, *113*, 7818-7825.
 103. Ndour, M.; Conchon, P.; D'Anna, B.; Ka, O.; George, C. Photochemistry of Mineral Dust Surface as a Potential Atmospheric Renoxification Process. *Geophysical Research Letters* **2009**, *36*, L05816.
 104. Nanayakkara, C. E.; Jayaweera, P. M.; Rubasinghege, G.; Baltrusaitis, J.; Grassian, V. H. Surface Photochemistry of Adsorbed Nitrate: The Role of Adsorbed Water in the Formation of Reduced Nitrogen Species on α -Fe₂O₃ Particle Surfaces. *The Journal of Physical Chemistry A* **2014**, *118*, 158-166.
 105. Atkinson, R.; Arey, J. Atmospheric Degradation of Volatile Organic Compounds. *Chemical Reviews* **2003**, *103*, 4605-4638.
 106. Keene, W. C.; Galloway, J. N.; Holden, J. D. Measurement of Weak Organic Acidity in Precipitation From Remote Areas of the World. *Journal of Geophysical Research: Oceans* **1983**, *88*, 5122-5130.
 107. Rubasinghege, G.; Grassian, V. H. Role(s) of Adsorbed Water in the Surface Chemistry of Environmental Interfaces. *Chemical Communications* **2013**, *49*, 3071-3094.
 108. Ketteler, G.; Yamamoto, S.; Bluhm, H.; Andersson, K.; Starr, D. E.; Ogletree, D. F.; Ogasawara, H.; Nilsson, A.; Salmeron, M. The Nature of Water Nucleation Sites on TiO₂(110) Surfaces Revealed by Ambient Pressure X-ray Photoelectron Spectroscopy. *The Journal of Physical Chemistry C* **2007**, *111*, 8278-8282.
 109. Vittadini, A.; Selloni, A.; Rotzinger, F. P.; Grätzel, M. Structure and Energetics of Water Adsorbed at TiO₂ Anatase (101) and (001) Surfaces. *Physical Review Letters* **1998**, *81*, 2954-2957.
 110. Blomquist, J.; Walle, L. E.; Uvdal, P.; Borg, A.; Sandell, A. Water Dissociation on Single Crystalline Anatase TiO₂(001) Studied by Photoelectron Spectroscopy. *The Journal of Physical Chemistry C* **2008**, *112*, 16616-16621.
 111. Rubasinghege, G.; Ogden, S.; Baltrusaitis, J.; Grassian, V. H. Heterogeneous Uptake and Adsorption of Gas-Phase Formic Acid on Oxide and Clay Particle Surfaces: The Roles of Surface Hydroxyl Groups and Adsorbed Water in Formic Acid Adsorption and the Impact of Formic Acid Adsorption on Water Uptake. *The Journal of Physical Chemistry A* **2013**, *117*, 11316-11327.

112. Ma, Q.; Liu, Y.; Liu, C.; Ma, J.; He, H. A Case Study of Asian Dust Storm Particles: Chemical Composition, Reactivity to SO₂ and Hygroscopic Properties. *Journal of Environmental Sciences* **2012**, *24*, 62-71.
113. Wijenayaka, L. A.; Rubasinghege, G.; Baltrusaitis, J.; Grassian, V. H. Surface Chemistry of α -FeOOH Nanorods and Microrods with Gas-phase Nitric Acid and Water Vapor: Insights into the Role of Particle Size, Surface Structure, and Surface Hydroxyl Groups in the Adsorption and Reactivity of α -FeOOH with Atmospheric Gases. *The Journal of Physical Chemistry C* **2012**, *116*, 12566-12577.
114. Baltrusaitis, J.; Chen, H.; Rubasinghege, G.; Grassian, V. H. Heterogeneous Atmospheric Chemistry of Lead Oxide Particles with Nitrogen Dioxide Increases Lead Solubility: Environmental and Health Implications. *Environmental Science & Technology* **2012**, *46*, 12806-12813.
115. Grassian, V. H. Chemical Reactions of Nitrogen Oxides on the Surface of Oxide, Carbonate, Soot, and Mineral Dust Particles: Implications for the Chemical Balance of the Troposphere. *The Journal of Physical Chemistry A* **2002**, *106*, 860-877.
116. Schuttlefield, J.; Al-Hosney, H.; Zachariah, A.; Grassian, V. H. Attenuated Total Reflection Fourier Transform Infrared Spectroscopy to Investigate Water Uptake and Phase Transitions in Atmospherically Relevant Particles. *Applied Spectroscopy* **2007**, *61*, 283-292.
117. Baltrusaitis, J.; Usher, C. R.; Grassian, V. H. Reactions of Sulfur Dioxide on Calcium Carbonate Single Crystal and Particle Surfaces at the Adsorbed Water Carbonate Interface. *Physical Chemistry Chemical Physics* **2007**, *9*, 3011-3024.
118. Baltrusaitis, J.; Jayaweera, P. M.; Grassian, V. H. XPS Study of Nitrogen Dioxide Adsorption on Metal Oxide Particle Surfaces Under Different Environmental Conditions. *Physical Chemistry Chemical Physics* **2009**, *11*, 8295-8305.
119. Fairley, N. CasaXPS 2.3.14. **1999-2008**.
120. Cwiertny, D. M.; Young, M. A.; Grassian, V. H. Chemistry and Photochemistry of Mineral Dust Aerosol. *Annual Review of Physical Chemistry* **2008**, *59*, 27-51.
121. Thompson, T. L.; Yates, J. T. Surface Science Studies of the Photoactivation of TiO₂ New Photochemical Processes. *Chemical Reviews* **2006**, *106*, 4428-4453.
122. Beaumont, S. K.; Gustafsson, R. J.; Lambert, R. M. Heterogeneous Photochemistry Relevant to the Troposphere: H₂O₂ Production During the Photochemical Reduction of NO₂ to HONO on UV-Illuminated TiO₂ Surfaces. *ChemPhysChem* **2009**, *10*, 331-333.

123. Goodman, A. L.; Li, P.; Usher, C. R.; Grassian, V. H. Heterogeneous Uptake of Sulfur Dioxide On Aluminum and Magnesium Oxide Particles. *The Journal of Physical Chemistry A* **2001**, *105*, 6109-6120.
124. Zhang, C.; Lindan, P. J. D. A density Functional Theory Study of Sulphur Dioxide Adsorption on Rutile $\text{TiO}_2(1\ 1\ 0)$. *Chemical Physics Letters* **2003**, *373*, 15-21.
125. Casarin, M.; Ferrigato, F.; Maccato, C.; Vittadini, A. SO_2 on $\text{TiO}_2(110)$ and $\text{Ti}_2\text{O}_3(1012)$ Nonpolar Surfaces: A DFT Study. *The Journal of Physical Chemistry B* **2005**, *109*, 12596-12602.
126. Grassian, V. H. Surface Science of Complex Environmental Interfaces: Oxide and Carbonate Surfaces in Dynamic Equilibrium With Water Vapor. *Surface Science* **2008**, *602*, 2955-2962.
127. Lange, F.; Hadjiivanov, K.; Schmelz, H.; Knäuper, H. Low temperature infrared study of carbon monoxide adsorption on sulfated titania. *Catalysis Letters* **1992**, *16*, 97-107.
128. Davydov, A.: *Molecular Spectroscopy of Oxide Catalyst Surfaces*; John Wiley & Sons, Ltd, 2003.
129. Deiana, C.; Fois, E.; Coluccia, S.; Martra, G. Surface Structure of TiO_2 P25 Nanoparticles: Infrared Study of Hydroxy Groups on Coordinative Defect Sites. *The Journal of Physical Chemistry C* **2010**, *114*, 21531-21538.
130. Dzwigaj, S.; Arrouvel, C.; Breysse, M.; Geantet, C.; Inoue, S.; Toulhoat, H.; Raybaud, P. DFT makes the morphologies of anatase- TiO_2 nanoparticles visible to IR spectroscopy. *Journal of Catalysis* **2005**, *236*, 245-250.
131. Zhang, M.; Wang, Q.; Chen, C. C.; Zang, L.; Ma, W. H.; Zhao, J. C. Oxygen Atom Transfer in the Photocatalytic Oxidation of Alcohols by TiO_2 : Oxygen Isotope Studies. *Angewandte Chemie-International Edition* **2009**, *48*, 6081-6084.
132. Karge, H. G.; Dalla Lana, I. G. IR Studies of Sulfur Dioxide Adsorption on a Claus Catalyst by Selective Poisoning of Sites. *The Journal of Physical Chemistry* **1984**, *88*, 1538-1543.
133. Goodsel, A. J.; Low, M. J. D.; Takezawa, N. Reactions of Gaseous Pollutants with Solids. II. Infrared Study of Sorption of Sulfur Dioxide on Magnesium Oxide. *Environmental Science & Technology* **1972**, *6*, 268-273.
134. Datta, A.; Cavell, R. G.; Tower, R. W.; George, Z. M. Claus Catalysis .1. Adsorption of SO_2 on the Alumina Catalyst Studied by Ftir and Electron-Paramagnetic-Res Spectroscopy. *Journal of Physical Chemistry* **1985**, *89*, 443-449.

135. Usher, C. R.; Al-Hosney, H.; Carlos-Cuellar, S.; Grassian, V. H. A Laboratory Study of the Heterogeneous Uptake and Oxidation of Sulfur Dioxide on Mineral Dust Particles. *Journal of Geophysical Research: Atmospheres* **2002**, *107*, 4713.
136. Liu, G.; Debnath, S.; Paul, K. W.; Han, W.; Hausner, D. B.; Hosein, H.-A.; Michel, F. M.; Parise, J. B.; Sparks, D. L.; Strongin, D. R. Characterization and Surface Reactivity of Ferrihydrite Nanoparticles Assembled in Ferritin. *Langmuir* **2006**, *22*, 9313-9321.
137. Lo, J. M. H.; Ziegler, T.; Clark, P. D. SO₂ Adsorption and Transformations on γ -Al₂O₃ Surfaces: A Density Functional Theory Study. *The Journal of Physical Chemistry C* **2010**, *114*, 10444-10454.
138. Zhang, Z.; Ewing, G. E. Infrared Spectroscopy of SO₂ Aqueous Solutions. *Spectrochimica Acta Part A: Molecular and Biomolecular Spectroscopy* **2002**, *58*, 2105-2113.
139. Fu, H.; Xu, T.; Yang, S.; Zhang, S.; Chen, J. Photoinduced Formation of Fe(III)-Sulfato Complexes on the Surface of α -Fe₂O₃ and Their Photochemical Performance. *The Journal of Physical Chemistry C* **2009**, *113*, 11316-11322.
140. Yamaguchi, T.; Jin, T.; Tanabe, K. Structure of acid sites on sulfur-promoted iron oxide. *The Journal of Physical Chemistry* **1986**, *90*, 3148-3152.
141. Grassian, V. H.; Schuttlefield, J. D.; Larsen, S. C. ATR-FTIR Spectroscopy in the Undergraduate Chemistry Laboratory. Part II: A Physical Chemistry Laboratory Experiment on Surface Adsorption. *Journal of Chemical Education* **2008**, *85*, 282-null.
142. Yang, Q.; Xie, C.; Xu, Z.; Gao, Z.; Du, Y. Synthesis of Highly Active Sulfate-Promoted Rutile Titania Nanoparticles with a Response to Visible Light. *The Journal of Physical Chemistry B* **2005**, *109*, 5554-5560.
143. Ma, Q.; Liu, Y.; He, H. Synergistic Effect between NO₂ and SO₂ in Their Adsorption and Reaction on γ -Alumina. *The Journal of Physical Chemistry A* **2008**, *112*, 6630-6635.
144. Tarbuck, T. L.; Richmond, G. L. Adsorption and Reaction of CO₂ and SO₂ at a Water Surface. *Journal of the American Chemical Society* **2006**, *128*, 3256-3267.
145. Reid, J. P.; Sayer, R. M. Heterogeneous Atmospheric Aerosol Chemistry: Laboratory Studies of Chemistry on Water Droplets. *Chemical Society Reviews* **2003**, *32*, 70-79.
146. Saur, O.; Bensitel, M.; Saad, A. B. M.; Lavalley, J. C.; Tripp, C. P.; Morrow, B. A. The structure and stability of sulfated alumina and titania. *Journal of Catalysis* **1986**, *99*, 104-110.

147. Pang, C. L.; Lindsay, R.; Thornton, G. Structure of Clean and Adsorbate-Covered Single-Crystal Rutile TiO₂ Surfaces. *Chemical Reviews* **2013**, *113*, 3887-3948.
148. Henderson, M. A.; Lyubinetsky, I. Molecular-Level Insights Into Photocatalysis from Scanning Probe Microscopy Studies on TiO₂(110). *Chemical Reviews* **2013**, *113*, 4428-4455.
149. Chen, X.; Mao, S. S. Titanium Dioxide Nanomaterials: Synthesis, Properties, Modifications, and Applications. *Chemical Reviews* **2007**, *107*, 2891-2959.
150. Jensen, S.; Friend, C. The Dynamic Roles of Interstitial and Surface Defects on Oxidation and Reduction Reactions on Titania. *Topics in Catalysis* **2013**, *56*, 1377-1388.
151. Baltrusaitis, J.; Schuttlefield, J.; Zeitler, E.; Grassian, V. H. Carbon Dioxide Adsorption on Oxide Nanoparticle Surfaces. *Chemical Engineering Journal* **2011**, *170*, 471-481.
152. Su, W.; Zhang, J.; Feng, Z.; Chen, T.; Ying, P.; Li, C. Surface Phases of TiO₂ Nanoparticles Studied by UV Raman Spectroscopy and FT-IR Spectroscopy. *The Journal of Physical Chemistry C* **2008**, *112*, 7710-7716.
153. Liao, L. F.; Lien, C. F.; Shieh, D. L.; Chen, M. T.; Lin, J. L. FTIR Study of Adsorption and Photoassisted Oxygen Isotopic Exchange of Carbon Monoxide, Carbon Dioxide, Carbonate, and Formate on TiO₂. *The Journal of Physical Chemistry B* **2002**, *106*, 11240-11245.
154. Martra, G. Lewis Acid and Base Sites at the Surface of Microcrystalline TiO₂ Anatase: Relationships Between Surface Morphology and Chemical Behaviour. *Applied Catalysis A: General* **2000**, *200*, 275-285.
155. Mino, L.; Spoto, G.; Bordiga, S.; Zecchina, A. Particles Morphology and Surface Properties As Investigated by HRTEM, FTIR, and Periodic DFT Calculations: From Pyrogenic TiO₂ (P25) to Nanoanatase. *The Journal of Physical Chemistry C* **2012**, *116*, 17008-17018.
156. Lavalley, J. C. Infrared Spectrometric Studies of the Surface Basicity of Metal Oxides and Zeolites Using Adsorbed Probe Molecules. *Catalysis Today* **1996**, *27*, 377-401.
157. Baltrusaitis, J.; Schuttlefield, J. D.; Zeitler, E.; Jensen, J. H.; Grassian, V. H. Surface Reactions of Carbon Dioxide at the Adsorbed Water-Oxide Interface. *The Journal of Physical Chemistry C* **2007**, *111*, 14870-14880.
158. Hadjiivanov, K.; Bushev, V.; Kantcheva, M.; Klissurski, D. Infrared Spectroscopy Study of the Species Arising During Nitrogen Dioxide Adsorption on Titania (anatase). *Langmuir* **1994**, *10*, 464-471.

159. Kantcheva, M. M.; Bushev, V. P.; Hadjiivanov, K. I. Nitrogen Dioxide Adsorption on Deuteroylated Titania (anatase). *Journal of the Chemical Society, Faraday Transactions* **1992**, 88, 3087-3089.
160. Szanyi, J. n.; Kwak, J. H.; Chimentao, R. J.; Peden, C. H. F. Effect of H₂O on the Adsorption of NO₂ on γ -Al₂O₃: An in Situ FTIR/MS Study. *The Journal of Physical Chemistry C* **2007**, 111, 2661-2669.
161. Haubrich, J.; Quiller, R. G.; Benz, L.; Liu, Z.; Friend, C. M. In Situ Ambient Pressure Studies of the Chemistry of NO₂ and Water on Rutile TiO₂(110). *Langmuir* **2010**, 26, 2445-2451.
162. Baltrusaitis, J.; Schuttlefield, J.; Jensen, J. H.; Grassian, V. H. FTIR Spectroscopy Combined with Quantum Chemical Calculations to Investigate Adsorbed Nitrate on Aluminium Oxide Surfaces in the Presence and Absence of Co-adsorbed Water. *Physical Chemistry Chemical Physics* **2007**, 9, 4970-4980.
163. Miller, T. M.; Grassian, V. H. Heterogeneous Chemistry of NO₂ on Mineral Oxide Particles: Spectroscopic Evidence for Oxide-coordinated and Water-solvated Surface Nitrate. *Geophysical Research Letters* **1998**, 25, 3835-3838.
164. Angelini, M. M.; Garrard, R. J.; Rosen, S. J.; Hinrichs, R. Z. Heterogeneous Reactions of Gaseous HNO₃ and NO₂ on the Clay Minerals Kaolinite and Pyrophyllite. *The Journal of Physical Chemistry A* **2007**, 111, 3326-3335.
165. Fenn, E. E.; Wong, D. B.; Fayer, M. D. Water Dynamics at Neutral and Ionic Interfaces. *Proceedings of the National Academy of Sciences* **2009**, 106, 15243-15248.
166. Fayer, M. D. Dynamics of Water Interacting with Interfaces, Molecules, and Ions. *Accounts of Chemical Research* **2012**, 45, 3-14.
167. Ma, Q.; He, H.; Liu, Y. In Situ DRIFTS Study of Hygroscopic Behavior of Mineral Aerosol. *Journal of Environmental Sciences* **2010**, 22, 555-560.
168. Nishino, N.; Finlayson-Pitts, B. J. Thermal and Photochemical Reactions of NO₂ on Chromium(iii) Oxide Surfaces at Atmospheric Pressure. *Physical Chemistry Chemical Physics* **2012**, 14, 15840-15848.
169. Goebbert, D. J.; Garand, E.; Wende, T.; Bergmann, R.; Meijer, G.; Asmis, K. R.; Neumark, D. M. Infrared Spectroscopy of the Microhydrated Nitrate Ions NO₃⁻ (H₂O)₁₋₆. *The Journal of Physical Chemistry A* **2009**, 113, 7584-7592.
170. Miller, Y.; Thomas, J. L.; Kemp, D. D.; Finlayson-Pitts, B. J.; Gordon, M. S.; Tobias, D. J.; Gerber, R. B. Structure of Large Nitrate-Water Clusters at Ambient Temperatures: Simulations with Effective Fragment Potentials and Force Fields

- with Implications for Atmospheric Chemistry. *The Journal of Physical Chemistry A* **2009**, *113*, 12805-12814.
171. Falkovich, A. H.; Schkolnik, G.; Ganor, E.; Rudich, Y. Adsorption of Organic Compounds Pertinent to Urban Environments onto Mineral Dust Particles. *Journal of Geophysical Research: Atmospheres* **2004**, *109*, D02208.
 172. Shen, X.; Zhao, Y.; Chen, Z.; Huang, D. Heterogeneous Reactions of Volatile Organic Compounds in the Atmosphere. *Atmospheric Environment* **2013**, *68*, 297-314.
 173. Khare, P.; Kumar, N.; Kumari, K. M.; Srivastava, S. S. Atmospheric Formic and Acetic Acids: An Overview. *Reviews of Geophysics* **1999**, *37*, 227-248.
 174. Bannan, T. J.; Bacak, A.; Muller, J. B. A.; Booth, A. M.; Jones, B.; Le Breton, M.; Leather, K. E.; Ghalaieny, M.; Xiao, P.; Shallcross, D. E.; Percival, C. J. Importance of Direct Anthropogenic Emissions of Formic Acid Measured by a Chemical Ionisation Mass Spectrometer (CIMS) During the Winter ClearfLo Campaign in London, January 2012. *Atmospheric Environment* **2014**, *83*, 301-310.
 175. Wang, Y.; Sun, M.; Li, P.; Li, Y.; Xue, L.; Wang, W. Variation of Low Molecular Weight Organic Acids in Precipitation and Cloudwater at High Elevation in South China. *Atmospheric Environment* **2011**, *45*, 6518-6525.
 176. Nolte, C. G.; Solomon, P. A.; Fall, T.; Salmon, L. G.; Cass, G. R. Seasonal and Spatial Characteristics of Formic and Acetic Acids Concentrations in the Southern California Atmosphere. *Environmental Science & Technology* **1997**, *31*, 2547-2553.
 177. Russell, L. M.; Maria, S. F.; Myneni, S. C. B. Mapping Organic Coatings on Atmospheric Particles. *Geophysical Research Letters* **2002**, *29*, 26-21-26-24.
 178. Iuga, C.; Sainz-Diaz, C. I.; Vivier-Bunge, A. Interaction Energies and Spectroscopic Effects in the Adsorption of Formic Acid on Mineral Aerosol Surface Models. *The Journal of Physical Chemistry C* **2012**, *116*, 2904-2914.
 179. Wu, L. Y.; Tong, S. R.; Hou, S. Q.; Ge, M. F. Influence of Temperature on the Heterogeneous Reaction of Formic Acid on α -Al₂O₃. *The Journal of Physical Chemistry A* **2012**, *116*, 10390-10396.
 180. Wu, L. Y.; Tong, S. R.; Zhou, L.; Wang, W. G.; Ge, M. F. Synergistic Effects between SO₂ and HCOOH on α -Fe₂O₃. *The Journal of Physical Chemistry A* **2013**, *117*, 3972-3979.

181. Miller, K. L.; Lee, C. W.; Falconer, J. L.; Medlin, J. W. Effect of Water on Formic Acid Photocatalytic Decomposition on TiO₂ and Pt/TiO₂. *Journal of Catalysis* **2010**, 275, 294-299.
182. Al-Hosney, H. A.; Carlos-Cuellar, S.; Baltrusaitis, J.; Grassian, V. H. Heterogeneous Uptake and Reactivity of Formic acid on Calcium Carbonate Particles: a Knudsen Cell Reactor, FTIR and SEM Study. *Physical Chemistry Chemical Physics* **2005**, 7, 3587-3595.
183. Liao, L. F.; Wu, W. C.; Chen, C. Y.; Lin, J. L. Photooxidation of Formic Acid vs Formate and Ethanol vs Ethoxy on TiO₂ and Effect of Adsorbed Water on the Rates of Formate and Formic Acid Photooxidation. *The Journal of Physical Chemistry B* **2001**, 105, 7678-7685.
184. Vittadini, A.; Selloni, A.; Rotzinger, F. P.; Grätzel, M. Formic Acid Adsorption on Dry and Hydrated TiO₂ Anatase (101) Surfaces by DFT Calculations. *The Journal of Physical Chemistry B* **2000**, 104, 1300-1306.
185. Miller, K. L.; Falconer, J. L.; Medlin, J. W. Effect of Water on the Adsorbed Structure of Formic Acid on TiO₂ Anatase(101). *Journal of Catalysis* **2011**, 278, 321-328.
186. Miller, K. L.; Musgrave, C. B.; Falconer, J. L.; Medlin, J. W. Effects of Water and Formic Acid Adsorption on the Electronic Structure of Anatase TiO₂(101). *The Journal of Physical Chemistry C* **2011**, 115, 2738-2749.
187. Hatch, C. D.; Gough, R. V.; Tolbert, M. A. Heterogeneous Uptake of the C1 to C4 Organic Acids on a Swelling Clay Mineral. *Atmospheric Chemistry and Physics* **2007**, 7, 4445-4458.
188. Vohs, J. M. Site Requirements for the Adsorption and Reaction of Oxygenates on Metal Oxide Surfaces. *Chemical Reviews* **2013**, 113, 4136-4163.
189. Savory, D. M.; McQuillan, A. J. Influence of Formate Adsorption and Protons on Shallow Trap Infrared Absorption (STIRA) of Anatase TiO₂ During Photocatalysis. *The Journal of Physical Chemistry C* **2013**, 117, 23645-23656.
190. Rotzinger, F. P.; Kesselman-Truttmann, J. M.; Hug, S. J.; Shklover, V.; Grätzel, M. Structure and Vibrational Spectrum of Formate and Acetate Adsorbed from Aqueous Solution onto the TiO₂ Rutile (110) Surface. *The Journal of Physical Chemistry B* **2004**, 108, 5004-5017.
191. Xu, M.; Noei, H.; Buchholz, M.; Muhler, M.; Wöll, C.; Wang, Y. Dissociation of Formic Acid on Anatase TiO₂(101) Probed by Vibrational Spectroscopy. *Catalysis Today* **2012**, 182, 12-15.

192. Panayotov, D. A.; Burrows, S. P.; Morris, J. R. Photooxidation Mechanism of Methanol on Rutile TiO₂ Nanoparticles. *The Journal of Physical Chemistry C* **2012**, *116*, 6623-6635.
193. Nakamoto, K.: *Applications in Coordination Chemistry, in Infrared and Raman Spectra of Inorganic and Coordination Compounds: Part B: Applications in Coordination, Organometallic, and Bioinorganic Chemistry*; 6th Edition ed.; John Wiley & Sons, Inc.: Hoboken, NJ, USA, 2008.
194. Nolan, N. T.; Seery, M. K.; Pillai, S. C. Spectroscopic Investigation of the Anatase-to-Rutile Transformation of Sol-Gel-Synthesized TiO₂ Photocatalysts. *The Journal of Physical Chemistry C* **2009**, *113*, 16151-16157.
195. El-Maazawi, M.; Finken, A. N.; Nair, A. B.; Grassian, V. H. Adsorption and Photocatalytic Oxidation of Acetone on TiO₂: An in Situ Transmission FT-IR Study. *Journal of Catalysis* **2000**, *191*, 138-146.
196. Tong, S. R.; Wu, L. Y.; Ge, M. F.; Wang, W. G.; Pu, Z. F. Heterogeneous Chemistry of Monocarboxylic Acids on α -Al₂O₃ at Different Relative Humidities. *Atmos. Chem. Phys.* **2010**, *10*, 7561-7574.
197. Nunzi, F.; De Angelis, F. DFT Investigations of Formic Acid Adsorption on Single-Wall TiO₂ Nanotubes: Effect of the Surface Curvature. *The Journal of Physical Chemistry C* **2010**, *115*, 2179-2186.
198. Muggli, D. S.; McCue, J. T.; Falconer, J. L. Mechanism of the Photocatalytic Oxidation of Ethanol on TiO₂. *Journal of Catalysis* **1998**, *173*, 470-483.
199. Ullerstam, M.; Johnson, M. S.; Vogt, R.; Ljungström, E. DRIFTS and Knudsen Cell Study of the Heterogeneous Reactivity of SO₂ and NO₂ on Mineral Dust. *Atmos. Chem. Phys.* **2003**, *3*, 2043-2051.
200. Underwood, G. M.; Li, P.; Al-Abadleh, H.; Grassian, V. H. A Knudsen Cell Study of the Heterogeneous Reactivity of Nitric Acid on Oxide and Mineral Dust Particles. *The Journal of Physical Chemistry A* **2001**, *105*, 6609-6620.
201. Mitoraj, D.; Beranek, R.; Kisch, H. Mechanism of Aerobic Visible Light Formic Acid Oxidation Catalyzed by Poly(tri-s-triazine) Modified Titania. *Photochemical & Photobiological Sciences* **2010**, *9*, 31-38.
202. Civiš, S.; Ferus, M.; Zukalová, M.; Kubát, P.; Kavan, L. Photochemistry and Gas-Phase FTIR Spectroscopy of Formic Acid Interaction with Anatase Ti¹⁸O₂ Nanoparticles. *The Journal of Physical Chemistry C* **2012**, *116*, 11200-11205.
203. Yu, Y.; Ezell, M. J.; Zelenyuk, A.; Imre, D.; Alexander, L.; Ortega, J.; Thomas, J. L.; Gogna, K.; Tobias, D. J.; D'Anna, B.; Harmon, C. W.; Johnson, S. N.; Finlayson-Pitts, B. J. Nitrate Ion Photochemistry at Interfaces: A New Mechanism

- for Oxidation of α -pinene. *Physical Chemistry Chemical Physics* **2008**, *10*, 3063-3071.
204. Jacobi, H. W.; Annor, T.; Quansah, E. Investigation of The Photochemical Decomposition of Nitrate, Hydrogen Peroxide, and Formaldehyde in Artificial Snow. *Journal of Photochemistry and Photobiology A: Chemistry* **2006**, *179*, 330-338.
 205. Honrath, R. E.; Peterson, M. C.; Guo, S.; Dibb, J. E.; Shepson, P. B.; Campbell, B. Evidence of NO_x Production Within or Upon Ice Particles in the Greenland Snowpack. *Geophysical Research Letters* **1999**, *26*, 695-698.
 206. Jones, A. E.; Weller, R.; Wolff, E. W.; Jacobi, H. W. Speciation and Rate of Photochemical NO and NO₂ Production in Antarctic Snow. *Geophysical Research Letters* **2000**, *27*, 345-348.
 207. Honrath, R. E.; Peterson, M. C.; Dziobak, M. P.; Dibb, J. E.; Arsenault, M. A.; Green, S. A. Release of NO_x from Sunlight-irradiated Midlatitude Snow. *Geophysical Research Letters* **2000**, *27*, 2237-2240.
 208. Mack, J.; Bolton, J. R. Photochemistry of Nitrite and Nitrate in Aqueous Solution: A Review. *Journal of Photochemistry and Photobiology A: Chemistry* **1999**, *128*, 1-13.
 209. Hudson, P. K.; Schwarz, J.; Baltrusaitis, J.; Gibson, E. R.; Grassian, V. H. A Spectroscopic Study of Atmospherically Relevant Concentrated Aqueous Nitrate Solutions. *The Journal of Physical Chemistry A* **2007**, *111*, 544-548.
 210. Minero, C.; Chiron, S.; Falletti, G.; Maurino, V.; Pelizzetti, E.; Ajassa, R.; Carlotti, M.; Vione, D. Photochemical Processes Involving Nitrite in Surface Water Samples. *Aquatic Sciences* **2007**, *69*, 71-85.
 211. Goldstein, S.; Rabani, J. Mechanism of Nitrite Formation by Nitrate Photolysis in Aqueous Solutions: The Role of Peroxynitrite, Nitrogen Dioxide and Hydroxyl Radical. *Journal of the American Chemical Society* **2007**, *129*, 10597-10601.
 212. Dubowski, Y.; Sumner, A. L.; Menke, E. J.; Gaspar, D. J.; Newberg, J. T.; Hoffman, R. C.; Penner, R. M.; Hemminger, J. C.; Finlayson-Pitts, B. J. Interactions of Gaseous Nitric Acid with Surfaces of Environmental Interest. *Physical Chemistry Chemical Physics* **2004**, *6*, 3879-3888.
 213. Rivera-Figueroa, A. M.; Sumner, A. L.; Finlayson-Pitts, B. J. Laboratory Studies of Potential Mechanisms of Renoxification of Tropospheric Nitric Acid. *Environmental Science & Technology* **2003**, *37*, 548-554.
 214. Baergen, A. M.; Donaldson, D. J. Photochemical Renoxification of Nitric Acid on Real Urban Grime. *Environmental Science & Technology* **2013**, *47*, 815-820.

215. Moussa, S. G.; Stern, A. C.; Raff, J. D.; Dilbeck, C. W.; Tobias, D. J.; Finlayson-Pitts, B. J. Experimental and Theoretical Studies of the Interaction of Gas Phase Nitric Acid and Water with a Self-assembled Monolayer. *Physical Chemistry Chemical Physics* **2013**, *15*, 448-458.
216. Frinak, E. K.; Wermeille, S. J.; Mashburn, C. D.; Tolbert, M. A.; Pursell, C. J. Heterogeneous Reaction of Gaseous Nitric Acid on γ -Phase Iron(III) Oxide. *The Journal of Physical Chemistry A* **2004**, *108*, 1560-1566.
217. Mashburn, C. D.; Frinak, E. K.; Tolbert, M. A. Heterogeneous Uptake of Nitric Acid on Na-Montmorillonite Clay as a Function of Relative Humidity. *Journal of Geophysical Research: Atmospheres* **2006**, *111*, D15213.
218. Gankanda, A.; Grassian, V. H. Nitrate Photochemistry in NaY Zeolite: Product Formation and Product Stability under Different Environmental Conditions. *The Journal of Physical Chemistry A* **2013**, *117*, 2205-2212.
219. Kleffmann, J. Daytime Sources of Nitrous Acid (HONO) in the Atmospheric Boundary Layer. *ChemPhysChem* **2007**, *8*, 1137-1144.
220. Schwertmann, U.; Cornell, R. M.: *Iron Oxides : Structure, Properties, Reactions, Occurrences and Uses (2nd Edition)*; Wiley-VCH: Hoboken, NJ, USA, 2007.
221. Torres, J.; Perry, C. C.; Bransfield, S. J.; Fairbrother, D. H. Low-Temperature Oxidation of Nitrided Iron Surfaces. *The Journal of Physical Chemistry B* **2003**, *107*, 5558-5567.
222. Rodriguez, J. A.; Jirsak, T.; Liu, G.; Hrbek, J.; Dvorak, J.; Maiti, A. Chemistry of NO₂ on Oxide Surfaces: Formation of NO₃ on TiO₂(110) and NO₂↔O Vacancy Interactions. *Journal of the American Chemical Society* **2001**, *123*, 9597-9605.
223. Schmitz, P. J.; Baird, R. J. NO and NO₂ Adsorption on Barium Oxide: Model Study of the Trapping Stage of NO_x Conversion via Lean NO_x Traps. *The Journal of Physical Chemistry B* **2002**, *106*, 4172-4180.
224. Jirsak, T.; Kuhn, M.; Rodriguez, J. A. Chemistry of NO₂ on Mo(110): Decomposition Reactions and Formation of MoO₂. *Surface Science* **2000**, *457*, 254-266.
225. Rusu, C. N.; Yates, J. T. Photochemistry of NO Chemisorbed on TiO₂(110) and TiO₂ Powders. *The Journal of Physical Chemistry B* **2000**, *104*, 1729-1737.
226. Overbury, S. H.; Mullins, D. R.; Huntley, D. R.; Kundakovic, L. Chemisorption and Reaction of NO and N₂O on Oxidized and Reduced Ceria Surfaces Studied by Soft X-Ray Photoemission Spectroscopy and Desorption Spectroscopy. *Journal of Catalysis* **1999**, *186*, 296-309.

227. Warschkow, O.; Ellis, D. E.; Hwang, J.; Mansourian-Hadavi, N.; Mason, T. O. Defects and Charge Transport near the Hematite (0001) Surface: An Atomistic Study of Oxygen Vacancies. *Journal of the American Ceramic Society* **2002**, *85*, 213-220.
228. Henderson, M. A. Evidence for Bicarbonate Formation on Vacuum Annealed TiO₂(110) Resulting from a Precursor-mediated Interaction Between CO₂ and H₂O. *Surface Science* **1998**, *400*, 203-219.
229. El Zein, A.; Romanias, M. N.; Bedjanian, Y. Kinetics and Products of Heterogeneous Reaction of HONO with Fe₂O₃ and Arizona Test Dust. *Environmental Science & Technology* **2013**, *47*, 6325-6331.
230. Mogili, P. K.; Kleiber, P. D.; Young, M. A.; Grassian, V. H. Heterogeneous Uptake of Ozone on Reactive Components of Mineral Dust Aerosol: An Environmental Aerosol Reaction Chamber Study. *The Journal of Physical Chemistry A* **2006**, *110*, 13799-13807.
231. Schuttlefield, J.; Rubasinghege, G.; El-Maazawi, M.; Bone, J.; Grassian, V. H. Photochemistry of Adsorbed Nitrate. *Journal of the American Chemical Society* **2008**, *130*, 12210-12211.
232. Finlayson-Pitts, B. J.; Wingen, L. M.; Sumner, A. L.; Syomin, D.; Ramazan, K. A. The Heterogeneous Hydrolysis of NO₂ in Laboratory Systems and in Outdoor and Indoor Atmospheres: An Integrated Mechanism. *Physical Chemistry Chemical Physics* **2003**, *5*, 223-242.
233. Monge, M. E.; D'Anna, B.; George, C. Nitrogen Dioxide Removal and Nitrous Acid Formation on Titanium Oxide Surfaces-An Air Quality Remediation Process? *Physical Chemistry Chemical Physics* **2010**, *12*, 8991-8998.
234. Wiesen, P.; Kleffmann, J.; Kurtenbach, R.; Becker, K. H. Mechanistic Study of the Heterogeneous Conversion of NO₂ into HONO and N₂O on Acid Surfaces. *Faraday Discussions* **1995**, *100*, 121-127.
235. Malecki, A.; Maleka, B. Formation of N₂O During Thermal Decomposition of d-metal Hydrates Nitrates. *Thermochimica Acta* **2006**, *446*, 113-116.